Abderrahmane Benchirouf

Carbonaceous Nanofillers and Poly (3,4-ethylenedioxythiophene) Poly (styrenesulfonate) Nanocomposites for Wireless Sensing Applications

Scientific Reports on Measurement and Sensor Technology

Volume 8
Prof- Dr.-Ing. Olfa Kanoun (Editor)

Abderrahmane Benchirouf

Carbonaceous Nanofillers and Poly (3,4-ethylenedioxythiophene) Poly(styrenesulfonate) Nanocomposites for Wireless Sensing Applications

TECHNISCHE UNIVERSITÄT
CHEMNITZ

Universitätsverlag Chemnitz
2018

Impressum

Bibliografische Information der Deutschen Nationalbibliothek

Die Deutsche Nationalbibliothek verzeichnet diese Publikation in der Deutschen Nationalbibliografie; detaillierte bibliografische Angaben sind im Internet über http://www.dnb.de abrufbar.

Titelgrafik: Chemnitz School of Metrology
Satz/Layout: Abderrahmane Benchirouf

Technische Universität Chemnitz/Universitätsbibliothek
Universitätsverlag Chemnitz
09107 Chemnitz
https://www.tu-chemnitz.de/ub/univerlag

readbox unipress
in der readbox publishing GmbH
Am Hawerkamp 31
48155 Münster
http://unipress.readbox.net

ISSN 2509-5102 print - ISSN 2509-5110 online

ISBN 978-3-96100-068-5

http://nbn-resolving.de/urn:nbn:de:bsz:ch1-qucosa2-319037

TECHNISCHE UNIVERSITÄT
CHEMNITZ

Carbonaceous Nanofillers and Poly(3,4-ethylenedioxythiophene) Poly(styrenesulfonate) Nanocomposites for Wireless Sensing Applications

Von der Fakultät für Elektrotechnik und Informationstechnik
der
Technischen Universität Chemnitz

genehmigte

Dissertationzur Erlangung des akademischen Grades

Doktor-Ingenieur
(Dr.-Ing.)

vorgelegt

von: M. Sc. Abderrahmane Benchirouf
geboren in: Gharien (Libyen)

Gutachter:
Univ.-Prof. Dr.-Ing Olfa Kanoun (Technische Universitat Chemnitz)
Univ.-Prof. Dr. Ulrich Theodor Schwarz (Technische Universitat Chemnitz)

Tag der Einreichung: 16. Januar 2018
Tag der Verteidigung: 21. August 2018

to my parents Souhila & Amor Benchirouf

Bibliographic Description

Benchirouf, Abderrahmane

Carbonaceous Nanofillers and Poly (3,4-ethylenedioxythiophene) Poly(styrenesulfonate) Nanocomposites for Wireless Sensing Applications

Dissertation at the Faculty of Electrical Engineering and Information Technology
Technical University of Chemnitz, Professorship of Electrical Measurements and Sensor Technology, 2018

180 pages, 125 Figures, 23 Tables, 336 References

The current state of wireless sensing technologies possesses a good reliability in terms of time response and sensing on movable parts or in embedded structures. Nevertheless, these technologies involve energy supply such as battery and suffer from low resolution and bulky signal conditioning system for data processing. Thus, a RFID passive wireless sensor is a good candidate to overcome these issues. The feasibility of implementing microstrip patch antennas for sensing application were successfully investigated; however, low sensitivity was always a big issue to be concerned. Sensors based on nanocomposites attracted a lot of attention because of their excellent performance in term of light weight, high sensitivity, good stability and high resistance to corrosion but it lacks the capability of high conductivity, which limit their implication into RFID applications. This work introduces a novel high sensitive passive wireless strain and temperature sensors based on nanocomposites as sensing layer. To accomplish this, intrinsically conductive polymer based on carbon nanofillers nanocomposites are deeply studied and characterized. Then it's performance is evaluated. Among them a novel tertiary nanocomposite is introduced, which opens the gate to new nanocomposite applications and thus broadens the application spectrum. Understanding the transport mechanism to improve the conductivity of the nanocomposite and extracting individually different models based on physical explanation of their piezoresistivity, and behavior under temperature and humidity have been developed. Afterwards, selected nanocomposites based on their high sensitivity to either strain or temperature are chosen to be used as sensing layer for patch antenna. The fabricated patch antenna has only one fundamental frequency, by determining the shift in its resonance frequency as function of the desired property to be measured; the wireless sensor characteristics are then examined. For strain sensing, the effect of strain is tested experimentally with the help of end-loaded beam measurement setup. For temperature sensing, the sensors are loaded in a controlled temperature/humid chamber and with the help of a vector network analyzer, the sensitivity of the antennas are extracted by acquiring the shift in the resonance frequency. The fabricated wireless sensors based on patch antenna are fabricated on very low lossy material to improve their gain and radiation pattern. This approach could be expanded also to include different type of substrates such as stretchable substrates i.e. elastomer polymer, very thing substrates such as Kapton, paper-based substrates or liquid crystal polymer.

Keywords: intrinsic conductive polymer, carbon nanotubes, graphene oxide, nanocomposite and wireless sensors

Bibliographische Beschreibung

Benchirouf, Abderrahmane

Kohlenstoffnanomaterial/PEDOT:PSS Nanokomposite für drahtlose Sensoranwendungen

Dissertation an der Fakultät für Elektrotechnik und Informationstechnik der
Technischen Universität Chemnitz, Professur für Mess- und Sensortechnik, 2018

180 Seiten, 125 Abbildungen, 23 Tabellen, 336 Literaturstellen

Derzeitige drahtlose Sensortechnologien besitzten eine gute Zuverlässigkeit in Bezug auf Zeitverhalten und Erfassung auf beweglichen Teilen oder in eingebetteten Strukturen. Dennoch beinhalten diese Technologien die Energieversorgung wie die z.B. mit Batterie und und weisen eine niedrige Auflösung, sowie eine schwierige Signalkonditionierung und Datenverarbeitung auf. RFID Sensoren sind in der Lage diese Probleme zu überwinden. Die Machbarkeit von Patch-Antennen für Sensoranwendungen wurde gezeigt. Herausforderung bleibt die geringe Empfindlichkeit und die begrenzte elektrische Leitfähigkeit, welches den Anwendungsbereich einschränkt. Andererseits sind die Sensoren auf der Basis von Nanokompositen empfindlicher als konventionelle Sensoren und zeichnen sich durch geringes Gewicht, Korrosionsbeständigkeit und mechanische Stabilität aus. Diese Arbeit beschäftigt sich mit neue hochempfindliche, passive drahtlose Dehnungs- und Temperaturssensoren, die auf Nanokompositen als Sensorschicht basieren. Um dies zu erreichen, werden intrinsisch leitfähige Polymer-basierte Kohlenstoff-Nanofiller-Nanokomposite hergestellt, charakterisiert und ihre Eingenschaften diskutiert. Darunter wird eine neuartige tertiäre Nanokomposit-Klasse eingeführt, die Potential für diverse Nanokompositen-Anwendungen hat und damit das Anwendungsspektrum erweitert. Die Transportmechanismen jedes Nanokomposits, die maßgeblich bestimmend für die Piezoresitivität, sowie das Temperatur- und Feuchtigkeitsverhalten sind, wurden mit Hilfe von unterschiedlichen physikalischen Modellen diskutiert. Danach wurden ausgewählte Nanokomposite auf der Basis ihrer hohen Empfindlichkeit gegenüber Belastung, Temperatur oder Feuchtigkeit ausgewählt, um als Sensorschicht der Patchantenne verwendet zu werden. Die gefertigte Patch-Antenne hat eine Grundfrequenz, die sich in Abhängigkeit der gewünschten Messgröße verschiebt. die drahtlosen Sensorcharakteristiken wurden dann geschätzt. Für die Dehnungsmessung wird der Effekt der Belastung experimentell mit Hilfe des Biegebalken getestet. Für die Temperaturmessung wurden die Sensoren in eine kontrollierte Temperatur/ Feuchtekammer positioniert und mit Hilfe eines Vektor-Netzwerk-Analysators wurde die Empfindlichkeit der Patch-Antennen durch Erfassen der Verschiebung der Resonanzfrequenz extrahiert. Die gefertigte drahtlosen Patch-Antennen wurden auf Materialien mit geringem Verlustfaktor hergestellt, um ihre Abstrahlcharakteristiken zu verbessern. Dieser Ansatz wurde auch gewählt, ist auf verschiedene Arten von Substraten anwendbarwie z.B. Elastomere, Kapton, Papier und Flüssigkristallpolymere.

Schlagwörter: Intrinsisch leitfähige Polymere, Kohlenstoffnanoröhren, Graphenoxid, Nanokomposite und drahtlose Sensoren

Contents

List of Abbreviations

ABS	Acrylonitrile-Butadiene-Styrene
ADAS	Active Data Acquisition System
AFM	Atomic Force Microscopy
AgNW	Silver Nanowire
CA	Contact Angle
CELT	Charging Energy Limit Tunneling
CMC	Critical Micelle Concentration
CMPA	Circular Microstrip Patch Antenna
CNF	Carbon Nanofiller
CNT	Carbon Nanotube
CTAB	Cethyltrimethylammonium
CVD	Chemical Vapor Deposition
DAS	Data Acquisition System
DC	Direct Current
DCB	1,2 Dichlorobenzene
DMF	Dimethylformamidem
DNA	Deoxyribonucleic Acid
DSC	Differential Scanning Calorimetry
ECP	Electrically Conductive Polymer
EMI	Electromagnetic Interference
FET	Field Effect Transistor
FR4	Glass-Reinforced Epoxy Laminate
FTIR	Fourier Transform Infrared Spectroscopy
GO	Graphene Oxide

HDPE	High Density Polyethylene
HF	High Frequency
HNO3	Nitric Acid
HOMO	Highest Occupied Molecular Orbital
HRTEM	High Resolution Tranmission Electron Microsopy
H2SO4	Sulfuric Acid
ITO	Indium Tin Oxide
LC	Inductor-Capacitor
IC	Integrated Circuit
ICP	Intrinsically Conductive Polymer
KClO3	Potassium Chlorate
KMnO4	Potassium Permanganate
LF	Low Frequency
LTCC	Low Temperature Co-fired Ceramic
LUMO	Lowest Unoccupied Molecular Orbital
MEMS	Micro Electro Mechanical System
MPA	Microstrip Patch Antenna
MWCNT	Multi-Walled Carbon Nanotube
NaBH4	Sodium Borohydride
NaCh	Sodium Cholrate
NH3	Ammonia Gas
NIR	Near-Infrared
NMP	N-Methyl-Pyrrolidone
NO3	Nitrate Gas
ODM	Optical Digital Microscopy
OLED	Organic Light Emitting Diode
PA	Polyacetylene
PANI	Polyaniline
P3AT	Poly(3-alkyl)Thiophene

PC	Polycarbonate
PDMS	Polydimethylsiloxane
PE	Polyethylene
PECVD	Plasma Enhanced Chemical Vapor Deposition
PEDOT	Poly(3,4-Ethylene Dioxythiophene)
PEDOT:PSS	Poly(3,4-Ethylene Dioxythiophene) Poly-(Styrene Sulfonic Acid)
PEEK	Polyether Ether Ketone
PET	Poly(Ethylene Terephthalate)
PH	Potential of Hydrogene
PL	Photoluminescence
PMMA	Poly(Methyl Methacrylate)
PP	Polypropylene
PPh	Polyphenylene
PPP	Polyparaphenylene
PPV	Polyparaphenylene Vinylene
PPy	Polypyrole
PS	Polystyrene
PSS	Poly-(Styrene Sulfonic Acid)
PT	Polythiophene
PTFE	Polytetrafluoroethylene
PU	Polyurethane
PVA	Poly(Vinyl Alcohol)
PVDE	Poly(Vinylidene Fluoride)
PVP	Poly Vinyl Pyrrolidone
RFID	Radio Frequency Indentification
RMPA	Rectangular Microstrip Patch Antenna
SC	Sodium Cholate
SDBS	Sodium Dodecylbenzene Sulfonate
SDS	Sodium Dodecyl Sulfate
SEBS	Styrene-Ethylene/Butylene-Styrene
SEM	Scanning Electron Microscopy
SHF	Super High Frequency
SHM	Structural Health Monitoring
SO3H	Sulfonic Acid
ST	Surface Tension
SWCNT	Single-Walled Carbon Nanotube

TCR	Temperature Coefficient of Resistance
TEM	Tranmission Electron Microsopy
UHF	Ultra High Frequency
UV-Vis	Ultra Violet Visible
UWB	Ultra Wideband
VLSI	Very Large Scale Interconnect
VNA	Vector Network Analyzer
VRH	Variable Range Hopping
XPS	X-Ray Photoelectron Spectroscopy

List of Symbols

f	Frequency	GHz
L	Length	m
S_{11}	Scattering parameters	dB
T	Temperature	°C
ε_r	Permitivity	F/m
σ_r	Conductivity	S/m
Gn	Gain antenna	dB
μ_c	Chemical potential	eV
Tg	Glass transition temperature	°C
d	Density	g/cm^3
η	Viscosity	Pa.s
E_{gap}	Energy Bandgap	eV
k_b	Boltzmann constant	eV.K^{-1}
γ_0	C-C tight binding energy	eV
J	Current density	A/m^2
G	Quantum conductance	S
e	Electron charge	C
h	Planck's constant	eV.s
E	Young's Modulus	TPa
σ_T	Tensile strength	GPa
F	Force	N
κ	Thermal conductivity	W/mK
vdW	van der Waals force	eV/nm
P	Pressure	Pa
V	Voltage	V
I	Electrical current	A
C_s	Specific capacitance	F/g
ϕ	Conductive filler volume	vol.%
ϕ_ρ	Percolation threshold	wt.%
ρ	Resistivity	Ω.m
$R_{tunelling}$	Tunneling resistance	kΩ

A	Cross section area	mm^2
m_e	Electron mass	kg
G	Shear modulus	MPa
E_{33}	Axial elastic modulus	MPa
E_{11}	Transverse elastic modulus	MPa
G_{12}	In-plane shear modulus	Pa
ϕ_s	Volume fraction at percolation threshold	vol.%
t	Thickness	μm
V	Volume	μl
ν_{sg}	Solid–gas surface (interfacial) energy	mJ/m^2
ν_{sl}	Solid–liquid surface (interfacial) energy	mJ/m^2
ν_{lg}	Liquid–gas surface (interfacial) energy	mJ/m^2
CA	Contact angle	$^\circ$
λ	Wavelength	nm
υ	Light frequency	Hz
σ_s	Surface conductivity	S/m
ρ	Bulk resistivity	Ω.m
ρ	Sheet resistance	$\Omega.sq^{-1}$
f_{res}	Resonance frequency of antenna	GHz
I	Moment of inertia	m^4
m	Mass	g
a	Acceleration	m/s
σ	Stress	N/m^2
γ	Surface tension	N/m
A	Optical absorption	$\%$
α	Absorption coefficient	L.g^{-1}.cm^{-1}
Ψ	Colloidal concentration	wt.%
TCR	Temperature coefficient of resistance	C^{-1}
e_g	Activation energy	eV
R_{inx}	Input resistance at antenna edge	Ω
Z	Impedance	Ω
g	Feed-inset gap	μm
α_{re}	Thermal coefficient of substrate	K^{-1}
α_L	Thermal coefficient of patch	K^{-1}

t	Scaling factor
k	Gauge factor
Q	Quality factor
ν	Poisson's ratio

M	Bending moment
ε_r	Dielectric constant
ζ	Aspect ratio of the nanofiller
α	Carbon nanotube waviness parameter

1 Introduction

A broad interest is shown in both research and practical of electrically conductive polymers (ECPs) and their related applications in a wide range of industrial sectors, which range from electronics and automotive to biomedical and aerospace, to name a few. This is clearly reflected, by the award of the Nobel prize in 2000 in Chemistry that went to Alan J. Heeger, Alan G. MacDiarmid and Hideki Shirakawa for the discovery and development of conductive polymers. These demands are projected to go up with steady emergence of new applications and advances in material synthesis and manufacturing techniques. ECPs have many advantages in comparison with the conventional metals for different applications, including low weight and ease of processing, among others.

Another edge of ECPs is their broad and tunable conductivity spectrum (Figure 1.1), which can be exploited for a sort of applications such as: Antistatic, static dissipation, electromagnetic interference shielding (EMI). To further improve their properties, carbon nanofillers (CNF) can offer better conductive performance with minimal effects to the intrinsic properties of the hosting polymers. Thanks to the excellent electrical, mechanical, thermal and optical properties, CNF-based nanocomposites also possess a range of additional properties suitable for multi-functional and high-performance applications such as wireless sensing. On one side, as it is shown in Figure 1.1, composites have limited conductivity compared to metals, which limits their applicability in the wireless communication. On the other side, increasing the conductivity alters the sensing properties such as strain, pressure etc. As these physical phenomena are based on the change in the internal bandgap of the material, and high conductive materials have very small or even no bandgap, therefore they possess very low sensitivity when they are used in this type of applications. Apparently, using nanocomposites can overcome this problem, due to the exceptional properties, tunable conductivity and high sensitivity.

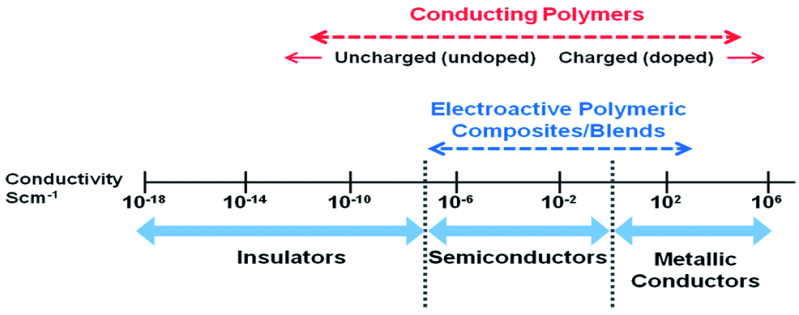

Figure 1.1: Electrical conductivity spectrum of polymers and composites. Reproduced from RSC Advances ©2015 published in [1].

1.1 Objectives

One of the most important intrinsic conducting polymers is poly(3,4-ethylene dioxythiophene) polystyrene sulfonate (PEDOT:PSS), which has the highest conductivity available in the market. Thus, many studies reported a wide application areas of the PEDOT:PSS in organic solar cells, flexible electrodes, gas sensors, and other chemi-sensing systems. Nanocomposites using intrinsic conductive polymers as a matrix and carbon nanotubes (CNTs) and/or graphene oxide (GO) as nanofillers have up to now limited focus, and less importance is engaged on the fundamental understanding of CNT and/or GO-ECPs piezoresistive, hygroscopic properties and the nature of their transport mechanism. By better understanding the piezoresistive and hygroscopic characteristics, an enhancement in the application response and even new application areas such a wireless sensing can be explored. Besides, a very few research has been done on using nanocomposites for wireless passive sensing of strain and temperature.

Figure 1.2 depicts an overview of the approach used in this dissertation, and the aims of this research are summarized as follows:

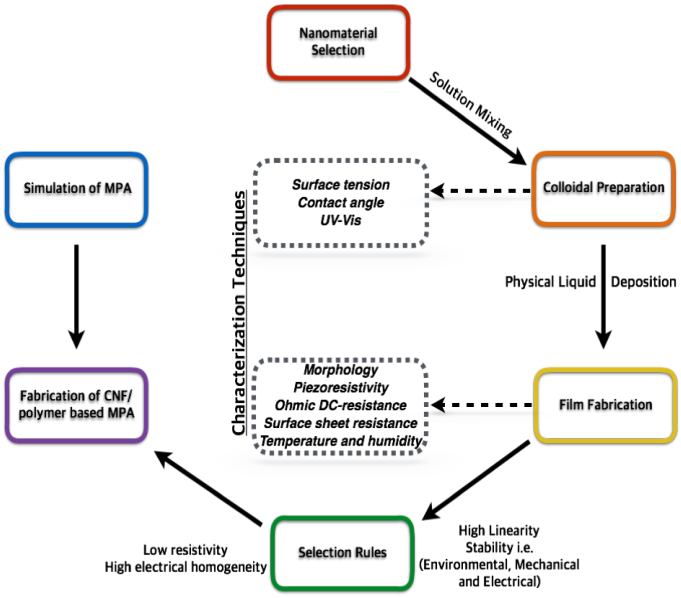

Figure 1.2: Methodology overview of this work

- Selection and development of nanocomposites with high conductivity and adequate sensing properties.
- Design of an appropriate experiment methodology to optimize the nanocomposite dispersion quality.
- Fabrication of different types of CNF/intrinsic polymer nanocomposites and characterize their morphological, optical and electromechanical properties to understand the effect of integration of CNF in the polymer matrix experimentally.
- Understanding the nature of the transport mechanism occurring within this type of nanocomposites.
- Introduction of a novel tertiary nanocomposite based on hybrid CNF/intrinsic conductive polymer, which includes two different types of conductive nanofillers to produce high

conductive, high strain sensitive nanocomposite and characterize their electrical and mechanical properties in terms of its transport conduction.

- Definition of selection rules for nanocomposites, which are suitable for wireless sensing and prove the feasibility of using them as sensing layer upon a microstrip patch antennas (MPAs) for passive wireless sensing.
- Multiphysics modeling of passive wireless sensors based on patch antenna for strain sensing, and temperature measurements and prediction of their behavior in real applications.

1.2 Thesis Outline

This dissertation is organized as follows. Chapter 2 is devoted to a literature review on wireless sensing with the main focus on MPAs as passive sensing elements for strain and temperature sensing, to recognize the existing gaps in this field. After that an essay of using nanomaterials such as functionalized CNTs, pristine PEDOT:PSS and nanowires for sensing application is illustrated.
In chapter 3, a review is given on conjugated polymers with emphasis on PEDOT:PSS, carbon nanotube and graphene oxide and their nanocomposites. Afterwards, the basic understanding of the electrical characteristics of the CNF/intrinsic conductive polymer and the parameters influencing its conductivity is pointed out.
Chapter 4 details the preparation steps of different nanocomposites namely, MWCNT: SDBS/PEDOT:PSS, GO:MWCNT and GO:MWCNT/PEDOT:PSS. Additionally, for the GO-nanocomposites, chemical reduction is described. Next, the films fabrication is explained. Then, a detailed explanation of all the characterization techniques used in this work is given.
Chapter 5 aims to discuss the experimental results of the MWCNT:SDBS/PEDOT:PSS nanocomposite. Here the physiochemical properties in terms of contact angle and surface tension are explained, tuning the optical bandgap of the nanocomposite using different MWCNT contents is studied using the UV-Vis spectroscopy. The DC-ohmic resistance and the surface conductivity of the films based on MWCNT:SDBS/ PEDOT:PSS is investigated and the electronic transport occurring is explained. Next the piezoresistive property of the films are studied using a universal test machine and the model describing its piezoresistivity is derived. The effect of temperature and humidity is studied and the resulting behavior is described.
Chapter 6 is devoted to discuss the experimental results of GO:MWCNT nanocomposites. The surface tension and the contact angle are studied to understand the physiochemical characteristics of the aqueous colloids. Using Tauc plot, the change in the optical bandgap is demonstrated and explained. The piezoresistivity of the films based GO:MWCNT is investigated using a universal test machine and the effect of the temperature and the humidity is also characterized and the resulting behaviors are explained.
In chapter 7, a novel tertiary nanocomposite GO:MWCNT/PEDOT:PSS is proposed to produce nanocomposite with synergetic properties of PEDTO:PSS and GO:MWCNT. The surface wettability in terms of contact angle and surface tension are studied to determine how good is the intermolecular interaction between this nanocomposite and the flexible polymer substrate. The DC-ohmic resistance and surface conductivity is deeply investigated before and after the chemical reduction and the improvement in the electronic transport is explained. The piezoresistive property of the films are studied before and after the chemical reduction and the model describing its piezoresistivity behavior is introduced. The impact of the environmental effect is described.

Chapter 8 is devoted to test the feasibility of using the obove-mentioned nanocomposites for wireless sensing based on MPA. Multiphysics and electromagnetic simulation of the patch antenna for strain sensing is illustrated, and the experimental results of using the MPA for strain and temperature measurements are explored. Research summary and future work are outlined in Chapter 9. Outline of the thesis is depicted in Figure 1.3.

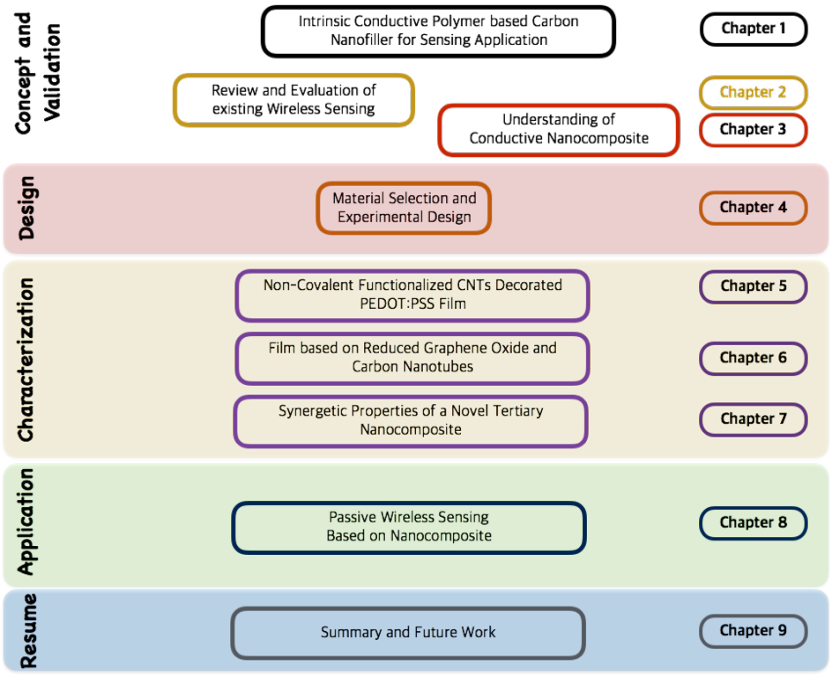

Figure 1.3: Outline of the main topics covered in this dissertation

2 State-of-the-Art of Passive Wireless Sensors

In structural health monitoring (SHM), medical and aerospace applications; strain gauges, temperature sensors and humidity sensors are extensively needed. Hence, the sensors determine any change in the desired physical phenomena such as force, temperature or humidity, the signal is transferred to the data acquisition system (DAS) for signal processing and analysis. The DAS is located sometimes far away from where the sensor is installed. This whole setup makes the sensing system complex and makes it difficult to maintain robust and limits its lifetime, accordingly arises the maintenance cost if the sensors or the wires are damaged or degraded. The difficulty to be implemented in the movable, rotational and vibrational parts, is another problem that limits its application. Besides, an extra weight is introduced if the sensor array is implemented on a wide area such as aircraft wing (Figure 2.1). Another related problem is the deviation caused by the change in the resistance of the wires due to changes of the temperature. Its low sensitivity, low resolution, and sensitivity to EMI attribute to the difficulty too.

Figure 2.1: Strain sensor array installed on NASA aircraft [2] Credits: NASA / Tom Tschida

2.1 Classification of Wireless Sensors

In order to overcome the limitations of the conventional sensors, researchers started to explore and seek other solutions and technologies to achieve more advancement and reliability to the current state-of-art available system. Particularly, implementing wireless sensors initially eliminate the wires and thus reduce the installation and the maintenance costs. An extensive review of the wireless strain sensors in SHM in both academic and industry is deep explained in [3]. The development of wireless sensors could be divided into four generations, as illustrated in Figure 2.2[1].

[1]Reference of the pictures from left to right: [4], [5], [6] and [7], respectively.

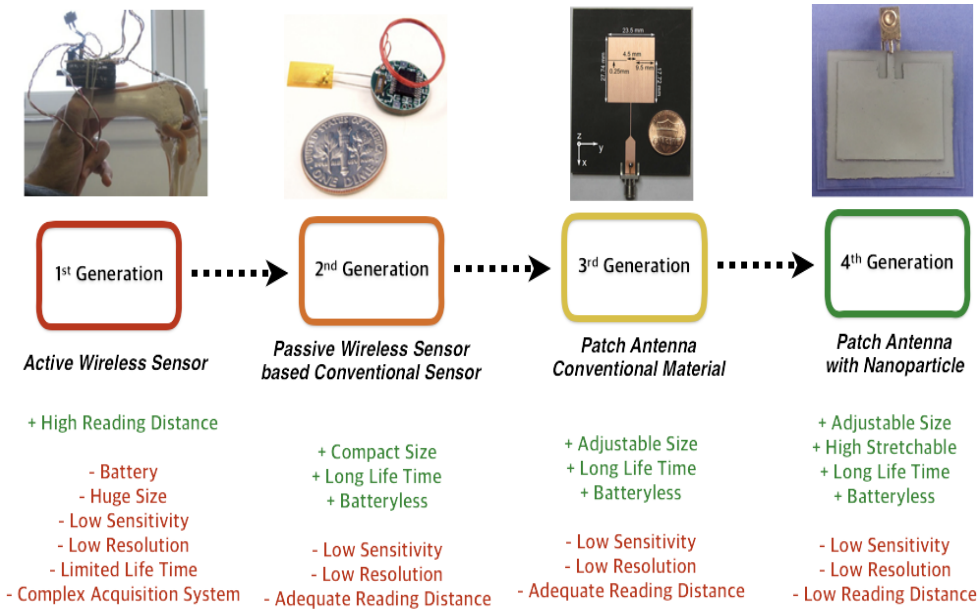

Figure 2.2: Classification of wireless sensors

2.2 Active Wireless Sensors

In the 1^{st} generation, active wireless sensors have been developed, where sensors such as strain gauge, temperature sensor, humidity sensor, accelerometer, among others is connected to an autonomous active data acquisition system (ADAS). The sensor measures the desired physical phenomena and the signal is then transferred to the ADAS, which includes a sensor interface, computing core, actuation interface and wireless radio transmission [3]. Beside that the 1^{st} generation eradicates the cable connections, still these types of sensors suffer from some limitations of the traditional sensors, such as low sensitivity and low resolution, because they acquire the sensing data based on conventional sensors. The wireless unit contains of a complex acquisition system that consists of an analog-to-digital converter and a microprocessor for data sampling and data processing, and a wireless transceiver to communicate with the main reader station. Thus, these devices are active devices i.e. a power supply (battery) is always required, which limits its lifetime and increases the power consumption. Therefore, the system is more complex, bigger, expensive and it limits its application areas (Figure 2.2). Therefore, developing batteryless sensors (passive) are explored.

2.3 Passive Wireless Sensors Coupled Traditional Sensors

The 2^{nd} generation of the wireless sensors applies the principles of the radio frequency identification (RFID) technology in sensors. An RFID sensor system consists of a reader station and a passive tag, as it is shown in Figure 2.3. The reader consists of a power source, acquisition system and an antenna. The generated signal is sent by the reader antenna to the Tag (sensor), which is passively activated and the backscattered signals are received wirelessly by the reader antenna. The RFID sensor and the tag design can

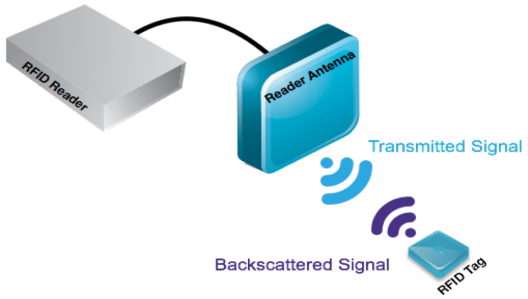

Figure 2.3: Components of RFID wireless sensing system

use different working frequency bands, such as low frequency (LF), high frequency (HF), ultrahigh frequency (UHF), super high frequency (SHF) and microwave. The UHF, SHF and microwave frequencies are more favorable than the low frequency range, as the reading distance in this frequency range is longer and can reach up to 30m. The antenna in this frequency range is comparable in size to the wavelength of the frequency, therefore it uses usually radiative coupling to communicate between the reader and the tag rather than coupling principle used in the LF and HF tags. Also, since the tag is resizeable, it can be easily implemented and embedded in structures [8-9]. Likewise, this generation of RFID sensor kept the same sensing principle as in the 1^{st} generation, i.e. using a traditional sensor as sensing element and implements a passive wireless system. Therefore, if the lifetime problem is solved, other issues such as the low sensitivity and the low resolution are still existing.

2.4 Patch Antenna as Wireless Sensor Element

RFID tags in the SHF frequency range are relatively size compact and costly effective; however, efforts are done to simply eliminate the circuitry located on the tag which converts the measured physical quantity into frequency, also to make the tag flexible. Antennas are thereby the most important component in RFID tag sensor. Different frequency-tunable antennas have been reported for use as strain, temperature and humidity sensors, such as variable capacitors [10], metamaterials [11-13], piezoelectric resonators [14-15], RCL-antenna winding [16], dipole antennas [17] and Meander-line antenna [18-20]. Among different types of antennas, microstrip patch antenna (MPA) have decisive advantages due to its simple design, easy fabrication and low profile. This represents the 3^{rd} generation of the wireless sensor, where the antenna is used for communication and as sensing element. In the following, two applications of the MPA is discussed, mainly strain and temperature sensing.

2.4.1 Patch Antenna as Wireless Strain Sensor

The first design of the MPA for strain/vibration sensing is introduced by Das et al. The proposed design consists of a piezoelectric-dielectric-strip grating based a multilayer antenna, that works on modulation mode, where any introduced strain changes the voltage of the piezoelectric layer located on the patch antenna [21]. This change is added up to the voltage generated due to the received electromagnetic waves from the reader, the resulting modulated signal is transmitted back to the reader. To separate the sensing and

actuating functionalities, a grating technique is added to the system. However, these two different functionalities are activated separately using orthogonal polarization. Although, the proposed patch antenna can work at different frequencies by stacking different patches on each other, the sensor can be interrogated only at very small distances about few millimeters. The first real MPA strain sensor is proposed by Tata et al., which is basically a single frequency MPA with feedline inset operating at 20GHz [22]. Tata et al. used a conventional micromachining technique to fabricate a patch antenna on 50μm flexible polyimide Kapton substrate. The MPA is mounted on a cantilever beam, and the effect of beam deflection on the change of its resonance frequency is tested and evaluated. The physical dimension of the proposed microstrip feedline antenna and the fabricated MPA is illustrated in Figure 2.4. Although the relationship between the strain and the change in the resonance frequency of the antenna is derived, the Poisson's ratio of the material is not taken into consideration and it is assumed that it is the same for the patch and the substrate material. The strain range is from 0- 0.55% and due to the mismatch effect, a shift in the resonance frequency is measured to be about 1.55GHz. Good agreement between the simulation and the experimental results are obtained, and a strain sensitivity along its length direction is about -22.8kHz/$\mu\epsilon$ and almost no change along the width direction is obtained.

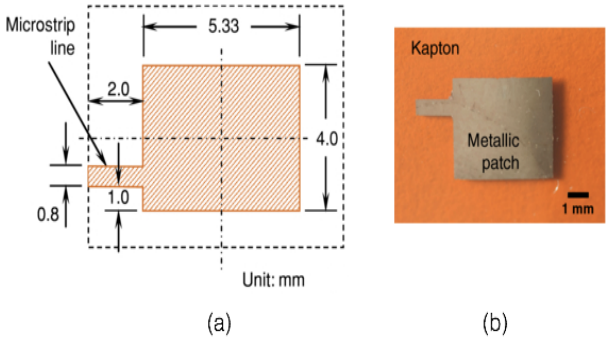

Figure 2.4: (a) Physical dimensions of the microstrip feedline patch antenna, (b) Fabricated antenna on flexible Kapton substrate. Reproduced from IOP Publishing ©2008 published in [23]

To sense the strain in different directions, Tata et al. proposed a double resonance metallic rectangular microstrip flexible patch antenna working in the X-Ku band, i.e. 15.8GHz and 20.5GHz [23]. As illustrated in Figure 2.5, if the strain is along the patch's length, a shift of the resonance frequency is toward a lower band and it shifts to a higher band if the strain is along the patch's width. The strain sensitivity along the antenna's length and width is monitored to be -15.5kHz/$\mu\epsilon$ and 9.2kHz/$\mu\epsilon$, respectively. Even if the strain sensitivity is low, Tata et al. showed the ability of the patch antenna to be used for strain direction determination. Furthermore, Mohammad et al. [24] and Deshmukh et al. [25] have demonstrated that the patch antenna can be used also to detect and measure the crack orientation on metallic structures, as these structures can act as ground plane for the patch antenna. Thus, if any crack occurs in the structure, an increase in the current path length through the patch antenna occurs, which results in a down-shift of the initial resonance frequency of the patch antenna, and by measuring the change in the antenna resonance frequencies, the crack growth can be detected and quantified. The crack detector sensor based dual-frequency MPA is able to maintain cyclic loadings up to 97000 cycles [24, 26]. Instead of a rectangular patch antenna, which can determine the strain only in one direction if it is resonating at single frequency, a circular microstrip patch antenna

(CMPA) is proposed by Daliri et al. for strain sensing regardless of its direction for SHM [27]. A mathematical analytical model is derived to determine the relationship between the change in the resonance frequency of the CMPA as a function of the strain. The antenna is designed to resonate at 1.5GHz on FR4 substrate having thickness of 1.5mm. The CMPA is excited by a linearly polarized double horn antenna and the strain validation experiment is done using a 3-points bend test with 25$\mu\epsilon$ as maximum strain generated through the bending. Good agreement between the simulation and the experimental results reached only till measurement range of 15$\mu\epsilon$, while the authors did not explain about the reasons. Although the sensor behavior is linear, but the strain sensitivity is only 10kHz/$\mu\epsilon$ and the interrogation distance is limited to only 5cm. To further improve the strain sensitivity, Daliri introduced a rectangular slot in the middle of the CMPA strain sensor. The slotted CMPA improves the strain sensitivity three times higher than the non-slotted CMPA [28]. Also, Daliri et al. enhanced the interrogation distance by using a substrate with low losses and high permittivity that results in high CMPA quality factor, consequently the interrogation distance is increased up to 20cm [29]. Yi et al. proposed a folded rectangular MPA working at 921.637MHz. Here, an integrated IC-chip for wireless interrogation is used instead of the light-activated switch proposed by Dashmukh [30] (Figure 2.6). This MPA strain sensor can detect small strains lower than 20$\mu\epsilon$ and goes up till 10.000$\mu\epsilon$ with an interrogation distance up to 2.1m. The working principle of this sensor is based on the impedance mismatch of the antenna and the IC-chip; whilst for any strain, a change in the impedance is introduced and measured. However, the transmitted signal from the RFID tag is not sharp enough to determine the exact resonance frequency, this results in low strain sensitivity of -727Hz/$\mu\epsilon$. Thus, the shift in the resonance frequency is extracted using a curve fitting technique. The effect of the antenna substrate thickness on the reading distance and strain transfer compared to a conventional strain gauge is also investigated. The sensor was used to monitor uni-directional crack growth, and as a sensor array to determine the strain simultaneously in different locations [30-31]. By introducing slots on the patch antenna, the interrogation distance increases to 2.1m, and slightly increases the strain sensitivity of about -790Hz/$\mu\epsilon$ [31].

Moreover, Ahbe et al. proposed a dual-frequency MPA with one and two feed-insets operating at 2.9GHz and 5.8GHz for multidirectional strain measurements [6]. The strain effect is studied as a function of the change in the return loss and radiation characteristic of the

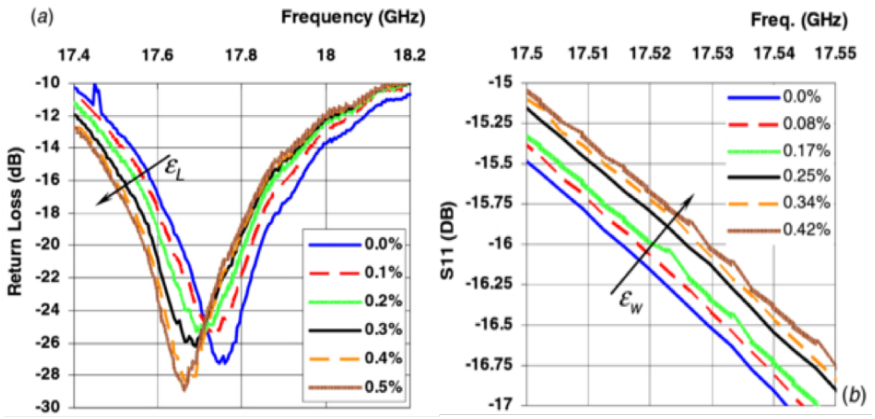

Figure 2.5: Shift in the resonance frequency along (a) Patch's length, (b) Patch's width. Reproduced from IOP Publishing ©2008 published in [23].

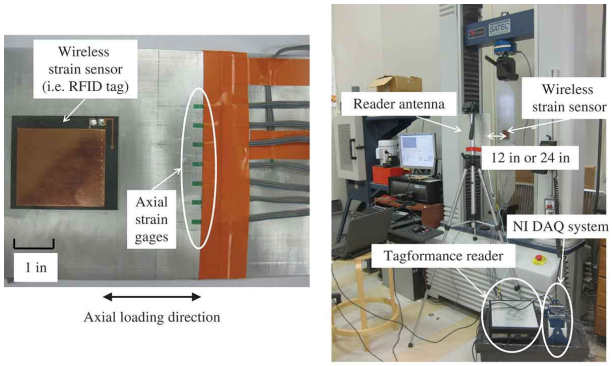

Figure 2.6: Wireless strain sensing using copper patch antenna (a) Fabricated strain sensor based folded patch antenna mounted on cantilever beam, (b) Measurement setup for the tensile tests. Copyright ©Taylor and Francis Group, LLC 2011 published in [30]

antenna. The MPA is fabricated on Rogers RT/Duroid 5880 substrate having a thickness of 1.575mm, the proposed antennas and their optimized physical dimensions are depicted in Figure 2.7. The main reason for the proposed one-feed inset design (Figure 2.7 (a)) is to miniaturize the sensor. However, to use the sensor in a doubler-based system, a multiplexer or a power divider has to be adapted to deliver and extract the signals from the two-feed antenna (Figure 2.7 (b)). The cantilever beam setup is used to evaluate the MPA functionality and the antenna is connected to a vector network analyzer (VNA), then the strain is varied between $0\mu\epsilon$ to $2500\mu\epsilon$, subsequently the change in the return losses are recorded. For comparison reasons, strain gauges are mounted on the top side of the cantilever to register the exact level of the strain.

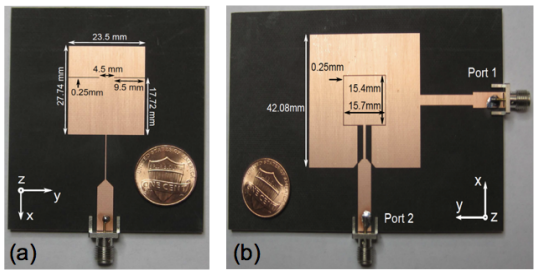

Figure 2.7: Passive wireless strain sensor based dual-frequency MPA (a) One inset antenna, (b) Two inset antenna. Copyright ©IEEE, 2012 published in [6]

Table 2.1 shows the strain sensitivity results for both antennas along the length and width directions. It is shown from Table 2.1 that, the one-feed inset MPA has higher strain sensitivity along the MPA's length compared to the double-feed inset MPA, this is referred to its miniaturization. As the previously proposed MPA strain sensors showed a low sensitivity along its length and its width, Salmani et al. proposed a multiband antenna that resonates at multiple frequencies for determination of a multidirectional strain and to improve the strain sensitivity [32]. The multiband MPA has an array of slots along its length, thus any applied force changes the dimensions of these slots beside the change in the patch dimension itself. Consequently, if the strain is along the length or the width, a shift in its initial resonance frequency to a higher or a lower value occurs. The MPA is designed to have a first resonance frequency at 5.07GHz and it is fabricated on Rogers RT/Duroid substrate with a thickness

of 0.254mm. A schematic of the proposed multiband slotted MPA is shown in Figure 2.8. The simulation results in Figure 2.9 show an improvement in the strain sensitivity compared to the structures proposed in [23] and [6], which are -57.3kHz/$\mu\epsilon$ and 13.8kHz/$\mu\epsilon$ for the strain along the length and width, respectively.

Table 2.1: Comparison of strain sensitivity using one and two-feed inset MPA [6]

Type of Antenna	Resonance Frequency (GHz)	Sensitivity (kHz/$\mu\epsilon$)	
		X-direction	Y-direction
One-feed inset	2.9	-2.2	0.06
	5.8	-3.1	0.62
Two-feed inset	2.9	-0.6	-0.73
	5.8	-0.6	0.59

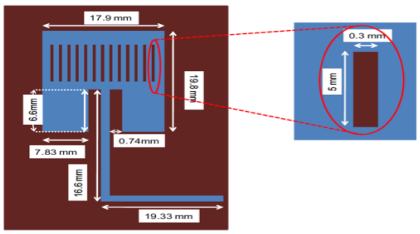

Figure 2.8: Slotted patch microstrip antenna for wireless strain sensing. Copyright ©IEEE, 2011 published in [32]

To further improve the strain sensitivity, Thai et al. loaded the end-node of the MPA with an open loop circuit [33]. A cantilever at the gap of the open loop is introduced, the proposed design is illustrated in Figure 2.10. The fabrication process of the structure is relatively complicate. The antenna is designed to operate at 3GHz on 100μm Kapton substrate with a dielectric constant of 3.4. First, the cantilever is fabricated on Kapton substrate with 50μm thick, then the cantilever is manually assembled onto the open loop circuit. The cantilever is bended in one direction along the antenna's length and it gives a strain from 0 to 0.7%. The authors claimed that the proposed prototype achieved a sensitivity of 1.26% frequency shift per 1% strain. However, and due to the limited fabrication capability and the manual rapid assembling, the results are not reproducible.

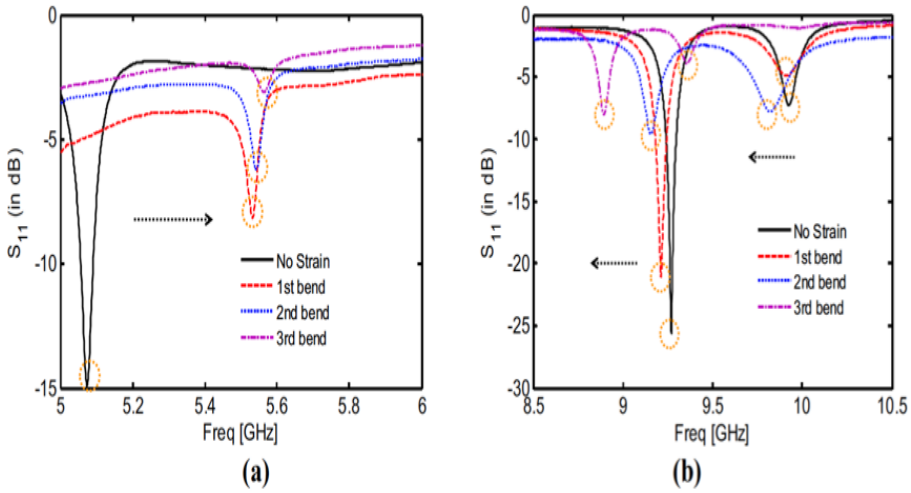

Figure 2.9: Shift of resonance frequency as function of strain for slotted MPA along (a) Patch's length (b) Patch's width. Copyright ©IEEE, 2011 published in [32]

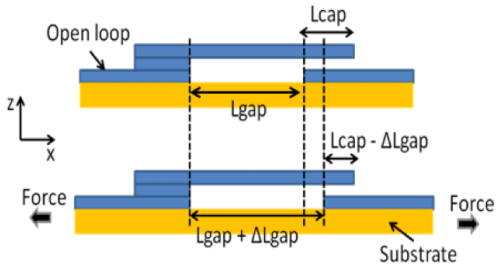

Figure 2.10: Cross section of the cantilever implemented on the modified loop loaded working as wireless strain sensor. Copyright ©IEEE, 2013 published in [33]

As demonstrated in [26], the single resonance MPA is highly sensitive to crack propagation in the ground plane than the double resonance MPA. In SHM, cracks might cover structures with large areas, therefore Xu et al. proposed a sensor array from four MPAs connected to a frequency divider multiplexer [34]. Thus, the crack propagation that occurs on specific locations of the structure affects only one antenna from the set, if two of the antennas are designed to work at two different frequencies. The crack sensor array based MPA can be activated using an impedance-switching circuit for spatial division multiplexing; hence, by focusing a beam of light on that photocell sensor, the antenna sensors can be selectively interrogated, the full sensor design is illustrated in Figure 2.11 [35]. It is concluded that the proposed crack determination sensor can detect the crack growth with sub-millimeter resolution and non-linear trend. The frequency shift increases as the crack grows toward the center of the patch antenna, i.e. the crack detection sensitivity increases as the crack grows deep into the patch antenna as shown in Figure 2.12. In addition, the authors stated that the smaller antennas exhibited higher crack sensitivities.

In order to improve the stress transfer between the cantilever beam and the MPA, Wang et al. designed four sets of different dual-frequency MPA on very thin polyimide flexible substrates, having a thickness of 50μm and dielectric constant ϵ_r of 3.4, and MPAs are working between 2.5GHz and 20.5GHz (Figure 2.13) [36]. Although a good sensor flexibility is reached, the sensitivity is comparable to what was reached by previous researchers. The strain sensitivity

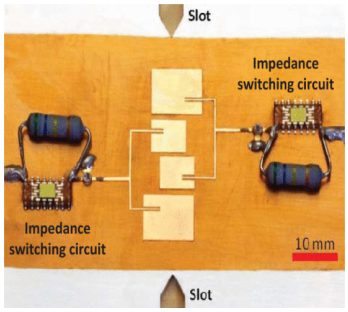

Figure 2.11: MPA array for crack orientation with photocell sensor. Copyright ©IEEE, 2013 published in [35]

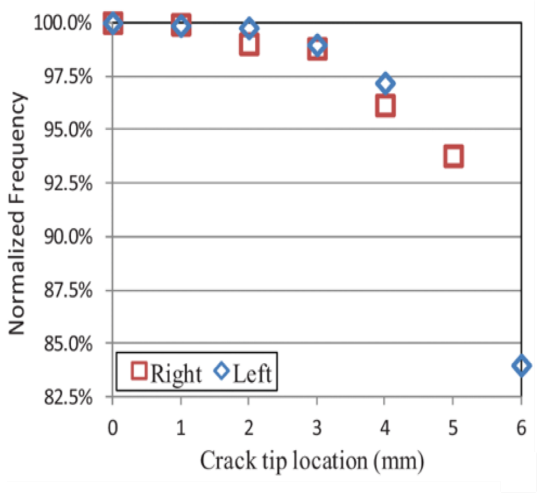

Figure 2.12: Shift in the antenna's resonant frequencies with crack propagation. Copyright ©IEEE, 2013 published in [35]

is between 20.5kHz/$\mu\epsilon$ and 46.8kHz/$\mu\epsilon$ for the strain along the length direction. The authors concluded that the MPA with a larger dimension or a higher resonance frequency have a better resolution for strain sensing. To determine the influence of the substrate dielectric constant on the strain characteristics, Sharma et al. designed a slotted rectangular MPA on three different substrates, namely FR4, Polyimide and RT/Duroid 5880 [37]. The simulation results show that independent on the substrate type, a good linearity is obtained in the resonance frequency as function of the strain. However, the MPA based on Polyimide and RT/Duroid 5880 substrate shows better sensitivity compared to the MPA based FR4 substrate.

2.4.2 Patch Antenna as Temperature Sensor

Beside strain and crack orientation, the effect of the temperature on the MPA made by different substrates is reported by Maurya et al. The temperature compensation technique is presented, and the effect of temperature is simulated from 27°C to 117°C for FR4, Quartz, Polyimide and Teflon substrates [38]. From Table 2.2, it can be concluded that the lower the dielectric constant of the substrate is, the higher the sensitivity is. The shift in the resonance frequency of the patch antenna is mainly due to the change of the dielectric constant of the substrate material. However, this sensitivity is still too low to be used in real temperature

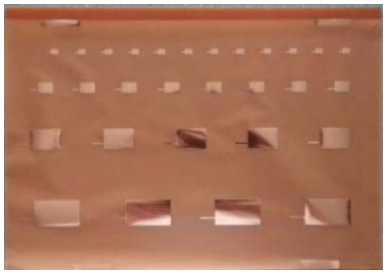

Figure 2.13: Prototype of wireless strain sensor on Kapton substrate. Copyright ©IEEE, 2015 published in [36]

applications. Based on that principle, Cheng et al, fabricated a novel wireless passive

Table 2.2: Temperature sensitivity of MPA for different substrate materials

Substrate	ϵ_r	F_{res}@27°C (GHz)	F_{norm}(%)
FR4	4.4	2.94	-0.76
Quartz	3.7	3.13	-0.85
Polyimide	3.5	3.25	-0.84
Teflon	2.1	4.08	-1.47

temperature sensor based on a reflective patch antenna for harsh environmental temperature applications, as shown in Figure 2.14 [39]. The patch antenna resonates at 5.07GHz with a platinum as patch material and alumina as substrate material having a dielectric constant of 9.7 and a thickness of 0.635mm. A monotonic decrease in the resonance frequency of the patch resonator occurs due to the increase in the dielectric constant of the alumina substrate as a function of the temperature. As the temperature changes from 50°C to 1050°C, the resonance frequency reduces from 5.07GHz to 4.58GHz, this corresponds to a change in the dielectric constant of the alumina substrate from 9.7 to 11.4; therefore, the temperature sensitivity is calculated to be 0.58MHz/°C. Although, only one resonance frequency is really

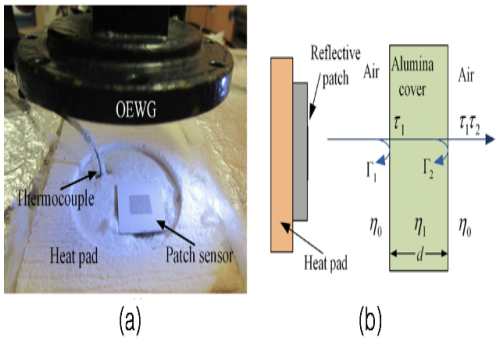

Figure 2.14: (a) Sensor measurement using an open-ended waveguide and (b) Schematic showing the wave reflections due to the alumina board cover with a thickness d = 0.635mm. Copyright ©Elsevier, 2015 published in [39]

needed for the temperature measurement, Sanders et al. fabricated temperature sensors based on dual-frequency MPA bonded on different metal bases (copper, aluminum and steel) on a selected commercial ceramic-filled polytetrafluoroethylene (PTFE) known as substrate RO3006, which has bi-linear temperature-dielectric constant relationship in the temperature

range from -100°C to 250°C [40]. The designed patch resonates at 5GHz and 6GHz, the temperature is varied from 40°C to 110°C. The antenna and its scattering parameters are illustrated in Figure 2.15. The results show the feasibility of using the MPA for wireless temperature sensing. However, a calibration of the thermal coefficient of dielectric constant of the substrate (TCD$_k$), and the mismatch between thermal strains of the substrate and the patch material must be taken into consideration. The temperature sensitivity of the proposed wireless temperature sensor bonded on different materials is summarized in Table 2.3. Similar work is done by Yao et al.; hence instead of using dual-frequency, a single

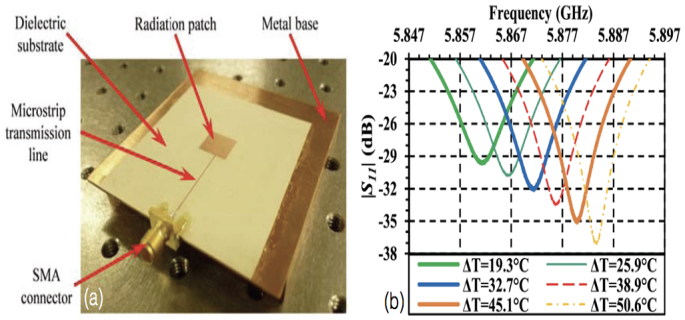

Figure 2.15: (a) Prototype temperature sensor bonded to a copper base, and (b) Return loss at different temperature increments. Copyright ©IEEE, 2015 published in [40]

Table 2.3: Measured temperature sensitivity and values of the TCD_k calculated from the experimental data redraw based on [40]

Base Material	Theoritical	TM_{010} Mode		TM_{001} Mode	
	k_T (ppm/°C)	k_T (ppm/°C)	TCD_k (ppm/°C)	k_T (ppm/°C)	TCD_k (ppm/°C)
Aluminuim	56.4	152.87	-352.94	145.41	-338.02
Copper	63.0	133.05	-300.10	142.60	-319.19
Steel	68.3	118.72	-260.85	116.24	-256.48

frequency MPA working at 2.45GHz on Rogers RO3210 substrate is used [41]. The proposed wireless temperature sensor is tested from 20°C to 280°C and the temperature sensitivity is 195.13ppm/°C, which is slightly higher than the one proposed by Sanders et al. in [40]. Tan et al. investigated a wireless passive temperature sensor based on a resonator antenna integrated MPA for harsh environmental applications [42].

The proposed model is based on a low-temperature co-fired ceramic (LTCC) substrate, because it has a permittivity that varies monotonously with the temperature. The proposed antenna and the measurement setup is demonstrated in Figure 2.16. Similarly, a linear decrease in the resonance frequency with an increase in temperature to within 400°C at a 30mm reading distance is recorded, with a sensitivity of 0.24MHz/°C. The antenna polarity influences the readout signal significantly; thus to extract the sweep of the frequency, a time-domain grating method for filtering a background signal is presented. Although the above-mentioned MPAs show a good feasibility as a battery-less wireless strain and temperature sensors, its low sensitivity, complex MEMS based fabrication method and sensing application area are very limited. This is referred to the metallic layer, mostly copper, which is used as sensing layer for the desired application. Therefore, it is often used for strain determination and crack orientation, also the linear change in the permittivity of the substrate due to the temperature is limited. Although, some methods are introduced

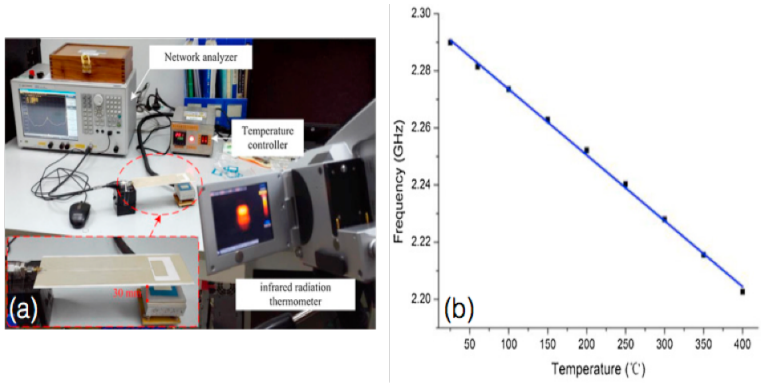

Figure 2.16: Wireless temperature MPA sensor proposed by Tan et al. (a) Measurement setup, (b) Fitting of the change in the frequency versus temperature. Copyright ©Elsevier, 2015 published in [42]

to improve the sensitivity, such as slotted MPA, no big improvement in the sensitivity is remarked. Whilst for temperature a broad range of isolating materials can be used as substrates, only a very limited number of materials has a linear change in the permittivity as function of temperature, so the sensitivity remains always low.

2.5 Nanomaterials for Sensitivity Improvement

In order to widen the range of applications, it is necessary to fabricate sensitive MPAs to either strain and/or temperature, in a way that the shift in the resonance frequency is better detectable. Once these issues are addressed, these new sensors could be implemented either as stand-alone or in an array for wireless sensing. Also, conventional MPA wireless sensors operating in harsh or in gas environments may suffer from corrosion or oxidation, thus it is important to implement new corrosion-resistive materials. Recently, nanomaterials are proposed as effective sensing materials for strain, temperature, humidity and to detect other physical phenomenon. Among many nanomaterials, intrinsic conductive polymer, carbon nanotubes and graphene oxide have been investigated for the development of sensors, transistors, solar cells, flexible displays and so forth. However, the studies on antenna conductive polymer are very limited and there is no review on using nanomaterials as passive UHF RFID sensors. Available inks i.e. silver nanoparticles suffer from low conductivity to replace the copper patch used in the MPA. Also, high post-processing temperature (about 400°C) has to be adopted to improve their conductivity after the deposition, while most used RFID substrates have a glass temperature below 200°C. Beside the low conductivity, the used inks are not sensitive to strain and temperature, thus it is not possible to use them for wireless sensing. Nanocomposites which have an adjustable conductivity, can provide a good impedance matching and high gain antenna and they are also sensitive to the required physical phenomena. Among others, intrinsically conductive polymers such as PEDOT:PSS, and nanomaterials such as carbon nanotubes and reduced graphene oxide show excellent electrical, mechanical, and chemical properties, which make them good candidates for the new generation of passive wireless sensors. For UHF applications, and when a metallic patch is deposited on the substrate, it is necessary to have a thickness of more than the skin depth at the working frequency of the antenna. Using intrinsically conductive polymers, a good antenna performance can be obtained even if the patch thickness is a fraction of

the skin depth [43]. Due to its high conductivity and commercial availability, PEDOT:PSS is proposed to be used for antenna design as transparent flexible meandering and dipole antenna [44-45], patch antenna [43], co-planar waveguide [46], ultra-wideband (UWB) microstrip [47]. However, most of the proposed antennas exhibited a low efficiency due to the low conductivity compared to the copper based on antennas. Lately, Manzari et al. used a hygroscopic property of the PEDOT:PSS for humidity sensing, and accordingly proposed a new family of polymer-doped wireless ambient humidity sensors; the PEDOT:PSS is used as sensing H-shaped slot on 4mm Teflon substrate in a folded planar structure [48]. The working principle of the proposed wireless sensor is based on the change of the polymer's dielectric properties due to the water adsorption/ absorption, this leads to the variation of both input impedance and losses of the antenna, which leads to the modification of the antenna resonance frequency. As shown in Figure 2.17, different layouts of the deposited PEDOT:PSS are investigated and the resulting sensitivities are compared. The layouts (A, D and F) show the best sensitivity to humidity and are summarized in Table 2.4.

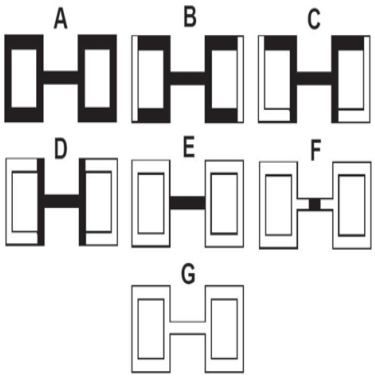

Figure 2.17: Different layouts of humidity PEDOT:PSS wireless sensor. Copyright ©IEEE, 2012 published in [48]

Table 2.4: Sensitivities of selected patterns in terms on the measured turn-on and the backscattered power [48]

	RH_{low}-RH_{high}	Sensitivity (dB/RH)		
		Case A	Case D	Case F
Turn-on	50-80	0.13	0.12	0.08
	50-100	0.10	0.05	0.05
Backscattered power	50-80	0.18	0.20	0.12
	80-100	0.13	0.05	0.05

Abbasi et al. proposed two models of wireless humidity sensors. The first model is based on microstrip-feed rectangular slot antenna and the second model is based on two port filter with a split ring of rectangular shape, both are either loaded with one or two blocks of PEDOT:PSS layer as sensing layer [49]. The designed antenna resonates at 2.65GHz on low permittivity Roger's substrate (RT/Duroid 5880) of 2.3 and a thickness of 1.29mm. A 2x2mm^2 PEDOT:PSS layer is deposited on two different positions as shown in Figure 2.18. When the humidity changes, water absorption leads to change the polymer's dielectric property and thus a mismatch in the input impedance of the antenna occurs; consequently, a shift in the resonance frequency is registered. A shift from 880MHz to 995MHz is recorded

for a change in humidity from 40% to 100%. The sensitivity is then 217kHz/%RH, which is higher than the one recorded previously by Manzari in [48]. Chen et al. fabricated

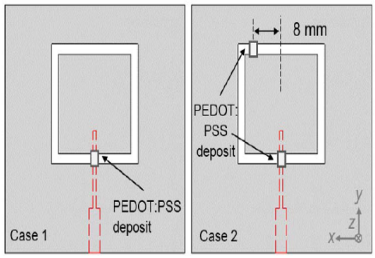

Figure 2.18: Wireless humidity MPA (case 1) one block, (case 2) two blocks of 2x2mm^2 PEDOT:PSS layer. Copyright ©IEEE, 2015 published in [49]

a flexible slotted MPA based on PEDOT:PSS with an efficiency of about 82% and fully reversible conformability [47]. The fabricated antenna (Figure 2.19) is made on highly flexible Cuming Microwave C-Foam PF-4 foam with thickness of 1.6mm, the antenna is designed to resonate at 5.8GHz. Compared to the copper antenna, the PEDOT:PSS antennas have broader bandwidth due to the higher losses in the conductance at microwave range. It also showed that bending the antenna did not cause any change or shift in the resonance frequency, thus it cannot be used for strain sensing. Carbon nanomaterials, such as CNTs

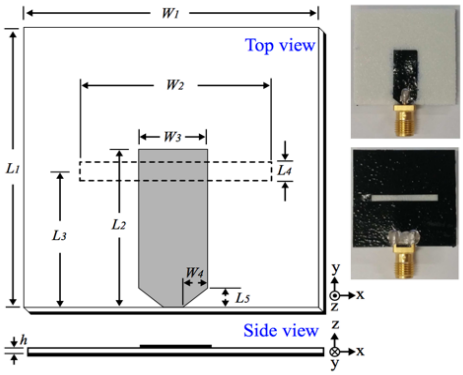

Figure 2.19: From left to right: the antenna configuration and the realized PEDOT:PSS antenna. Copyright ©IEEE, 2015 published in [47]

have favorable electrical, mechanical and chemical properties, therefore it is investigated in nano-electronics as channel material for VLSI interconnects [50-52], as transistors [53-54] and in nano-antenna applications [55]. However, pristine CNT dipole antennas exhibit an AC resistance of several kilo-ohm per micrometer (about 10kΩ/μm), this is referred to the high aspect ratio that causes high conduction losses and accordingly decreases its efficiency for microwave applications [56-58]. Consequently, CNT arrays and nanocomposites based on CNT are suggested to increase the efficiency [59]. However, as it will be explained in section 3.7, the conductivity of the CNT nanocomposites depends strongly on the polymer matrix, orientation and alignment, aspect ratio, curvature and processing methods of the CNTs. Above several MHz, the reactance of the CNT films depends strongly on the frequency, thus the CNT based films are limited to be used only in dc or LF band. However, many efforts are implemented to use the CNT nanocomposites for antenna applications, such as for conformal load bearing antenna [60], inverted F-antenna [61], planar antenna [62] and UWB [59,

63]. It is generally remarked that, no degradation in the gain and/or far-field radiation properties is observed. The first effort to use CNTs in the wireless sensing application is done by Yang et al. in 2009 for gas sensing. Yang et al. used an inkjet printing to deposit a film of SWCNTs functionalized dimethylformamide (SWCNT:DMF) on dipole antenna printed on paper substrate to make a bio-friendly passive wireless ammonia gas (NO_3) sensor [19]. Instead of dipole antenna, Occhiuzzi et al. used a buckypaper films on monopole antenna for ammonia gas detection. Low sensitivity and long recovery time are observed [18, 65]. To improve the sensitivity, Lee et al. used inkjet printing to deposit a film of a commercial dispersion of SWCNT functionalized with polyaminobenzene sulfonic acid (SWCNT:PABS) on the MPA stub to fabricate high sensitive NO_3 passive wireless gas sensor [19]. Keller et al. simulated a meshed patch antenna based on metallic and semi-metallic CNT threads to be used as NH_3 passive wireless gas sensor [65]. The MPA exhibits a resonance frequency at 27.85GHz with a bandwidth of 2.1GHz at -10dB. A shift to the left side of spectrum (decrease) is observed in dependence on ammonia (NH_3) concentration due to the change of the permittivity (ϵ_r) and conductivity (σ_r) of the CNT thread. A change of approximately 60MHz is recorded for concentration of 10.000rpm NH_3. Other applications rather than gas sensing are also proposed, such as E-textiles [66] and bio-application [67]. In [66], the E-textile based MPA has a gain of 6dB at 2GHz, which is 2dB less than a copper made MPA, this decrease in the gain is due to the loss within the E-textile conductor. As CNTs based nanocomposites show an excellent feasibility as strain, pressure, temperature and humidity sensors, it is possible to use them as sensing layer for wireless sensing applications. The first real utilization of the CNT nanocomposite MPA for force/displacement sensing application is proposed by Tang et al. They deposited a MWCNT film on PDMS substrate to form a stretchable MPA for possible wireless pressure sensors application, the MWCNT film is coated by a thin gold layer to improve the conductivity of the patch (Figure 2.20 (a)) [68]. The MWCNTs are mixed with cellulose ester, then a vacuum filtration and transfer method are used to fabricate the films with different thicknesses. As depicted in Figure 2.20 (b), the simulation results show that the conductivity of the patch affects significantly the resonance frequency and the gain of the antenna. The minimum required conductivity is found to be 10^5S/m. The fabricated MPA resonates at 5.2GHz with S_{11} of -20dB and radiation efficiency up to 61%, which is appropriate for RFID sensors. Under a displacement of 2500μm resulting from a stretch test, changes of only 0.5% in the gold layer is reached. Using a frequency-tuning capability, the resonance frequency can be tuned by 6.5% with a displacement of 1500μm, which is higher than its counterpart MEMS antennas [68]. With the same principle, Feng et al. spray-coated functionalized MWCNTs (f-MWCNTs) on inkjet printed silver interdigital electrodes (IDEs) and loaded it to an UHF coplanar waveguide antenna. Inside an environmental chamber and at constant temperature of 25°C, the shift of the resonance frequency is determined when the humidity is varied from 20 to 95%RH [69]. Schematic of the working principle of the proposed humidity sensor and the deposited MWCNTs layer on the IDEs is shown in Figure 2.21. Although this sensor shows an acceptable sensitivity, the recovery time is very long about 2 hours because of the strong hydrogen bonding between the water molecules and the f-MWCNTs. Therefore, it is proposed to use a heater at the backside of the electrodes to shorten the recovery time, but this arises the complexity of the sensor. Lately, Puchades et al. fabricated and characterized a dipole antenna made with both bulk MWCNT sheets and SWCNT films for communication proposes [70]. The fabrication of a dipole antenna resonating at 1.5-2GHz is successfully established on soda-lime glass substrate and then covered with Kapton tape, the performance

in terms of S_{11} is investigated by varying the arm's length of the MWCNT-sheet and the doped SWCNT film dipole antenna (Figure 2.22). The experimental results indicate that, for an adequate antenna resonance (-10dB) a minimum sheet resistance of 10Ω/sq is required if a mismatch exists between the antenna and the CNT film. For sheet resistance above 40Ω/sq, the antenna is not be able to reflect all the power delivered by the VNA. Beside PEDOT:PSS and CNTs, graphene and graphene oxide also can bring significant benefits for passive antennas sensing, as graphene has extraordinary electrical, chemical and mechanical properties. Though the exceptional characteristics, relatively few applications have been exploded for microwave application.

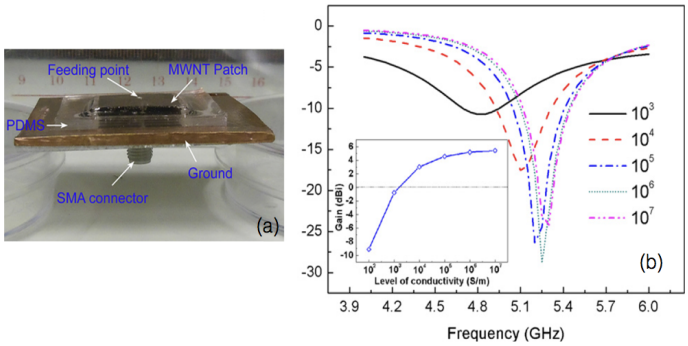

Figure 2.20: (a) Snapshot picture of probe-fed antenna, (b) Simulation results of radiation performance related to resistance of the MWCNT films. Copyright ©Elsevier, 2012 published in [68]

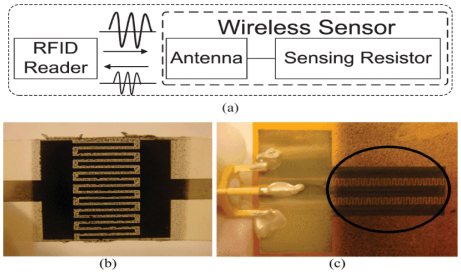

Figure 2.21: (a) Schematic of RFID humidity wireless sensor. (b) Snapshot of the spray-coated MWCNTs on IDEs. (c) Photograph of the copling between the MWCNTs resistor and a coplanar waveguide for high frequency characterization. Copyright ©IEEE, 2012 published in [68]

The main reason is its high surface resistance compared to metals at micro and mm-waves frequency, thus it has mostly a bad conductive surface at this frequency range. Gomez-Dias et al. analyzed using monolayer graphene sheet as patch layer for a MPA when it is fed by a metallic microstrip to completely eliminate the influence of its radiation [71- 72]. From Figure 2.23 (a), it can be concluded that the resonance frequency can be tuned by changing slightly the chemical potential (μ_c) of the graphene sheet, this is due to the weak dependence of the surface reactance on the chemical potential at the microwave band [72]. Also the radiation efficiency is very low due to the high losses caused by the high surface resistance, and therefore it dissipates a huge amount of the received input energy (Figure 2.23 (b)).
GO has an analogous structure of graphene decorated by oxygen functional groups, which makes it hydrophilic but also highly insolating. However, adopting either chemical or thermal

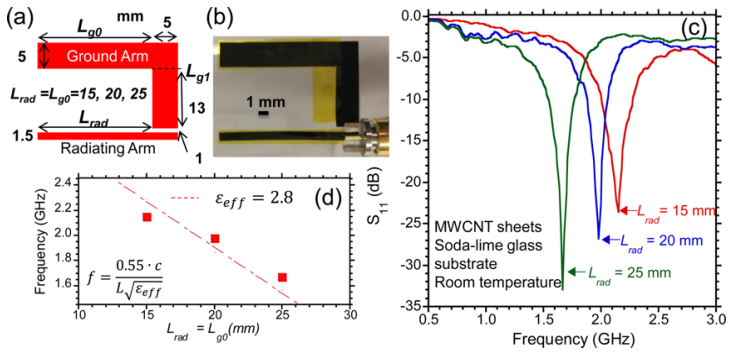

Figure 2.22: (a) Schematic of dipole antenna two radiating arms, (b) Image of representative dipole antenna fabricated with MWCNT sheet material and (c) S_{11} of MWCNT dipole antennas fabricated with a radiating arm width W= 1.5mm. (d) Measured frequency of resonance as a function of the radiating arm lengths of the MWCNT antennas. Copyright ©ACS publications, 2016 published in [70]

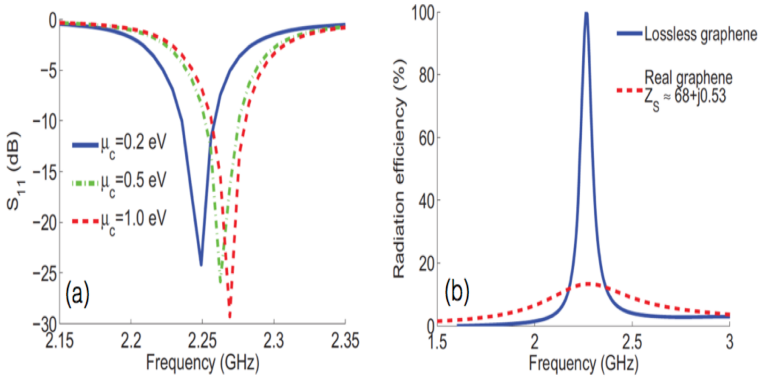

Figure 2.23: Return loss of monolayer graphene based MPA at different values of the chemical potential. Reprinted with permission from IEICE, copyright ©2016 IEICE, permission No.: 17SA0082 [72]

reduction, the electrical properties can be improved, as it will be described in section 3.4.6. Thus, it becomes an alternative candidate, which can be used for patch antennas. GO has shown to have a high sensitivity for humidity. Zhang et al. used it for wireless humidity sensors; the shift in the resonance frequency of the sensor as a result of humidity is basically due to the change in the capacitance of the inductor-capacitor (LC) tank circuit of the planar spiral inductor, which is fixed on an FR4 substrate (Figure 2.24 (a)) [73]. The proposed sensor is working in HF-band with an initial resonance frequency of 39.04MHz, and the monitored humidity range is from 15 to 95%RH (Figure 2.24 (b)).

As an improvement of the exciting passive wireless strain sensor based antenna, Song et al. fabricated a stretchable, mechanically tunable and reversibly deformable MPA using polydimethylsiloxane (PDMS) as substrate material and screen-printed silver nanowires (AgNW) as patch layer (Figure 2.25) [7]. Two patch antennas are designed, the first one is with one element MPA working at 3GHz and the second is a 2-element patch array working at 6GHz. Good agreement between the simulation and the experimental results of the radiating pattern under tensile strain is concluded, due to the losses in the PDMS and the AgNW, the radiation efficiency is about 41.53% which is about 15% less than its similar counterpart copper MPA. For the strain tensile tests, the antenna is fixed on a home-made

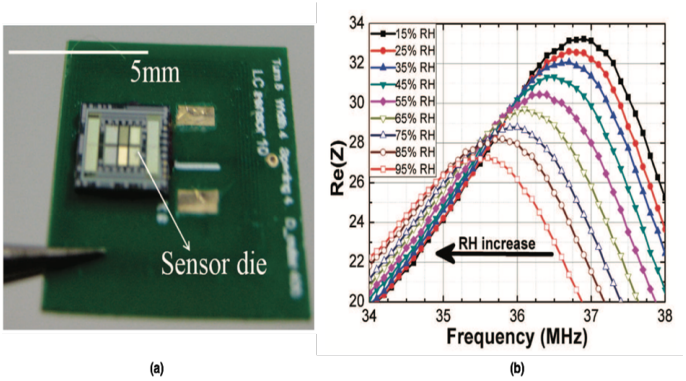

Figure 2.24: LC-type passive wireless humidity sensor (a) Optical inset, (b) Return loss change under different values of humidity. Copyright ©IEEE, 2013 published in [73]

mechanical testing stage, where all the components are insulators, the strain is varied from 0% to 15% along the patch width direction. Figure 2.26 shows results of simulation and experimental of the MPA under tensile strain from 0% to 15% for one loading and unloading cycle. As demonstrated by [23] increasing the strain along the patch width increases linearly the resonance frequency, and a small hysteresis is noted after the unloading cycle. The authors claimed that the antenna has a good stability even after several bending, twisting and rolling tests.

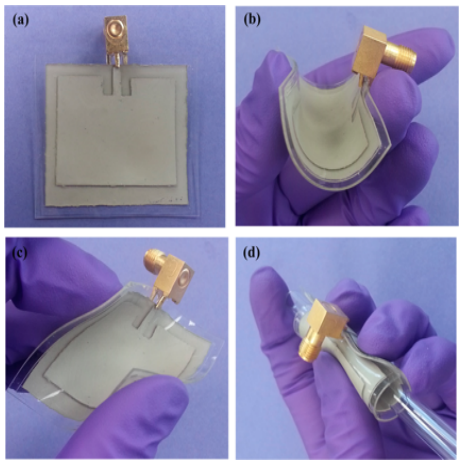

Figure 2.25: Photographs of a stretchable microstrip patch antenna composed of AgNW/PDMS flexible conductor: (a) Relaxed, (b) Bent, (c) Twisted and (d) Rolled. Copyright ©ACS publishing, 2014 published in [7]

2.6 Evaluation of State of the Art Solutions

As stated previously, the MPA is successfully implemented for passive wireless sensors mainly for strain, temperature and humidity. However, limited sensitivity is always a big issue. For strain sensing, different approaches are proposed to improve the strain sensitivity, such as different patch layouts, multiband antenna, slots on the patch, different working frequencies and substrates with different dielectric materials. On one side, single frequency rectangular patches have higher sensitivity than the multi resonating and the circular patches. On the

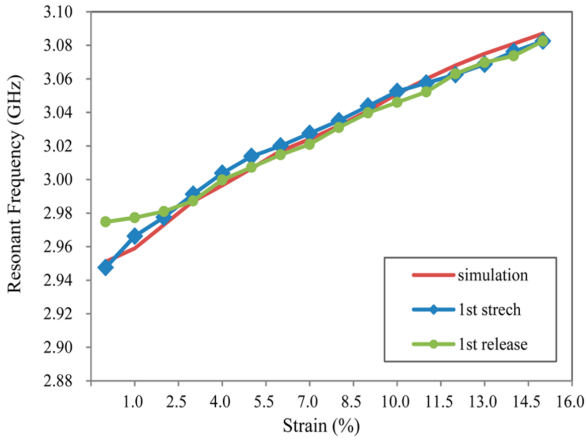

Figure 2.26: Comparison of simulated and measured resonant frequency of the AgNW/ PDMS microstrip patch antenna under tensile strain. Copyright ©ACS publishing, 2014 published in [7]

other side, the double and multi resonance rectangular patches and circular patches have the ability of multidirectional strain sensing. The reading distance of the patch antenna is improved either by introducing some slots on the patch or using folded patch; however, the strain sensitivity is dramatically decreased. Beside that, the reading distance can be also increased by using substrates with low loss and high permittivity. Also, complicate techniques are used to fabricate these antennas. It is also noticeable that, the strain sensitivity along the patch's length is always higher than along its width. Using thin substrates to improve the strain transfer between the object under test and the MPA did not really improve the strain sensitivity. A comparison between different patch antennas used for wireless strain sensing is in Table 2.5. For wireless temperature sensors, broad range of dielectric materials can be used as substrates for MPAs, but only very limited number of these materials have a linear change in the dielectric constant as function of temperature, so the temperature sensitivity remains always low and limited. Nevertheless, for temperature sensing, low permittivity substrate materials show higher temperature sensitivity than substrates with high dielectric constant. Also, the type of the patch metal did not really influence the temperature sensitivity. Using nanomaterials, such as PEDOT:PSS, CNTs and GO did not improve the sensitivity as it is expected. This is referred to the low conductivity of the fabricated nanocomposite which introduces high losses when it is used as load of the patch antenna. PEDOT:PSS shows a broad bandwidth due to the high losses in the conductance in the microwave range; also, no strain sensitivity is remarked. Due to its hygroscopic property, it is mainly used for wireless humidity sensing. CNTs and GO are mainly used for gas and humidity sensing and it is assumed that the minimum required conductivity for a good gain patch antenna must be 10^5S/m. To use them for strain sensing, the CNTs are deposited on gold layer, and this improves the strain sensitivity to 6.5% for a displacement of 1.5mm. Another proposed way to improve the conductivity is to use a mixture between SWCNTs and MWCNTs to form a layer with $10\Omega.sq^{-1}$. Although the resonance frequency of MPA based graphene can be adjust by means of its chemical potential, depositing a monolayer graphene on different substrate is still challenging; thus, it makes the fabrication of graphene based on patch antenna complicate and too expensive. Generally, the high losses introduced by CNT and graphene materials make them a good candidate in the DC-LF

band application. To overcome these obstacles, an innovative and novel solution must be implemented. Therefore, the development of novel nanocomposites to be used as patch layer as well as keeping the sensing properties will improve dramatically the strain, temperature or humidity characteristics. These nanocomposites should satisfy the requirements of an RFID sensor such as high conductivity, and good linearity and high sensitivity. This is actually very challenging, as property like conductivity and piezoresistivity are lying on two different paths. Whereas increasing the conductivity decreases the piezoresistivity of the material and therefore decreases the sensitivity and vice versa. For the metallic patch antenna as strain sensor, the low strain sensitivity is caused by the change of geometry resulting from the applied force which changes the resistance and consequently the resonance frequency shifts. However, the piezoresistivity of metals is low, thus it is negligible. Besides this challenge, the

Table 2.5: Summary of MPA used for strain sensing

Ref.	Substrate Thickness (μm)	Frequency (GHz)	Strain Range ($\mu\epsilon$)	Sensitivity (kHz/$\mu\epsilon$)
Tata et al. [22]	50	20	0 -550$\times 10^3$	22.8
Tata et al. [23]*	50	15.8 and 20.5	0 -550$\times 10^3$	15.5 and 9.2
Daliri et al.[28]	1500	1.5	25	10
Yi et al. [31]	790	0.921	0-500	-0.790
Ahbe et al.[6]	1500	2.9 and 5.8	0-2500	-2.2 and -3.1
Thai et al.[33]	100	3	0-7$\times 10^3$	1.26
Wang et al. [36]	50	2.5 to 20.5	0-363	20.5 and 46.8
Song et al. [7]**	1500	3 and 6	0-150$\times 10^3$	53.7

* This is a circular shape instread of rectangular shape used in all other patches.
** Patch made with AgNw instead of copper used in all other patches.

fabrication and structuring of the nanocomposites are crucial, thus it requires processing techniques to obtain the desired characteristics. To meet the minimum requirement for a good antenna gain, the conductivity of the nanocomposite must be around 10^5S/m. Using CNT, PEDOT:PSS and GO, different nanocomposites are fabricated and used as sensing layer to get a high sensitive wireless strain and temperature or humidity sensors. Three different nanocomposites are studied, CNT and PEDOT:PSS, GO and CNTs and GO, CNT and PEDOT:PSS. The fabrication method used to manufacture these nanocomposites is explained in the next chapter and the experimental steps are described in Chapter 4.

Background on Nanocomposite 3

In this chapter a general overview about conjugated polymers, their synthesis, properties and applications are introduced. Besides, a brief introduction to carbon nanotubes and graphene oxide is given. These include their properties, synthesis and major applications. Afterwards, different techniques used to prepare the polymer nanocomposites is covered. Then understanding the origin of the electrical properties of the polymer nanocomposite and the parameters influencing its conductivity are explained.

3.1 Conjugated Polymers

Polymers consist of long chain-like repeated chemical units called monomers, joined end to end to form a chain molecule. If the monomers have only one type of basic chemical unit, the polymer is named homo-polymer; if there are more than one type of monomers, then the polymer is named co-polymer. Generally, polymers can be classified into different groups depending on the property of interests. Based on the chemical composition, polymers can be organic, this means that carbon is the main element of its repeating units, or inorganic polymers where chain-like structure that does not include carbon such as aluminum nitride polymer and silicon polymer (glass) or hybrid polymers, that contains a mixture of inorganic and organic components such as silicon rubber. Based on how the monomers are linked to each other, the polymers can be categorized as: Thermoplastics, thermosetting and elastomers polymers. The thermoplastics polymers can be molded and remolded by heating it many times, as it does not suffer from any chemical changes if it's treated with temperature. They contain of a tangled mass of molecules in its molten state. If they are cooled down below the glass transition temperature (Tg), they form a glass or they may crystallize. On the other hand, the thermosetting polymers can be formed only once and therefore can be molded only once. This is because the molecules within the polymer network are heavily cross-linked to three-dimensional network. In contrary to thermoset, elastomers, known also as rubbers, are lightly cross-linked, i.e. they cannot be melt in the conventional sense by temperature. On cooling, they are partially crystalize or glassy. They have reversible stretchable properties if they are under high stress forces. In terms of electrical conductivity, the polymers are insulator due to their high bandgap, which blocks the electrons in the valence band and therefore they get very high resistance values i.e. very low conductivity around 10^{-6}-10^{-18}S/cm as depicted previously in Figure 1.1.
However, in 1977 a tremendous discovery of new class of polymers took place, by doping organic conjugate hydrocarbon such as polyacetylene (PA) with Halogens, the conductivity of the polymer enhanced dramatically, this is referred to the presence of alternating carbon-carbon double bonds along the backbone structures of PA, which enables the overlapping of π-orbital along the molecule chain-like structure [74-75]. Due to the electron-transport characteristics, this new class of polymers is regarded as semiconductors or even sometimes as conductors. This class is called conjugated polymers also known as synthetic metals or intrinsically conductive polymers [74]. Although, the first studies focused on the improvement of the electrical properties of PA, further developments found a way to realize other

types of conducting polymers such as polyphenylene (PPh), polypyrole (PPy), polythiophene (PTs), polyaniline (PANI) and their derivatives and Figure 3.1 illustrates the chemical composition of the most important synthetic metals. These conjugated polymers have good conductivity, which can reach 10^5S/cm as well as a good stability in air. Beside their good conductivity, the ICPs suffer from lack of solubility in organic solvents, which restricts their implementation in the realtime application. Different efforts have been enrolled to make them soluble in solvents. In 1993, PANI was successfully dispersed in organic solvent called m-cresol, although a low conductivity was recorded around 10S/cm, a new epoch of soluble conductive polymers is released [76]. Among others, the polythiophene derivative, poly (3,4-ethylenedioxythiophene) (PEDOT) has been intensively studied because of its remarkable electrical, chemical and mechanical properties [77-79]. However, the poor solubility of this polymer in water and organic solvents limits its application in the field of flexible electronics [80]. Bayer AG company prepared the first commercial water-soluble polyelectrolyte ICP based on poly(3,4-ethylene dioxythiophene) (PEDOT) doped with poly-(styrene sulfonic acid) (PSS) known shortly as PEDOT:PSS. The doping process makes the PEDOT:PSS to be a hole conductive colloidal suspension, which makes it widely used in solar cells as hole injection layer instead of the brittle indium tin oxide (ITO), also the electronic properties of the intrinsically polymer can be tuned by controlling the chemical structure, doping condition and the alignment of the polymer chain [81]. Accordingly, PEDOT:PSS has found applications in flexible electronics, radio-frequency identification tags (RFID) [82], field effect transistors (FET) [83-84], transparent electrodes [85], solar cells [86-88] and sensors [89-90].

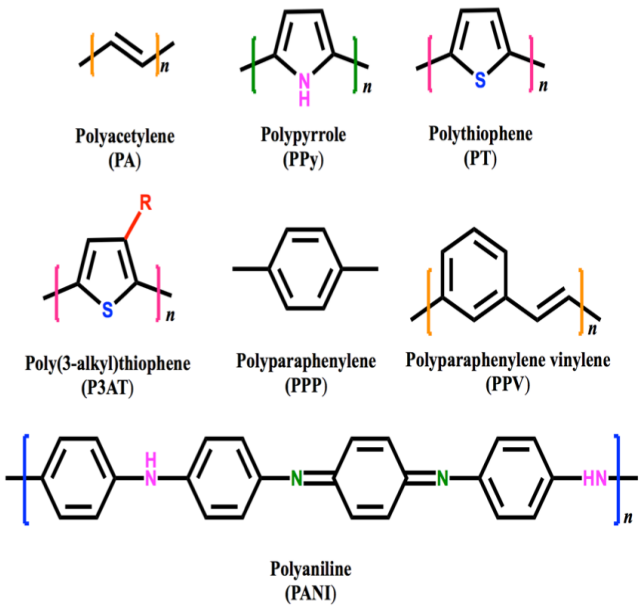

Figure 3.1: Chemical structures of the most commonly used ICPs

3.2 Synthesis of PEDOT:PSS

The availability of PEDOT:PSS as an aqueous dispersion with variant conductivity, made it one of the most successful intrinsic conductive polymer in the market. The PSS is used as counter anion for the PEDOT by chemical oxidation to form a stable polyelectrolyte complex,

therefore the PEDOT:PSS can be dispersed in water. This dispersion is then deposited onto different substrates using different techniques such as drop casting, inkjet printing and layer-by-layer deposition. The 3D-chemical structure of the PEDOT and the PSS monomers is depicted in Figure 3.2. PSS has outstanding properties such as its solubility in water, high transparency as films within the visible light spectrum, its commercial availability in different large range of molecular weights, made it a suitable candidate for use as counterion for PEDOT, therefore, the PEDOT:PSS dispersion is stabilized by the excess PSS. The PEDOT on the other side is a derivative of polythiophene and is commonly prepared by oxidative polymerization or self-oxidation of ethylenedioxythiophene (EDOT) monomer. The oxidized PEDOT is not stable and may decompose if the used oxidant is highly concentrated [81]. Thus, the counterions of PEDOT through the electrochemical polymerization is necessary for charge balancing and the Coulomic interaction forces keep the PEDOT chains attached to the PSS chains [81]. It is assumed that the degree of polymerization is limited to PEDOT segment, which has molecular weight between 1000 and 2500 with collection of oligomers having up to 20 repeating units, and as the PSS has much higher molecular weight about 500.000, it will keep the PEDOT chain dispersed in water [91]. The structure of the PEDOT:PSS is

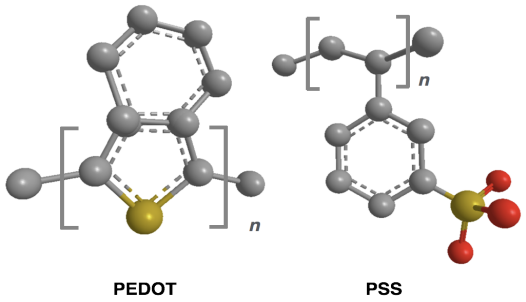

Figure 3.2: 3D molecular structure of PEDOT and PSS polymer

outlined into different structures as it is shown in Figure 3.3. In the primary structure named also as the chemical structure (Figure 3.3 a), each styrene ring of PSS monomer is bounded to one acidic sulfonate (SO_3H) group of the PEDOT. Because of acid doping, the PEDOT acts as proton acceptor rather than electron donor. Thus, the positive charge on the PEDOT segment attracts the negative charge on the SO_3H group. Since this process happens along the polymer chain, PEDOT and PSS becomes closely linked. However, the high conductivity is due to the unpaired-electron that remains on the PEDOT chain highly mobile along the conjugated backbone [92, 93]. In the secondary structure (Figure 3.3), the PEDOT and PSS chains are bonded by the Coulombic attraction, these attraction forces introduce a stress in the polymer chains due to the mismatch between the PEDOT oligomers and PSS chains, therefore the PEDOT:PSS chains adopt a coiled structure and thus introduce a localization of the positive charges [94]. Whereas in the tertiary structure (Figure 3.3 c), the PEDOT:PSS form core/shell structure known also as gel structure in the aqueous solution due to the hydrophilic PSS and hydrophobic PEDOT chains, with particles consisting of around 90-95% water, with the conductive PEDOT segment is core-rich and it is surrounded by the insulating PSS is shell-rich of the grain [95]. Depending on the desired application, such as printed electronics, organic field effect transistors (OFET), polymer capacitors, hole injection layers in the OLEDs displays and as hole transport layer in organic solar cells, different commercial aqueous dispersions of PEDOT:PSS are proposed. Depending on additives type, particle size, conductivity, doping concentration and solid content, wide variety of PEDOT:PSS are

available in the market, the most important dispersions mainly the Clevios P from Company Hereaus (known before as Bayer AG) version are summarized in Table 3.1.

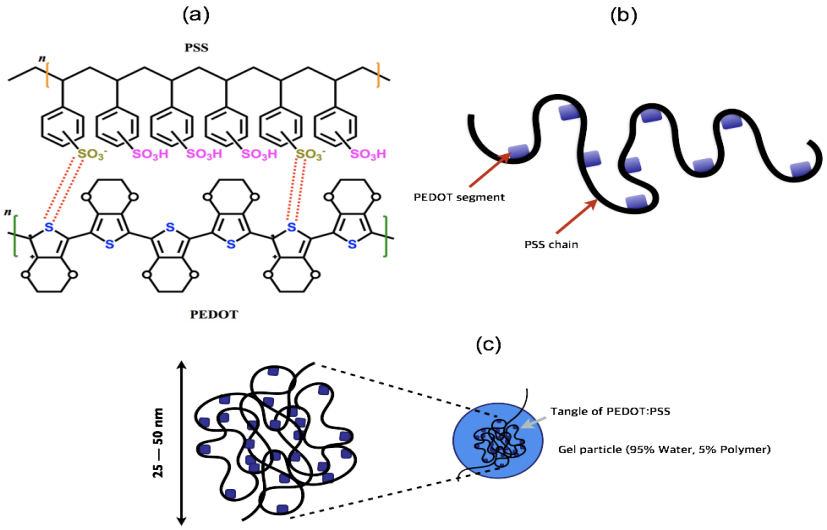

Figure 3.3: Building structure of PEDOT:PSS (a) Primary, (b) Secondary and (c) Tertiary. Reworked based on [95]

Table 3.1: Properties of the Clevios commercial PEDOT:PSS dispersion

Product Name	Solid Content (%)	PEDOT:PSS Ratio	Viscosity (mPas)	Additives (ppm)		Resistivity
				Sodium	Sulfate	
PVP AI 4083	1.3-1.7	1:6	5-12	400	40	500-5000
PVP CH 8000	2.4-3.0	1:20	2- 20	400	60	1×10^{4}-3×10^{5}
P	1.2-1.4	—	60-100	500	80	
P T2	1.05-1.3	—	150	—	—	750
PH	1.2-1.4	—	15-30	500	80	10×10^{6}
PH500	1.0-1.3	1:2.5	8-25	—	—	3.33×10^{-3}
PH 1000	1.0-1.3	1:2.5	15-50	—	—	1.17×10^{-3}

* all the dispersions have a dark blue color and are odorless.
** due to the PSS content, it has an acidic property with PH value between 1.0-2.5 at room temperature
*** boiling point at 100 and density around $1 g/cm^3$ at 20°C.

3.3 Electronic Transport in the Intrinsic Conductive Polymer

The alternating single and double carbon-carbon bond in the conjugated polymer makes its conjugated π-orbitals chain-like structure unique in terms of its electronic conduction, which differs from that of metals and inorganic semiconductors. For each two neighboring atoms, an overlapping of the pz-orbitals forms a bonding orbital (π-bonds) and an anti-bonding orbital (π^*-bonds) above and below the plane of the molecule respectively [96]. The interaction of these two orbitals form a continuous two bands, the valence and conduction band which are named chemically as the Lowest Unoccupied Molecular Orbital (LUMO), the Highest Occupied Molecular Orbital (HOMO), respectively. Therefore, the charge carries available in the valence band i.e. electrons are mobile and delocalize, as it is shown in Figure 3.4 [97]. The low conductivity with a small bandgap about meV arises from the inequality of the bond length distribution along the polymer chain backbone, where the C-C

bonds are longer then the C=C bonds. Depending on the symmetry of the polymer chain (high symmetry or low symmetry), the solitons or polarons and bipolarons are the charge carries, respectively. For low symmetry polymer, few solitons with their discrete bandgaps are available in the Fermi level. After doping, the concentration of the solitons increases. The solitons can be either positively charged if the doping process is an oxidation process, or negatively charged if the doping process is a reduction process. The energy bandgap of these solitons interacts and overlaps on each other if the concentration of the solitons is high due to the increase of the doping rate. These overlapping forms a solitons band instead of the discrete bands between the LUMO and the HOMO levels. As the doping degree increases more, the solitons-band broaden to overcome the LUMO and HOMO levels and thus the polymer shows a conductive behavior [97]. In the non-doped state of the low symmetric polymer chain, the polymer behaves as an insulator, with a bandgap between the LUMO and HOMO. After oxidation process, the polymer is positively charged by removing the electrons from its conjugated π-system, and therefore keep the pz-orbital unfilled. The interaction of conjugated π-system of two neighboring pz orbitals forms two discrete energy levels, 0.5eV above the LUMO and 0.5eV below the HOMO in the Fermi level called as polaron level. Increasing the doping degree leads to the coupling between the polarons together and consequently the formation of the bipolaron with two positive charges and no unpaired electrons [97]. Dissimilar to the solitons, the bipolarons have continues band structure located 0.75eV from LUMO and HOMO within the Fermi level. Increasing the doping, the bipolarons overlap and form a continues band along the bandgap from valence band to the conduction band, and thus the polymer behaves as metallic-like behavior. However, doping and oxidation introduce a disorder to the conjugated π-system and consequently the appearance of kinks, cross-links and impurities disrupts the π-system. Thus, hopping between the polymer parts dominates the electronic transport and therefore the polymer resembles to a three-dimensional semiconductor [98]. The occurrence of the disorder in the Fermi level of the ICPs induces localization of the charge carriers and subsequently hopping conductance mechanism occurs. Therefore, the Fermi Liquid theory is often used to describe the electronic transport of the standard 3D-conductors [98]. The conductivity as function of temperature within the disordered organic polymer is reported to follow the Mott's variable range hopping [91, 99-100]:

$$\sigma = \sigma_o \times exp^{(\frac{-T_0}{T})^{\frac{1}{S}}} \tag{3.1}$$

where, σ_o is the characteristic conductance at characteristic temperature T_0, S is the dimensionality of the system which varies between 0 and 2. T_0 can be calculated as follow:

$$T_0 = (16/k_b) \times N(E_f) \times L_\perp \times L_\parallel \tag{3.2}$$

where k_b is the Boltzmann's constant, $N(E_f)$ is the density of the states at the Fermi level, $L_\perp$ and $L_\parallel$ is the localization length in the perpendicular and parallel direction, respectively [97].

3.4 Carbon Nanomaterials

Carbon in its different allotropes was the corner stone of the human kind revolution, from burning wood to metallurgic processes to selling boats, to pushing steam engines to nanotechnology. Different allotropes are due to the special and different atomic and bonding arrangement to the nearest neighbor atoms, which is known as the hybridization

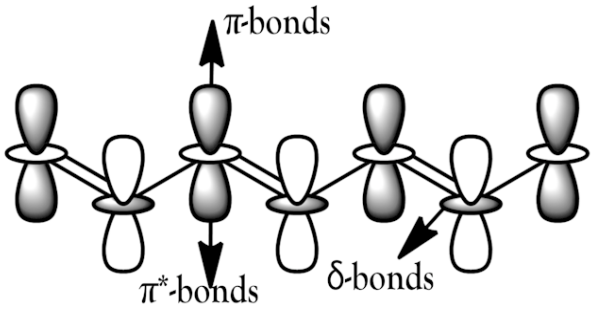

Figure 3.4: Building structure of PEDOT:PSS with double bonds at the backbone

state. The first well-known carbon allotropes are amorphous carbon, graphite and diamond, after the discovery of the buckminsterfullerene C_{60} known also as fullerene buckyballs in 1985 [101], carbon nanotubes (CNTs) in 1991 [102] and graphene in 2004 [103] new carbon allotropes are recognized. Therefore, a new classification of the carbon allotropes based on their hybridization type and dimensionality raised, as shown in Figure 3.5. The different allotropes provide us with broad range of materials with properties that changes dramatically from one form to another, whereas the diamond is an insulating carbon form due to its sp^3 hybridization states that blocks the free movement the charge carrier; C_{60}, CNT and graphene show very high conductivity due to its sp^2 hybridization state, where the charge carrier can move even without scattering (ballistic transport). Thus, carbon nanomaterials have a broad research and application areas starting from reinforcement fillers, energy storage, drug delivery to devices and transistors in nanoscale [1].

3.4.1 Carbon Nanotubes

The first indication of the synthesis of the carbon nanotubes was in 1952 in the Russian Journal of Physical Chemistry by Radushkevich and Lukyanovich published in Russian language, however, due to the low resolution of the transmission electron microscopy (TEM) available that time, they have described their finding as long carbon filaments with inner cavity i.e. tubular nature [108]. Beside that the original work was published in Russian, so the western scientists had difficulties to access to the Russian publications, nevertheless further works were conducted to further investigate the properties of the carbon filament from the thermal decomposition of gaseous hydrocarbon, more details is found in [109]. Iijima in 1991 could identify concentric carbon microtubules in the nanometer size made by arc discharge using a high resolution transmission electron microscopy (HRTEM), he called these structures multi-walled carbon nanotubes (MWCNTs) [102]. Two years later, single carbon microtubules were achieved and therefore they were named single-walled carbon nanotubes (SWCNTs) [110-111]. Carbon nanotubes can be conceptually labeled as cylindrically shaped molecules formed from rolling-up single (SWCNT) or multilayer (MWCNT) of graphene sheets of sp^2 bonded carbon atoms that are densely packed in a honeycomb crystal lattice with hexagonal unit cell consisting of two double bonded C atoms that repeat and make a complete sheet of graphene, as it displayed in Figure 3.6. In case of the MWCNT, two models are usually used to describe its structure, the Russian Doll model and the Parchment model [112]. In the Russian Doll model, the graphene sheets are

[1] Photo credit of Fig. 3.5: * [104], ** [105], *** [106] Reproduced with permission from Luca Ortolani, **** [107]

arranged in concentric cylinders, but in the Parchment model, the graphene sheet is rolled around itself, resembling a scroll of parchment. The interlayer constant separation between the internal tubes is 3.4Å, which is slightly greater than the distance between graphene layers in graphite, which is approximately 3.35Å [112]. The structure of the CNT and therefore its properties are determined by the way in which the graphene sheet is rolled into tubes, and it is usually described as the tube chirality, known also as helicity or wrapping, and it is represented by a pair of indices (n, m). These indicate the number of unit vectors along two directions in the honeycomb crystal lattice of graphene (Figure 3.6), it is also expressed by the circumferential vector, $C_h = n\overrightarrow{x} + m\overrightarrow{y}$ [112-113].
Thus, three types of chirality are specified as armchair (n, n), zigzag ($n = 0$, or $m = 0$), or chiral (all others) (Figure 3.6). Chirality has significant impact on the electronic properties of the CNTs. All armchair tubes with n=m have a metallic conductive behavior with zero bandgap. Whilst, the tubes with $n - m$=$3i$ (i being an integer and $m \neq 0$) are semiconductor with a bandgap on the order of a few meV, whereas tubes with $n - m \neq$ 3i are semiconductors with a bandgap of ca. 0.5-1eV, therefore it is worth mentioning that 2/3 CNTs are semiconducting and other 1/3 are metallic [113]. As the MWCNTs contains tubes arranged in a concentric manner containing a different diversity of tube chirality, thus it is more complex to predict their electronic properties.

3.4.2 Properties of Carbon Nanotubes

CNTs are 1D systems with tube diameter in the nanometer range, this arises the effects of the quantum properties on the CNT characteristics. CNTs can have either metallic or semiconducting behavior depending on their chirality, number of walls, aspect ratio and

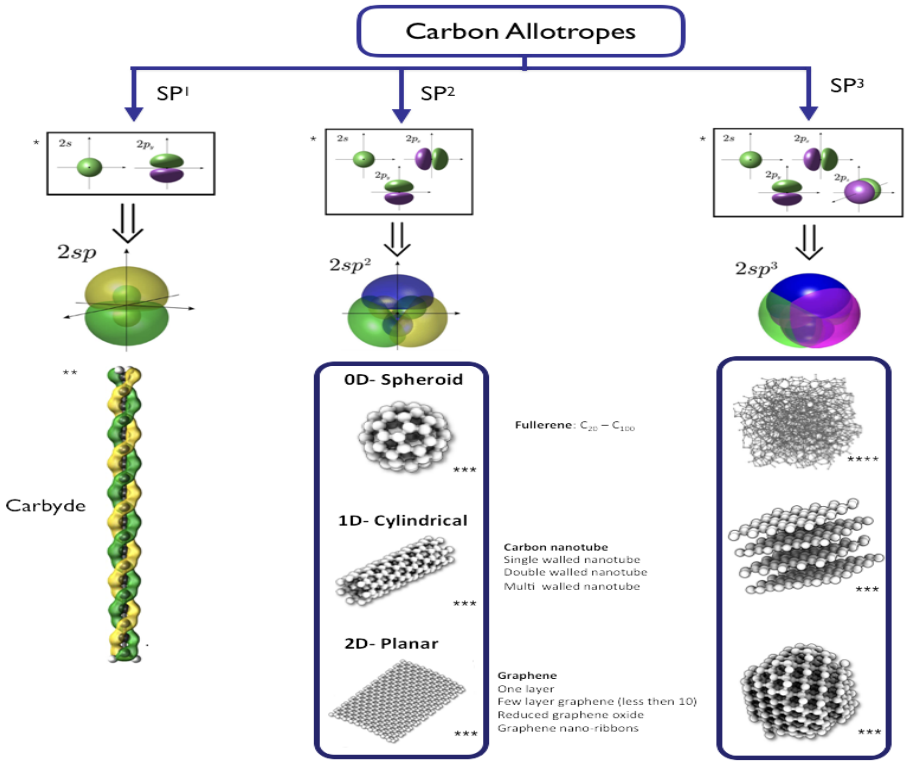

Figure 3.5: Carbon structural families based on their hybridization state

synthesis method [114]. For a defect free tube and perfect contacts with electrodes, a metallic CNTs can transport the electrons ballistically and without striking with the crystal structure, therefore no loss in energy is caused and theoretically no resistance can be measured. While the MWCNTs show metallic behavior properties due to the interaction between the multiple walls of the MWCNTs, only transport through scattering is taking place, whereas the semiconducting CNTs show also scattering of the electrons, therefore increasing the length of a CNT increases the resistance [115-116]. For the SWCNT, the energy bandgap (E_{gap}) depends strongly on the tube diameter, which is given by following equation [115]:

$$E_{gap} = \frac{2\gamma_0 a_{c-c}}{d} \tag{3.3}$$

Where γ_0 is the C-C tight binding overlap energy (2.45eV), the nearest neighbor C-C distance about 1.42Å, and d is the nanotube diameter.

However, for the MWCNTs and due to the confinement effects that arise due to the tube circumferences, the MWCNT behave like quantum wires with a high degree of graphitization and conductivity around 10^3S/cm along the tube axis with very high current density around 10^7A/cm^2 [117]. The MWCNTs are assumed to be metallic tubes, thus the density of states near the Fermi level are almost constant and its conductance (G) is given by [118],

$$G = G_0 \times M = (\frac{2e^2}{h}) \times M \tag{3.4}$$

Where, G_0 is the quantum conductance $(12.9\text{k}\Omega)^{-1}$, M is an apparent number of conducting channels including coupling and intertube coupling effects in addition to intrinsic channels and e is the electron charge, h is the Planck's constant.

In terms of mechanical properties, CNTs show outstanding mechanical characteristics, for instance the Young's modulus of SWCNTs was measured to be 2.8- 3.6TPa, while for the

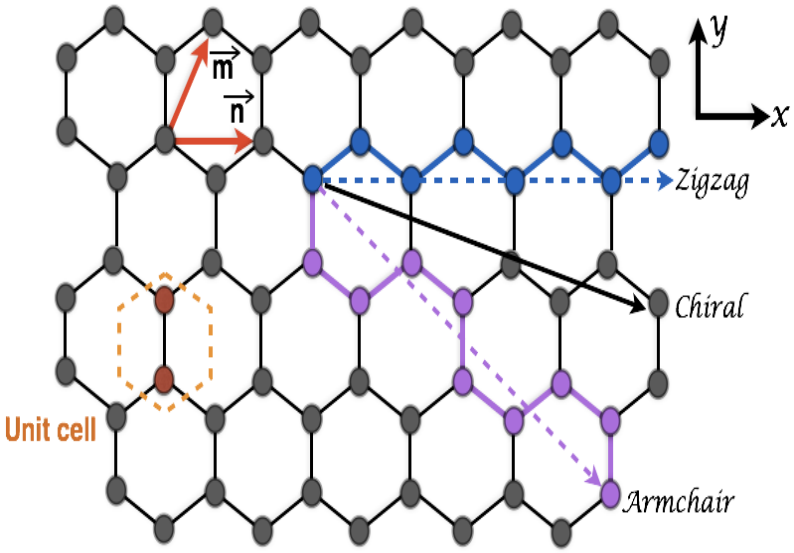

Figure 3.6: Honeycomb crystal lattice of graphene with chiral vectors for determining the structure of the CNT

MWCNTs was found to be around 1.7- 2.4TPa, and tensile strength around 50- 200GPa, which is several hundred times higher than of the steel, this excellent mechanical properties are attributed to the strong sigma bonds between the carbon atoms [119]. CNTs possess also excellent thermal stability up to 2800°C in vacuum and 750°C in air; with low lateral thermal conductivity and high axial thermal conductivity up to 10.000W/mK depending on the tube diameter [120], which is almost five times higher than the best available commercial synthetic diamond (1.000-2200W/mK) [121]. The CNTs tend also to form agglomerates due to the strong van der Waals (vdW) attraction forces between them which is considered to be around 0.5eV/nm [122], this limit the entire use of its properties and thus its applicability in the realtime application. Besides that, CNTs suffer from the low solubility in water and organic solvents; which makes the side functionalization of the CNTs crucial to overcome this issue and extract their maximum functionality. Doping using different functional groups, DNA chains and decoration with specific organic and inorganic molecules were attached to the sidewall of the CNT for the specific chemical or biological application [123].

3.4.3 Synthesis of Carbon Nanotubes

To bring the CNTs to the industrial applications, a development of large-scale production techniques of nanotubes is required. Thus, in 1992, Ebbesen and Ajayan introduced a method for the large scale synthesis of nanotubes [124], since then wide witnessed significant research efforts in efficient and high-yield nanotube growth methods were conducted, mainly, arc-discharge, laser ablation, thermal synthesis and Plasma Enhanced Chemical Vapor Deposition (PECVD) were introduced. Next arc-discharge, laser ablation, and thermal synthesis is very briefly explained; more details are found in [125-128] for broader overview and deeper understanding of those synthesis methods and other issues.

Arc Discharge

It is the first method that was successfully used to synthesize CNTs in small quantities. It consists of circular graphite electrodes with diameters between 5 to 20mm and gap of 1mm. The electrodes are placed in inert air, typically Helium (He) or Argon (Ar) at a pressure of 13 to 130kPa [126], as it is shown in Figure 3.7. A low voltage and high current typically around (12 to 25V) and (50 to 120A) is applied between the cathode and the anode, this generates an arc-induced plasma that evaporates the carbon atoms from the graphite, and CNTs are formed on the anode. Whereas the MWCNT can be formed without a catalyst, the SWCNT can only be formed by adding metal catalyst to the anode such as iron or cobalt [126]. In this method, the diameter of the SWCNT can be controlled by tailoring the Ar:He gas ratio, with high Ar ratio leads to smaller SWCNT diameter [129]. Beside that the amount of the produced CNTs in this method is very small (few grams only), it needs extensive purification steps to remove the amorphous carbon, small fullerenes and metal catalyst particles that are naturally produced in the process.

Laser Ablation

The arc discharge and laser ablation have analogous working principle, when pure graphite is used as anode, it produced MWCNT and fullerenes, whilst using a metal-impregnated graphite anode to produce SWCNTs [125, 127]. As it is shown in Figure 3.8 (a), a graphite composite target (anode) that is placed in a quartz tube furnace at around 1200°C under an inert atmosphere of about 60KPa of Ar or He, then a laser beam is focused on the anode and

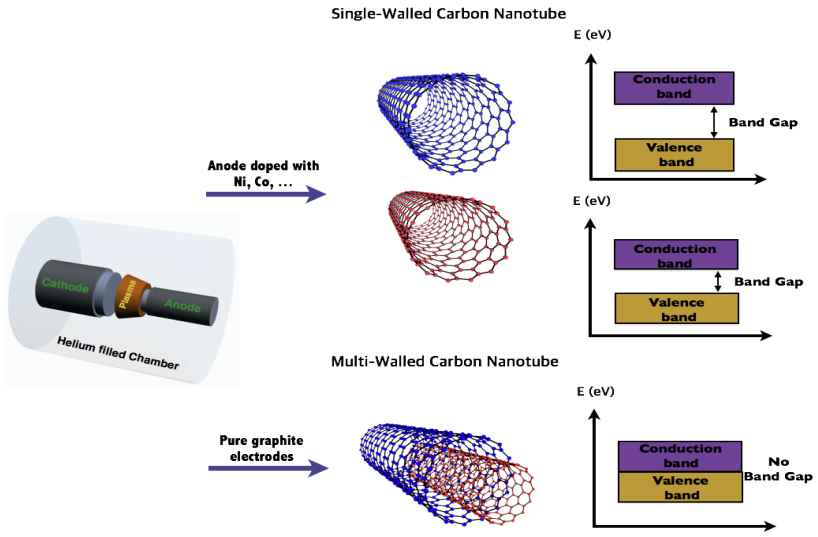

Figure 3.7: Schematics of CNT synthesis using arc discharge method

swept uniformly across the graphite target surface. The carbon atoms are evaporated from the surface of the target and then CNTs are collected on a cooled substrate at the end of the chamber [125, 127].

Thermal Synthesis

The thermal synthesis covers numerous different synthesis methods, including chemical vapor deposition (CVD), high-pressure carbon monoxide synthesis and flame synthesis. Among them, CVD has the highest potential for mass production of carbon nanotubes (Figure 3.8 (b)). Here, an alumina/quartz substrate with material catalyst (e.g. iron, nickel) deposited onto its surface is placed into a tubular furnace between 500°C-1200°C and a hydrocarbon gas such as ethanol or carbon monoxide is slowly pumped into the furnace, the CNTs produced have a yield that can exceed 99% (weight percent of final material) [127].

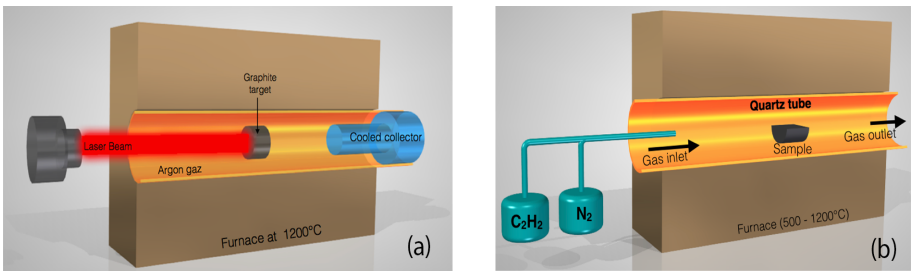

Figure 3.8: Schematics of CNT synthesis using (a) Laser ablation and (b) CVD method

3.4.4 Graphene Oxide

Graphene oxide (GO) is a non-stoichiometric macromolecule regarded as a wrinkled one atomic layer of the two-dimensional graphene sheet decorated with various oxygenated functional groups on its basal plane and peripheries, with lateral dimension between few

nanometers to several microns, and thickness of 1nm. Depending on the preparation method and therefore the type of the acids and oxidants used, different functional groups were proposed. To name few, carboxyl, hydroxyl, epoxy, lactones, which determine the acid behavior of the colloidal [130]. The ketone, pyrones, chromenes, ester and carbonyls functional structures, which determine the basic behavior of the colloidal [130]. Those functional groups give the polar properties to the GO [131, 134]. Extensive studies have been done to clarify the chemical composition of the GO, and how the functional groups are distributed on its plane, these differences are referred mainly to the nonstoichiometric nature and the strong hygroscopicity of the dehydrated graphite oxide [135, 138]. However, it is still controversial and unclear which model is the most accurate. The electronic, mechanical, optical and electrochemical properties of the GO are strongly depending on those functional groups. Figure 3.9 illustrates a model proposed by Lerf, which is assumed to be the most accurate one [131].

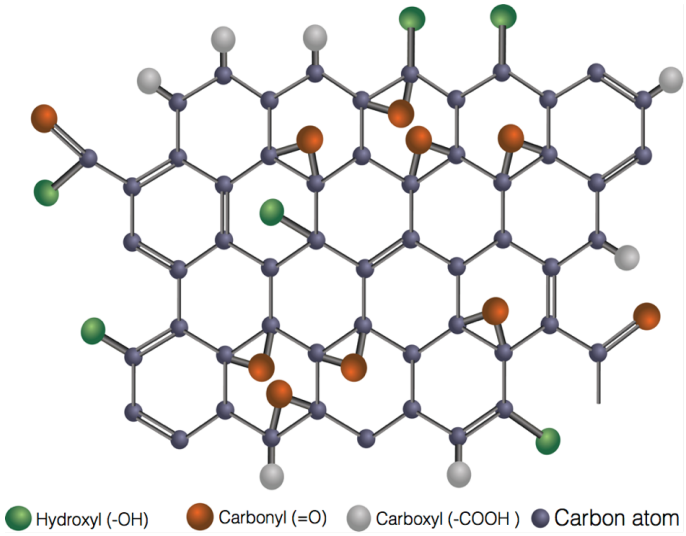

Figure 3.9: Illustration of the chemical structure of graphene oxide, reworked based on [131]

3.4.5 Synthesis of Graphene Oxide

Synthesis of graphite oxide was to the first time in the mid-1800s by Brodie [139] and later by Staudenmaier [140]. But these methods are time consuming and use very hazardous oxidants. Hummers proposed a new way to overcome the pre-mentioned drawbacks [141], lately other methods were also proposed based on the variation of Brodie, Staudenmaier and mainly Hummers methods [142]. Basically, preparation of the GO implicates the chemical oxidation of the natural graphite flakes in the existence of strong acids and oxidants. Whereas Brodie and Staudenmaier used a mixture of potassium chlorate $(KClO_3)$ with nitric acid (HNO_3) to intercalate the graphite flakes to graphene oxide, Hummers on the other side treated the graphite flakes with potassium permanganate $(KMnO_4)$ and sulfuric acid (H_2SO_4) to oxidize the graphene flakes. The degree of oxidation can be controlled by varying the synthesis conditions, strong acid mixtures and the precursors of the graphite.

3.4.6 Exfoliation and Reduction of Graphite Oxide

Upon oxidation, the polar oxygen functional groups decorate the basal plane of the GO, making it hydrophilic. Thus, GO can be dispersed easily in water and exfoliated in other solvents [143]. The generated sp^3 hybridized due to the covalent bonds between the carbon atom and the functionalization group disrupts the extended sp^2 conjugated network of the graphene-like lattice structured, therefore the ratio between the sp^2 and sp^3 determine the degree of functionalization [138, 142]. The dispersion of the GO can be achieved by stirring and/or mild ultrasonication of GO sheets in solvents, this process weakens the van der Waals attraction forces between the graphite platelets, and consequently simplifies the exfoliation of GO in aqueous solutions [144], the exfoliation of the graphite to graphene oxide is depicted in Figure 3.10. The existence of the functional groups in basal plane of the GO assists the possibility to use them as sites to attract numerous electro-active species such as CNTs through covalent or non-covalent bonds to form defined sensitive systems [145, 147]. Though the GO sheets are considered to be an insulator due to their large

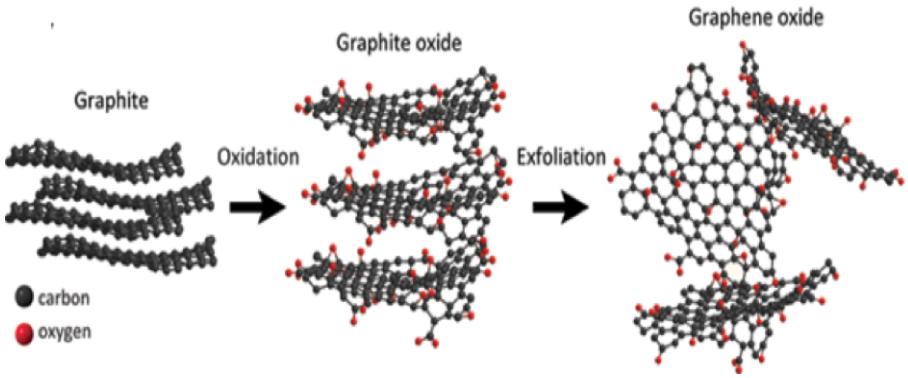

Figure 3.10: Schematic of oxidation and exfoliation of the graphite to graphene oxide. Reproduced with permission from InTech's Publishing ©2016 published in [148] under CC BY 3.0 license

bandgap between σ-states of its sp^3-bonded carbons but using thermal annealing or chemical reducing agents the graphene-like aromatic (sp^2-bonded carbons) structure can be largely restored. In the former case, the reduction of the GO is obtained by heating up the GO sheets in vacuum or an inert atmosphere (e.g., argon) [149, 150]. In the later reduction method, different reducing agents are used to chemically reduce the colloidal dispersion such as hydrazine, hydroquinone, sodium borohydride $(NaBH_4)$ [151], glucose, fructose, vitamin C (ascorbic acid) [152-153], Hydroiodic acids [154-155] and strongly alkaline solutions [146]. Using hydrazine involves great attention because it is hazardous, highly toxic and potentially explosive. Different reduction methods have been used to produce reduced GO with considerable grain size and improved electrical conductivity then the pristine GO, nevertheless additional enhancements are required in order to totally remove the oxygen surrounding defects in the graphene-like lattice. The reduction of GO reduces the bandgap and therefore tune the ratio of the sp^2 and sp^3 fractions, consequently transforms the GO from an insulator state to a semiconductor [156-158]. Though the reduction of GO can be partially used to restore the graphene-like aromatic properties of the GO, it introduces some residual defects to its basal plane such as remaining oxygen atoms [159], Stone-Wales defects (pentagon-heptagon pairs) [159-160] and holes [160] due to loss of carbon atoms

in the form of CO or CO_2 from the basal plane and therefore the conductivity will be limited [158].

3.4.7 Properties of Graphene Oxide

GO exhibits various excellent mechanical, optical, chemical reactivity and thermal properties; this is referred to its specific 2D structure and the presence of numerous oxygen functional groups at its peripheries. Because it is atomically thin the GO/rGO has a high transparency in the visible spectrum, thus it has been widely investigated to replace indium tin oxide (ITO) in organic solar cells [156, 161], organic light-emitting diodes (OLEDs) [162-163]. The GO sheets demonstrate an improved chemical activity compared with pristine graphene due to the existence of the oxygen functional groups in its plane and edges structure. The conductivity of the GO and rGO sheets depends strongly on their chemical and atomic structures and therefore it varies based on the synthesis and reduction methods. As previously mentioned, the GO films exhibit insulating properties with large bandgap due to the presence of sp^3 bonds in the graphene-like plane of the GO. However, chemical or thermal reduction of the GO improves drastically its conductivity. Depending on the reduction level, the conductivity of the rGO film can reach about 3000S/cm [138]. In addition to these interesting features, GO exhibits photoluminescence (PL) at the near-infrared (NIR), visible (vis) and ultraviolet wavelength range, as a result of recombination of sp^2 hybridized electron-hole pairs located in the carbon plane cluster which is embedded within an sp^3 matrix, for this reason the GO has a high potential in bio-sensing and optoelectronics applications [156, 164]. The 2D structure of the GO makes it also a good candidate to be used as electrodes for the batteries, as it has a high specific surface area and good electron mobility. For this reason, a determined active species could be attached to its surface and further activates the electron transfer at electrode surface. Furthermore, rGO shows a good potential for ultracapacitors application even more than CNTs, due to its very high electrochemical capacitance and excellent cycle performance. Whereas the specific capacitance was found to be 165 and 86F/g for rGO and CNTs, respectively. Besides the pre-mentioned properties, the GO has also a very interesting mechanical properties with Young's modulus of 0.7nm monolayer around 207.6±23.4GPa [156], and about 0.25±0.15TPa for the monolayer chemically rGO [166]. Due to the presence of a large number of oxygen-containing functional groups and structural defects, GO exhibits an enhanced chemical activity compared to the other carbon nano-allotropes such as pristine graphene, this gives the possibility for selectively chemical functionalization with DNA, polymer chains, CNTs and/ or nanoparticles [143].

3.5 Composites of Conducting Polymer with Carbon Nanomaterials

Basically, the idea to add nanofillers in polymer aims to bring novel functionalities to the polymer without altering its inherent properties and/or improving an exciting polymer inherent characteristic. Carbon nanomaterials among others have been widely integrated, in particular CNTs and GO, this is referred as mentioned in sections 3.4.2 and 3.4.7 to its exceptional properties such as electronic, thermal, electrical, mechanical and optical properties. Their nano-sized unique structure facilitates its interaction with the polymer chain to achieve synergetic properties of the new nanostructured nanocomposites.

3.5.1 Carbon Nanotube based Nanocomposites

Although CNTs have excellent properties, the use of CNTs in realtime applications is limited due to the low processability and insolubility. Therefore, the functionalization of the CNT using polymers (nanocomposites) is a key to use CNTs in different applications. Nanocomposites based on CNTs and polymer can achieve improved physical and mechanical properties compared to the pure polymer. On one hand, CNTs based insulating polymers such as Epoxy [167], PDMS [168], PVA [169], PA-6 and PC and PE [170], PEEK [171- 172], PSS [125] were deeply investigated for strain, pressure, optical, chemical and biological sensors. On the other hand, nanocomposites fabricated based on ICPs, such as PA [173], P3AT [174], PANI [175- 176], PEDOT [79, 177] were also profoundly explored for different application areas such as layer injection in solar cells, photovoltaic cells, field emitters, electrode for batteries, sensors and electro-catalysis. Among others ICPs, PEDOT:PSS has been intensively studied because of their remarkable electronic, chemical and mechanical properties as previously mentioned. Additionally, it has a very high conductivity compared with other commercially available polymers. Therefore, it has been widely used in sensing application such as humidity and strain, and as hole injection layer in solar cells.

3.5.2 Nanocomposites of Graphene Oxide

Revelations of the electronic, electrical, optical and mechanical properties of the GO have put emphasis on the development of nanocomposites based on GO and broaden its application field and make it industrially available. The existence of functional groups in the plane and the edges of the GO, give the possibility to interact with organic and inorganic materials to form functional hybrid nanocomposites with tailored unusual properties [143, 156, 178-180]. Thus, functionalization with polymers is an effective route for improving the GO dispersion. Thus it is possible to integrate GO into an excellent compatible polymer material in the absence of any aggregation [180]. Different types of polymers are used to produce conducting nanocomposites with improved physicochemical, mechanical and optical properties. Among them, polypropylene [182-183], PVA [184], epoxy [185], Poly(methyl methacrylate) PMMA [186], polyaniline PANI [187-188], Nafion [189-190], high-density polyethylene HDPE [191], PEDOT:PSS [157], and silicone rubber [192-193].

3.6 Fabrication of Polymer Nanocomposites

The properties of polymer matrix based on nanocomposites depend strongly on the chemistry of polymer matrices, type of nanofillers and the processing method. Recently, different preparation techniques were acquired to improve the properties of the nanocomposites. Essentially, the interaction and the bonding between the CNF and the polymer matrix at the surface has a major impact on the final property of the nanocomposite. The processing methods can be divided into covalent and non-covalent approaches, depending on the type of the interaction between the CNF and the polymer.

3.6.1 Non-Covalent Dispersion Methods

In the non-covalent interaction, either a solution-based or melt mixing method is involved. In the solution method, CNFs are dispersed in either water or solvents via an enthalpy-driven interaction, such as π-π, CH-π, NH-π, etc, between the CNT surface and the dispersants

and/or entropy-driven interaction; i.e. hydrophobic interaction using surfactants (Figure 3.11) to fabricate the aqueous colloids and then mix it with polymer [194]. The preparation of the aqueous CNF suspensions is typically done with the help of sonication, which is a mechanical method that is frequently employed in combination with surfactants to exfoliate, disperse or de-bundle CNF during the mixing process. Hence, this technique is more suitable for the water-soluble polymers such as PEDOT:PSS, poly vinyl pyrrolidone (PVP), PVA, PDMS, poly(methyl methacrylate) (PMMA). Sonication time and sonication energy are main parameters that determine the degree of extra dispersibility or the degree of exfoliation [195-196]. Whilst, the longer the sonication time, the better the aqueous suspension is, but the more defects on the CNF surface are, the insufficient sonication energy leads to insufficient dispersion of CNFs. So, the processing parameters must be optimized to reach an equilibrium state and consequently to lower the percolation threshold of the nanocomposite. To promote CNF surfactant dispersions, the employment of different surfactants such as sodium dodecyl sulfate (SDS), sodium dodecylbenzene sulfonate (SDBS), sodium cholate (SC), cethyltrimethylammonium bromide (CTAB), Tween and Triton X [194, 197] and organic solvents such as 1,2 dichlorobenzene (DCB), Methan, acetone, chloroform, N-methyl-pyrrolidone (NMP), dimethylformamide (DMF) was reported in literature [198, 200]. Typically, the exfoliation of the CNF in the solution is achieved by adsorption of the surfactant on the surface of the CNF. A possible adsorption mechanism on the surface of the CNTs is shown in Figure 3.12. CNTs can be encapsulated within cylindrical micelles, or covered with either hemispherical micelles, or randomly adsorbed molecules [201]. The adsorption on the CNF surface lowers the surface tension of the aqueous solution and thus prevents the re-aggregation of the carbon fillers, due to the strong van der Waals attractions between them.

In the melt mixing method, a polymer melt and powder filler are mixed under high shear

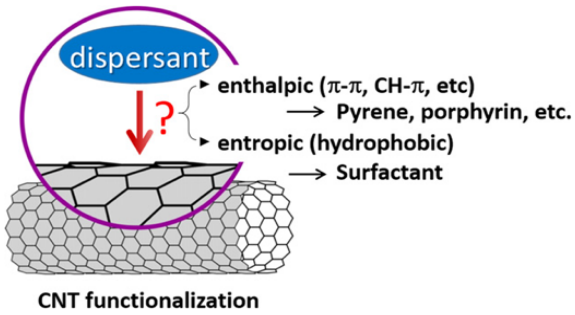

Figure 3.11: Dispersant-CNT interactions. Copyright ©IOP Publishing, 2015 published in [194]

forces of the material between screw and barrel, as it is shown in Figure 3.13. It is widely applied for the industrial application with thermoplastic polymers due to its low cost and large production scalability. Lately, it was reported that such method does not provide the same level of dispersion of the filler and does not effectively break the agglomeration of the CNF as in solvent mixing or as in situ polymerization methods [142, 202-203]. Melt mixing/blending is revealed to fabricate various types of CNT/polymer nanocomposites, such as polycarbonate (PC), poly(ethylene terephthalate) (PET), polyurethane (PU), polystyrene (PS), polypropylene (PP) and acryloni-trile-butadiene-styrene (ABS) [205-207]. For the GO-derived fillers, it was successfully used in the exfoliation of rGO in various thermoplastic polymer matrices, for example styrene-ethylene/butylene-styrene (SEBS) [208], polypropylene (PP) [209], Poly(vinylidene fluoride) (PVDF) [210-211]. However, it is notable that,

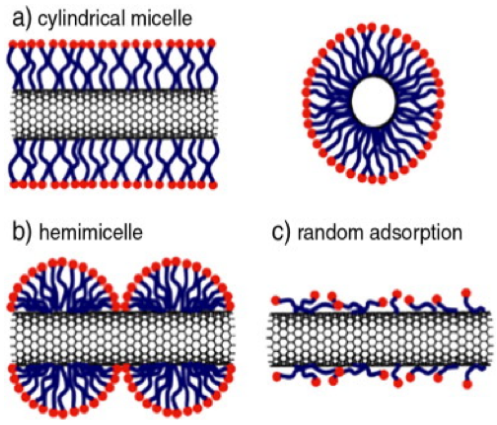

Figure 3.12: Different adsorption mechanism on the surface of the CNTs. Copyright ©IOP Publishing, 2008 published in [201]

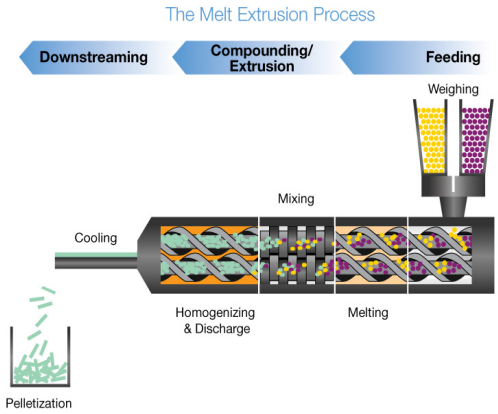

Figure 3.13: Hot melt extrusion process of CNT/ Polymer [204]

due to the high temperature used in melt mixing, the GO platelets can be reduced thermally with very low bulk density [212-213]. The high shear forces and high temperature used in the melt-mixing technique, can lead to the fragmentation of the CNF and/ or polymer chain scission, i.e. deterioration of nanocomposites. Therefore, optimization of these parameters is highly recommended to achieve nanocomposites with high sensing properties and slow aging rate.

3.6.2 Non-Covalent In-Situ Polymerization

For some polymers which are insoluble and thermally unstable, it is not possible to process them by solution mixing and melts processing, then in-situ polymerization is the appropriate method. In this method as it is shown in Figure 3.14, the CNF is mixed with a monomer or multiple monomers, in the presence or absence of solvent followed by polymerization. Therefore, this technique enables the grafting of polymer molecules on the surface of the CNF i.e. CNT or GO and accordingly leads to better dispersion and stronger binding between CNF and polymeric host matrix. Many reports reveal the use of in situ polymerization methods to produce nanocomposites based on CNT or GO with a variety of polymers, such as MWCNT/PS and PMMA/MWCNT [214], MWCNT/PEDOT:PSS [84], MWCNT/PPy [215],

etc. In the GO-derived polymer nanocomposites, the monomer intercalates between the layers of the GO and then it follows the polymerization separating the layers. Therefore, it is named sometimes as intercalation polymerization. Examples of typically used polymers are, poly(vinyl acetate) [142, 216] and poly(aniline) (PANI) [217-218]. To improve further the GO dispersion quality and its linkage to the polymer the use of a macro-initiator was proposed [219].

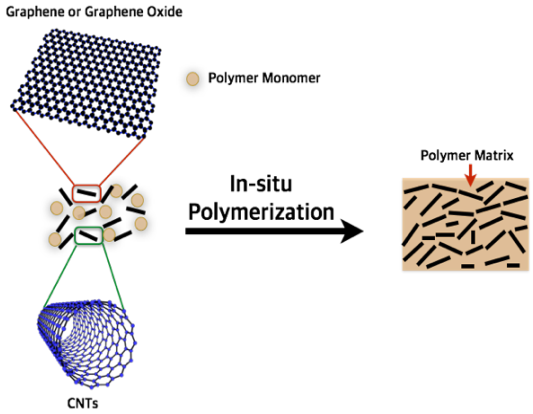

Figure 3.14: Schematic of the in-situ polymerization of the CNT and or GO/ polymer nanocomposites

3.6.3 CNF-based Composites with Covalent Bonds

To achieve the advantages of CNFs and to enhance the properties of CNF/polymer nanocomposites, a covalent functionalization is proposed. In case of the CNT, the functionalization is taking place at defects on its walls and/or at the end caps [220]. Despite the CNTs, GO platelets contain already on its surface a reactive functional groups and thus different approaches for introducing covalent bonds between GO platelets and polymers have been verified. Generally, grafting-from and grafting-to approaches have been used for the attachment of a broad range of polymers with CNF [221]. Figure 3.15 and Figure 3.16 show the most used strategies for covalent functionalization of GO and CNTs, respectively.

3.7 Electrical Properties of CNFs and Nanocomposites

3.7.1 Percolation Threshold of Nanocomposites

Adding nanofiller to the insulating polymer improves its properties, either electrical conductivity and/or storage modulus. However, at certain filler concentration, rapid increase in these properties occurs, this point is called percolation threshold which is either electrical or rheological. It was shown that the rheological percolation can be either lower [223-225], similar [226-228] or higher [229-230] than the electrical percolation threshold. Therefore, in order to make the insulating polymer matrix to be electrically conductive nanocomposite, the concentration of the conducting filler either CNT or GO must be above the electrical percolation threshold. Generally, the increase in conductivity as a function of filler loading once

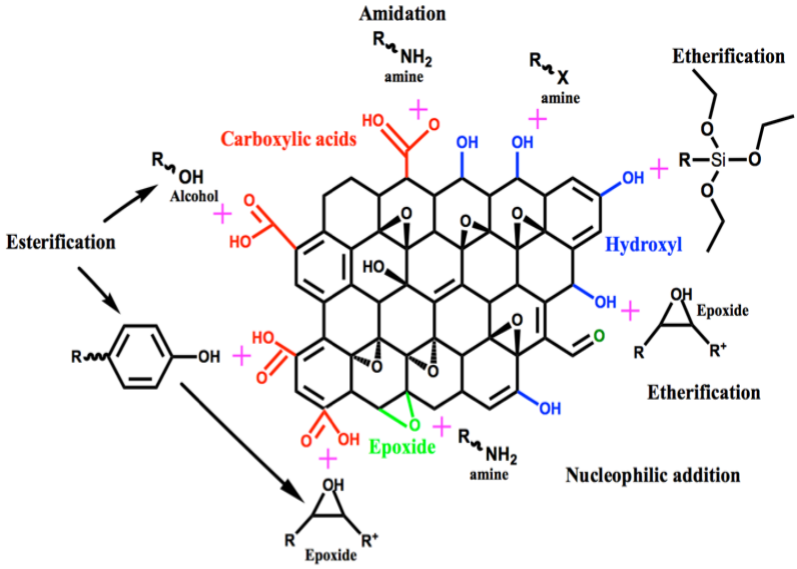

Figure 3.15: Grafting reactions to functionalize GO surface via covalent bonds. Redrawen based on [148]

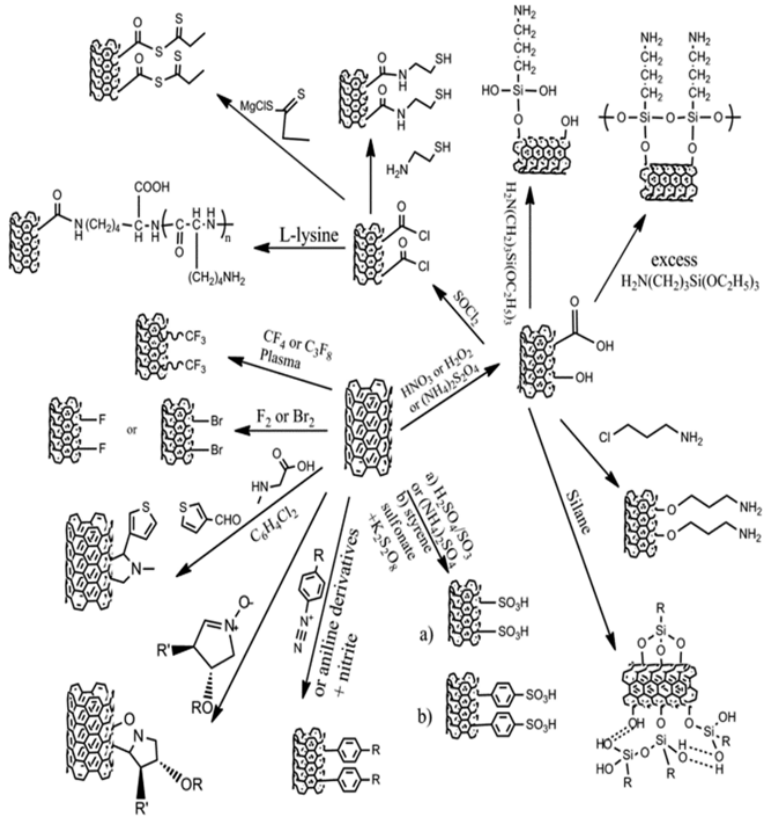

Figure 3.16: Grafting reactions to functionalize CNTs surface via covalent bonds. Reproduced with permission from Wiley-VCH Verlag GmbH & Co. KGaA published in [222]

electrical percolation has been achieved can be modeled by a simple power-law expression (equation 3.5) [231], as displayed in Figure 3.17,

$$\sigma = \sigma_o(\phi\text{-}\phi_c)^t, \; for \phi > \phi_c \tag{3.5}$$

Where $\sigma_o$is the initial electrical conductivity of the polymer, ϕ is the conductive filler volume fraction, ϕ_c is the percolation threshold, and t is a scaling exponent.

Thus, the randomly filler/polymer network can be regarded as complex network consisting of parallel and series resistors. So, the total network resistance is an accumulation of different resistance phenomena: intrinsic resistance and tunneling resistance.

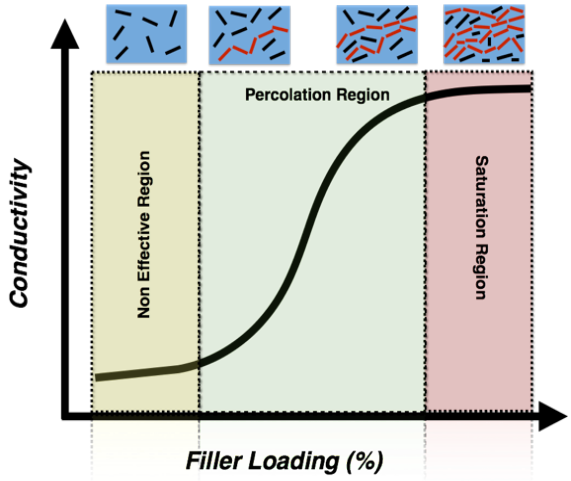

Figure 3.17: Description of the percolation threshold

Intrinsic Resistance

As shown in section 3.4.2, for CNTs free of defects and with perfect ohmic contacts, an electron can be moved freely without scattering through the tube i.e. ballistic electronic transport can take place, and thus no resistance can be measured. This is valid for only metallic CNTs, whereas for semiconducting CNTs scattering effects are taking place [232]. The maximum length at which an electron can move ballistically and therefore can pass through a CNT without scattering is called the mean free path. Experimentally, it was proved that the CNT has a momentum mean free path of more than 30μm [232]. Although, the transport in CNTs is ballistic, an internal resistance exists always, and depending on the tube length and the type of contacts, its value might change from few to several kΩ per unit length [232]. The intrinsic resistance of the CNTs (R_{int}) is given by [233],

$$R_{int} = \left(\frac{\rho L}{\pi R^2}\right) \tag{3.6}$$

where ρ is the nanotube resistivity, L and R are the length and the radius of the tube, respectively.

Typically, metallic CNT has a resistivity as low as $10^{-6}\Omega$m, given this resistivity, from previously, it is calculated using equation 3.6 that the intrinsic tube resistance of the CNTs used in this work is around $6.5\times10^{3}\Omega$, which has an average length of 1μm and an average diameter of 7nm.

Tunneling Resistance

In the nanocomposite, if the embedded filler particles within the polymer get close enough to each other, typically 1-2nm [234], the electrons can jump from one filler to another through the polymer medium, this is a typical quantum phenomenon called tunneling. The van der Wales distance depends typically on the polymer type and the potential barrier difference between the filler and the polymer matrix. The value of the tunneling resistance can be estimated using Simon's formula [235]:

$$R_{tunneling} = \frac{V}{AJ} = \frac{h^2 \times d}{A \times e^2 \times \sqrt{2m\lambda}} exp((\frac{4\pi d}{\hbar})\sqrt{2m\lambda)} \tag{3.7}$$

where V is the potential difference, J is the tunneling density, A is the cross-sectional area of the filler, $\hbar$ is Planck's constant, d is the distance between filers, e is the electron charge, m is the electron mass and h is the height of the electrical barrier of the polymer.

As it is very difficult to measure the tunneling resistance, many calculations were conducted to estimate this resistance. For instance, the tunneling resistance of two CNT separated by 1nm embedded in epoxy matrix, the values range from around 2nm to 3nm for CNT tube diameter of 8nm [233]. Different parameters affect the change in the tunneling resistance such as contact area, contact gap, junction type (metallic/metallic or metallic/semiconducting) polymer molecule size and degree of dispersibility. However, the intrinsic tube resistance is significantly smaller compared to the tunneling resistance hence negligible. Consequently, the main conduction mechanism in any nanocomposites containing conducting fillers takes place mainly via tunneling between the filler particles through the thin polymer layers between them.

3.7.2 Influence Effects on Nanocomposites Conductivity

Beside the types of nanofillers, nature of polymer, fabrication process and the tunneling distance between the nanofillers, other issues such as orientation and alignment, aspect ratio, curvature, processing methods, wrinkles and folds etc. may also affect the total conductivity of nanocomposites. These are briefly discussed in the next section.

Orientation and Alignment

The sensing properties of the nanocomposites vary drastically based on how the nanofiller are oriented within the polymer matrix. As result, the electrical and the mechanical characteristic depends strongly on the orientation of the CNTs [172, 236-237]. The electrical conductivity of the randomly distributed network based on CNT changes depending on the orientation of CNTs. The networks with a complete random distribution show an isotropic behavior, whereas the aligned networks show orthotropic behavior [238]. The alignment of CNTs is the pre-determination of the CNTs orientation either during the growth (vertically alignment) or by the post-processing (in-plane) in the polymer matrix using controllable technical methods such as mechanical forces either stretching forces [170, 239-241], or uniaxial compressive pressure [242], or using electrical fields [238, 243] or magnetic fields [244-246]. Other methods are also described in [207, 247-248]. The mechanical properties are also altered by the orientation, for instance, the aligned CNT network has an improved effective axial elastic modulus (E_{33}) compared to the random CNT network, while the shear modulus (G)

of the random network was better compared to the aligned network, as it is shown in Figure 3.18.

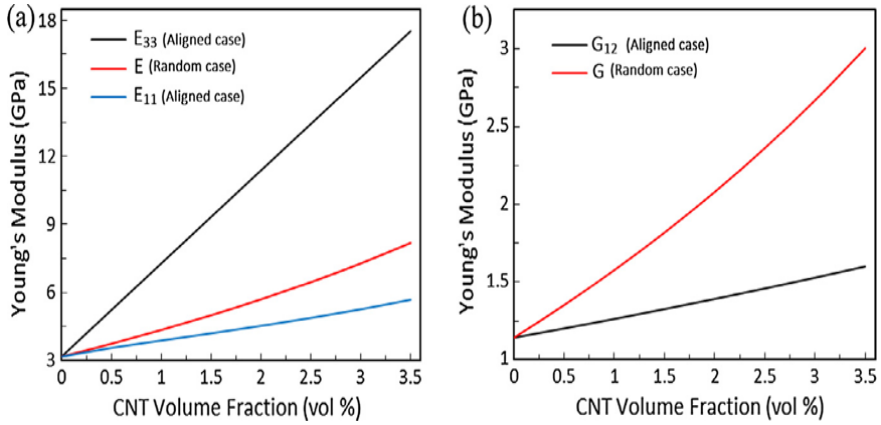

Figure 3.18: Effect of CNT orientation on bulk elastic moduli of CNT/epoxy composites (a) Alignment along the axes with (E) is the effective Young's modulus, (E_{33}) is the effective axial and (E_{11}) is the transverse Young's, (b) Alignment along the shear with (G) is the effective shear, and (G_{12}) is the in-plane shear modulus. Reprinted from Elsevier published in [249]

Aspect Ratio

One big difference between the conventional fillers such as carbon black, carbon fiber and the nanofillers such as CNTs, graphene and graphene oxide is the aspect ratio. For the CNTs, the aspect ratio is the ratio between its diameter and its length, with diameter ranging between 1nm and 100nm and length up too few millimeters, the longest CNTs grown up to date achieve 550mm [250]. The high aspect ratio lowers the nanofiller content used to reinforce the polymer i.e. the percolation threshold can be reached with less number of fillers and therefore higher conductive nanocomposites can be fabricated with less CNTs [251]. Thus, nanocomposites with very low CNT filler were realized [234, 252], the lowest percolation threshold reported up to date is 0.0025wt.% [253]. For the CNTs, the relationship between the aspect ratio and the percolation threshold (Φ_p) is presented below:

$$\Phi_p = \frac{d}{2L} \tag{3.8}$$

where d is the CNT diameter, and L is the CNT length.

Using Eq. 3.8, the percolation threshold using the CNTs used in this work can be reached by 0.0035wt.% CNT, if the preparation parameters are well optimized. The aspect ratio of GO is extremely high compared to the CNT, this is referred to the monoatomic thickness of the grain size of the graphene platelets to its lateral size (lateral size on the order of 10μm and thickness in the order of 1nm). Thus, GO shows network formation in both polymeric systems at very low content, much lower than that of CNT needed to realize same characteristics. Assuming that the GO have disc-shape nanosize which is randomly distributed in the matrix and the aspect ratio of the nano-filler (ζ) is [254]:

$$\zeta = 3 \times \frac{\Phi_s}{\Phi_p} \tag{3.9}$$

where Φ_s is the volume fraction at the onset of percolation of interpenetrating of the randomly packed spheres.

Curvature

The embedded CNTs in the polymer matrix exhibit significant curvature known also as waviness. The curvature of the CNTs is simply defined as the angle by which two neighbor CNTs are deviating from each other, it is considered in [249-255] as key factor in controlling the functionality of the nanocomposite. The experimental study of the curvature and its effect on the related sensing properties is very difficult, therefore up to now, only numerical studies based on molecular dynamics simulations or micromechanical modeling are conducted to investigate this effect [249]. The simulation results based on the micromechanical model is depicted in Figure 3.19, it shows the effect of the waviness on the Young's modulus (E) of the CNT-epoxy nanocomposites. The waviness parameter (α) is 0, if the CNT is perfectly aligned. The Young's modulus of the perfectly aligned network shows an enhancement over the randomly oriented network especially for high CNT volume fraction. Thus, it is well noticeable that increasing the waviness between the CNT segments increases the percolation threshold. However, the waviness i.e. curved CNTs have limited effect on the percolation threshold compared to the aspect ratio or aggregation [255].

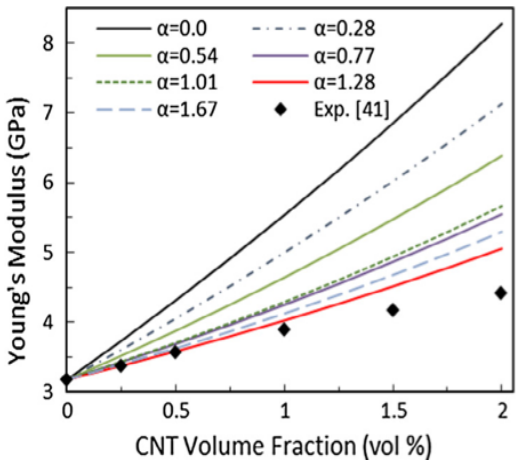

Figure 3.19: Effect of CNT waviness on the Young's moduli of CNT-epoxy nanocomposites. Reprinted from [249]. Reproduced with permission from Elsevier

3.8 Nanocomposites Fabrication Methodology

In section 2.5, CNTs, GO and PEDOT:PSS showed a good feasability to be used for wireless sensors but their low conductivity prevent them to reach a good antenna characteristics and thus gave a low sensitivity. Consequently, fabricating nanocomposites based on these nanomaterials can improve the conductivity and thus it can be used for wireless sensors. Using these nanomaterials, three nanocomposites are proposed, CNTs and PEDOT:PSS, GO and MWCNTs and a novel tertiary GO, MWCNT and PEDOT:PSS. In section 3.6, the way in which the CNF filled nanocomposites are prepared, influence how these fillers are distributed in the polymer matrix and thus influences the electrical conductivity. It is proven from experiments that, at the same filler volume fraction, the electrical conductivity is higher for in situ polymerized and solvent blended samples than melt blended [207, 255]. In the CNTs and PEDOT:PSS nanocomposites and as the CNTs possess low processability and insolubility due to the high Van der Waals forces between them, CNTs are first dispersed non-covalently in a surfactant to fabricate the aqueous suspension and then mixed with PEDOT:PSS via a solution mixing method. Using surfactants to disperse CNTs might influence the sensitivity of the nanocomposite to the environmental conditions [255]. Thus, beside using surfactant to disperse the CNTs, GO arises as a good candidate to disperse the CNTs due to the presence of functional groups in the edges of the GO. Therefore, GO can be principally used as a dispersant to suspend the agglomerated CNTs and develop a solution processing process for producing GO:CNT hybrid nanocomposites. The synthesize of the hybrid nanomaterial GO:MWCNTs employs the self-assembly of GO and MWCNTs. Compared to the pristine MWCNTs, this nanocomposite can be well dispersed in GO aqueous solution via the π-π interaction, which stabilizes the hydrophobic property of the nanotubes, and gives the MWCNTs with a negative charge [146-147]. MWCNTs dispersed in GO dispersion are expected to have interesting thermal and mechanical properties, due to the exceptional thermal and mechanical properties of both GO and CNTs. To improve the electrical characteristics of the GO:MWCNTs hybrid nanocomposites, PEDOT:PSS is added to it. The reason for that is the inherent electrical properties of each of the nanomaterial. These three nanomaterials are conductive, consequently, it is expected to reach a nanocomposites with a very high conductivity and improved characteristics of the GO:MWCNTs hybrid nanocomposites. As the PEDOT:PSS is water-soluble polymer and the GO:MWCNTs is an aqueous suspension, the most suitable technique used to fabricate this novel tertiary nanocomposite is the solution mixing method. Beside that, there is an analogy in the structure of these nanomaterials i.e. the benzene ring, which arises the π-π interaction between the GO, MWCNTs and PEDOT:PSS. The experimental steps used to prepare each of this nanocomposite is explained in the next chapter.

4 Materials and Experimental Methods

This chapter contains three main sections, the first one discusses the materials used in this thesis, the second section addresses the fabrication methods of the aqueous dispersion as well as the deposition method used to fabricate the films, and the third section reviews the experimental techniques used for the characterization of both the aqueous dispersion and the films based nanocomposites.

4.1 Nanocomposites Preparation Methods

Solution processing is a mutual technique used for preparing the polymer/CNF nanocomposites. Prior nanocomposite fabrication, a surface modification of the CNFs (either covalent or non-covalent) is required via energetic agitation (magnetic or mechanic stirring, reflux or sonication). Next, the aqueous dispersion is added to the polymer so the polymer chains intercalate between the conductive nanofillers. Afterwards, the solvent is removed by thermal evaporation either during the aqueous state or after the film deposition. A schematic displaying the different steps used in the solution processing technique is depicted in Figure 4.1. The CVD grown MWCNTs are purchased from Southwest Nano Technology and they are used without further purification, functionalization or chemical treatments. As mentioned by the supplier, the MWCNTs have a degree of purity greater than 95%, outer diameter between 6nm to 9nm and lengths less than 1μm [256]. The GO is purchased from Graphene laboratories Inc. and it is used as supplied without any further purification or functionalization. The GO has a concentration of 0.5wt.%, it consists of 79% carbon and 20% oxygen with flake size ranging from 0.5μm to 5μm with at least 60% of the aqueous dispersion has a thickness of one atomic layer [257]. The PEDOT:PSS is purchased from the company Heraeus Precious Metals GmbH & Co. KG., having a commercial name of Clevios PH 1000. The PEDOT:PSS is in form of aqueous dispersion (1.3wt.% in H_2O) and has 0.5wt.% of PEDOT and 0.8wt.% PSS content. The PEDOT to PSS ratio is 1:2.5 by weight, the aqueous dispersion has a dark blue color and is odorless. Different combinations of MWCNT, with/without GO in PEDOT:PSS matrix are formulated. The preparation process of each prepared nanocomposite is explained in the following.

4.1.1 MWCNT:SDBS/PEDOT:PSS

In this nanocomposite, MWCNTs are non-covalently functionalized using surfactant then mixed with PEDOT:PSS. Because of its high dispersibility, sodium dodecyl benzene sulfonate (SDBS) is selected. This dispersibility is coming from its negative charge and benzene ring [205, 258- 260]. Different MWCNTs contents are dispersed in 0.2wt.% of SDBS, which is around its critical micelle concentration (CMC) value. The aqueous suspension is sonicated for 30min at 15% of the maximum power of a horn sonicator (Bandelin GM 3200) at 0.5s cycling time. The sonication process is done in an ice-bath to avoid overheating. After the

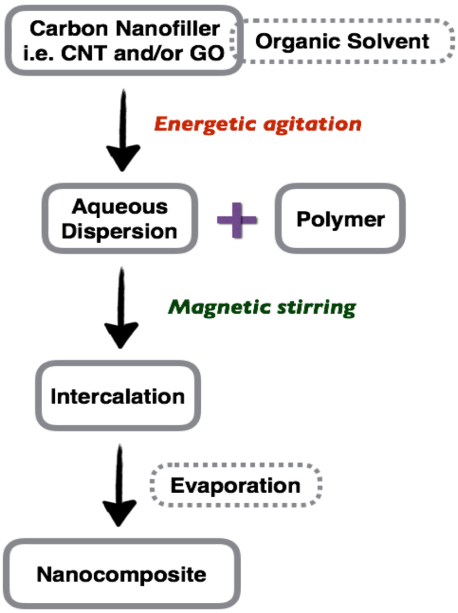

Figure 4.1: Schematic of typical steps of nanocomposites preparation using solution processing

stable saturated CNT dispersion is achieved, the CNT suspension is centrifuged at 5000rpm for 40min aiming to separate large agglomerated CNTs, amorphous carbon and residual catalytic material. Only 80% of the upper part of the prepared CNT suspension is removed. Afterwards, the aqueous dispersion is then mixed with 1:1 volume ratio of PEDOT:PSS, this aqueous suspension is stirred magnetically at 1600rpm for 15min to improve the intercalation between the polymer and the MWCNT dispersion. Figure 4.2 shows schematic of the preparation process of MWCNT:SDBS/PEDOT:PSS nanocomposite.

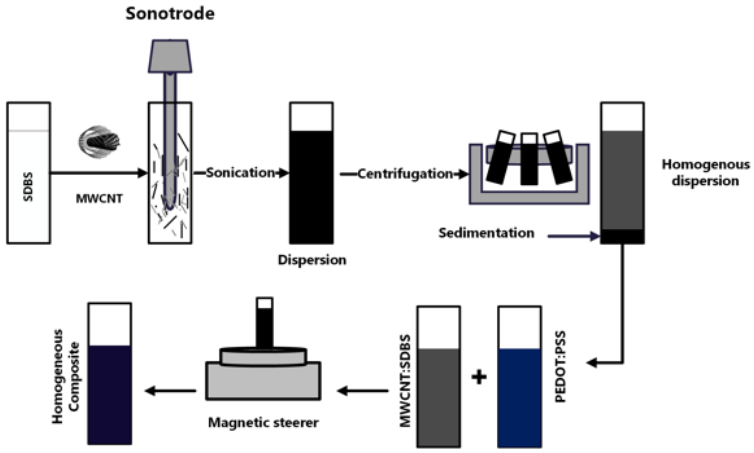

Figure 4.2: MWCNT:SDBS/PEDOT:PSS nanocomposite preparation process

4.1.2 GO:MWCNT

As explained in section 3.4.4, the GO is visualized as graphene sheet with its basal plane decorated by oxygen-containing groups. Therefore, GO aqueous colloid is used as surfactant to disperse the MWCNTs. In this nanocomposite, MWCNTs are dispersed in GO using

sonication cavity. Different MWCNT contents are directly suspended in the GO aqueous colloids. This mixture is sonicated and centrifugated using the same parameters as in 4.1.1. To guarantee that the prepared films have high homogeneity, only the upper 80% of the prepared solution is removed after centrifugation. Figure 4.3 depicts a schematic description of this preparation method.

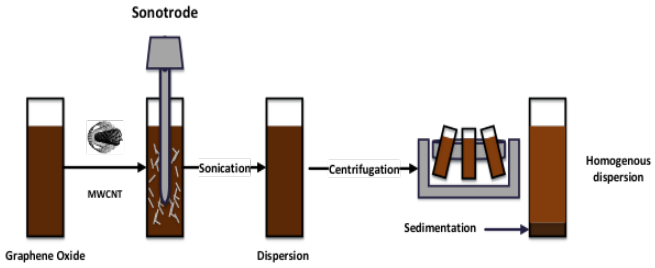

Figure 4.3: GO:MWCNT nanocomposite preparation process

4.1.3 GO:MWCNT/PEDOT:PSS

This nanocomposite is introduced as novel nanocomposite class that includes two different nanofillers instead of one. Therefore, it is called a tertiary nanocomposite. The GO:MWCNT nanocomposite as described in section 4.1.2 is mixed with different volume ratios (1:1, 1:1.3 and 1:3) of PEDOT:PSS using a magnetic stirrer at 1600rpm for 15min. The Figure 4.4 illustrates schematically the preparation procedure of GO:MWCNT/PEDOT:PSS nanocomposite.

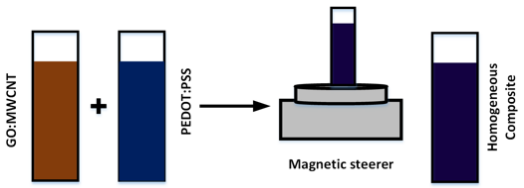

Figure 4.4: GO:MWCNT/PEDOT:PSS nanocomposite preparation process

4.2 Fabrication of Films Based on Nanocomposites

This section explains the substrate pre-treatment method, the deposition method used for the film fabrication, and the chemical reduction used to reduce the films based on GO.

4.2.1 Substrate Treatment

Prior deposition, the polymer substrates namely Kapton HN500 are cleaned in order to remove contaminations from the surface. First, the substrates are sonicated in bath of isopropanol for 10min, then rinsed in bath filled with Di-H_2O for another 10min. Afterwards, they are dried under N_2 and finally baked in an oven at 110°C for 1 hour to dry all the water molecules from the substrate surface.

4.2.2 Deposition Method

For deposition, a mask covering the Kapton HN500 substrate is patterned as rectangular shape (2.5×0.5cm). Using physical liquid deposition, a volume of 62.5μL is used in order to achieve high reproducibility. After the deposition, the films are kept drying in the air for 24 hours, then the mask is removed and the electrodes are made using silver paste to improve the contacts on both sides of the films. The metallic wires are connected with the help of silicone epoxy on the films (Figure 4.5). Finally, the prepared films are baked in the oven for 30min at 80°C. Three films or more from each dispersion are taken into account to ensure good reproducibility and dispersion quality.

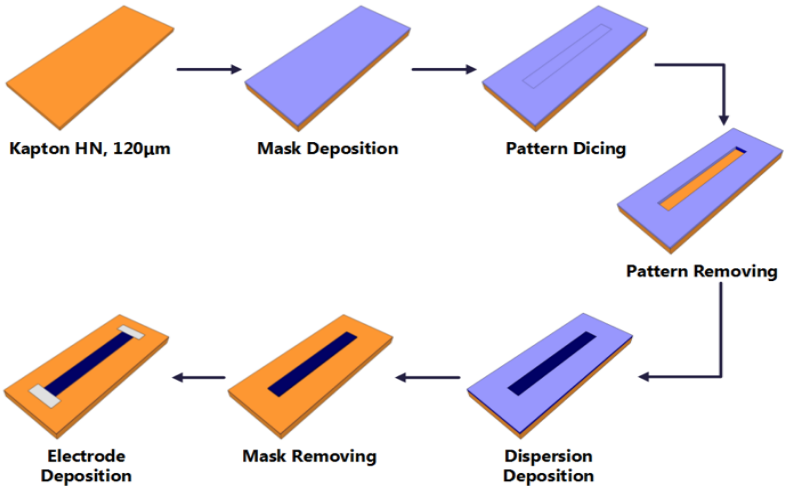

Figure 4.5: Film deposition and electrode pattern

4.2.3 Chemical Reduction Method

Before chemical reduction, the films based GO have an insulating behavior because of the non-stoichiometric chemical composition of the host GO matrix and the presence of the oxidant in the GO that prevents the formation of percolation paths among the sp^2 carbon clusters. Therefore, the resistances of the films are larger than $1G\Omega$. Among others, the hydroiodic acid is well investigated for GO reduction and thus it is chosen as reducent agent in this work [213]. After the chemical reduction, it is well observed that the electrical conductivity of the films increases. The reduction time is 3min, because longer time leads to affect the adhesion between the nanocomposite and the substrate, while no big change in the conductivity is observed. After chemical reduction and in order to remove the residuals, cleaning the surface with isopropanol then Di-H_2O followed by drying with N_2 is carried out. Figure 4.6 shows the steps of the chemical reduction.

4.3 Characterization of Raw and Nanocomposite Materials

The chemico-physical, optical, structural, electrical, mechanical and environmental properties of the carbon nanocomposites are characterized utilizing various experimental techniques

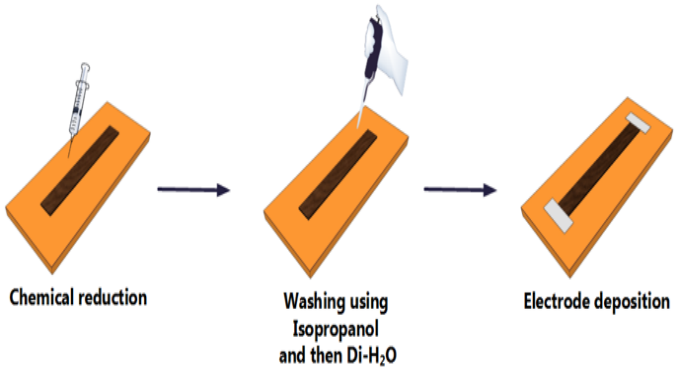

Figure 4.6: Chemical reduction of the films based GO

including tests of the surface tension, contact angle, optical spectroscopy, electron/atomic microscopes, electrical source meters, tensile tests and tests under controlled temperature and humidity. The details of each measurement setup, conditions and the parameters of each experiment are described in the following sections.

4.3.1 Surface Tension and Contact Angle

Surface tension and contact angle are conducted using pendant drop method by the contact angle measurement system G2 from KRUSS. The DSA2 v2.1 tool used to analyze the surface tension and contact angle data. For the surface tension, the nanocomposite is loaded in a syringe having a needle with an inner diameter of 0.26mm. With the help of an internal control system; a droplet of the sample with a volume of 25μl is suspended at the tip of the needle. A camera system captures and transmits a realtime image of the droplet to the computer and the DSA2 tool software analyses the drop shape and computes the surface tension of the droplet. For each nanocomposite and to consider the random deviation, 10 readings are taken and an average value is calculated. As it is shown in Figure 4.7, the contact angle formed between solid to liquid and liquid to gas interface is measured. For the contact angle, the droplet with a volume of 25μl is deposited on the treated polyimide substrate (Kapton HN500). The image of the droplet on the substrate is transmitted to the system and a DSA2 tool software is used to evaluate the contact angle using the Young's equation:

$$\nu_{sg} = \nu_{ls} + \nu_{lg} \times \cos\theta \tag{4.1}$$

where ν_{sg} is the surface tension at solid and gas interface, ν_{ls} is the surface tension at liquid and solid interface and ν_{lg} is the surface tension at liquid and gas interface.

If the system has a contact angle of $\leq$90°, then the system is hydrophilic. Whereas if the contact angle is $\geq$90°, then the system is hydrophobic.

The surface energy of the substrate is determined before and after the surface treatment, to define whether the substrate treatment improves the adhesion or not. The Owens, Wendt, Rabel and Kaelble model, known shortly as OWRK method is used to calculate the surface energy of the substrate (equation 4.2)[261].

$$\nu_{sl} = \nu_s + \nu_l - 2 \times (\sqrt{{\nu_s}^D \times {\nu_l}^D} + \sqrt{{\nu_s}^P \times {\nu_l}^P}) \tag{4.2}$$

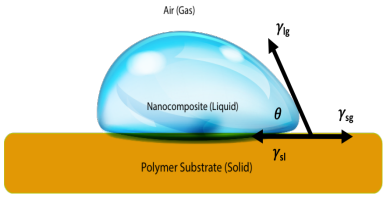

Figure 4.7: Schematic illustration of contact angle measurement

where ν_{sl} is the surface tension at solid and liquid interface, ν_s is the surface tension of the solid, ν_l is the surface tension of the liquid, ν_s^D is the disperse part of the solid, ν_l^D is the disperse part of the liquid, ν_s^P is the polar part of the solid and ν_l^P is the polar part of the liquid.

By determining the contact angle of three different reference liquids namely; Di-H_2O, ethylene glycol and diiodomethane using the Young's equation 4.1, and by the substitution in equation 4.2, the surface free energy is calculated and the polar part and the disperse part are determined.

4.3.2 Optical Spectroscopy

Absorption measurements in the range of 400-1300nm are carried out to study the optical properties of the prepared nanocomposites using a Lambda 900 UV-Vis/NIR spectrometer from PerkinElmer. As the dispersion had a very dark color, a dilution process is necessary to ensure good transparency of the dispersion. All the dispersions are diluted in Di-H_2O with volume ratio 50:1 H_2O to dispersion. The measurements are performed in a quartz cuvette with 10mm thickness. The bandgap of the nanocomposite is calculated from the Tauc plot using the following equation:

$$(\alpha h\nu)^{1/m} = k(h\nu - E_g) \tag{4.3}$$

where α is the absorption coefficient, h is the Plank's constant, ν is the frequency, k is a constant, E_g is the optical bandgap and m is a constant equals to 1/2 for an allowed direct energy gap, 2 for an allowed indirect energy gap and 3/2 for a forbidden direct energy gap.

The relationship between the change in the bandgap as function of the filler concentration is then extracted.

4.3.3 Surface Morphology

Optical digital microscopy (ODM), scanning electron microscopy (SEM) and atomic force microscopy (AFM) are carried out to determine the surface morphology and the microstructure of the nanocomposites.
A square of 5×5mm was patterned on Si-wafer and the suspension was drop casted onto it. The ODM is carried out using Keyence digital microscope VHX-500 under different magnifications to study the microscopic structure and the morphology of the deposited materials.
SEM images are taken with a Nova NanoSEM 200 Scanning Electon Microscope, operating at an acceleration voltage up to 20kV (spatial resolution: 1.7nm at 1kV, 1nm at 15kV) and a working distance of 5mm, and a spot size of 2.5-5μm.

AFM from Agilent 5420 SPM/Atomic Force Microscope is used to study the surface topography of the deposited samples, operating in the tapping mode at a frequency around 200Hz. The tip used in the AFM is made of Golden Silicon (NSG01-A).

4.3.4 Surface Analysis

As some of the nanocomposite are treated chemically to improve their conductivity, it is necessary to collect quantitative and qualitative information about the changes occurred on the surface of the nanocomposite after the chemical reduction. X-ray Photoelectron Spectroscopy (XPS) and Raman are both used for this issue. XPS measurements are performed with an ESCALAB 250Xi XPS Microprobe (Thermo Scientific) equipped with a monochromatized Al Kα X-ray source (hν = 1486.6eV). The survey and high-resolution spectra are acquired at a bandpass energy of 200eV and 20eV, respectively and XPSpeak41 software is used to perform curve fitting. Raman spectroscopy is performed with the 514.7nm line of diode pumped solid state (DPSS) laser (Cobolt) at a spectral resolution of about 2cm^{-1} using LabRam HR800 micro-Raman system equipped with the liquid nitrogen cooled CCD detector at room temperature. The incident laser power under the microscope objective (100x) is 0.1mW.

4.3.5 DC-Electrical Properties

Both the ohmic DC-resistance and sheet resistance are measured as follows. The DC-resistance of the films are measured using a Keithley 2602 dual-channel source meters with 4-wires measurement setup. To collect the resistance measurements, a sweep voltage of $\pm$5V is applied, then the film bulk conductivity (σ_s) is calculated using the following equation:

$$\sigma_s = 1/(\rho_s) \tag{4.4}$$

Where σ_s is the film conductivity and ρ_s is the bulk resistivity.

The bulk resistivity ρ_s is calculated as follow:

$$\rho_s = \frac{R \times W \times t}{L} (\Omega.cm) \tag{4.5}$$

Where L is the active length between the electrodes of the sample, W is the sample width, t is the sample thickness and R is the resistance of the sample.

For the sheet resistance (ρ), the nanocomposites are drop casted on square shaped substrate 1×1cm^2 with the same optimized volume used for the film fabrication (see section 4.2.2). The distance between the pins is 1.4mm, and the head pin is connected to Keithley 2602 dual-channel source meters with 4-wires measurement setup to collect the resistance. The sheet resistance is calculated as stated in equation 4.6. All the measurements are done under Faraday's cage to reduce the effect of surrounding noise. To check the electrical homogeneity and the uniformity of the nanocomposites, all measurements are conducted on three different positions on the substrate, as shown in Figure 4.8. On each position, three measurements in raw are carried out and the results are averaged to reduce the random deviations.

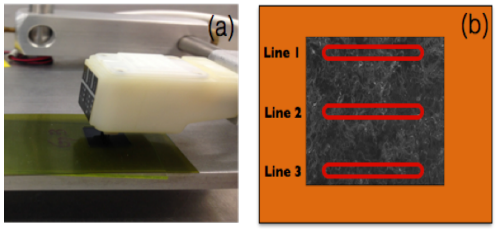

Figure 4.8: Electrical characterization (a) Pin position on the substrate, (b) Schematic of the measured position

$$\rho = \frac{\pi \times V}{\ln(2) \times I} (\Omega / sq^{-1}) \tag{4.6}$$

Where ρ is sheet resistance, V is the applied voltage and I is the measured current.

4.3.6 Tensile Tests

The tensile test is used in order to examined the piezoresistivity of the films. The piezoresistive evaluation is carried out at room temperature using universal test machine Inspekt 10 table (Hegawald & Peschke, Meβ- und Prüftechnik GmbH). Here, two Kapton HN500 substrates are used with different thicknesses 125μm and 250μm, respectively. The samples are then loaded in the universal test machine and stretched in the axial direction (in-plane) at a constant load speed of 1mm/min. For the 120μm substrate, the applied force is varied from 0N to 60N, a step size of 5N for loading and unloading is applied. And for the 250μm substrate, the force is varied from 0N to 120N, a step size of 10N for loading and unloading is applied. By the help of extensometer, the change in the substrate's length is measured and consequently the strain (ϵ) at the maximum applied force is determined approximately using equation 4.7 to be 0.5% and 1.2% for the 125μm and 250μm, respectively. These ranges are chosen to ensure that the applied force is in the elastic region of each polyamide films.

$$\epsilon = \frac{\Delta l}{l_0} \tag{4.7}$$

where ϵ is the strain, l_0 is the initial substrate length before loading, and Δl is the length's change.

The samples are then connected to host computer using Keithley 2602 dual-channel sourcemeter (Keithley Instruments Inc., Cleveland, OH, USA) with 4-wires technique to collect the change in the resistance under the applied force. The measurement setup of the tensile test is shown in Figure 4.9. At each step force, the I-V characteristic is measured by applying voltage from -0.5 to 0.5V and the resulting current is recorded by a Keithley 2602 sourcemeter connected to a host computer through GPIB/USB cable. Later the resistance profile of the specimen is calculated. At least three independent samples of each particular nanocomposite are investigated to ensure high reproducibility. The measurement process of all specimen is accomplished in the same way. The piezoresistive sensitivity of the films is evaluated by means of the gauge factor (k), defined as,

$$k = \frac{\Delta R / R_0}{\epsilon} \tag{4.8}$$

where R_0 is the initial resistance before loading, ΔR is the change of the resistance, and ϵ is the strain.

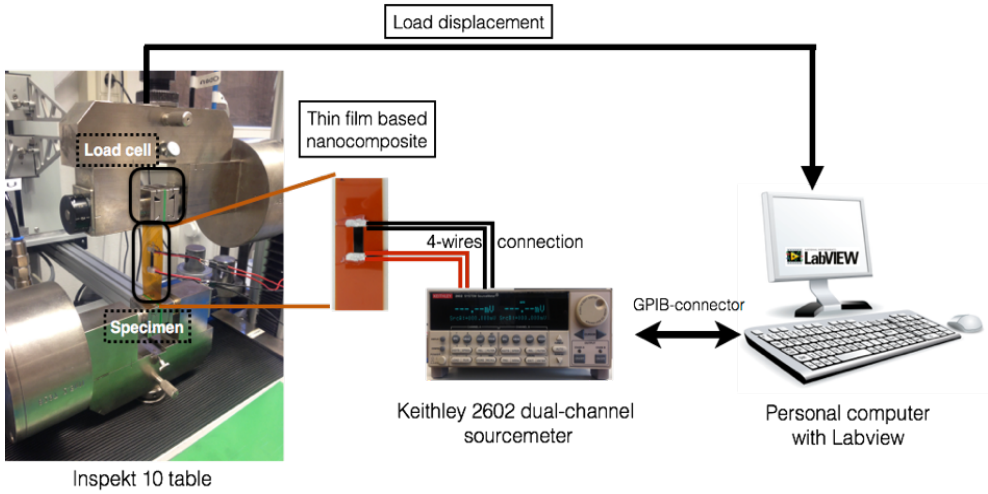

Figure 4.9: Schematic representation for piezoresistivity evaluation

4.3.7 Environmental Study

Both temperature and humidity effects on the transport mechanisms of the films are investigated. For the temperature measurements, the samples are located in Vötsch VT 4002 environmental chamber, the temperature range is set between 10°C and 80°C. The rate of temperature change is 10°C/hour at both heating and cooling cycles. The samples are connected to the Keithley 2602 dual-channel source meter with 4-wires technique to accumulate the resistance data. For the humidity measurement, the samples are placed inside the Vötsch VC^3 4018 humidity chamber. The measurement setup is shown in Figure 4.10. The relative humidity is set between 10%RH to 90%RH, with rate change of 5%RH each 30min during the humidification and the dehumidification stages. The sample resistances are measured each 5min with a 10-pulse voltage signal having 500mV amplitude, then the values are averaged.

4.3.8 Wireless Testing

The validation of the wireless strain sensing of the fabricated MPA patch antenna is conducted using an end-loaded cantilever beam. A cantilever beam made of Polycarbonate (PC) is fixed on oneside and kept free on other side. The antenna is fixed in the middle of the PC cantilever beam (L/2). Different loads are applied at the free end of the beam. Using a network analyzer (Agilent PNA n5222a), the resonance frequency is monitored when a load is applied at the end of the cantilever (deflection occurs), and thus the strain sensitivity of the patch strain sensor is calculated, the measurement setup is shown in Figure 4.11. The strain sensitivity is calculated as proportion of the relative change in the resonance frequency and the resulting strain;

$$S_{strain} = \frac{\Delta f / f_0}{\epsilon} \tag{4.9}$$

where Δf is the change in resonance frequency, f_0 is the resonance frequency at no load and ϵ is the strain.

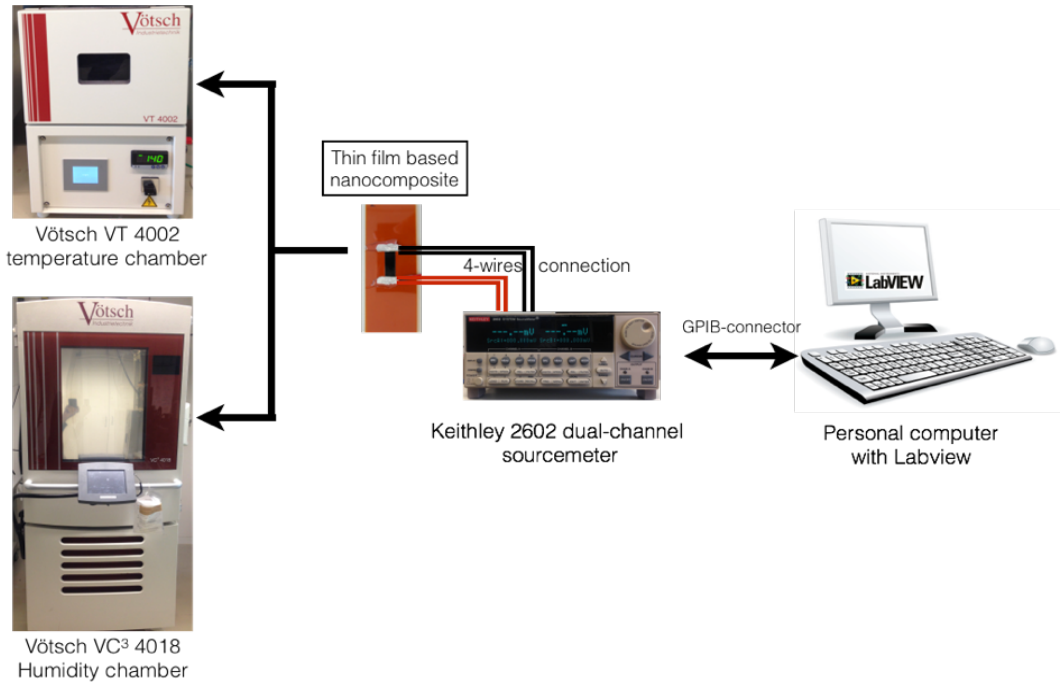

Figure 4.10: Measurement setup for temperature/humidity sensing

Using the cantilever beam theory, the stress is calculated as function of the beam deflection under applied weight. Thus, the strain (ϵ) equals to;

$$\epsilon = \frac{Mh}{2IE} \tag{4.10}$$

where M is the bending moment, h is the beam thickness, I is the bending moment of inertia of the beam's cross section area and E is the Young's modulus of the beam material. For M=F(L-x), where F is the applied force, L is the length of the beam and x is the location on which the antenna is located from the fixed end of the cantilever beam. For the rectangular beam, $I = wh^3/12$ where w is the beam width and h is the beam thickness. The dimensions of the cantilever beam are (L×w×h=200×20.22×4.11mm) and the E of polycarbonate is about 2.3 GPa [262]. All the patch antennas are fixed at the middle of the beam and the applied weight are changed from 80g to 480g with a step of 80g. The applied force (F) can be estimated using the Newton's second law as follows:

$$F = m \times a \tag{4.11}$$

where m is the mass in kg and a is the acceleration (9.81 m/s).

A schematic of the strain measurement setup is illustrated in Figure 4.12. Using the previous information, the strain located at the MPA (ϵ_x) can be calculated as follows:

$$\epsilon_x = \frac{6F(L-x)}{Ewh^3} \tag{4.12}$$

Based on Hooks law, the stress (σ) is linear relationship between the strain (ϵ_x) and the Young's modulus,

$$\sigma = E \times \epsilon_x \tag{4.13}$$

For the wireless temperature sensing, the MPA is connected the RF coaxial cable of the network analyzer and kept inside the temperature chamber then the shift in the resonance frequency in monitored as function of temperature.

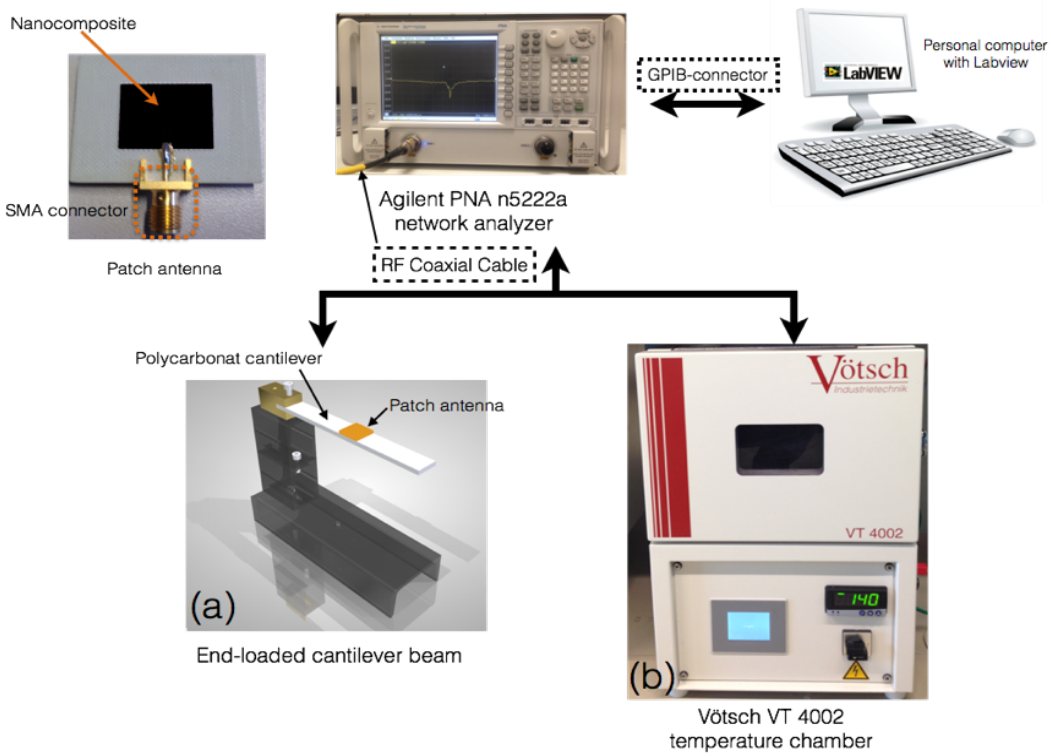

Figure 4.11: Measurement setup for wireless (a) Strain, (b) Temperature

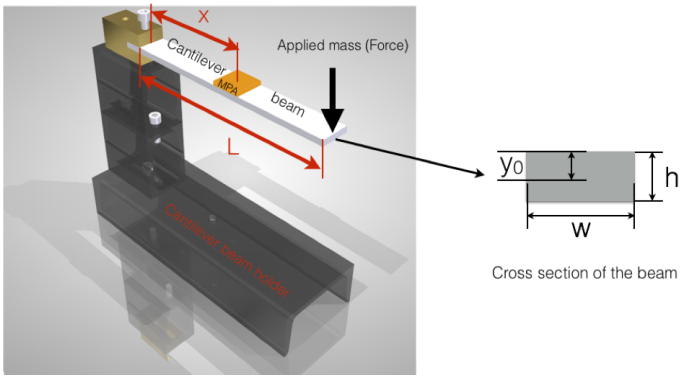

Figure 4.12: Illustration of the end-loaded cantilever beam setup for wireless strain sensing

The difference between the sensor input and output is known in the field of measurement techniques as the hysteresis. The Figure 4.13 shows a typical graph of hysteresis. The middle point (X_m) of first cycle is calculated using the equation 4.14. Afterwards, the hysteresis in % is calculated using the equation 4.15 as follows,

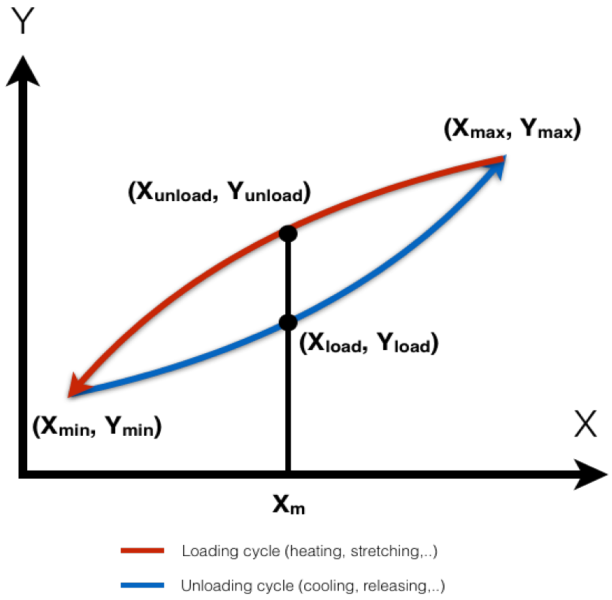

Figure 4.13: Illustration of typical hysteresis graph

$$X_m = \frac{X_{max} - X_{min}}{2} + X_{min} \tag{4.14}$$

$$Hysteresis(\%) = \frac{Y_{unload} - Y_{load}}{Y_{max} - Y_{min}} \times 100 \tag{4.15}$$

5 Non-Covalent Functionalized MWCNTs Decorated PEDOT:PSS

In this chapter, MWCNTs dispersed in PEDOT:PSS are analytically and systematically studied. The chemico-physical properties include the effect of MWCNT content on the surface tension and contact angle and tuning the bandgap of the nanocomposites are investigated and discussed. The change in the microstructural morphology of the films based MWCNT:SDBS/PEDOT:PSS using different microscopic techniques is explored. Besides, the nature of the transport and charge mobility of the nanocomposite is explained when it is mechanically stressed and under temperature and humidity environment.

5.1 Chemico-Physical Characterization

In general, the contact angle is influenced by the chemical nature and surface roughness of the substrate [263]. The surface energy of the untreated Kapton HN500 is 40.02mJ.m^{-2} whereas for the treated substrate is 44.41mJ.m^{-2}. In which the contribution of the polar part is 13.69mJ.m^{-2} and 19.95mJ.m^{-2} for untreated and treated substrates, respectively. Therefore, the treated substrate has a higher wetting property than the untreated one, and it is used for all further investigations. For the surface tension, the increase of the MWCNTs content in the nanocomposites shows an ignorable effect, around 4mN/m from 40.7mN/m to 40.3mN/m for 0.025wt.% and 0.1wt.% MWCNTs, respectively. The surface tension of the non-covalent MWCNT decorated PEDOT:PSS has shown a low value compared to the pure PEDOT:PSS, which is 67.1mN/m. The decrease of the hydrophobicity is mainly due to the presence of the SDBS surfactant, that lowers the surface tension of the nanocomposite as it is shown in Table 5.1, whereas the CNT content has almost no influence. The contact angle gives an information about the adhesion of the nanocomposite to the substrate. All the MWCNT:SDBS/PEDOT:PSS nanocomposites show very good wettability properties with contact angle between 24° and 38° (Figure 5.1), which is less than the pristine PEDOT:PSS (78°). A slight increase in the contact angle is measured with increasing MWCNT loading, as it is predicted in Figure 5.1. The reason for this increase could not be explained and needs more investigations in further work.

Table 5.1: Surface tension of PEDOT:PSS and its nanocomposites

MWCNT Content (wt.%)	Surface Tension (mN/m)		
	$MWCNT:SDBS$	$RawPEDOT:PSS$	$MWCNT:SDBS/PEDOT:PSS$
0.025	32.9		40.7
0.05	33.7		40.5
0.075	33.9	67.1	40.0
0.1	34.0		40.3

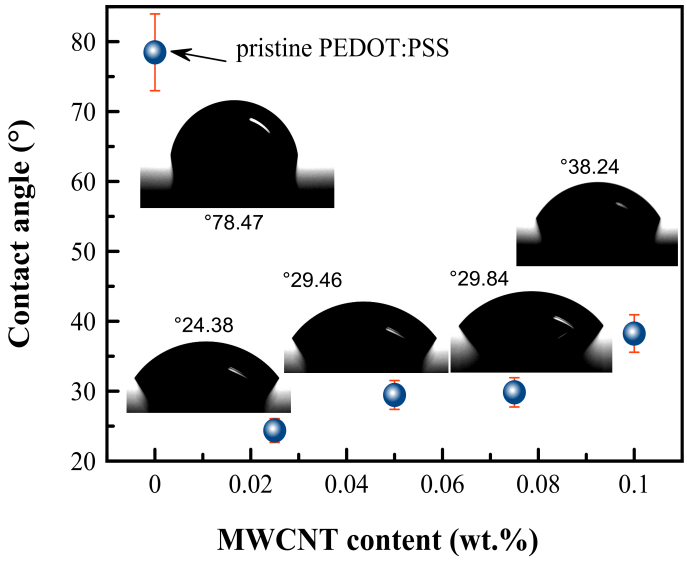

Figure 5.1: Contact angle of the MWCNT:SDBS/PEDOT:PSS aqueous dispersion

5.2 Morphological Investigations

The morphology of the MWCNT:SDBS/PEDOT:PSS films is examined using the ODM, AFM and SEM. As it is shown in Figure 5.2 (a-c), big agglomeration islands (spherical grain structure) of PEDOT:PSS are formed due to the nature of this core-shell co-polymer, where PEDOT is the core part and PSS is the shell part, as it is defined previously by Lang et al. [264]. The PEDOT:PSS films consists of disconnected, conducting PEDOT-rich grains with weak phase separation [264-266]. The van der Waals attraction forces are strong between the CNTs, thus a high entangled and curled MWCNTs is clearly revealed (Figure 5.2 d-f). Moreover, the surface morphology of the MWCNT:SDBS/PEDOT:PSS film shows that MWCNTs are well-dispersed and well-connected with one another in the polymer matrix (Figure 5.2 (g-i)), which is an indication of a good wrapping of the MWCNTs by the PEDOT:PSS chains. The MWCNTs content in the nanocomposite, determines also the degree of the films surface roughness, whereas for the pristine PEDOT:PSS a value of 3.68nm is achieved, it increases from 6.49nm to 11.68nm when increasing the MWCNT content from 0.025wt.% to 0.1wt.%.

5.3 Tuning the Optical Bandgap

The optical properties of the MWCNT:SDBS/PEDOT:PSS are characterized by a discrete excitonic transition from valence electronic bands to conduction bands using the UV-Vis spectroscopy. Bundled CNTs are not active in the optical spectrum from 350nm and 1200nm, due to the tunneling coupling and the migration of photons from large bandgap to small bandgap [87, 91, 264, 267-268]. Therefore, only the individual CNTs are able to absorb the photons of the incident light and exhibit 1D van Hove singularities that appear at characteristic bands [269-271]. Figure 5.3 shows the UV-Vis spectra of the MWCNT:SDBS/PEDOT:PSS colloids. In the visible spectrum (400nm- 760nm), either for pristine PEDOT:PSS or the nanocomposites, low absorption is observed with a modest monotonic increase of absorbance that occurs with increasing the wavelength. Above 700nm, a broad peak is observed, which is referred to

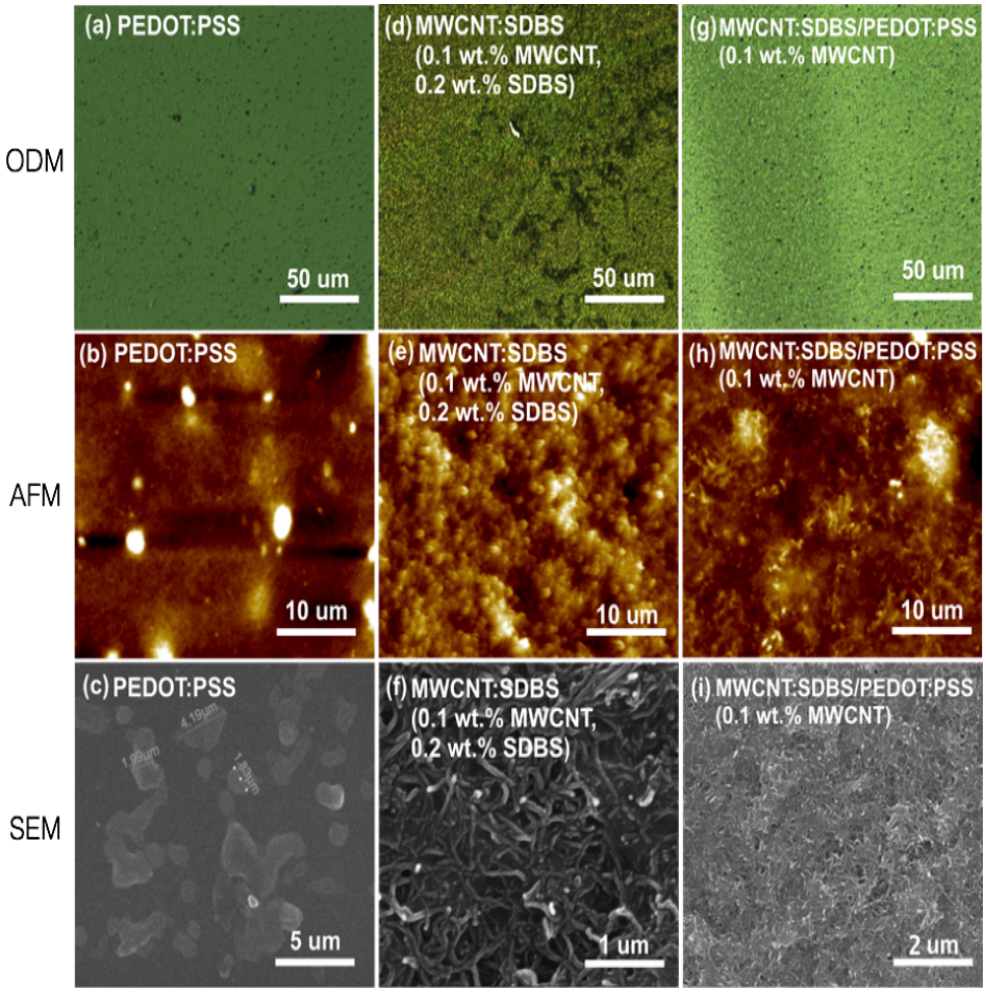

Figure 5.2: Morphology of (a-c) PEDOT:PSS, (d-f) MWCNT:SDBS, and (g-i) MWCNT: SDBS/PEDOT:PSS films observed with ODM, AFM and SEM

the long molecule chain of the PEDOT:PSS as well as its better molecule alignment [272]. In the near infrared region (NIR-region) and for high MWCNT content, three sharp absorption peaks at 850, 970 and 1200nm are defined, indicating the occurrence of a new local states in the Fermi level between the valence and the conduction band [272-273]. The peak at 850nm is attributed to the π-polaron charge transition, whereas the sharp peaks at 970nm and 1200nm are attributed to the bipolaron transitions associated with benzoid/quinoid structure [273]. The appearance of the sharp peaks in the NIR-region, confirms the good wrapping and intercalation between the MWCNT and the PEDOT:PSS at 0.1wt.% MWCNT, as confirmed in Figure 5.2. This promotes more electron transfer and leads to the formation of a polaron and finally a bipolaron states. Above 1236nm (NIR-region), a free carrier tail is observed, which is a characteristic for highly conducting state due to the high doping degree. The Lambert-Beer law (equation 5.1) is applied to determine the absorption coefficient (α) at wavelength of 500nm (Figure 5.4 (a)).

$$A = \alpha \times t \times C \tag{5.1}$$

where A is the absorbance, α is the absorption coefficient, t is the cuvette thickness and C is the concentration.

A linear relationship between the absorbance and the MWCNT concentration is extracted, by determining the slope of the curve, the absorption coefficient is $5.8 L.g^{-1}.cm^{-1}$. From Figure 5.4 (a), it can be seen that the absorbance at 500nm increases with increasing the amount of MWCNT dispersed in PEDOT:PSS. The increase trend confirms the homogeneous distribution of the MWCNTs within the PEDOT:PSS due to the presence of more individual CNTs in the colloid. Considering an indirect bandgap of 3.07eV for PEDOT:PSS, the optical bandgap of the hybrid nanocomposite is calculated from Tauc plot. It can be seen from Figure 5.4 (b) that the increase of the MWCNTs content in the PEDOT:PSS results in a linear decrease of optical bandgap due to the partial recovery of the π-conjugation system, which leads to the formation of the bipolaron states at high CNT content [274-275]. The optical bandgap decreases to 2.7eV, 2.68eV, 2.61eV and 2.46eV for 0.025wt.%, 0.05wt.%, 0.075wt.% and 0.1wt.% MWCNT, respectively.

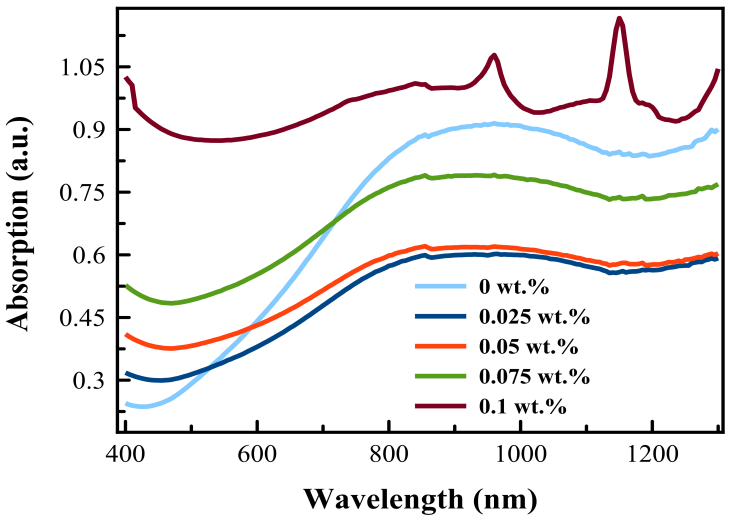

Figure 5.3: UV-Vis spectra of different concentration of MWCNT:SDBS dissolved in PEDOT:PSS

5.4 Transport and Charge Mobility

Figure 5.5 shows the film conductivity as a function of the MWCNTs concentration with/without PEDOT:PSS. The films without polymer and at low CNT content possess relatively high resistance i.e. low conductivity. The conductivity of the randomly oriented MWCNT:SDBS films is about 6.9±1.4S/m, 25.8±2.1S/m, 40.5±3.8S/m and 160.0±11.1S/m for 0.025wt.%, 0.05wt.%, 0.075wt.% and 0.1wt.%, respectively. While for the pristine PEDOT:PSS films have an initial conductivity of 25.5±2.3S/m. Figure 5.5 shows also that with addition of MWCNTs to the PEDOT:PSS matrix, the conductivity increases by several order of magnitude from 149.1±11.9S/m to 836.6±1.5S/m for 0.025wt.% to 0.1wt.%, respectively. Not only the conductivity of the nanocomposites is improved but also the corresponding standard deviations are significantly reduced, which indicates a good reproducibility improvement. The sheet resistance is measured at three different lines and the values are depicted in Table 5.2. The sheet resistance of the MWCNT:SDBS/PEDOT:PSS nanocomposite is about 20-450

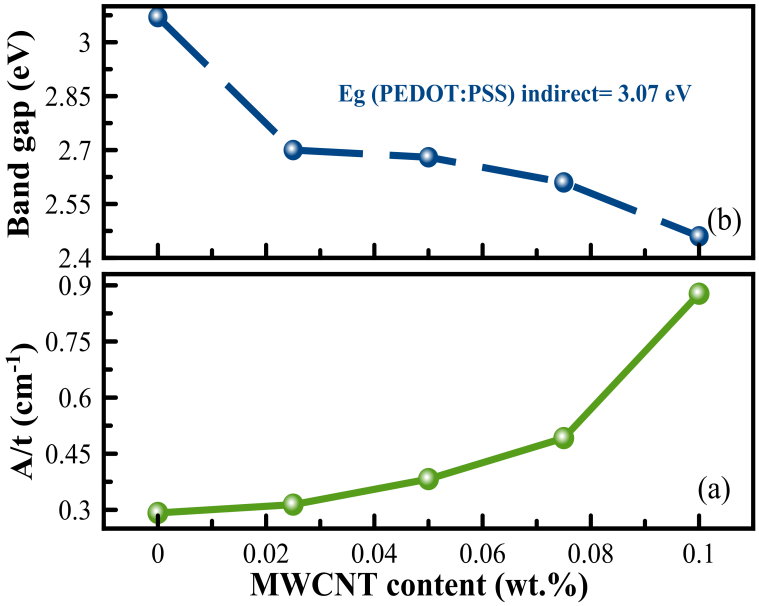

Figure 5.4: Tauc plot of different MWCNT content dissolved in PEDOT:PSS, (a) Absorption coefficient, (b) Change in the optical bandgap

orders lower than the MWCNT:SDBS and the pristine PEDOT:PSS films. The average sheet resistance of the films without PEDOT:PSS decreases from 321.1kΩ.sq^{-1} to 12.9kΩ.sq^{-1} for 0.025wt.% and 0.1wt.% MWCNTs, respectively. For the films with PEDOT:PSS, it decreases from 5.5kΩ.sq^{-1} to 1.3kΩ.sq^{-1} for 0.025wt.% and 0.1wt.% MWCNT, respectively. The electronic transport within MWCNT:SDBS/PEDOT:PSS films is explained using superposition of the PEDOT:PSS and MWCNT individually. The influence of the SDBS in this case is ignored as after deposition, all the films are baked in the oven at temperature of 80°C (this temperature is enough to evaporate all the SDBS molecules from the films, as it is above it's glass temperature) and then washed with distilled water (as it is explained in section 4.2.2), so all the residues of the SDBS are removed.

The presence of alternating C-C double bonds along the backbone structure of the PEDOT:PSS leads to electron hopping from one PEDOT segment to the neighboring one which enables the overlapping of π-orbital along the molecule, and therefore the electronic transport is governed by electron hopping between the conjugated PEDOT chain or the neighboring chains, resembling a 3-D semiconductor system [276-277]. The PEDOT:PSS has anisotropic conductivity, thus the high deviation in its conductivity is due to the influence of the morphology on the π-conjugate system [265]. The strong interfacial coupling through the π interaction between the MWCNT and the thiophene rings of PEDOT promotes the electronic density transfer between them, so the mobility of the charge carrier is more delocalized in the PEDOT chain and consequently, the conductivity is improved (Figure 5.5) [278]. The formation of more conductive paths in the polymer matrix results in the construction of a dense 3D physical contact network (Figure 5.2 (i)), consequently, the charge transport is dominated by the CNT. Adding CNTs improves also the electrical homogeneity of the nanocomposite, for this reason the electrical standard deviation sharply improves for high CNT content.

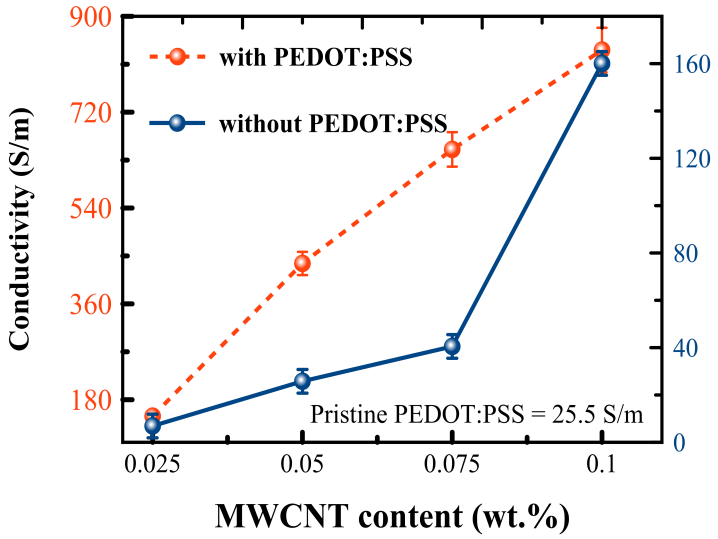

Figure 5.5: Electrical conductivity of the MWCNT:SDBS/PEDOT:PSS films

5.5 Piezoresistive Response of the MWCNT:SDBS/PEDOT:PSS Films

The piezoresistive property of the MWCNT:SDBS/PEDOT:PSS films is investigated by measuring in-situ the change in the electrical resistance under mechanical force (Figure 5.6 (a)). All the films show a good linear trend behavior with a correlation coefficient (R_2) between 0.977-0.994 for 0.0wt.% and 0.05wt.% MWCNT, respectively, which indicates a high linearity of these films under strain as it is shown in Figure 5.6 (b). For the pristine PEDOT:PSS films, a decrease of resistance is measured as the applied force increases, and the gauge factor is -2.7. This negative piezoresistive behavior of the PEDOT:PSS is corresponding mainly to its physical structure. Under strain, the PSS chain gets aligned in the direction of the applied force, this reduces the hopping distance between the PEDOT segments, consequently an increase in the number of the charge carriers that hopp from one PEDOT segment to another neighbor segment occurs, which leads to improve the conductivity and therefore reduce the film resistance [279-280], a model describing the piezoresistivity of the PEDOT:PSS films is shown in Figure 5.7. For the specimens having MWCNTs, two different behaviors can be clearly distinguished (Figure 5.6). At MWCNT content below 0.05wt.%, a negative piezoresistive behavior is noticed, which is the same piezoresistive behavior as the pristine PEDOT:PSS but with less sensitivity. At MWCNT content above 0.05wt.%, a positive piezoresistive behavior occurs with relatively low gauge factor k=1.7 and 2 for 0.075wt.% and 0.1wt.% MWCNT content, respectively. For the CNT/ polymer nanocomposite, the piezoresistive behavior of this nanocomposite is explained as follow: the PEDOT:PSS has a negative piezoresistive behavior, while the MWCNTs have a positive piezoresistive behavior, thus the resulting piezoresistive behavior depends on the part that dominates the conduction mechanism within the film.

The piezoresistivity of pristine MWCNT film is mainly due to the change in the tunneling distance between the CNTs and the reorientation of the tubes when it is under an applied force [255]. At MWCNT below 0.05wt.%, the PEDOT:PSS dominates the piezoresistive be-

Table 5.2: Sheet resistance of MWCNT:SDBS/PEDOT:PSS films

MWCNT Content (wt.%)	Sheet Resistance ($k\Omega.sq^{-1}$)		
	$MWCNT:SDBS$	$RawPEDOT:PSS$	$MWCNT:SDBS/PEDOT:PSS$
0.0		19.4	
		16.9	
		19.6	
0.025	527.9		2.2
	290.7		1.4
	145.6		1.4
0.05	89.3		1.4
	69.8		1.3
	91.1		1.8
0.075	21.3		1.3
	23.1		1.4
	35.2		1.2
0.1	14.0		1.1
	11.7		1.2
	13.1		1.1

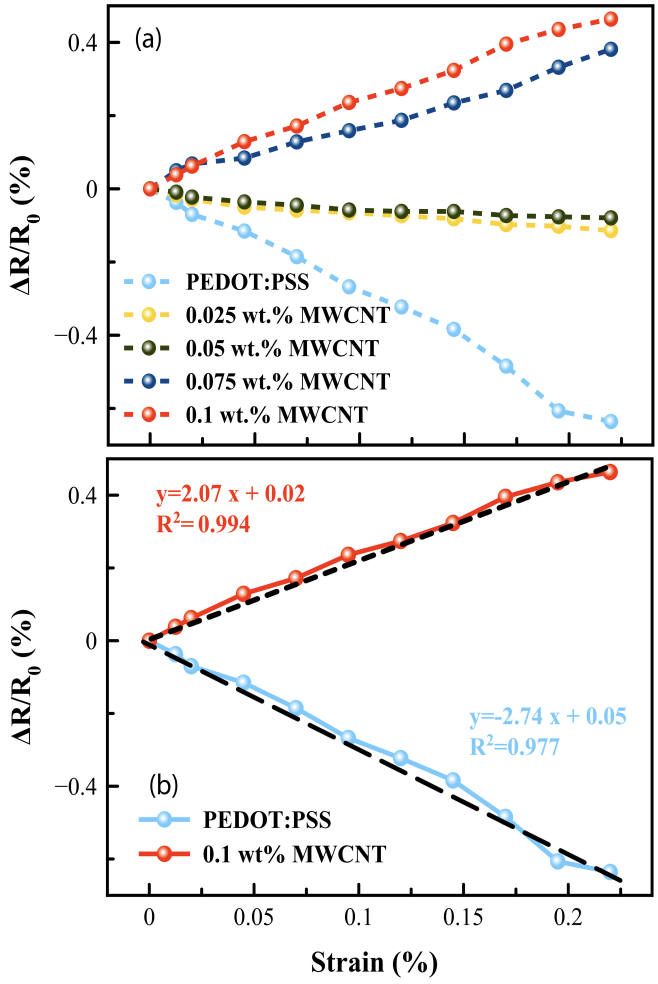

Figure 5.6: (a) Piezoresistivity and (b) Linear fitting of films based MWCNT:SDBS/ PEDOT:PSS as function of MWCNT contents

havior because the electron hopping through the PEDOT segments dominates the conduction (as it is proven in section 5.4). As the MWCNT is added to the polymer matrix, the strain sensitivity decreases due to the different piezoresistive behavior of the PEDOT:PSS and the MWCNTs. At a critical MWCNT value which stated at 0.05wt.%, the piezoresistivity of the MWCNTs starts to dominate within the nanocomposite, which confirms also that the type of the conduction is determined by the CNTs. At 0.1wt.% MWCNT, the current is passing mainly through the CNTs, thus any change in the tunneling distance due to an applied force, changes the resistance of the film. A piezoresistive model for high MWCNT content is depicted in Figure 5.7 (b).

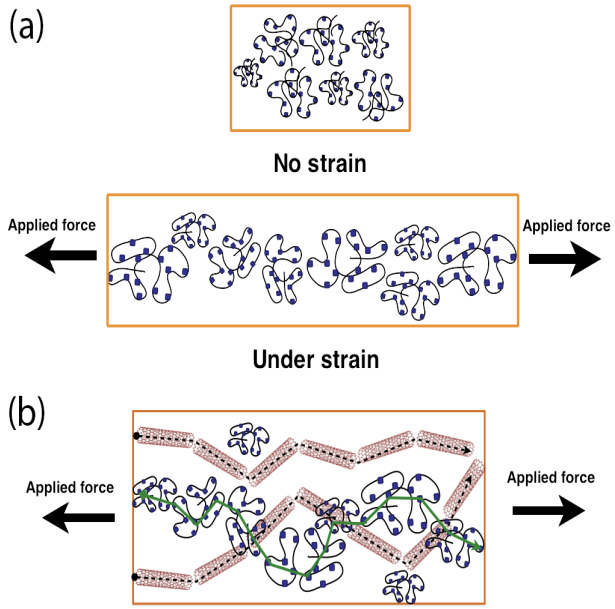

Figure 5.7: Schematic description of the piezoresistivity behavior of (a) PEDOT:PSS and (b) MWCNT:SDBS/PEDOT:PSS films at high MWCNT contents

5.6 Resistance Dependency on Temperature Influence

The effect of the temperature is investigated as resistance-temperature dependency at different CNT content. Figure 5.8 plots the change in the DC-resistance as a function of the temperature between 20°C and 80°C for MWCNT:SDBS/PEDOT:PSS nanocomposites having 0.025wt.%, 0.05wt.%, 0.075wt.% and 0.1wt.% MWCNTs. The resistance-temperature dependency response of the films decreases nonlinearly as the temperature increases, thus the resistance of pristine PEDOT:PSS decreases from 50kΩ to 16.5kΩ at 20°C to 80°C, respectively. This drop-in resistance is due to the partial removal of the water and solvent molecules from the films (in the next section the effect of the humidity is studied, where it shows the effect of the water molecules on the conduction of these films). With increasing the temperature, more electrons get an activation energy to cross more PEDOT segments and thus resulting in the decrease of the film resistance. The MWCNT:SDBS/PEDOT:PSS films showed less sensitivity to temperature than the pure PEDOT: PSS and the temperature influence decreases with increasing CNT content. The resistance of the films with 0.025wt.%,

0.05wt.%, 0.075wt.% and 0.1 wt.% at 20°C are 7.06kΩ, 6.82kΩ, 2.91kΩ and 1.92kΩ and decreases to 2.88kΩ, 2.87kΩ, 1.74kΩ and 1.24kΩ at 80°C (Figure 5.9). As mentioned in section 5.4, the randomly distributed network of the MWCNT dominates largely the conduction of the nanocomposite and thus the resistance-temperature response. Hence, the major conductive mechanism results from the tunneling barriers between CNTs, which dominates the overall film resistances especially at high CNT concentration [281-284]. While increasing the temperature, more thermal energy activation is afforded to the motion of electrons to overcome easily the potential barrier between MWCNTs, which results in the decrease of the film resistance. But at high CNT concentration, a dense network is formed (Figure 5.2 (g-i)), therefore many paths are already included in the conduction. Therfore, the activation of few new paths due to temperature, is not affecting so much the conductivity, thus the change in the conductivity is low.

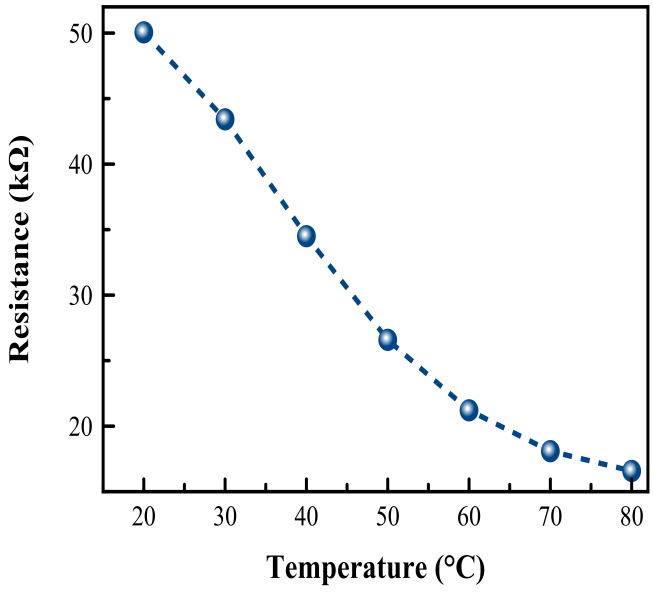

Figure 5.8: DC-resistance of PEDOT:PSS film as function of temperature

5.7 Resistance Dependency on Humidity Influence

Because the PEDOT:PSS has a hygroscopic property, it is necessary to examine the influence of the humidity on the electrical property of the films based PEDOT:PSS. The change in electrical resistance of the pristine PEDOT:PSS films as a function of relative humidity at different temperatures (50°C, 60°C and 70°C) is shown in Figure 5.10. The resistance increases exponentially up to 70%RH then it starts to decrease sharply. This decrease is referred to the formation of a water meniscus layer on the surface of the PEDOT:PSS film adsorbed by the PSS part of the polymer [285]. As mentioned in section 5.4, the conduction in the conjugated polymer PEDOT:PSS is mainly due to the electron hopping between the PEDOT adjacent, whereas the PSS chains are responsible for water adsorption due to its hydrophilic properties. As the humidity increases; the PSS chains adsorb more water

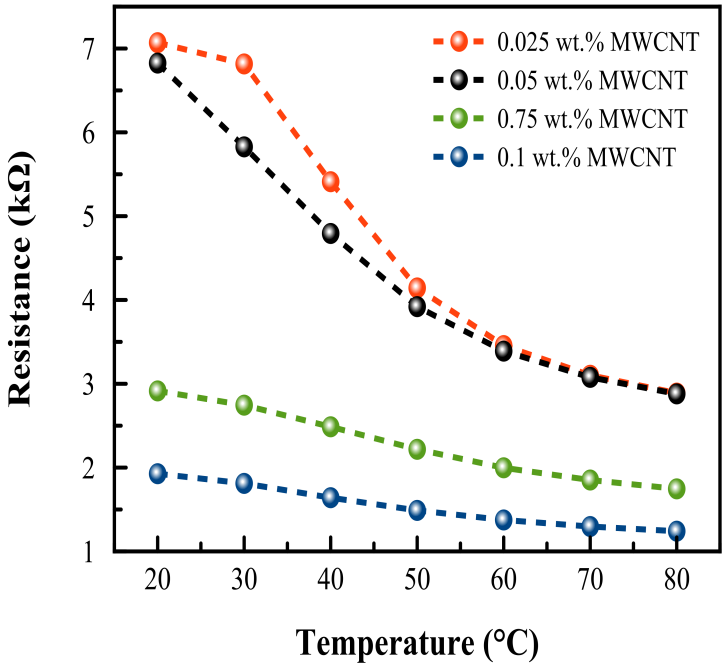

Figure 5.9: DC-resistance of MWCNT:SDBS/PEDOT:PSS nanocomposite film as function of temperature

molecules (for relative humidity from 10% to 70%), and thus the hydrogen bonds between the PSS are weakened [286], as shown in the following equation:

$$H_2O + PSS(HSO_3) \longrightarrow H_3O^+ + PSS(SO_3)^- \tag{5.2}$$

Consequently, the distance between the adjacent PEDOT (conductive part of the polymer) increases and therefore the hopping of charges (the movement of the electrons) between the PEDOT parts become harder so the film resistance increases with increasing humidity. A schematic describing the adsorption of water molecules on the PSS chain is illustrated in Figure 5.11. The uptake peak in this case is at 70%RH, whereas other works showed differernt uptake peaks, this shift in the uptake peak corresponds to the hygroscopic nature of the PEDOT:PSS film, owing to the amount of the PSS available in the PEDOT:PSS [285-286]. The effect of humidity cycling is studied at reference temperature of 70°C, as it is depicted in Figure 5.12. Four cycles are applied to the pristine PEDOT:PSS films. The sensitivity at the first cycle is the highest and more cycles reduce the sensitivity until it remains constant after the third cycle, this is attributed to the annealing of samples, as it is seen in Figure 5.10. Similar behavior is regarded for the MWCNT:SDBS/PEDOT:PSS films with low sensitivity than the pristine PEDOT:PSS. However, increasing the CNT content and the working temperature introduces a damping in the resistance tendency, as it is depicted in Figure 5.13. Figure 5.14 (a) and (c) give a schematic view of the randomly distributed CNT networks at low and high CNT contents, respectively. The film morphology and CNT distribution at low and high MWCNT concentration are given in Figure 5.14 (b) and (d). Generally, there are two current paths across the MWCNT and the PEDOT:PSS film:

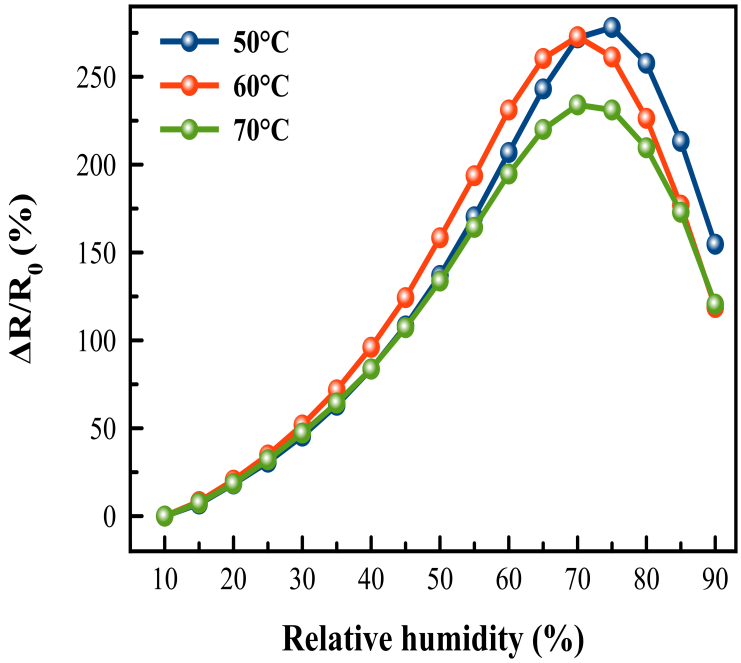

Figure 5.10: Humidity dependence of film resistance of pristine PEDOT:PSS at different temperatures

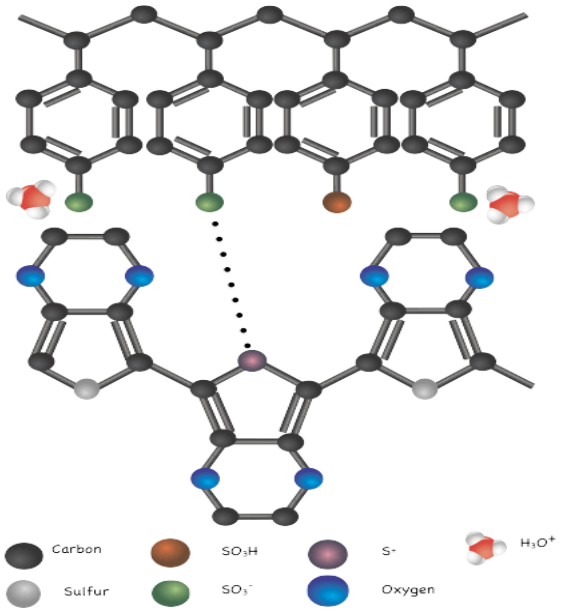

Figure 5.11: Interaction of water molecules with the PSS chain

1. At 50°C and at low CNT content (Figure 5.14 (a)), the intertube distance between CNTs is relatively large, and therefore the dominant current is passing through the PEDOT segments in the PEDOT:PSS chain as result of the hopping process. Since the distance between the electrodes is larger than the length of the CNTs, the CNT junction resistance is more dominant than the internal resistance of the CNT film [287-288].

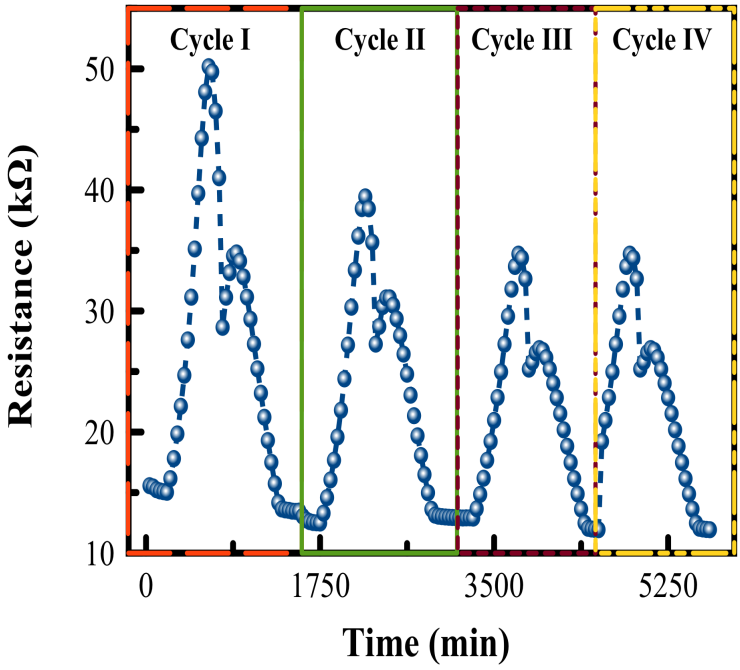

Figure 5.12: Cycling test of the PEDOT:PSS films under humidity environment

2. At 60°C and 70°C, the hydrogen bonds between the water molecules and the PSS chain becomes weaker [286, 289], so that the adsorption of H_2O on the CNT walls becomes lower. For this reason, the tunneling barriers between CNT junctions decrease and more charge carriers can be transported through the barriers. Therefore, the sensitivity drops dramatically.

As shown in Figure 5.10 and Figure 5.13, the behavior of the MWCNT:SDBS/PEDOT: PSS films in dependence on the relative humidity are non-linear in the range 10%RH to 70%RH. The linear regression model is adapted for all the samples to linearize the model, in case of pristine PEDOT:PSS films, the correlation coefficient (R^2) of 0.9699, which indicates a good linearity, thus it is a good candidate for humidity sensing applications. The linearization equation used for PEDOT:PSS films is the following,

$$R = 828.28 \times (\%RH)3398.67 \tag{5.3}$$

Based on that, the sensitivity (S_h) is calculated using the following equation:

$$S_h = (\Delta R/R_0)/(\Delta \%RH) \tag{5.4}$$

Where ΔR is the change of resistance of a pristine PEDOT:PSS film, R_0 is the resistance measured at RH=10%, and Δ%RH is the change of the relative humidity.

It can be concluded from Table 5.3 that the sensitivity of the pristine PEDOT:PSS films at 50°C is the highest compared to the nanocomposites with CNT content and at other investigated temperature i.e. 60°C and 70°C. Which enables the PEDOT:PSS films to be used as humidity sensors up to 70%RH.

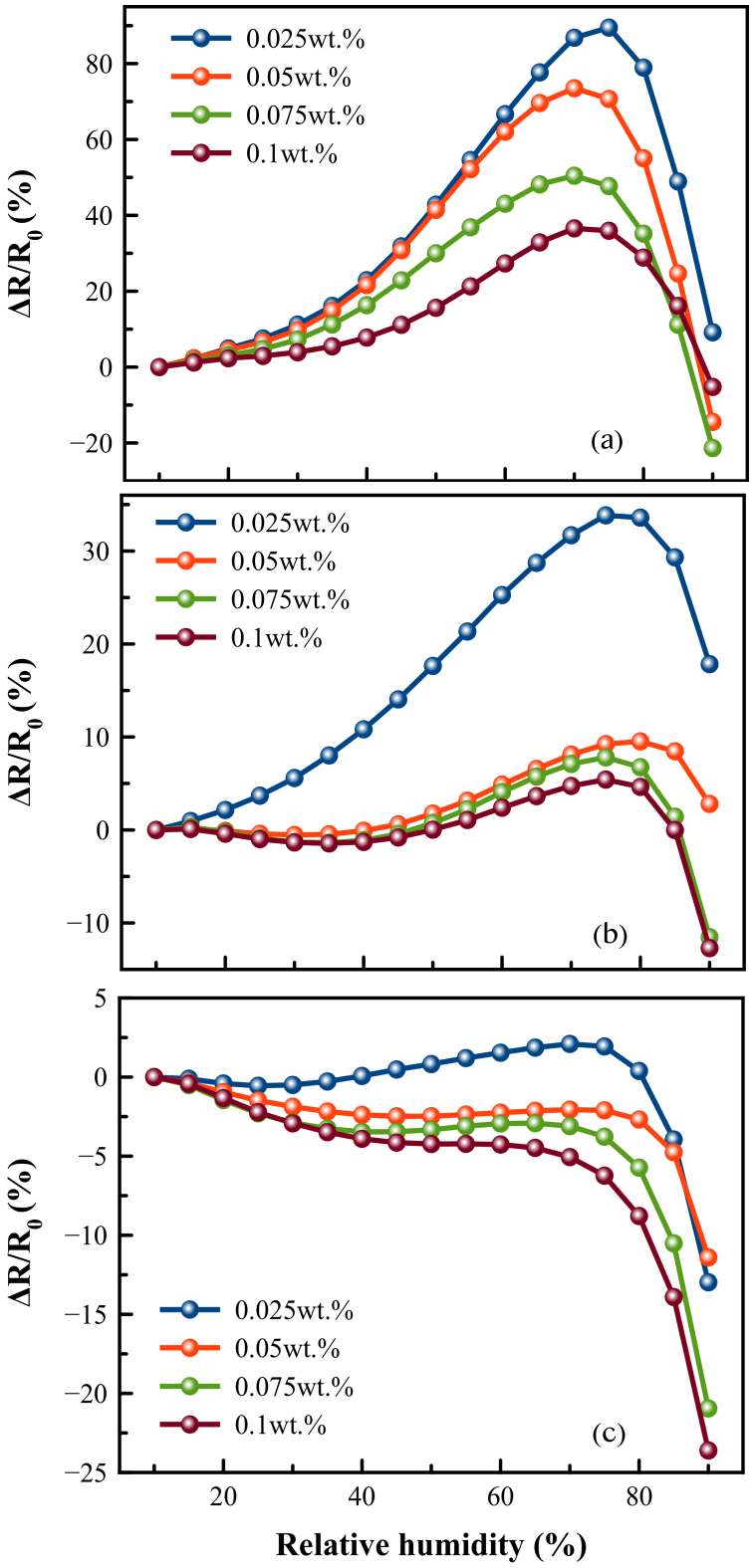

Figure 5.13: Change in electrical resistance of MWCNT:SDBS/PEDOT:PSS films with respect to RH at (a) 50°C (b) 60°C and (c) 70°C

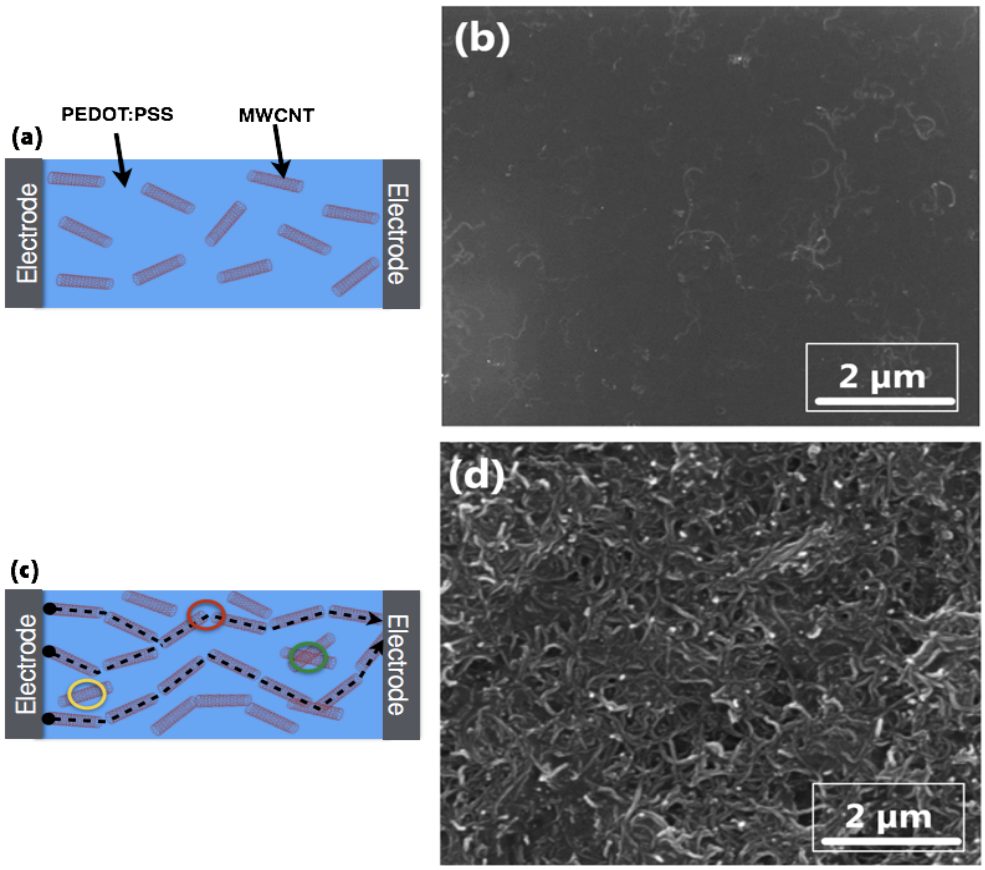

Figure 5.14: CNT random distribution in PEDT:PSS: (a) Schematic illustration at 0.025wt.% MWCNT, (b) SEM image at 0.025wt.% MWCNT, (c) Schematic illustration at 0.1wt.% MWCNT and (d) SEM image at 0.1wt.% MWCNT (red: tunneling effect, green: CNT barrier, yellow: single CNT)

Table 5.3: Sensitivity to humidity of MWCNT:SDBS/PEDOT:PSS films of different MWCNT content at different working temperatures

Temperature (°C)	Sensitivity to humidity ($10^{-3}/\%RH$)				
	$0.0wt.\%$	$0.025wt.\%$	$0.05wt.\%$	$0.075wt.\%$	$0.1wt.\%$
50	45.4	14.4	12.2	8.4	6.0
60	45.3	5.2	1.3	1.1	-7.0
70	38.9	0.8	0.5	-3.4	-3.0

Film Based on rGO and MWCNTs

6

In this section, films based on rGO and MWCNTs are systematically investigated. rGO:MWCNT are prepared using the solution mixing as explained in 4.1.2. The contact angle and surface tension are determined to investigate the wettability of the hybrid nanocomposites to the flexible polymer substrate, optical properties are studied using UV-Vis and the morphology of the films are investigated using SEM. Because the GO is an insulator, a reducing agent which is hydroiodic acid, is used to improve the electrical conductivity. The piezoresistivity of the films is conducted by electromechanical measurement. Besides that, the temperature and humidity influence on the charge mobility are investigated and the related behavior is well explained.

6.1 Chemico-Physical Characterization

The pristine GO shows a good hydrophilic property i.e. adhesion, with contact angle of 73.5°. Adding MWCNTs to the GO matrix improves slightly the adhesion between the nanocomposite and the substrate, consequently the contact angle decreases to 66.5°, 65.3° and 64.1° for 0.01, 0.025 and 0.05 wt.% MWCNT content, respectively (Figure 6.1). The hydrophilic property of the GO is mainly due to presence of the hydroxyl and epoxy polar groups [290-291], the MWCNT is wrapped by those polar groups and therefore the hydrophilicity is higher. The value recorded for the surface tension for the GO is 65.4mN/m and for the GO:MWCNT is 63.1mN/m, 61.9mN/m and 56.7mN/m for 0.01wt.%, 0.025wt.% and 0.05wt.% MWCNT content, respectively.

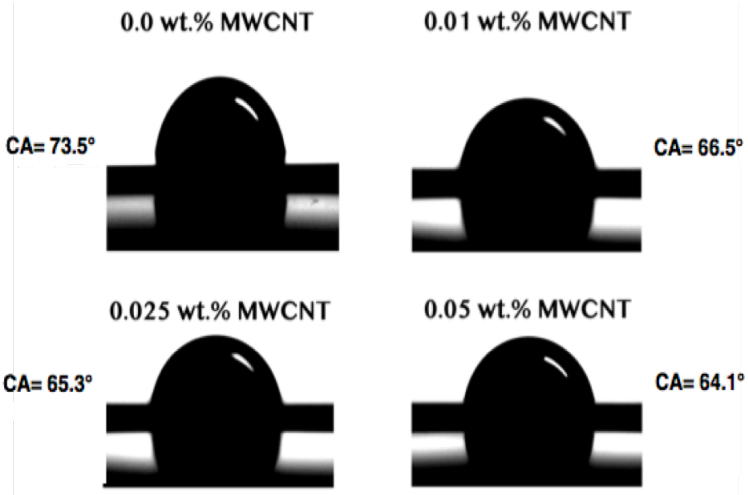

Figure 6.1: Contact angle of the GO:MWCNT colloids

6.2 Structural Analysis using XPS and Raman Spectroscopy

To understand deeply the effect of the chemical reduction on the structural surface of the GO:MWCNT films, XPS and Raman measurements are conducted. Using XPS, the types of functional groups can be qualitatively determined. By Raman spectroscopy, the degree of defects caused by the chemical reduction can be extracted. To quantify the effectiveness of the chemical reduction, the C1s XPS spectra for non-reduced and reduced GO and GO:MWCNT are investigated and shown in Figure 6.2. Before evaluating the XPS spectrum, a Shirley background correction is performed prior using the Guassian-Lorentzian function for curve fitting. From the C1s spectrum in Figure 6.2 and Figure 6.3, the effect of the reduction is clearly seen by the damping of hydroxyl groups (C-OH) peak at binding energy of 285.9eV for the rGO and rGO:MWCNT compared to the GO and GO:MWCNT, this peak is representative for the oxygen-containing functional groups. For the non-reduced GO in Figure 6.2 (a) and GO:MWCNT in Figure 6.3 (a), a strong characteristic peak at binding energy of 284.6eV are identified and assigned to aromatic and hydrogenated C (C=C/C–C). Besides, other oxygen-containing functional groups appears after the deconvolution of the C1s namely, carbonyl C (C=O) at 288.1eV and carboxylate C (O=C-OH) at 289.7eV [133, 292-295]. After chemical reduction, a hump appears at 291.1eV which is assigned to the $\pi - \pi^*$ shake-up satellite, as it is depicted in Figure 6.2 (b) and Figure 6.3 (b) [292, 296]. For the rGO, rGO:MWCNT, the intensity of oxygen-containing functional groups peaks is much lower than the GO (Figure 6.2 (a) and Figure 6.3 (a)), which is an indicator of an effective chemical reduction process treatment. The removal of the oxygen-functional groups is a sign of restoration of the sp^2-hybridized structures from the sp^3-hybridized rings [293, 297]. Additionally, no carbon to nitrogen bounding is observed. Figure 6.4 shows

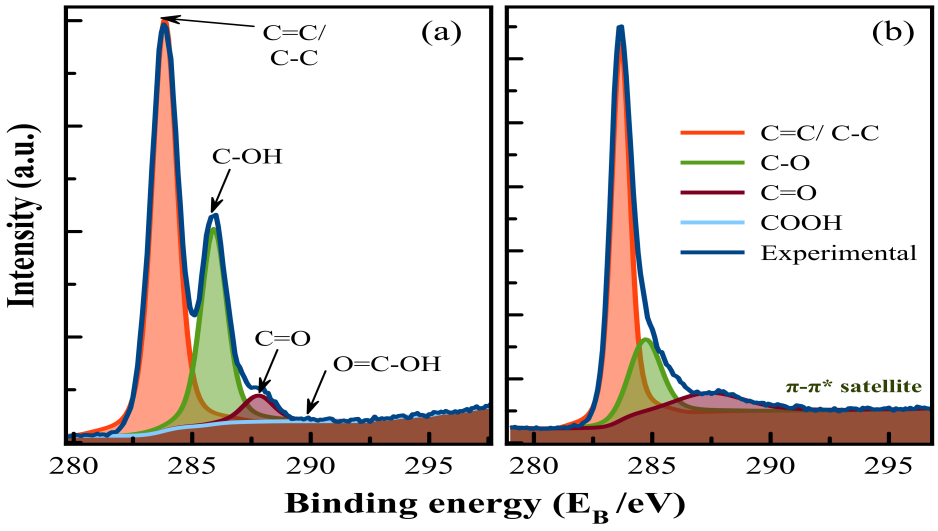

Figure 6.2: C1s XPS spectra of a) GO; b) rGO film

a Raman spectrum of GO:MWCNT and rGO:MWCNT at 0.05wt.% MWCNTs, which is a typical spectrum observed in GO and rGO sheets [158]. The presence of the G band at about 1601cm^{-1} implies the C-C vibrations of carbon with an sp^2 orbital structure of the GO and its derivatives, is referred to the graphitic nature of GO. The existence of the D band at about

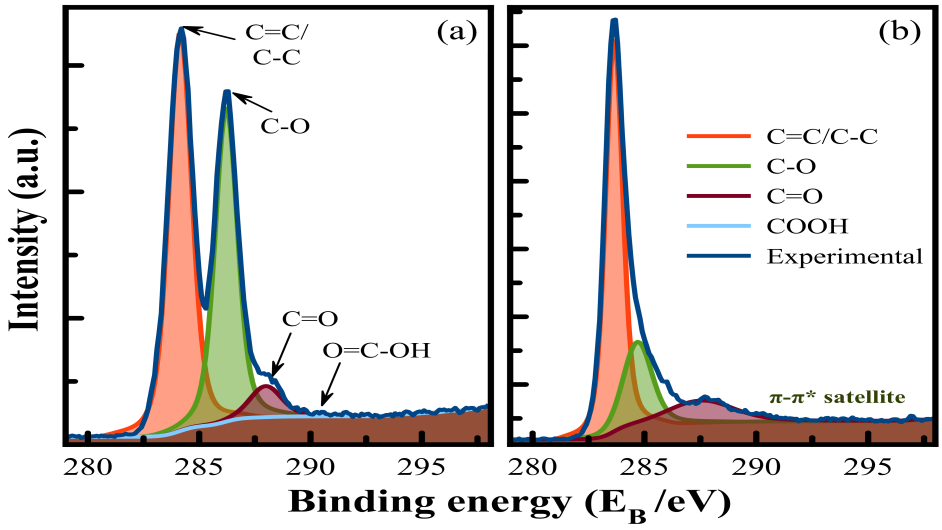

Figure 6.3: C1s XPS spectra of a) GO:MWCNT; b) rGO:MWCNT at 0.05wt.% MWCNT

1353cm^{-1} indicates the disorder induced vibrations of the C-C bond. Raman analysis shows considerable defects in the rGO:MWCNT films evidenced by the ratio I_D/I_G, whereas for non-reduced GO:MWCNT is 0.92 and for reduced I_D/I_G is 1.38. Treating the films with high concentrated acid such as Hydroiodic acid introduces some structural changes on the surface of the samples. These distortions are appearing as wrinkles due to the removal of the hydroxyl and epoxide functionalities from the GO as confirmed by XPS measurement [145-146, 179]. The SEM morphological structure is shown in Figure 6.5, which shows also

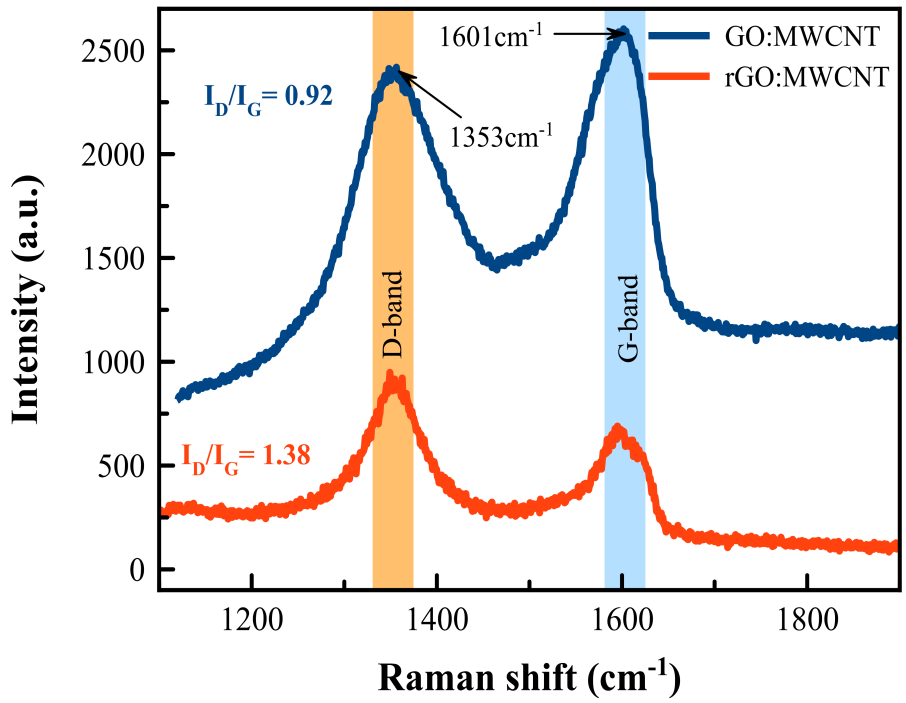

Figure 6.4: Raman spectra of GO:MWCNT before and after reduction at 0.05wt.% MWCNT

that the graphene layers are coated over the whole area with CNTs and this confirms the good dispersion quality of MWCNTs in GO aqueous colloids.

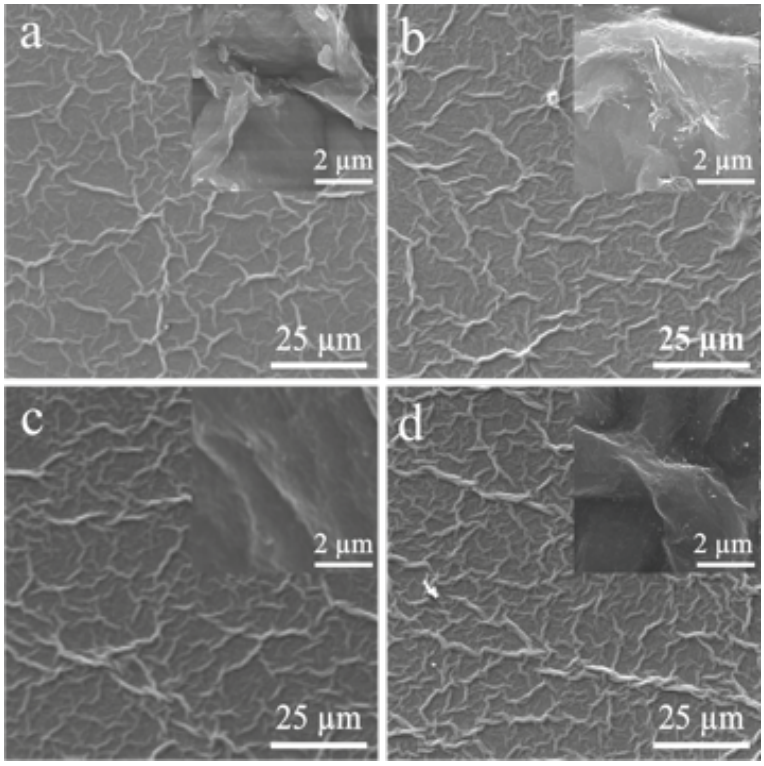

Figure 6.5: Morphology of films based on (a) 0.5wt.% rGO, (b) 0.01wt.% rGO:MWCNT, (c) 0.025wt.% rGO:MWCNT and (d) 0.05wt.% rGO:MWCNT

6.3 Charge Mobility in rGO:MWCNT Films

As described in section 6.2, before the chemical reduction the films have an insulating behavior due to the non-stoichiometric chemical composition of the host GO matrix and the presence of the oxidant in the GO that prevents the formation of percolation paths among the sp^2 carbon clusters. Therefore, the resistances of the films are greater than 1GΩ. Treating the films with reactant agent such as hydroiodic acid helps to remove the oxygen-functional groups from the GO layers as it is proved in the previous section, and thus improves the charge carrier transport within the nanocomposite. Therefore and after the chemical reduction, it is well observed that the electrical conductivity of the films increased with the amount of MWCNTs content (Figure 6.6). The increase in conductivity of films based on rGO:MWCNT hybrid nanomaterial is a result of the strong $\pi - \pi$ interfacial coupling between the MWCNT and the rGO, that promotes more mobile charge carrier delocalization between the electronic density of both [298]. Also, at higher CNT content, more conductive paths are participating in the conduction mechanism as well as the distance between the matrix/filler junctions decreases i.e. CNT/CNT, CNT/GO junctions. However, the films are not optically transparent. For the rGO, the films have an electrical conductivity of 4.8×10^2S/m. In case of rGO:MWCNT, the conductivities are 6.27×10^2S/m, 8.2×10^2S/m and 1.1×10^4S/m for 0.01wt.%, 0.025wt.% and 0.05wt.% MWCNTs, respectively. Beside

the improvement in the conductivity by the MWCNTs (Figure 6.6), the film reproducibility improved significantly.

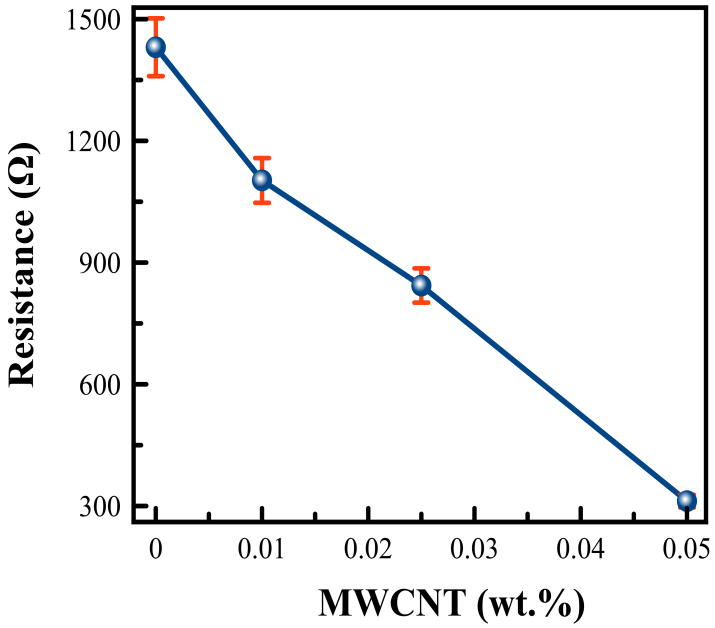

Figure 6.6: DC-ohmic resistance of the chemically reduced GO:MWCNT film as function of the MWCNT content

6.4 Tuning the Bandgap of the GO:MWCNT

The UV-Vis spectrum of the rGO:MWCNT films (Figure 6.7) shows two peaks at 970nm and 1200nm, which are attributed to the asymmetric stretch of $S(OH)_2$ bonds and its first overtone [299]. From Figure 6.7, it can be clearly seen that the absorbance increases with the amount of MWCNT content dissolved in GO. The absorption coefficient (α) at 600nm, a linear relationship between the absorbance and the MWCNT concentration is extracted, while the absorption coefficient is calculated to be approximately $8 L.g^{-1}.cm^{-1}$. Considering an indirect bandgap of 2.76eV for reduced graphene oxide, the optical bandgap of the hybrid nanocomposite is calculated from Tauc plot, as depicted in Figure 6.8. It can be seen that the increase of the MWCNTs content in the GO results in a linear decrease of bandgap due to the partial recovery of the π-conjugation system [298, 300-301], this leads to the improvement in the conductivity as it was shown in section 6.3. The bandgap decreases from 2.76eV, 2.74eV, 2.7eV to 2.63eV for 0wt.%, 0.01wt.%, 0.025wt.% and 0.05wt.% MWCNT, respectively.

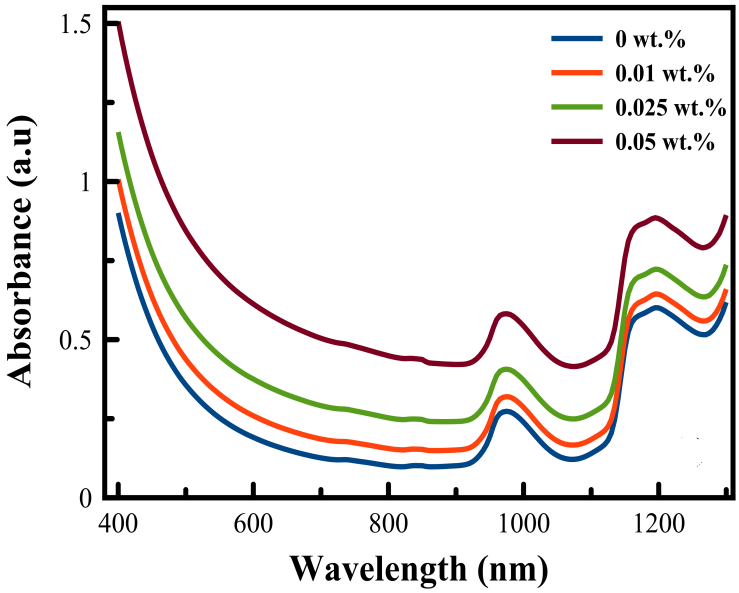

Figure 6.7: UV-Vis spectra of MWCNT dissolved in GO at different MWCNT content

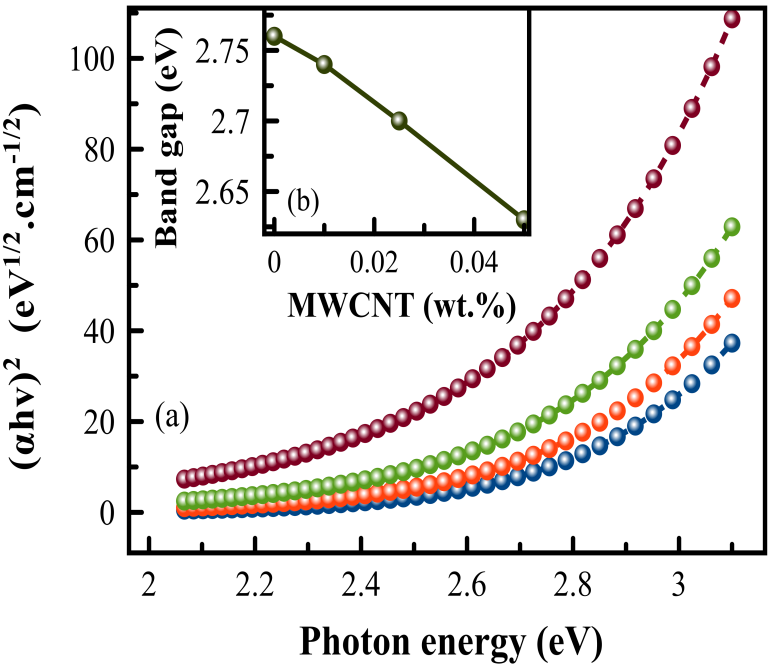

Figure 6.8: (a) Tauc plot of different MWCNT content dissolved in GO, (b) Optical bandgap energy of the rGO:MWCNT nanocomposite. Blue: 0.0wt.%, red: 0.01wt.%, green: 0.025wt.% and brown: 0.05wt.% MWCNT

6.5 Piezoresistive Response of the rGO:MWCNT Films

The piezoresistive performances of the rGO:MWCNT films are shown in Figure 6.9 as normalized change of resistance-strain relationships under an axial tension. The correlation coefficient (R_2) is ranging between 0.982-0.965 for 0.01wt.% and 0.05wt.% MWCNT content, respectively, which indicates a high linearity response of these films under strain. It can be also concluded from Figure 6.9 that the strain sensitivity of the films decreases with increasing the MWCNT content, with a gauge factor of 8.4 for 0.01wt.%, 1.1 for 0.025wt.% and 0.6 for 0.05wt.% MWCNTs. The positive piezoresistivity behavior of the rGO:MWCNT films is an accumulation of different aspects, that can be summarized in the following:

1. For rGO, an elongation of the bond length between the C atoms in the benzene ring that might occur [165, 302]. As the strain in this case is low, it is not sufficient to alter the C-C bonding, so this aspect is totally negligible.
2. Change in the rGO tunneling distance due to the change in GO interlayer sheet distances.
3. For the MWCNTs, the reorientation of the CNTs and the change in the tunneling distance between the adjacent CNTs.
4. The change in the number of tunneling contacts formed between the rGO and MWCNT within the conduction network significantly changes the total film resistance under strain.

The change of some or all of the previous aspects leads to the change of the films resistance when it is strained. Figure 6.10 represents a schematic of the piezoresistive behavior of the rGO:MWCNT films. The low strain sensitivity at high CNT content is referred to the dense network formed by the CNTs and the GO. So, when the films undergo strain, some of the conduction paths are altered due to the change in the tunneling distance. However, and as there are already many available paths, this alteration is small thus the change in the resistance is little, which causes a low strain sensitivity.

6.6 Resistance Dependency on Temperature Influence

Here, the resistance-temperature response of the rGO:MWCNT films are investigated from 10°C to 80°C. For comparison reason, the relative resistivity (R/R_0) at 10°C is plotted as function of the temperature. From Figure 6.11, the resistivity decreases linearly as the temperature increases, accordingly the resistance of rGO decreases from 1.53kΩ to 91.8Ω at 10°C to 80°C, respectively. The rGO:MWCNT films show less sensitivity to temperature than the rGO film, and the sensitivity decreases by increasing the CNT content in the nanocomposite. The resistance of the films with 0.01wt.%, 0.025wt.% and 0.05wt.% MWCNT at 10°C are 1.2kΩ, 1kΩ and 914Ω and it decreases to 282Ω, 770Ω and 823Ω at 80°C. Tunneling is the dominant transport conduction in the hybrid rGO:MWCNT films. With increasing temperature more electrons get enough kinetic energy to overcome the CNT/CNT, CNT/GO and/or GO/GO barrier junction, thus resulting in an increase in the electrical conductivity. Increasing the CNT content in the hybrid nanocomposite introduces more conduction paths in the system and thus shrink the CNTs and GO sheets (section 6.5), increasing the temperature only few paths are activated and participate effectively in

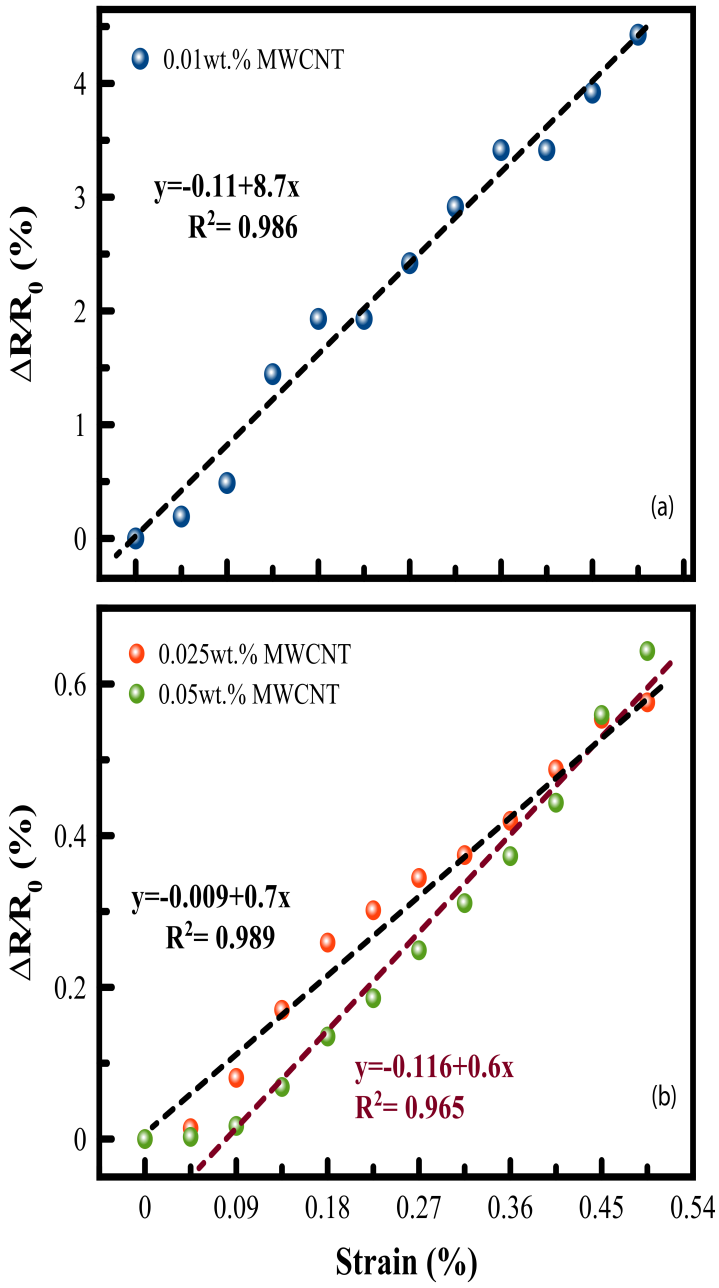

Figure 6.9: Resistance-strain relationship of rGO:MWCNT films under applied force (a) 0.01wt.% MWCNT, (b) 0.025wt.% MWCNT and 0.05wt.% MWCNT

the conduction mechanism, therefore the temperature sensitivity is altered and reduces at high CNT content. Generally, films based on rGO show excellent temperature sensitivity and high stability, especially for high CNT content, i.e. 0.05wt.% MWCNT. The heating and cooling cycles of the rGO:MWCNT at 0wt.%, 0.01wt.%, 0.025wt.% and 0.05wt.% is depicted in Figure 6.12. It can be observed that the initial and the final resistivity at 10°C is slightly different (electrical offset). The change in the resistance under temperature at the first cycle for rGO and 0.01wt.% MWCNT film is 106% and 76.5%, respectively, and it drops to 23% and 8.5% for 0.025wt.% and 0.05wt.% MWCNT, respectively. During the cooling cycles and at 10°C resistance, a small decreases in the resistivity (i.e. increase

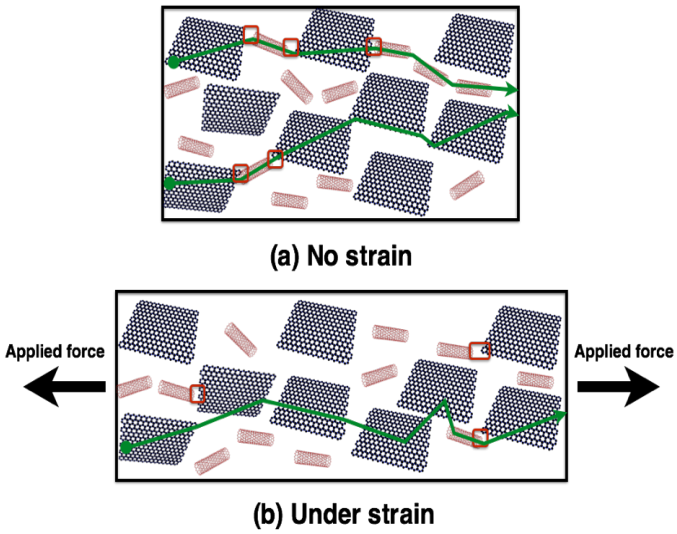

Figure 6.10: Piezoresistive effect in rGO:MWCNT films (a) no strain, (b) under strain (red: tunneling contacts between the rGO and MWCNT, green: conduction path)

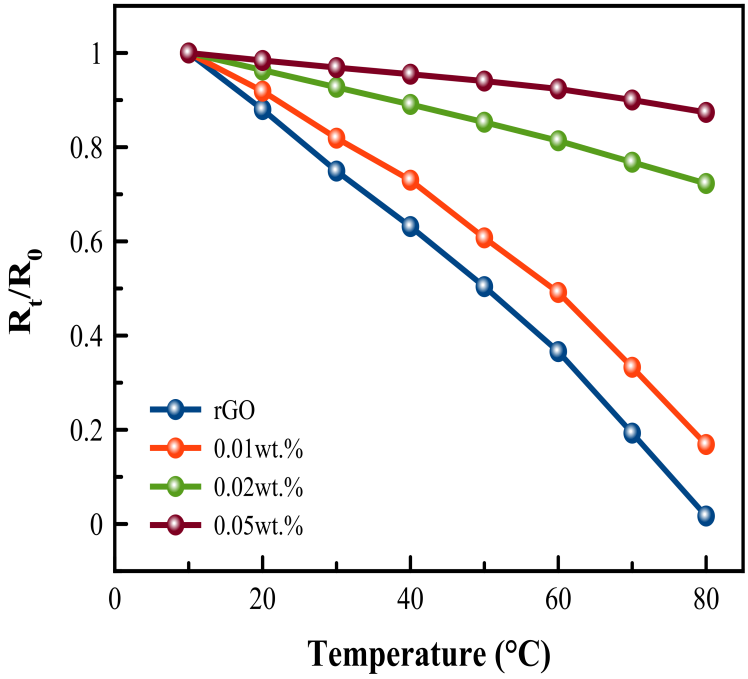

Figure 6.11: Relative resistivity-temperature behavior of rGO and rGO:MWCNT films

in the conductivity) is always observed, which can be referred to the re-agglomeration of the CNTs [303]. Additionally, the cycling test of the rGO and the rGO:MWCNT films have reproducible behavior within four repeated temperature cycles. Figure 6.12 reveals a hysteresis as the heating and cooling cycles do not follow the same trend. The change in the electrical resistivity during the heating-cooling cycle is not completely reversible, which may be due to the change in conducting paths network occurring during the heating cycle, but not completely recoverable during the cooling [303]. Table 6.1 shows that the hysteresis decreases for more cycles. During heating and cooling cycles, new formation and breakdown

of conductive paths is taking place, as the number of these cycles increases this process become less prominent and thus decreases the hysteresis. The hybrid nanocomposites show a negative temperature effect, this change with temperature is a typical behavior observed in disordered semiconductors with negative temperature coefficient, as it was stated previously in section 5.6.

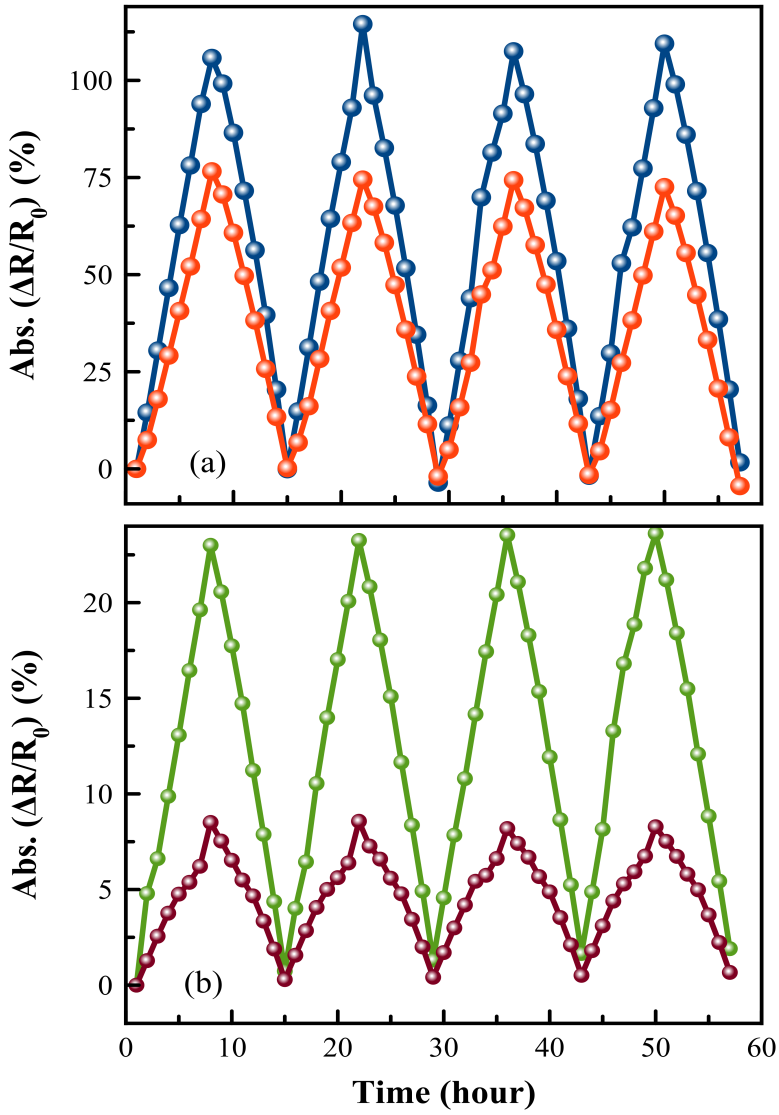

Figure 6.12: Temperature cycling tests of rGO:MWCNT films at 0.0wt.% (blue line) and 0.01wt.% (red line), 0.025wt.% (green line) and 0.05wt.% MWCNT content (brown line)

Table 6.1: Temperature hysteresis of rGO:MWCNT films

MWCNT Content (wt.%)	Hysteresis to temperature (%)			
	1^{st} cycle	2^{nd} cycle	3^{rd} cycle	4^{th} cycle
0.0	9.5	9.0	5.7	2.9
0.01	14.2	9.8	8.3	5.6
0.025	6.9	5.3	5.3	4.9
0.05	9.8	7.6	7.1	5.7

The temperature coefficient of resistance (TCR) is a characteristic parameter and it is given by;

$$TCR = \frac{\Delta R/R_0}{\Delta T} \tag{6.1}$$

where R_0 is the initial resistance at T =10°C (283.15K), ΔR is the change of the resistance, and ΔT is the change in the temperature.

Thus, TCR is 14.04 $\times 10^{-3}$, 11.87$\times 10^{-3}$, 3.95$\times 10^{-3}$ and 1.80$\times 10^{-3}$ K^{-1} for rGO, 0.01wt.%, 0.02wt.% and 0.05wt.% MWCNT, respectively. This calculated TCR for the rGO and its derivative nanocomposite is 20 orders higher than the reported carbon nanotube (7$\times 10^{-4}$ K^{-1}) [304] and 3.5 orders larger than the standard commercial platinum temperature sensors (39.2 $\times 10^{-4}$ K^{-1}) [305]. The logarithmic resistance temperature dependency of the rGO and rGO:MWCNT films is depicted in Figure 6.13. The behavior shown is for typical intermediate microstructure, which is a mixture of both highly ordered and disordered materials [306]. As the temperature decreases, a transition from activated to variable-range hopping (VRH) (equation 6.2) conduction is noticeable, this mixing transport behavior is attributed to the variation in the degrees of heterogeneity of the rGO:MWCNT microstructure. It is seen from Figure 6.13 that, two slopes at specific temperature regions, one at the lower temperature range (10°C– 45°C) and the other at higher temperature range (45°C– 80°C) which indicates that two activation energies are involved. The temperature at which the transition from drift to hopping transport occurs is called the hopping temperature (T_{hop}), which is occurring at the intersection between the Arrhenius and VRH fitting curves. The rGO:MWCNT hybrid nanocomposite is viewed as a 2D-VRH system. At high temperature, the Mott's model (equation 6.3) is used to describe the linear temperature dependency.

$$R(t) = R_0 exp(\frac{T_0}{T})^m \tag{6.2}$$

where T_0 is the characteristic temperature, T is the actual temperature and m is constant whereas: m= 1/3 for 2D-VRH system.

Table 6.2: Temperature coefficient of resistance of rGO:MWCNT films

MWCNT Content (wt.%)	TCR ($\times 10^{-3}$ K^{-1})
0.0	14.04
0.01	11.87
0.025	3.95
0.05	1.80

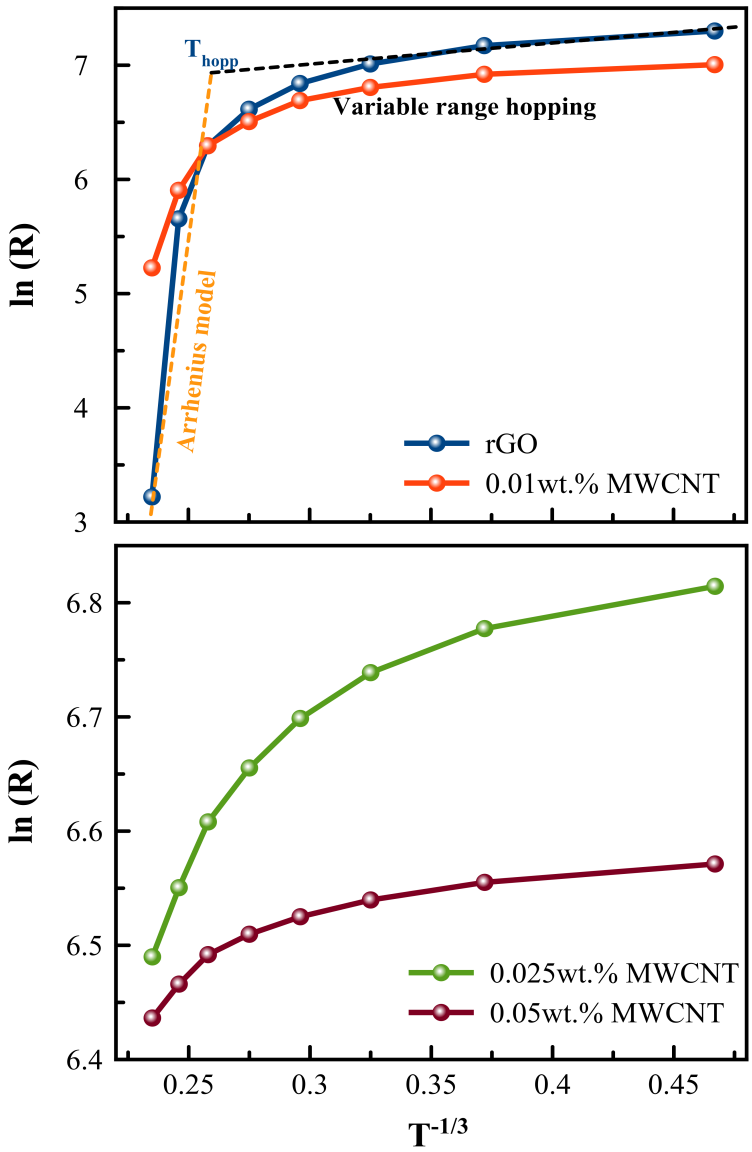

Figure 6.13: Plot of the logarithmic of resistance versus the reciprocal of temperature (1/T) for rGO:MWCNT at 0.0wt.% and 0.01wt.%, 0.025wt.% and 0.05wt.% MWCNT content

To describe the band conduction mechanism, the Arrhenius conduction activation model is commonly used:

$$R(t) = R_0 exp(\frac{E_g}{k_b T}) \tag{6.3}$$

where R_0 is the initial resistance, E_g is the activation energy, T is the actual temperature and k_b in the Boltzmann constant.

It is also noticed that the Arrhenius-like mode is not clearly observed for films with MWCNTs within the studied temperature range. It tends to shift to lower temperature while increasing the MWCNT content.

6.7 Influence of humidity on rGO:MWCNT Film Resistance

In section 5.7, it is shown that increasing the working temperature reduces the humidity effect, the change in the electrical resistance of rGO and rGO:MWCNT films as a function of RH from 10-95%RH at 50°C is shown in Figure 6.14. For RH<60% the resistance increases linearly, this increment is less than 2% for all the rGO:MWCNT films and about 3.1% for rGO film. Beyond RH>60%, the rGO and rGO:MWCNT film resistances start to increase dramatically and nonlinearly. The maximum change in the resistance is 15% for rGO film, and it decreases as the CNT content increases. Partially, an appearance of an uptake peak can be seen only for rGO and at low MWCNT content i.e. 0.01wt.%. The repeatability characteristics is measured for four cycles in the range of 10-70% RH, as it is depicted in Figure 6.15. The film characteristics under humid environment exhibit a good response-recovery behavior and excellent repeatability within the measured range. The repeatable error is determined as the ratio between the measurement at 10% RH of the first cycle and the fourth cycle. It is found to be 0.8%, 2.75%, 0.8% and 1.5% for 0wt.%, 0.01wt.%, 0.025wt.% and 0.05wt.% MWCNT, respectively. Although, the rGO:MWCNT films exhibit low sensitivity to humidity compared to the MWCNT:SDBS/PEDOT:PSS films and also to the films based GO, a good repeatability of the films is noticed caused by the multilayer structure of the rGO, that facilitates the release of water molecules from the GO interlayer for reaching dynamic equilibrium between the external humidity level and the internal water content [307]. While the rGO and rGO:MWCNT show an adequate response to the humidity, this hydrophilic property is mainly due to the presence of some epoxy and carboxyl functional groups at the edges of the GO platelets and therefore it is investigated to possibly used as humidity sensor [308-309]. As confirmed in section 6.2, the chemical reduction of the GO removes partially the functional groups from it but still some of the functional groups remain attached to the GO basal and edges. Due to its two-dimensional structure, the rGO films have high surface-to-volume ratio and hence a large density of surface vacancies. This gives rGO the ability to adsorb the water molecules from the outer environment. Independent on the reduction method, chemical [145], thermal [309-310], micromechanical cleaving of graphite [311], rGO film exhibits p-type semiconducting behavior; therefore, the positive charge carriers (holes) dominate the electronic transport of the film. For the rGO films, two mechanisms take place simultaneously under humid environment:

1. Adsorption of the water molecules on the surface of the rGO, therefore it behaves as electron donor, and increases the protonation [307, 309, 312].

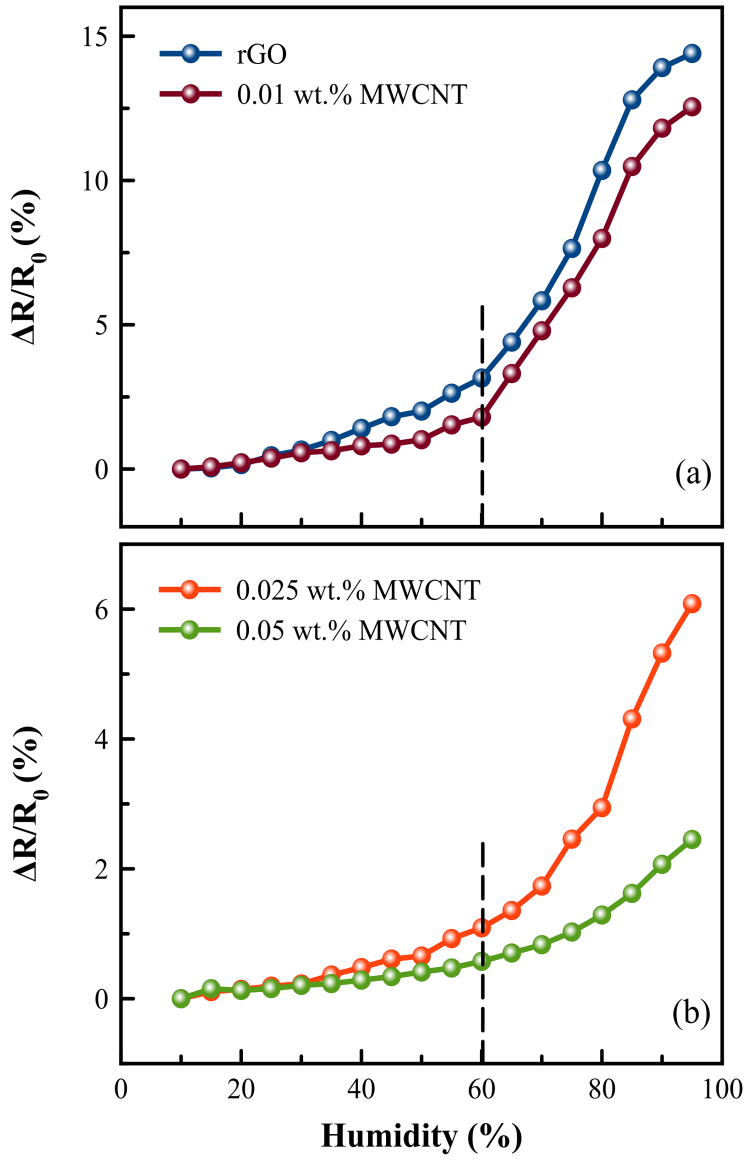

Figure 6.14: Humidity dependence of film resistance of (a) rGO and rGO:MWCNT (0.01wt.%), (b) rGO:MWCNT (0.025, and 0.05wt.%)

2. Swelling effect that leads to the absorption of the water molecules between the interlayer of the rGO.

At low RH, the adsorption of H_2O on the few remaining oxygen-functional groups in the basal plane and edges of the rGO dominates and thus it reduces the hole concentration of the p-type rGO films (Figure 6.16). Consequently, the film resistance increases slowly, so two different conduction mechanisms are working against each other. As the RH increases, the H_2O molecules penetrate deeper into GO multi-layer film and lead to an interlayer swelling effect [307]. The swelling effect increases the interlayer distance and therefore increases the film resistance dramatically [313]. At high RH, it is possible that the ionization of the adsorbed water molecule produces hydronium ions (H_3O) as charge carriers, thus the proton-hopping mechanism leads to an ionic conductivity [314], consequently the film resistance decreases. However, it is clearly observed that at high RH the swelling effect

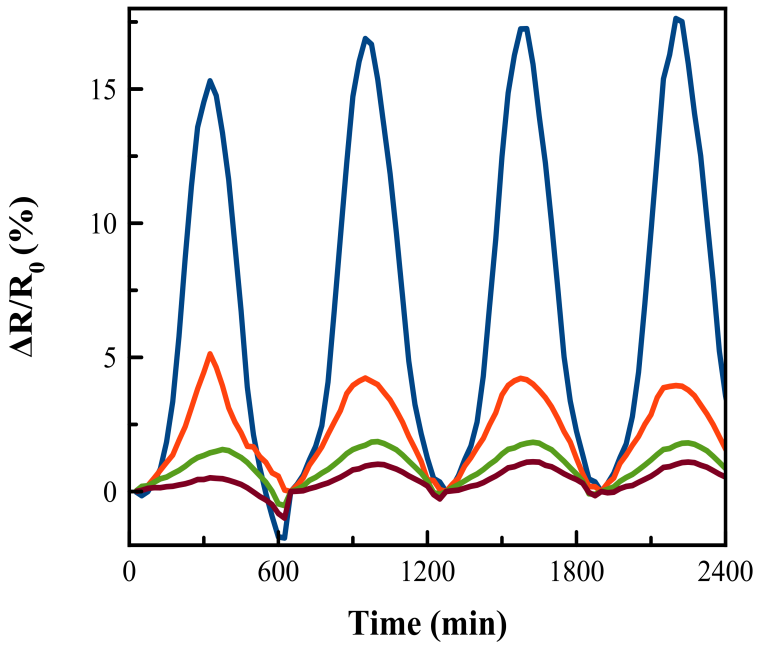

Figure 6.15: Cycling test of the films based rGO:MWCNT at 0.0wt.% MWCNT (blue line) and 0.01wt.% MWCNT (red line), 0.025wt.% (green line) and 0.05wt.% MWCNT (brown line)

dominates the conduction mechanism of the rGO film. For the rGO:MWCNT films and as it is concluded from the SEM images in Figure 6.5, the MWCNTs fill partially the gaps between the GO layers 'good coating' and thus at low RH%, no big change in the film resistance is remarked, as the main mechanism in this range is the interaction between the H_2O and the rGO surface. However, at high RH%, the sensitivity to humidity decreases compared to the pristine rGO film, because of the reduced in the swelling effect. The sensitivity to humidity (S_h) is calculated using Eq. 5.4, and the results are summarized in Table 6.3.

Table 6.3: Sensitivity of rGO:MWCNT films as a function of humidity at different MWCNT content

MWCNT Content (wt.%)	Sensitivity to Humidity $(1/\%RH)$	
	$RH < 60\%$	$RH > 60\%$
0.0	0.062	0.362
0.01	0.035	0.321
0.025	0.021	0.142
0.05	0.0112	0.053

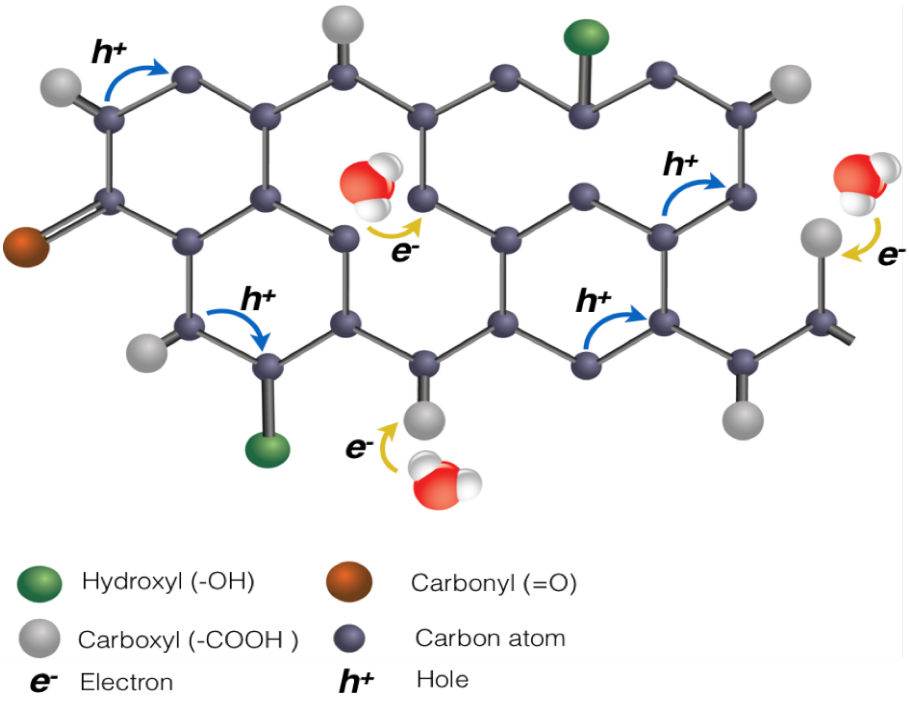

Figure 6.16: Transport mechanism of rGO films under humidity environment

7 Synergetic Properties of Novel Tertiary Nanocomposite

From previous chapter, it was highlighted that the nanocomposite with 0.01wt.% and 0.05wt.% MWCNT show promising strain and temperature characteristics. However, 0.01wt.% MWCNT has a high strain sensing property but low conductivity, which is not suitable to be used as sensing layer in the wireless application. To improve its conductivity, this nanocomposite is mixed with different volume ratio with the high intrinsic conductive polymer PEDOT:PSS, to make them more suitable for wireless sensing. In this context, totally a new tertiary nanocomposite is developed and investigated. Hence, in this section, films based on PEDOT:PSS, GO and MWCNTs are analytically explored. The preparation method is explained in section 4.1.3. The wettability properties in terms of contact angle and surface tension are studied. As one of the three used components is GO, the reduction process is necessary to improve the electrical properties of the novel nanocomposites. Electrical, mechanical and thermal behavior are systematically studied before and after the chemical reduction. Afterwards, the results of each technique are analyzed and the feasibility of the films as strain sensor and temperature sensors are discussed.

7.1 Chemico-Physical Characterization

All the GO:MWCNT/PEDOT:PSS nanocomposites demonstrate a good hydrophilic properties with contact angle between 64.85° and 69.06° for 1:1 and 1:3 mixing volume ratio (vol.), respectively (Figure 7.1), which is less than of the pristine PEDOT:PSS (78°). Increasing the polymer ratio within the nanocomposite increases the hydrophobicity. For the surface tension, the increase in the PEDOT:PSS ratio increases slightly its surface tension value by around 1mN/m from 67.5mN/m to 68.3mN/m for 1:1 and 1:3 volume ratio, respectively.

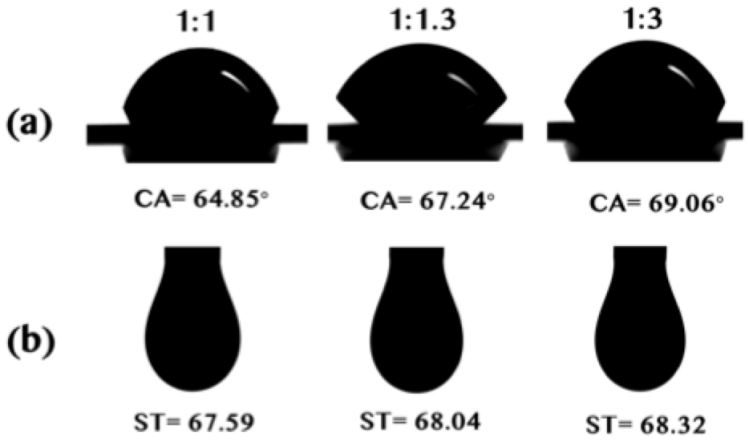

Figure 7.1: Chemico-physical properties of GO:MWCNT/PEDOT:PSS aqueous dispersion with different mixing ratio (a) Contact angle, (b) Surface tension

7.2 Electron Mobility of the Tertiary Hybrid Nanocomposite

The I-V characteristics of the GO:MWCNT/PEDOT:PSS based films are studied by applying a voltage of ±5V. Increasing the mixing ratio with the PEDOT:PSS, lowers the resistance of the GO:MWCNT/PEDOT:PSS nanocomposites, as it is shown in Figure 7.2. For the randomly oriented GO:MWCNT/PEDOT:PSS films, the DC-resistances are 32.71±0.81kΩ, 62.31±0.99kΩ, 56.36±2.02kΩ and 24.96±1.92kΩ at mixing ratio of 0:1, 1:1, 1:1.3 and 1:3, respectively. The resistance values are shown in Table 7.1. The increment in the resistance after adding the GO:MWCNT is due to the insulating properties of the GO as stated in section 6.2. This means that the conduction occurs mainly through the PEDOT segments in the PSS chains, which is acting as the host matrix material. After the chemical reduction, the conductivity increases dramatically for all the films. For the reduced PEDOT:PSS films, the conductivity increases radically from 0.11S/m to 6.57×10^5S/m. Whereas for the reduced GO:MWCNT/PEDOT:PSS films, small increase is remarked at different mixing ratio, the conductivity is 2.91×10^5, 3.25×10^5 and 5.50×10^5S/m at mixing ratio of 1:1, 1:1.3 and 1:3, respectively. Although, the chemical reduction improved the conductivity of the GO:MWCNT/PEDOT:PSS films, but still the conductivity of the reduced PEDOT:PSS is the highest. Therefore, it can be concluded that the conductivity through the PEDOT:PSS chain is dominating the transport mechanism in the films based tertiary hybrid nanocomposite before and after chemical reduction.

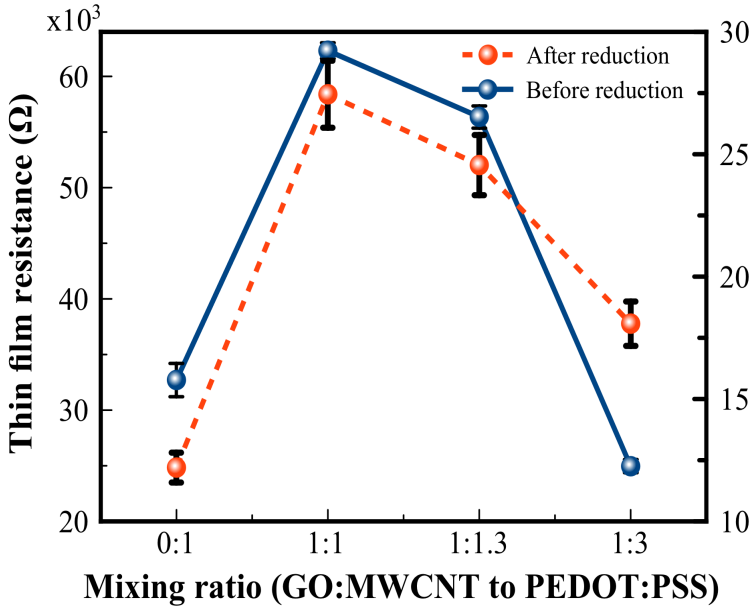

Figure 7.2: DC-electrical resistance of the films based GO:MWCNT/PEDOT:PSS before and after reduction

To ensure the film homogeneity, the sheet resistance of nanocomposites are measured at three different lines (as explained in section 4.3.5) and the values are shown in Table 7.2. The sheet resistance of the reduced GO:MWCNT/PEDOT:PSS nanocomposite is about 2000 orders lower than those of the non-reduced GO:MWCNT/PEDOT:PSS. For instance, the average sheet resistance of the PEDOT:PSS films reduces from 32.71±0.81kΩ.sq^{-1} to

Table 7.1: Resistance of the GO:MWCNT/PEDOT:PSS films

GO:MWCNT:PEDOT:PSS (vol.)	DC-Resistance (Ω)	
	Before reduction	After reduction
1:1	64.84×10^3	27.69
1:1.3	56.69×10^3	23.39
1:3	26.13×10^3	18.20
PEDOT:PSS	33.61×10^3	12.24

Table 7.2: Sheet resistance of GO:MWCNT/PEDOT:PSS films

Mixing ratio (vol.)	Sheet resistance ($\Omega.sq^{-1}$)	
	Before reduction ($\times10^3$)	After reduction
1:1	64.84	27.69
	61.12	27.3
	60.98	27.37
1:1.3	56.69	23.39
	58.21	22.9
	54.19	23.1
1:3	26.13	18.20
	25.65	17.96
	23.10	18.01
PEDOT:PSS	33.61	12.24
	31.97	11.97
	32.55	12.32

$12.17\pm0.18\Omega.sq^{-1}$.

The electronic transport in the GO:MWCNT/PEDOT:PSS films before and after reduction can be explained as follow:

1. Before chemical treatment and as the GO:MWCNT is added to the PEDOT:PSS, which has an insulation properties as shown in section 6.2, the electrons are trapped within GO:MWCNT and are not participating in the electrical conduction, thus the conduction through the PEDOT:PSS i.e. the hopping between conjugated parts of PEDOT segments and its neighboring chains is dominating the conduction mechanism, as it is shown from the electrical characterization in Figure 7.2 and as explained in section 5.4. At 1:3 mixing ratio, the conductivity become more that the pristine PEDOT:PSS, this is attributed to some free suspended CNTs in the GO:MWCNT supension, that are getting attached to the PEDOT:PSS, which forms extra conductive paths, that participate significantly in the conduction and consequently improves the conductivity.
2. Treating the films with hydriodic acid improves the conductivity dramatically, effect of the chemical reduction of the GO:MWCNT is shown in section 6.2. Beside that XPS measurement is conducted on specimen with PEDOT:PSS (Figure 7.3) and by combining the previous knowledge (section 6.2), the nature of the conduction transport for this type of hybrid nanocomposite can be clearly understood.

In section 5.3, it was shown that increasing in conductivity of the PEDOT:PSS nanocomposites leads to the appearance of the new states between the valence and conduction bands due to the formation of polarons and bipolarons. These charge carriers move freely through

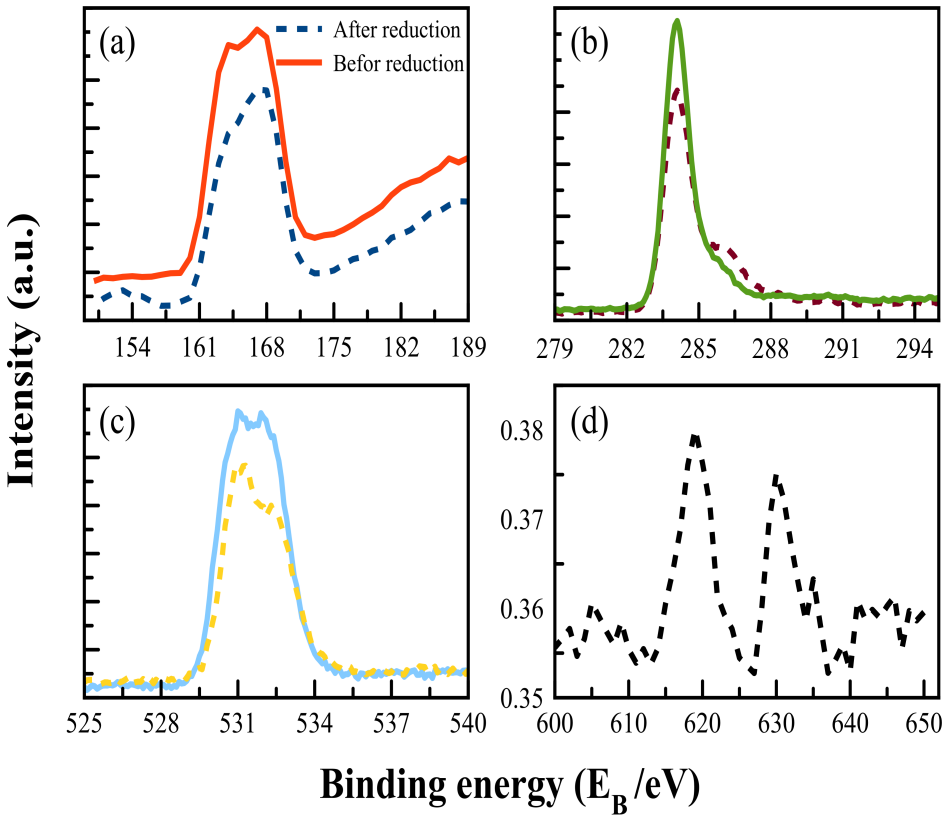

Figure 7.3: XPS spectrum of PEDOT:PSS before (continues line) and after (dashed line) HI treatment: (a) S2p, (b)C1s, (c) O1s and (d) low intensity HI peaks after post cleaning

the material, thus improves the conductivity. Treating the PEDOT:POSS films with HI agent leads to the increase in both the polarons and the uncoupled bipolarons transition. XPS measurements indicate the appearance of three peaks at 168eV, 284eV and 532eV as indicated in Figure 7.3. In Figure 7.3 (a), before reduction two XPS bands are appearing at binding energy between 164eV and 167eV, these peaks are referred to the sulfur atoms in PSS, unlikely in [313], these peaks appear at 166eV and 172eV. After treating the films with HI-acid, a damping in the S2p peaks appears, this is because a fraction of the PSS is removed from the PEDOT:PSS films during the HI treatment. The removal of the PSS from the PEDOT:PSS after the chemical treatment introduces some morphological (structural) distortion and it might also alter its crystallity as confirmed in [314]. Consequently, the interchain interaction among the PEDOT chains arises due to the conformational changes of the PEDOT chains, which change from a coil to linear or expanded-coil structure, thus the benzoid resonant structure of the PEDOT chain transforms to a quinoid structure [313]. In the C1s spectrum in Figure 7.3 (b), the appearance of two peaks at 284eV represents C-C bonds and C-O at 286eV. The HI treatment removes the C-O and thus leads to the restoration of some C-C bonds. As revealed in [313], Hydroiodic acid is represented with strong peaks at 630eV and 619eV. From Figure 7.3 (d), it is noticed the very low intensity of these peaks, which is an indication that all the acid residues are removed by the post cleaning steps mentioned in section 4.2.3. Beside the conductivity improvement, the chemical acid treatment alters the film thickness [86, 276], it is noticed that the thickness of films after the acid post-treatment decreases from 30 to 15nm, without affecting the film optical

transmittance. It is expected that the carrier concentration is higher in the pure PEDOT:PSS than the GO:MWCNT/PEDOT:PSS. As it is discussed in section 6.2, after the chemical reduction, the oxygen-functional groups of the GO are partially removed as well as the partial recovery of the lattice defects (π-system), this leads to the improvement of the electron transport in the GO:MWCNT. Consequently, an enhancement in the interfacial coupling between the MWCNT, rGO and the quinoid structure of the PEDOT occurs, which promoting more mobile charge carrier delocalization between the electronic density of this particles.

7.3 Piezoresistive Response of the Nanocomposite Films

The change in the electrical resistance of the films under mechanical uni-axial force is investigated to understand the piezoresistive response of the tertiary hybrid nanocomposite. Figure 7.4 depicts the change in the electrical resistance as a function of the strain (ϵ). For the non-reduced GO:MWCNT/PEDOT:PSS films, the piezoresistive behavior is the same behavior for the PEDOT:PSS based films i.e. a negative piezoresistive, this is referred to the dominating conduction current is passing through the PEDOT:PSS segments as explained in section 7.2. Increasing the amount of the PEDOT:PSS in the nanocomposite leads to reduce the linearity (R^2 correlation factor decreases) and alters the strain sensitivity. The gauge factors for GO:MWCNT/PEDOT:PSS films are 2.2, 1.4 and 1.39 for 1:1, 1:1.3 and 1:3 mixing volume, respectively. The characteristics of the reduced GO:MWCNT/PEDOT:PSS films under strain is shown in Figure 7.5. Unlike the non-reduced films, the chemically treated films show a positive piezoresistive behavior and two regions are clearly identified. The low sensitive region (region I), which is the region located below 0.55% strain (critical strain point) and the high strain sensitive region (region II), which is located at strain above 0.55%. The mixing volume of 1:1.3 gives the highest sensitivity in both regions compared to the other mixing volumes, with gauge factor of 11 and 97 in region I and region II, respectively. This is mixing volume is referred as the optimal maxing ratio between the GO:MWCNT and PEDOT:PSS. Nanocomposites with mixing volume of 1:1 and 1:3 show almost no strain sensitivity below the critical strain point and an adequate strain sensitivity above that. Table 7.3 summarizes the gauge factors of the films before and after reduction.

Table 7.3: Strain sensitivity of GO:MWCNT/PEDOT:PSS tertiary hybrid nanocomposite (I is strain region below 0.55% and II is strain region above 0.55%)

	Strain Sensitivity							
	PEDOT:PSS		1:1		1:1.3		1:3	
After reduction	I	II	I	II	I	II	I	II
	0.03	5.09	0.04	3.98	10.96	97	0.06	4.6

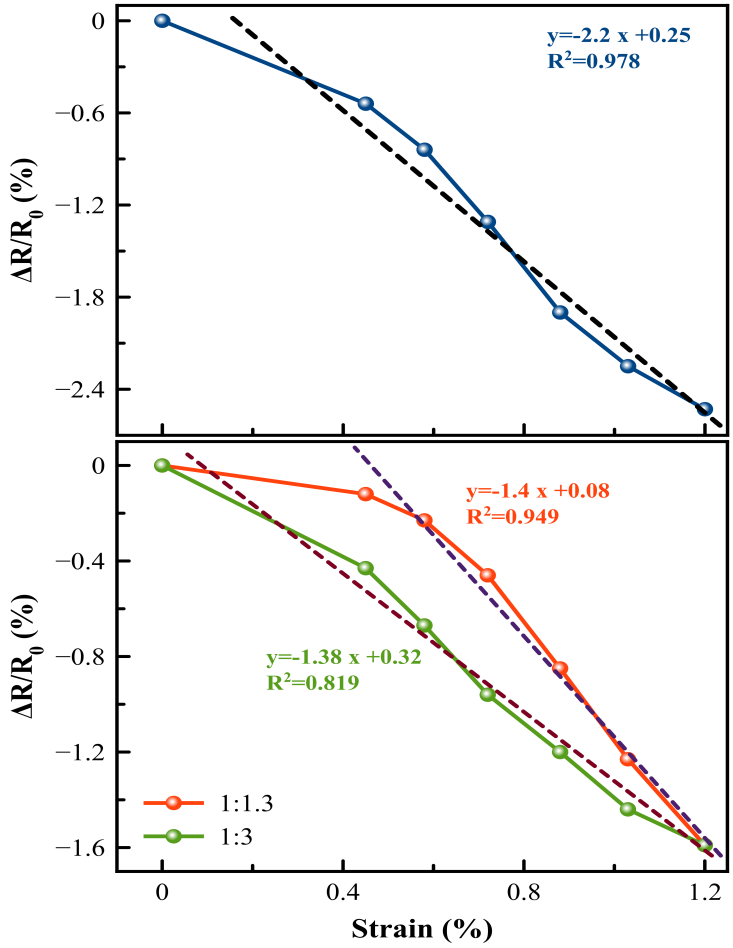

Figure 7.4: The piezoresistive behavior of non-reduced films based GO:MWCNT/ PEDOT:PSS (GO:MWCNT/PEDOT:PSS at different mixing ratio, blue: 1:1, red: 1:1.3 and green: 1:3)

The piezoresistivity of the reduced nanocomposite can be understood in the context of the percolation threshold. In this tertiary nanocomposites, each of PEDOT:PSS, MWCNTs and GO is forming a conduction path either individually or as combination with others. Therefore, the formed random network from this nanocomposite has a high conductivity and lies in the saturation region of the percolation threshold (Figure 3.17). For this reason, if a small force is applied, a small change in the tunneling and hopping distances between the nanoparticles (PEDOT, MWCNTs and GO) does not really affect the piezoresistivity of the nanocomposite, because sufficient paths for the currents to pass through are still available, so the strain sensitivity is negligible. As the strain increases, more paths are affected and thus more changes in the tunneling and hopping distances are introduced leading to an increase of the strain sensitivity. After the chemical treatment, most of the PSS is removed from the PEDOT:PSS, as it is shown in section 7.2. The high sensitivity is referred to a superposition of the individual piezoresistivity of each nanofiller, which is summarized in the following:

1. reduced PEDOT:PSS: alignment of the PEDOT segments along the applied force direction, which tend to increase the hopping distances between these segments and thus increases in the film resistance.
2. rGO: the change in the tunneling distances between the GO nanoplatelets.

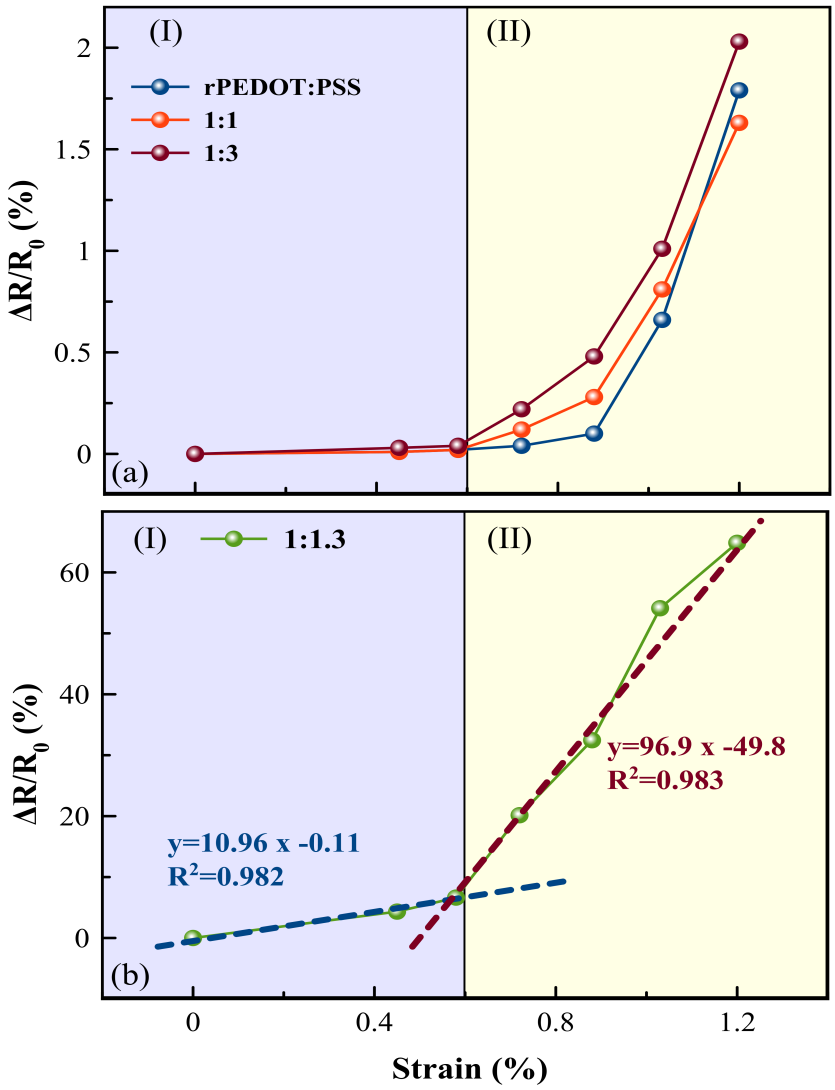

Figure 7.5: DC-electrical resistance of the reduced films based MWCNT:GO/ PEDOT:PSS under strain (a) PEDOT:PSS, 1:1 and 1:3 mixing ratio (b) 1:1.3 mixing ratio

3. MWCNTs: the reorientation and the change in the tunneling distances between the adjacent CNTs.
4. Change in the number of contacts formed between the PEDOT:PSS, GO and MWCNT within the network.

7.4 Temperature Sensitivity of the Tertiary Hybrid Nanocomposite

The resistance-temperature dependency response of the films based on GO:MWCNT/ PEDOT:PSS is shown in Figure 7.6, and the temperature is varied from 10°C to 80°C. It reveals that, the electrical resistivity decreases with an increase in the temperature and this trend is independent on the mixing ratio. The resistance of the non-reduced GO:MWCNT/PEDOT:PSS

Table 7.4: Hysteresis of the GO:MWCNT/ PEDOT:PSS tertiary hybrid nanocomposite under temperature cycling

Mixing Ratio (vol.)	Temperature hysteresis (%)	
	$1^{st} Cycle$	$5^{th} Cycle$
1:1	17.68	6.75
1:1.3	29.81	23.39
1:3	34.17	26.62

films decreases nonlinearly as the temperature increases, thus the resistance of the pristine PEDOT:PSS decreases from 50kΩ to 16.5kΩ at 10°C to 80°C, respectively. It is clearly seen that, the pristine PEDOT:PSS has the highest temperature change and it tends to decrease when it is mixed with GO:MWCNT. This is referred to the insulation properties of the GO:MWCNT (as shown in section 6.2), which reduce the hopping effect dominating the conduction mechanism in the PEDOT:PSS based films in this temperature range. The increase in the conductivity of the PEDOT:PSS under temperature is due to the thermal activation of the hole-polaron carrier in the PEDOT:PSS. The PEDOT:PSS is a 3D-VRH system therefore, the charge carrier under temperature is mainly due to the charging-energy limited tunneling (CELT), which is controlled by the tunneling effect between the conductive PEDOT segments separated by the PSS insulating grains [100, 315]. The cycling tests gives a good

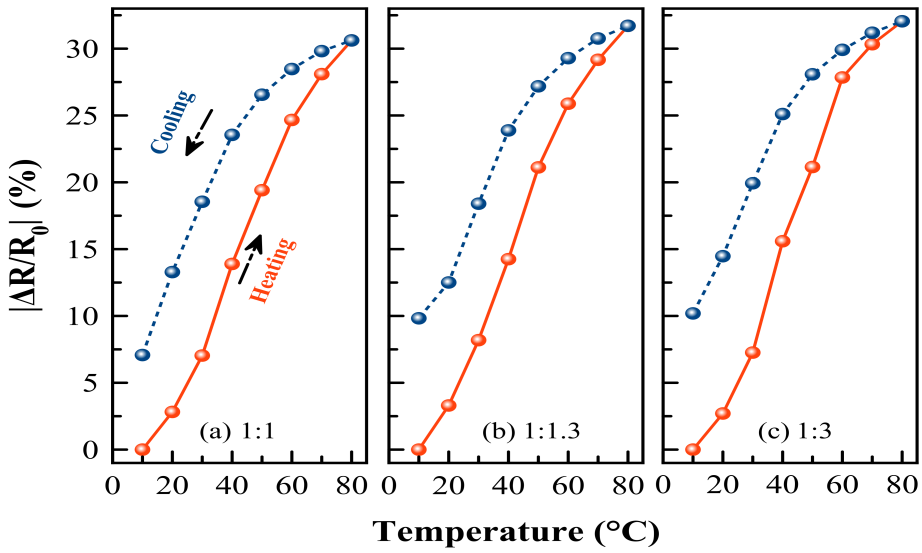

Figure 7.6: Temperature-resistance dependency of non-reduced GO:MWCNT/ PEDOT:PSS films at different PEDOT:PSS mixing ratio

reproducibility of the measurement, especially for mixing ratio of 1:1. It is observed that the hysteresis is higher in the first cycle than in the fifth cycle and the Table 7.4 shows the hysteresis values for the first and fifth cycles under temperature environment. It can be also concluded from the cycling tests that, the resistance-temperature dependency during the heating-cooling cycle is not totally reversible, which is attributed to some changes in conducting networks, this change in the conducting network takes place mainly during the heating cycle, but they are not completely recoverable during the cooling cycle [301]. The chemical treatments of the hybrid nanocomposite reduced the effect of the temperature

as it can be seen from Figure 7.7. However for rGO:MWCNT/PEDOT:PSS, the change in the resistivity under temperature has a positive temperature coefficient, i.e. increase the temperature increases the resistance. The mixing ratio of 1:3 has the lowest change in resistance. In order to understand this behavior, more investigations should be carried out. As discussed in section 5.6, the nature of the conduction mechanism can be extracted by

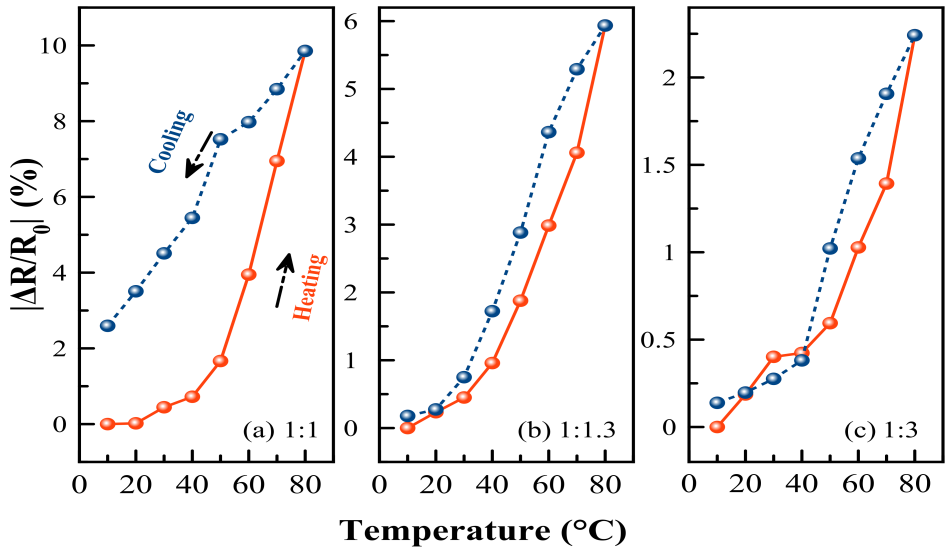

Figure 7.7: Temperature-resistance dependency of reduced films based (a) rPEDOT:PSS, (b) and (c) rGO:MWCNT/ PEDOT:PSS with different mixing ratio

fitting the conductivity to the general Mott's model; this model is typically used to describe the hopping mechanism:

$$\sigma = \sigma_o \times exp^{(\frac{-T_0}{T})^{\frac{1}{S}}} \quad (7.1)$$

where, σ_o is the characteristic conductance at characteristic temperature T_0, S an exponent related to the transport process.

The Figure 7.8 depicts a graph fitting of the nanocomposite of log conductivity versus $T^{-1/4}$. The results indicate nearly one activation energy for the hopping process for all the temperature range however, increasing the mixing ratio leads to the appearance of a second activation energy at temperature lower than 20°C. As mentioned previously, the temperature range was between 10°C and 80°C which is actually not broad enough to determine precisely the charge transport mechanism in this nanocomposite. Therefore, and for much deeper prediction, it is necessary to conduct the measurements at low temperatures. The conductivity in the VRH is attributed mainly to the disorder of lattice, which makes a spatial fluctuation in the potential of electrons [316]. Massrani et al. and Guillen et al. included that the VRH mechanism is estimated when $\mid T_0/T \mid$ is greater than 1 [317-318]. From the linear fitting in Figure 7.8, it can be concluded that the values of T_0 is equal to 8.37 $\times 10^3 K$, 10.52$\times 10^3 K$, 21.64$\times 10^3 K$ and 24.23$\times 10^3 K$ for PEDOT:PSS, 1:1, 1:1.3 and 1:3, respectively, both of which give T_0/T is greater that 1, thus confirming that in the investigated temperature range, the conductivity mechanism is due to 3D-VRH.

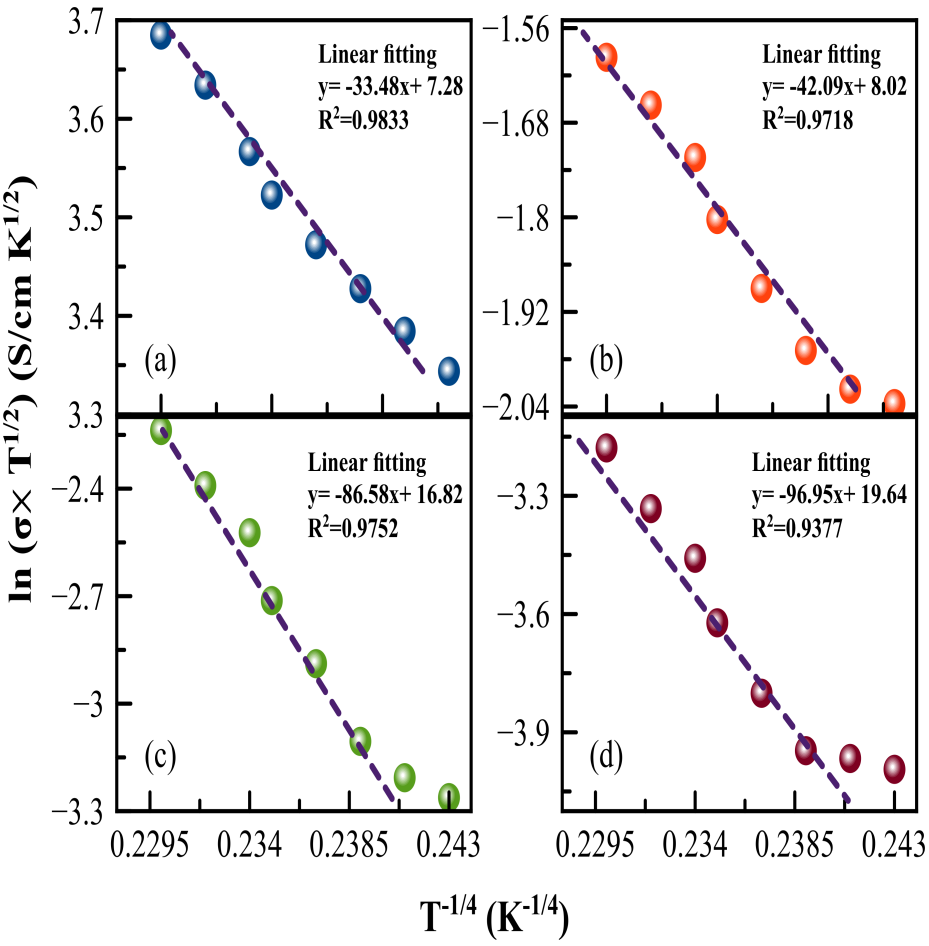

Figure 7.8: Algorithmic plot of conductivity and the reciprocal of temperature for the reduced films based (a) PEDOT:PSS, (b) 1:1, (c) 1:1.3 and (d) 1:3

8 Patch Antenna as Wireless Sensing Element

In this chapter, an overview of the patch antenna design especially rectangular microstrip patch antenna (MPA) with feed-inset is described and the analytical method used to design the MPA is illustrated. The design proposed in this work is then simulated using the electromagnetic simulation software CST studio suite, and the results are optimized to satisfy the required performance. To implement the patch antenna as strain or temperature sensor, the analytical formulas describing the relationship between the resonance frequency and the strain or temperature of the antenna is described theoretically and a numerical simulation is conducted to prove the feasibility of the proposed design as wireless strain sensor. Beside that, the principles used to predict the behavior of the microstrip antenna under temperature is explained.

8.1 Background about Patch Antenna

Passive wireless sensors have considerable advantages for measurement due to their simple installation and compactness without additional energy source. The design of the antenna is critical since any deformation or oxidation causes a change in its resonance frequency, which can be interpreted as a change in the measured quantity. Typically, gold, silver and copper are standard materials used for patch antenna. Among them, copper attracted more attention due its high reactivity and good conductivity and low costs. Microstrip devices are planar components for microwave and high frequency applications, which can replace bulky waveguides [319]. Historically, the concept of the microstrip patch antennas was first proposed in 1953 by Deschamps [320]. However, it was first practically realized in 1974 by Munson for space-borne application [321]. Lately, it became very popular due to its low profile ($t \ll \lambda_0$), light and limited weight, configurability to planar and non-planar surfaces, adjustable polarization to get a linear and circular polarizations, and ability to have single and multiple resonance frequency [319, 322]. Generally, the MPA consists of dielectric substrate having a thickness (t) and dielectric loss (ε_r), with an arbitrary shape patch layer on the topside and a metallic ground plane on the bottom side (Figure 8.1). Due to high conductivity, the upper and bottom side of the microstrip patch are made from copper. Different common shapes have been used as top layer of the patch such as square, rectangular, elliptical, etc (Figure 8.2). For any dielectric substrate covered by two metallic layers, an electromagnetic cavity is created with a specific resonance frequency that depend of the physical dimension of the patch, mainly the physical length (L) and the width (W) of the patch (Figure 8.1). Designing an antenna with good performance and high efficiency is critical, and the design parameters such as the substrate material; dimension of antenna and feeding technique, determine the performance of the MPA. The designed patterns are made in a way that the maximum radiation is perpendicular to the patch radiator. Therefore, some benchmarks must be considered in order to ensure this criterion [322]:

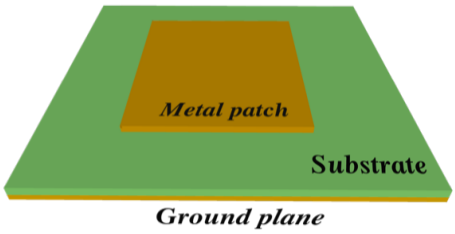

Figure 8.1: Typical structure of microstrip patch antenna

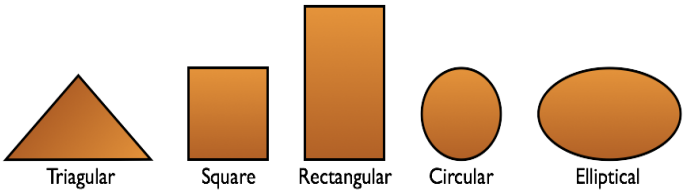

Figure 8.2: Different geometrical shapes of the patch antenna

1. The aspect ratio (W/L) must be less than 2, because a drop in the aperature efficiency occurs as the W/L increases beyond 2.
2. The patch antenna dimension should be in the range of $0.333\lambda_0 < L < 0.5\lambda_0$.
3. The thickness of the substrate must be in the range of $0.003\lambda_0 \leq t \leq \lambda_0$.
4. The dielectric constant of the substrate lies in the range of $2.2 \leq \varepsilon_r \leq 12$.

Practically for good antenna performance, thick substrates with low dielectric constant are more desirable as they exhibit improved efficiency, larger bandwidth, better radiation, but they suffer from the large element size [322]. However, and for microwave circuitry, thin substrates with higher dielectric constants are more required as on one side, they minimize the undesired radiation and coupling due to tightly bound fields, and have a smaller element size. On the other side, they are less efficient, with high losses and narrower bandwidths [322]. Generally, a compromise between the antenna characteristics and the antenna geometry must be fulfilled for each individual application. Typically, the patch antennas have high losses, which are described by the quality factor (Q). Some methods to improve the radiation and the bandwidth and therefore reduce the Q factor were introduced and studied [323]. For instance, increasing the substrate thickness is the most often way used to reduce Q, but this will lead to an increase in the surface wave and therefore the total delivered power to the antenna degrades its performance. By optimizing the antenna design such as using some critical radius [324], hi-lo structures [325], photonic bandgap structures [326- 327] and defected ground structures [328], the antenna efficiency can be improved.

8.2 Road-Map to Patch Antenna Design

MPAs become increasingly widespread as both feeds and array elements. The investigation of the electromagnetic fields is necessary to analyze the MPA, however the inhomogeneity and the complexity of these fields make this task very complicated. Therefore, different models were developed to analysis the microstrip antenna, such as the cavity model [329], the transmission line model [330] and full-wave model [331]. Among them, the transmission line model is the simplest and it gives a good physical insight, thus it is adopted in this work.

Prior design, MPA specifications such as resonance frequency, substrate dielectric material i.e. ε_r and the substrate thickness must be well defined, then the flow design of the MPA is summarized as follows [322]:

1. To ensure a good radiation efficiency, the patch width is given by

$$W = \frac{\upsilon_0}{2f_{res}}\sqrt{\frac{2}{\varepsilon_r+1}} \tag{8.1}$$

   where W is the patch width, ε_r is the dielectric constant of the substrate, υ_0 is the speed of light in the free space, f_{res} is the resonance frequency of the patch.

2. Part of the incident wave propagates in the substrate and other part is reflected in the air. For $W/t \gg 1$, most of the electric field lines are concentrated in the substrate and the dielectric constant of the substrate is slightly affected. The effective dielectric constant (ε_{eff}) is calculated using the following equation [322]:

$$\varepsilon_{eff} = \frac{\varepsilon_r+1}{2} + \frac{\varepsilon_r-1}{2}(1+12\times\frac{t}{W})^{-1/2} \tag{8.2}$$

3. The resonance frequency of a rectangular microstrip antenna depends mainly on the physical length (L) of the patch. The fringing fields at the two open ends of the patch add an imaginary extension to the antenna, so it looks greater than its physical dimensions. Therefore, an imaginary length extension (ΔL_{ext}) appears and influences the patch edges. The ΔL_{ext} depends linearly on the substrate thickness and effective dielectric constant and it is calculated as follow [322]:

$$\Delta L_{ext} = 0.412t \times \frac{(\varepsilon_r+0.33)(\frac{t}{W}+0.264)}{(\varepsilon_r\text{-}0.258)(\frac{t}{W}+0.831)} \tag{8.3}$$

4. Thus, the physical length of the patch can be calculated using [322]:

$$L = \frac{\upsilon_0}{2f_{res}\sqrt{\varepsilon_r}}\text{-}\Delta L_{ext} \tag{8.4}$$

5. From equations 8.3 and 8.4, the effective length (L_{eff}) of the patch is estimated as follow [322]:

$$L_{eff} = L + 2\Delta L_{ext} \tag{8.5}$$

Depending on the current flow direction, a rectangular MPA can radiate at two fundamental radiation modes: TM_{10} and TM_{01}. For the TM_{10} mode, the current flows along the length direction and for the TM_{01} mode current flows along the width direction and therefore, f_{10} and f_{01} are the resonance frequencies for TM_{10} and TM_{01}, respectively.

8.3 Antenna Feedline Design

Different methods have been introduced to feed the patch, among them microstrip line, coaxial, coupled, buried and slot feeds are widely used [319, 322, 332]. In this work, microstrip feedline is applied, as depicted in Figure 8.3, the microstrip conducting line is attached directly to the edge of the microstrip patch. To match the impedance of the patch with the impedance of the feed without any additional matching component, a proper

selection of an inset is introduced to the feedline. Experimentally, an inset has no influence on the resonance frequency of the microstrip antenna [319, 322]. The feed-inset point

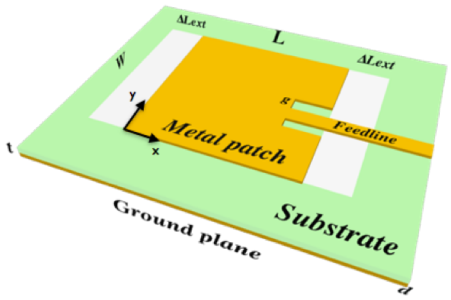

Figure 8.3: 3D-view of the microstrip patch antenna with feed-inset

and its dimensions are calculated based on equations 8.6 to 8.8, a theoretical derivation is out of the scope of this work [319, 322]. In order to minimize the high-order modes and cross-poles, the feed-inset point along the patch width is usually centered i.e. $y_0 = W/2$, therefore the feed point along the length can be calculated as follow [322],

$$x_0 = \frac{L}{\pi} \times \sqrt{\frac{50}{R_{inx}}} \tag{8.6}$$

where R_{inx} is the input resistance for the feed-inset along the x-axis, and R_{inx} is calculated as follow,

$$R_{inx} = \frac{90}{\varepsilon_r - 1} \times (\frac{\varepsilon_r \times L}{W_0})^2 \tag{8.7}$$

And the width of the microstrip line (W_0) is derived as follow:

$$\frac{W_0}{d} = \begin{cases} \dfrac{8e^A}{e^A - 2} & \text{if } \dfrac{W_0}{d} < 2, \\ \dfrac{2}{\pi}(B - 1 - ln(2B - 1) + \dfrac{\varepsilon_r - 1}{2\varepsilon_r}) & \\ \quad \times (ln(B - 1) + 0.39 - \dfrac{0.61}{\varepsilon_r}) & \text{if } \dfrac{W_0}{d} > 2 \end{cases} \tag{8.8}$$

where;

$$A = \frac{Z_0}{60}\sqrt{\frac{\varepsilon_r + 1}{2}} + \frac{\varepsilon_r - 1}{\varepsilon_r + 1} \times (0.23 + \frac{0.11}{\varepsilon_r})$$

$$B = \frac{377\pi}{2Z_0\sqrt{\varepsilon_r}}$$

where Z_0 is the characteristic impedance. Also, the notch width (G_{pf}) is usually adjusted based on trial and error method, however, some approaches were proposed to calculate it [333],

$$G_{pf} = \frac{v_0}{2 \times \sqrt{\varepsilon_r}} \times \frac{4.65 \times 10^{-12}}{f_{res}} \tag{8.9}$$

8.4 Design and Physical Dimensions of the Proposed Wireless MPA

It can be concluded from section 2.6 that, there is a trade-off between the antenna design and the sensor sensitivity. Where the single resonance rectangular MPA has a higher strain sensitivity than the multiple and the circular MPA, the strain sensitivity increases when the MPA is designed to work at high frequency such as SHF and microwave (Table 2.5). However, the circular and the multi-resonance MPA can determine the strain in different directions, whereas the single rectangular MPA is able to sense the strain only in one direction. For higher antenna gain, substrate with low loss and high dielectric constant is beneficial to improve the reading distance of the sensor. Therefore, the design proposed in this work is based on transmission line model with a feed-inset rectangular MPA resonating at IEEE C-band (SHF) i.e. 5.8GHz because sensors at this frequency range have small compact size, and adequate strain sensitivity compared to 2.4GHz (see Table 2.5) also at this frequency band, large amounts of data can be transmitted [319, 322]. A flexible thin low loss substrate named Isola IS680 having t of 508μm and ε_r of 3.38 and tangent loss of 0.035 is choosen. On the topside, it has a rectangular patch layer with feed-inset and on the bottom side a ground plane both made of copper with thickness of 18μm. By determining the resonance frequency and the substrate material, the design steps mentioned in section 8.2 and 8.3 are used to design the antenna, the values of the physical dimension of the microstrip patch are shown the Table 8.1. The calculated values are based on equations 8.1 to 8.7, whereas after inserting those values in the simulation software CST, some correction must be fulfilled due to the meshing effect and the presence of the notch width, thus a shift in the resonance frequency occurs as depicted in Figure 8.4 (a). The optimization is done keeping in mind the following criteria:

1. Resonance deviation not higher than 100MHz.
2. Acceptable gain loss.
3. Narrow bandwidth.

Table 8.1: Design parameters of the 5.8GHz microstrip patch antenna

Antenna Parameter	Calculated	Optimized
	Units (mm)	
Patch length	13.9	13.9
Patch width	17.5	18.5
Substrate length	24.8	27.8
Substrate width	31.8	37
Feed-inset point	5	5
Notch width	0.0	0.20
Feed-inset length	11.9	11.9
Microstrip line width	1	1

The simulated antenna based on the calculated values gives a resonance frequency at 5.67GHz, after patch width and notch width optimization the resonance frequency shifted to 5.71GHZ, which is 90MHz less than the desired resonance value of the MPA, also a very narrow bandwidth about 1.57% and gain loss below -10dB which is suitable for wireless sensing. This narrow bandwidth is important, so any small change in the resonance can

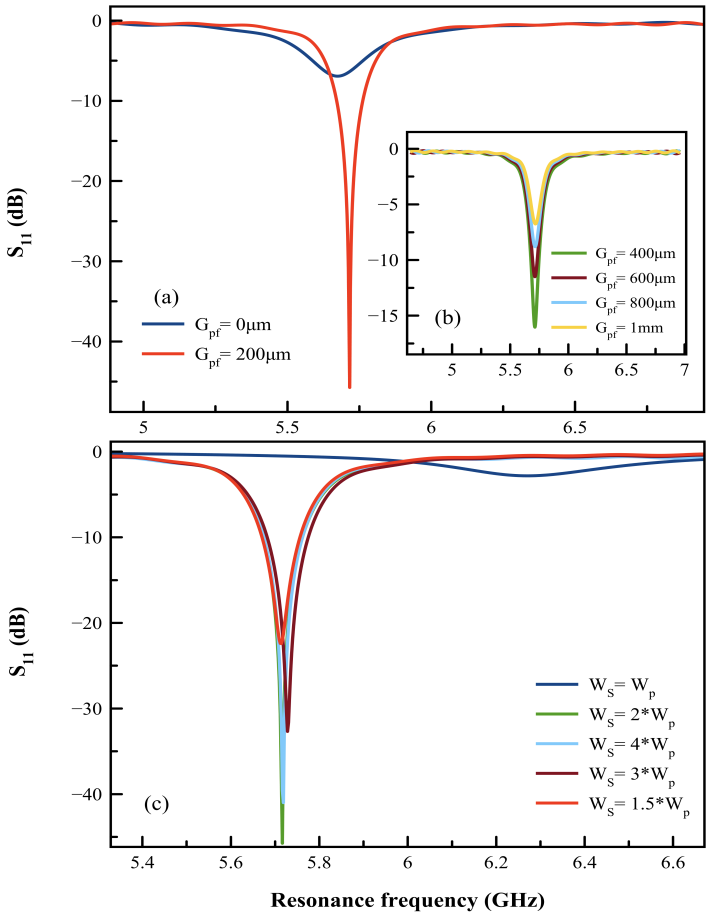

Figure 8.4: (a) and (b) Return loss of the 5.8GHz microstrip patch antenna at different G_{pf} values and (c) Effect of the ground dimension on the return loss of the 5.8GHz MPA

be easily detected and thus improves the sensor sensitivity. The notch width seems to play also an imprortant role to improve the bandwidth shape, as the width of 200μm gives the narrower bandwidth compared to other values as depicted in Figure 8.4 (b). Theoretically, the transmission line model is applicable to an infinite ground plane only. However, the size of the ground plane (W_s) affects the radiation pattern and the resonant frequency of a patch antenna. Therefore, it is very necessary to optimize its size to ensure a good antenna performance. The effect W_s with respect to the patch width (W_p) is illustrated in Figure 8.4. When the ground plane equals to the patch dimension, the patch resonates at higher frequency, this is resulting from the fringing fields that lies in the free space which lowers the dielectric constant of the substrate and thus increase the resonance frequency. As the ground dimensions are increased an improvement in the antenna properties is reached. The best performance is obtained when the ground dimension is twice the patch dimension, which is considered as the critical ground plane size. The antenna properties at this critical ground size in terms of far field gain and 3D radiation pattern are shown in Figure 8.5 and Figure 8.6, respectively. As it is shown in Figure 8.7, an excellent agreement is obtained between the resonance frequency of the simulated MPA and the fabricated MPA with 5.71 and 5.716GHz, respectively. The small deviation in the frequency is referred to the stray capacitance introduced through the soldering of the SMA connector.

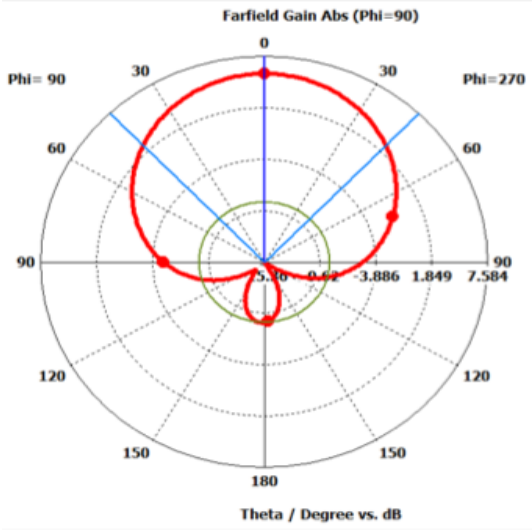

Figure 8.5: Far field gain of the 5.8GHz MPA

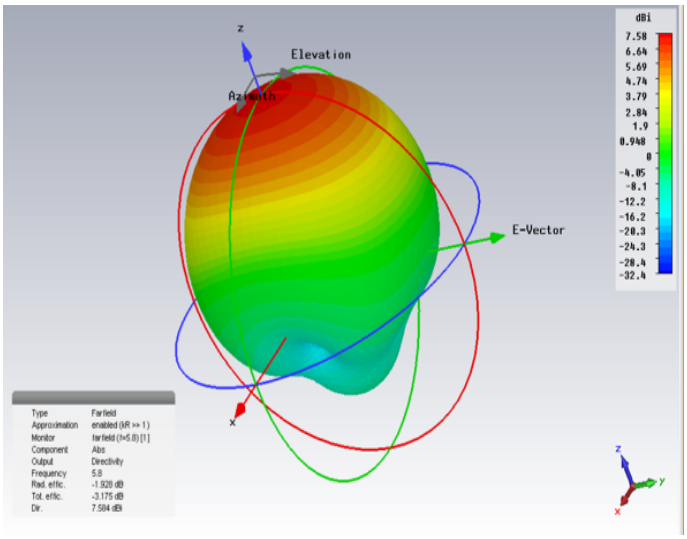

Figure 8.6: 3-D radiation pattern of the MPA at 5.8GHz

8.5 Wireless Sensing using Nanocomposite

To evaluate the use of the nanocomposites as sensing patch layer in the MPA, three different patterns are proposed and evaluated. The pattern that gives the best antenna characteristics, is used then as a wireless sensor.

1. A copper patch covered by a layer of nanocomposite, and thus named as the coated pattern (Figure 8.8 (b)).
2. Patch made only of nanocomposite, whereas the copper layer is etched out and is named as the nanocomposite pattern (Figure 8.8 (c)).
3. Hybrid pattern, which is made of copper feedline and nanocomposite patch (Figure 8.8 (d)).

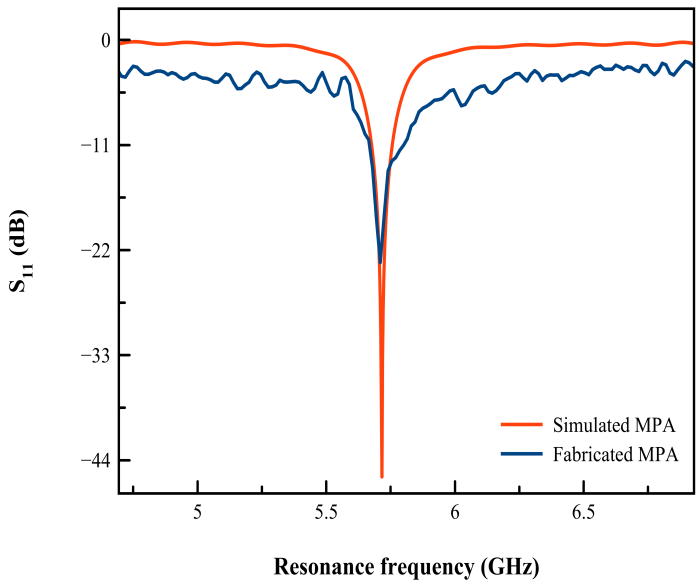

Figure 8.7: S_{11} of simulated and fabricated MPA based copper patch

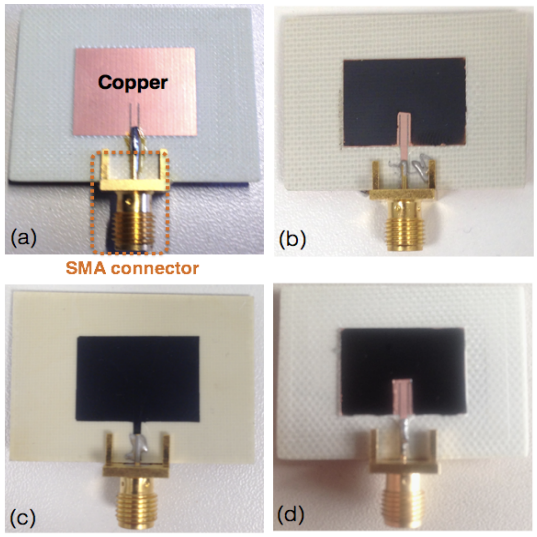

Figure 8.8: Fabricated microstrip patch antenna (a) Copper patch, (b) Coated pattern, (c) Nanocomposite patten and (d) Hybrid pattern

As it was explained in section 2.5, different attempts were carried out to incorporate the patch antenna as sensor beside using it for communication issues. For strain sensing, using copper as sensing layer results in a very low k-factor, as the copper is a hard material and the applied forces are small so that the resulting strain is in the microstrain range. Although some techniques were applied to improve the strain sensitivity, such as slots on the patch, circular patch and using thin substrates, but non-of-them improved really the strain sensitivity (section 2.6). Using SNWs as alternative to copper improved slightly the strain sensitivity. However, replacing the copper by more strain sensitive layer can reach better performance. Being able to adjust the conductivity of the nanocomposites, makes them a good candidate to replace a copper patches, however an appropriate nanocomposite

with conductivity in the range of 10^4S/m is necessary. Increasing the conductivity decreases the piezoresistivity of metals, because high conductive materials have no bandgap and its piezoresistivty is mainly due to the change in the dimension of the bulk material, which therefore changes its resistance (Ohm's Law). However, this change is very low and thus the strain sensitivity is low as well. In the previous chapters, different nanomaterials based on PEDOT:PSS, CNT and GO are investigated. A selection of nanocomposites for use as patch antenna is carried out, then the properties of the antenna are investigated for strain and temperature sensing, the results are compared to the standard copper patch antenna. From chapters 5, 6 and 7, different hybrid nanocomposites were investigated for sensing application, mainly temperature, humidity and strain. The results in chapter 5, PEDOT:PSS has shown excellent sensitivity to humidity. In chapter 6, it was seen that rGO:MWCNT with 0.05wt.% MWCNT has good temperature sensitivity with low effect of strain and humidity and conductivity of 10^4S/m. In chapter 7, the rGO:MWCNT/PEDOT:PSS with mixing ratio of 1:1.3 showed an excellent strain sensitivity with k-factor up to 97, whereas the effect of temperature is less than 3% and an electrical conductivity of 5×10^5S/m. A summary of the selected nanocomposites is shown in Table 8.2. The copper antenna is fabricated using photograving and etching process. The coated pattern (model 1) is fabricated in the following way: a mask is patterned on the antenna surface, the nanocomposite is then deposited only on the copper patch, keeping only the feedline inset uncoated (Figure 8.8 (b)). In the nanocomposite pattern (model 2), a plotter is used to pattern the patch dimension, however, due to the restriction of the plotter resolution, it was not possible to reach a gap inset of 200μm, afterwards, the nanocomposite is directly deposited on the substrate (Figure 8.8 (c)). The hybrid pattern (model 3), a copper patch is completely etched and only the copper feedline is not etched as shown in Figure 8.8 (d), then the nanocomposite is deposited (Figure 8.8 (d)). After deposition, the antenna are kept in air-drying for 24 hours and then dried in oven for 30min at 80°C to remove all the water molecules from the patch layer.

Table 8.2: Selected nanocomposite for different sensing application

Nanocomposite	Sensing application		
	Strain	Temperature	Humidity
PEDOT:PSS	–	–	✓
rGO:MWCNT	–	✓	–
rGO:MWCNT/PEDOT:PSS	✓	–	–

8.5.1 Evaluation of the Proposed Sensor Elements

The prepared antennas are connected to the VNA using a RF-coaxial cable. Among all the nanocomposite selected in Table 8.2, PEDOT:PSS shows a very bad adhesion to the substrate although different treatment methods are used (Figure 8.9). In the coated pattern, it is observed that the deposited nanocomposite layer on the copper patch layer introduced slightly a shift in the initial resonance frequency of the copper MPA, as it is shown in Figure 8.10 (a), as the deposited layer acts as dielectric material that affects the performance of the MPA. For the PEDOT:PSS and as the adhesion is very low, no effect is observed on the resonance frequency. Also, no chemical reduction is carried out as the hydriodic acid will also etch the copper patch beneath the nanocomposite layer. In the nanocomposite pattern, the S_{11} had a damping and no signal is measured, as depicted in Figure 8.10 (b). This is

resulting from the elimination of the antenna notch, that changes the characteristic of the MPA, these results are confirmed by the simulation results obtained from optimizing the notch gap as shown in Figure 8.4. From Figure 8.4, it is found that a gap of 200μm has the lowest return loss and thus all the MPAs are designed using this value. To avoid the problem of the gap elimination introduced in the nanocomposite pattern, a hybrid pattern is proposed. Here, all the copper patch layer is etched off and only the feedline inset is kept afterwards, the nanomaterial then is deposited. The antenna characteristics of this pattern is shown in Figure 8.11. Although, a shift in the resonance frequency is introduced, the return loss of the antenna is comparable to its copper counterparts, thus this pattern is selected to be used for wireless sensing.

To examine the reproducibility of the MPAs, three MPAs were deposited using rGO:MWCNT and rGO:MWCNT/PEDOT:PSS and the results are shown in Figure 8.12 and 8.13, respectively. It can be seen that, the samples show a reproducible characteristics especially for rGO:MWCNT/PEDOT:PSS, which is referred the high conductivity of this hybrid materials as explained in section 7.2.

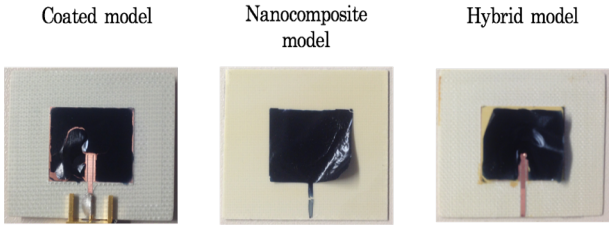

Figure 8.9: Adhesion problems of PEDOT:PSS MPA with different proposed models

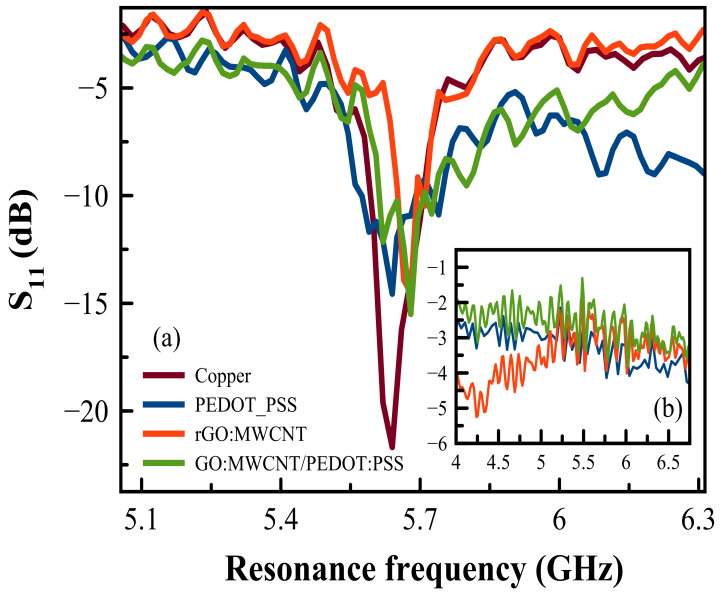

Figure 8.10: S_{11} of (a) The coated pattern, (b) The nanocomposite pattern

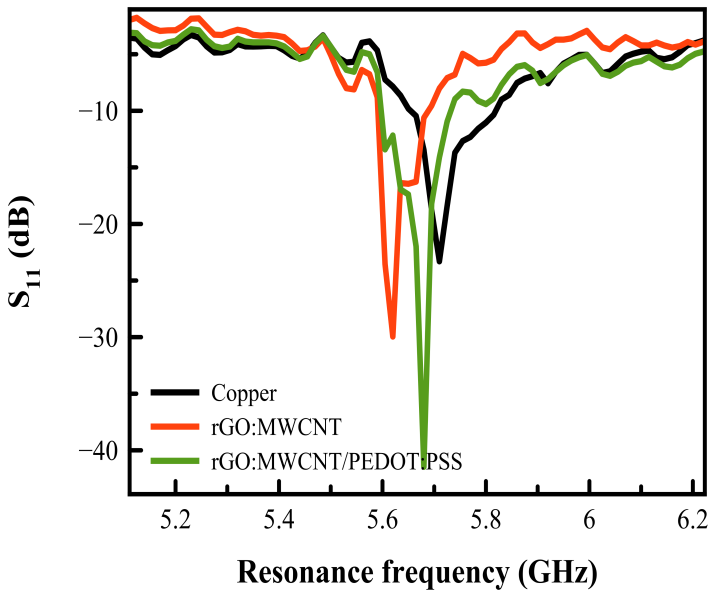

Figure 8.11: S_{11} of the hybrid pattern

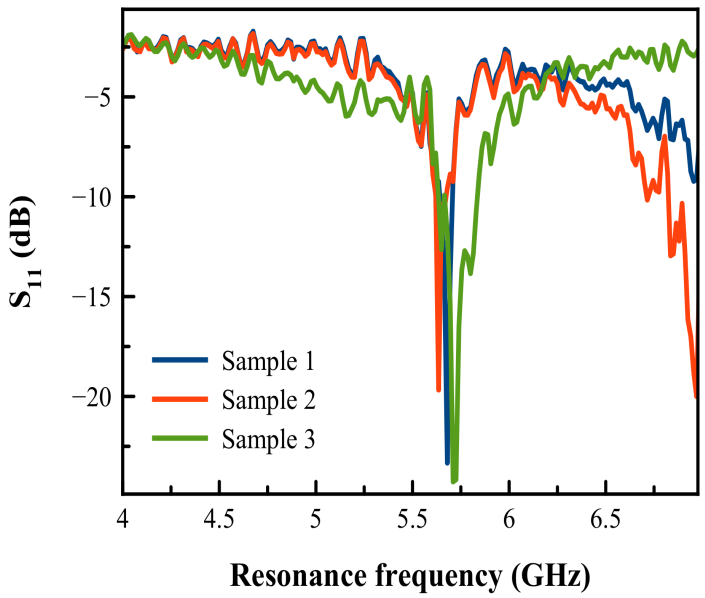

Figure 8.12: S_{11} of different samples of hybrid model using rGO:MWCNT

8.5.2 Wireless Strain Sensing

1. Electromagnetic Simulation of Patch Antenna for Strain Sensing

In this section, a MPA is simulated using software CST studio suite to be used as passive wireless strain sensor. The equations describing the change in the length, width and thickness of the patch antenna after applying a force (equations from 8.10 to 8.12) are builded-in in the software so the CST studio is used as multiphysics simulation tool beside using it to simulate the electromagnetic properties of the antenna.

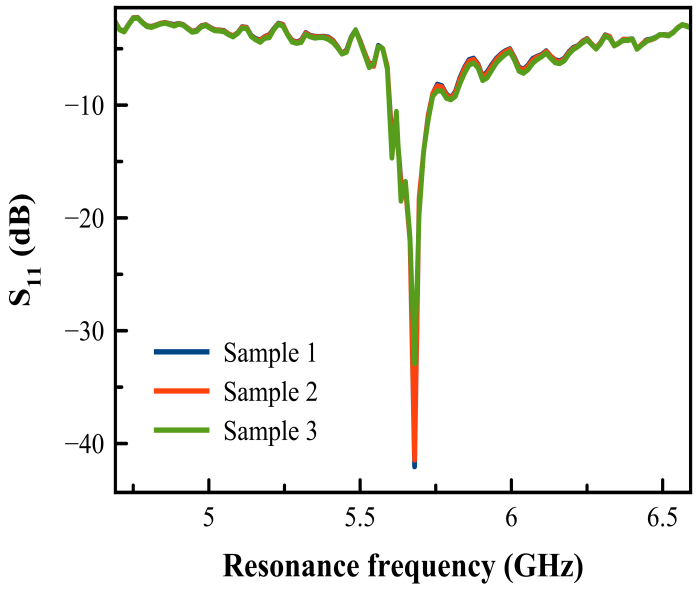

Figure 8.13: S_{11} of hybrid model using rGO:MWCNT/PEDOT:PSS

Under no strain, the antenna radiates at its initial resonance frequency. If a load is applied along the patch length direction (ϵ_L) on the free end of the cantilever, a small change in the patch's length (L_ϵ) occurs, which can be calculated as follow:

$$L_\epsilon = (1+\epsilon_L) \times L \tag{8.10}$$

Correspondingly, and due to the Poisson's effect (υ), a change in the patch width (W_ϵ) and substrate thickness (t_ϵ) of the antenna will also occur, which can be recalculated as follow,

$$W_\epsilon = (1\text{-}\epsilon_L \times \upsilon_p) \times W \tag{8.11}$$

$$t_\epsilon = (1+\epsilon_L \times \upsilon_s) \times t \tag{8.12}$$

where υ_p and υ_s are the Poisson ratios of the patch antenna and substrate, respectively.

The same case if the load is applied along the patch width direction (ϵ_w), beside the change in it's width, a change in its patch length and its substrate thickness also occurs. Thus, the previous Eqs. 8.10 to 8.12 must be reformulated and the corresponding width, and length under strain can be calculated as follow;

$$W_\epsilon = (1+\epsilon_w) \times W \tag{8.13}$$

$$L_\epsilon = (1\text{-}\epsilon_w \times \upsilon_p) \times L \tag{8.14}$$

$$t_\epsilon = (1\text{-}\epsilon_w \times \upsilon_s) \times t \tag{8.15}$$

Previously in [22], it was assumed that the Poisson's ratio of the metallic patch υ_p and the substrate material υ_s are identical. However, for correctness a specific Poisson ratio of each layer has to be considered. In the particular case values of 0.335 and 0.122 were used for υ_p and υ_s, respectively. In the first case, where the applied force is along the

patch length and by substituting Eqs. 8.10 to 8.12 in Eqs. from 8.1 to 8.5, the resonant frequency under strain can be expressed as,

$$f_{res}(\epsilon) = \frac{c}{2 \times \sqrt{\varepsilon_{eff}}} \times \frac{1}{L_\epsilon + \Delta L_{ext}} \tag{8.16}$$

where ε_{eff} is the effective dielectric constant of the substrate, $L_{(\epsilon)}$ is the patch antenna length along the applied load in the direction of the radiation mode and $\Delta L_{ext(\varepsilon)}$ is the change in the extended length.

ϵ_l is ranging from 0 to 0.6% with a step of 0.2%. The relative resonance frequency change is used to calculate its shift,

$$f_{norm} = \frac{\Delta f_{res}}{f_{res}(0)} \tag{8.17}$$

where $\Delta f_{res} = f_{res}(\epsilon_l)$ - $f_{res}(0)$, and $f_{res}(\epsilon_l)$ and $f_{res}(0)$ are the resonance frequencies at strained and initial state, respectively.

As illustrated in Figure 8.14 (a), a decrease of the resonance frequency to lower frequencies occurs if the load is applied along the antenna's physical length, and vice versa if the load is applied along the antenna's width (Figure 8.14 (b)). The strain sensitivity in both directions can be calculated as,

$$S_l = \frac{\Delta f_{res}}{f_{res}(0)} \times \frac{1}{\epsilon_l} \tag{8.18}$$

$$S_w = \frac{\Delta f_{res}}{f_{res}(0)} \times \frac{1}{\epsilon_w} \tag{8.19}$$

where S_l, S_w are the strain sensitivities along the length and width, respectively.

It is clearly seen from Figure 8.15 the linear relationship between the strain and the shift in the resonance frequency of the antenna, also the shift is more sensitive to strain along the length direction (-81.4kHz/$\mu\epsilon$) than these along the width direction (26.2kHz/$\mu\epsilon$). Independent on the used substrate material, the strain sensitivity remains always low, therefore another concept such as using nanocomposite as sensing layer, must be integrated in order to use the patch antenna for strain sensor. Table 8.3 shows a comparison results of MPA having different substrate materials used as wireless strain sensor.

Table 8.3: Comparison between different substrate as strain sensor based MPA

Strain Sensitivity (kHz/$\mu\epsilon$)	Rogers 5870	Isola 680	FR4
along the length	-92.9	-86.8	-90.2
along the width	27.0	27.1	26.2

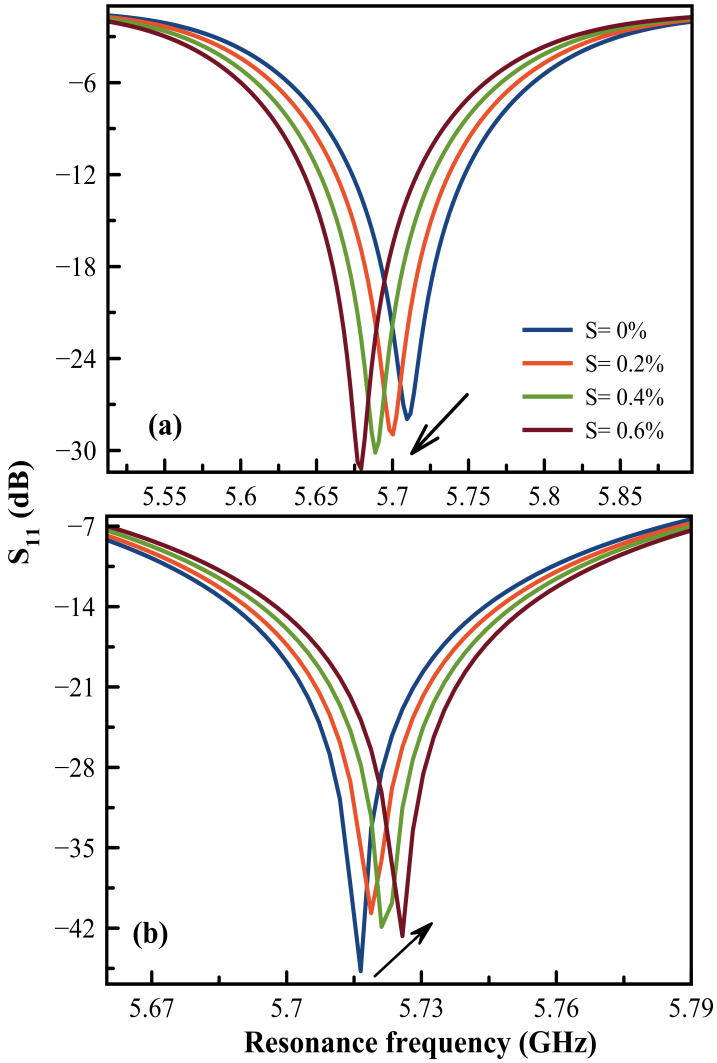

Figure 8.14: Simulation results of the shift in the antenna resonance frequency under applied load along the antenna's (a) length and (b) width

2. Nanocomposite Patch Antenna for Strain Sensing

In this section, the feasibility of using the patch antenna for wireless strain sensing is investigated. The copper patch antenna is used for comparison reason and the results are compared to the patch antenna based on nanocomposite. The copper MPA is fixed on cantilever beam and different load is applied at the end of the beam as it is depicted in the measurement setup in Figure 4.12. Figure 8.16 depicts that there is no change in the antenna characteristics when the cantilever beam is deflected under load, which is not in agreement with simulation results in section 8.5.1. This is referred to the stiffness of the copper patch layer as well as the small applied load. The maximum applied load is 480g which creates a strain of 0.36% in the beam. In order to improve the sensitivity, the copper is replaced by GO:MWCNT/PEDOT:PSS layer using the hybrid pattern explained in section 8.5.1. The MPA based rGO:MWCNT/PEDOT:PSS shows an improved sensitivity to strain as it is shown in Figure 8.17. As the load is applied along the MPA length, the shift in the resonance frequency is towards lower frequencies which is in total agreement with the simulation results.

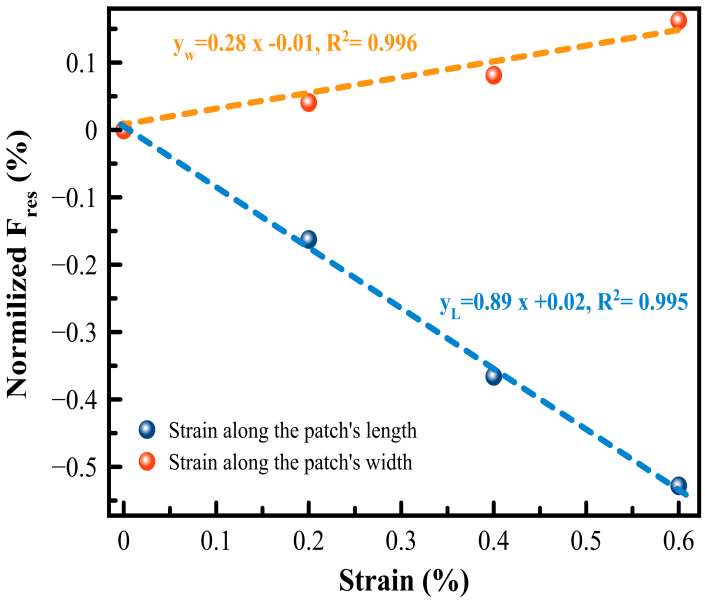

Figure 8.15: Strain sensitivity along the antenna's length and width

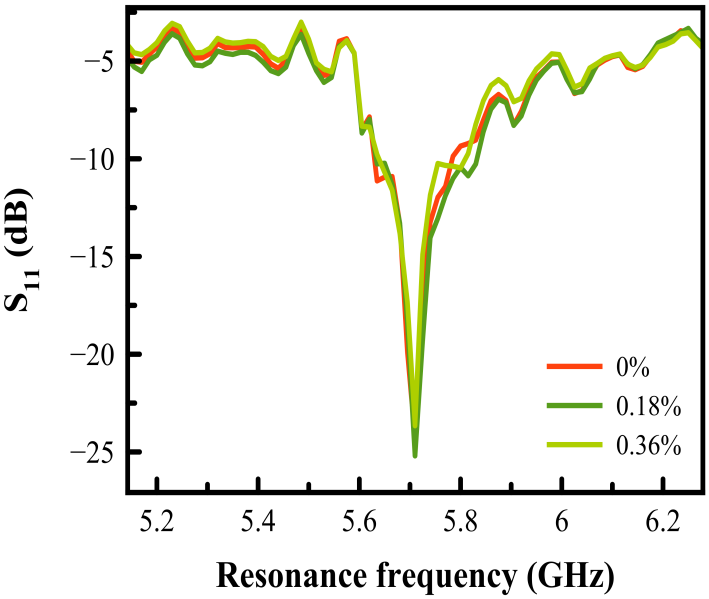

Figure 8.16: Strain sensitivity along the antenna's length

The relationship between the strain and change in the resonance frequency (Figure 8.18) is nonlinear. By linearization, the strain sensitivity is extracted to be about -4MHz/$\mu\varepsilon$ (the minus sign is because the resonance frequency decreases with increasing the load). The obtained strain sensitivity in this work is 784 times higher than the patch antenna working at same resonance frequency proposed by Ahbe et al. [7] (3rd generation) and 93 times higher than the wireless strain antenna proposed by Song et al. [7] made of silver nanoparticles (4th generation). The results are compared in Table 8.4.
A hysteresis of 15.76% is measured in the first cycle, this tends to decrease to 11.39% in the 10^{th} cycle. In Figure 8.19, the cycling test shows also a very stable response of the MPA rGO:MWCNT/PEDOT:PSS with a decrease in the non loading resonance frequency

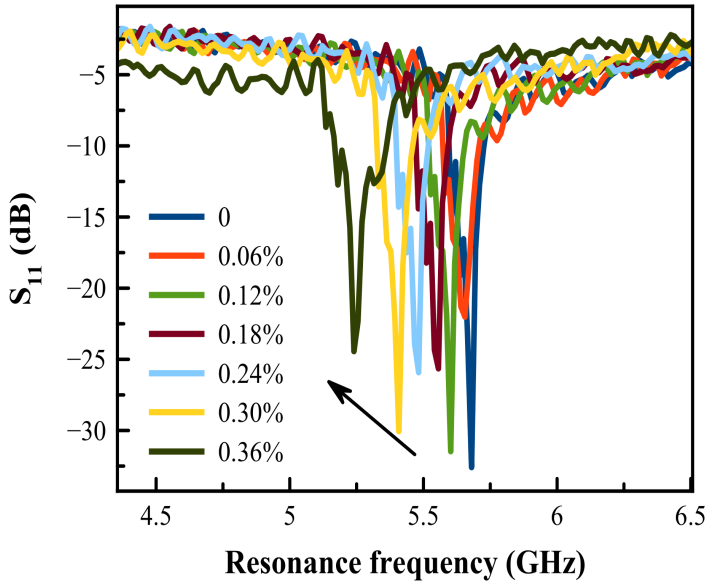

Figure 8.17: Strain sensitivity of MPA with rGO:MWCNT/PEDOT:PSS as patch layer

of about 110KHz after the 4th cycle with represents a change of 0.1% from the initital resonance frequency (f_{res}=5.68GHz).

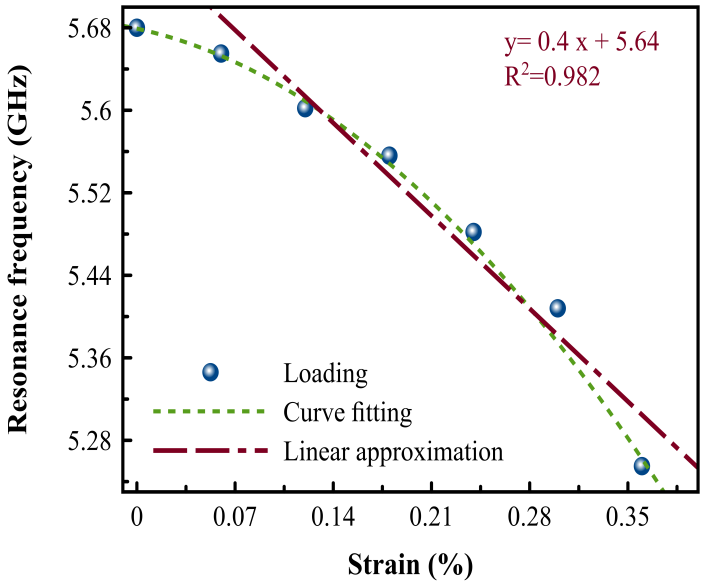

Figure 8.18: Fitting of rGO:MWCNT/PEDOT:PSS MPA wireless strain sensor

8.5.3 Nanocomposite Patch Antenna for Temperature Sensing

To use the MPA for temperature sensing, the copper patch material is replaced by rGO:MWCNT with 0.05wt.% MWCNT. Here, the measurement principle is based on the change/deformation of four parameters:

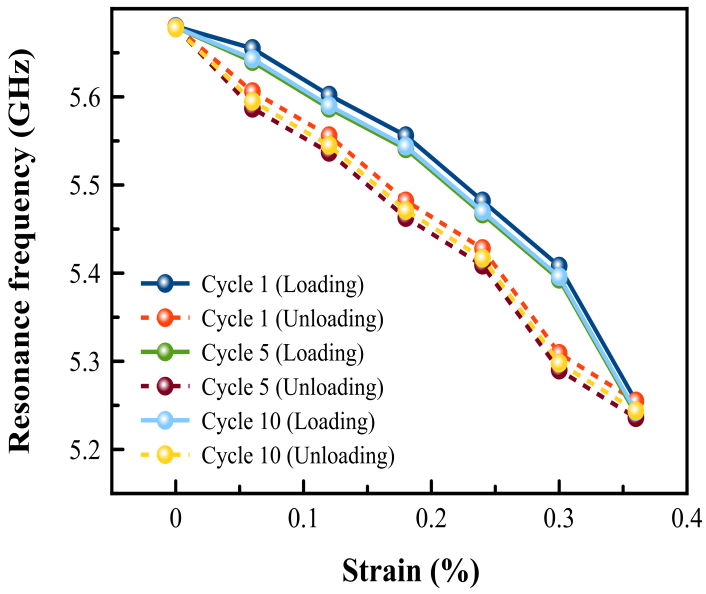

Figure 8.19: Cycling test response of rGO:MWCNT/PEDOT:PSS MPA wireless strain sensor

Table 8.4: Summary of MPA used for strain sensing

Ref.	Substrate Thinckness (μm)	Frequency (GHz)	Strain Range ($\mu\epsilon$)	Sensitivity (kHz/$\mu\epsilon$)
Tata et al. [22]	50	20	0 -550$\times 10^3$	22.8
Tata et al. [23]*	50	15.8 and 20.5	0 -550$\times 10^3$	15.5 and 9.2
Daliri et al.[28]	1500	1.5	25	10
Yi et al. [31]	790	0.921	0-500	-0.790
Ahbe et al.[6]	1500	2.9 and 5.8	0-2500	-2.2 and -3.1
Thai et al.[33]	100	3	0-7$\times 10^3$	1.26
Wang et al. [36]	50	2.5 to 20.5	0-363	20.5 and 46.8
Song et al. [7]**	1500	3 and 6	0-150$\times 10^3$	53.7
This work	500	5.8	0-3600$\times 10^3$	4000

* This is a circular shape instread of rectangular shape used in all other patches.
** Patch made with AgNw instead of copper used in all other patches.

1. Antenna physical dimensions.
2. Dielectric constant of the substrate.
3. Conductivity of the patch material.
4. Dielectric loss of the patch material.

Here, instead of using ISOLA 680, the glass-reinforced epoxy laminate (FR-4) flexible substrate having thickness of 500μm and dielectric constant of 4.3 is used. The ISOLA 680 has a very stable dielectric constant up to 260°C and therefore the change to temperature is negligible. The fabricated antenna for wireless temperature sensing is depicted in Figure 8.20, and for comparison reasons the copper MPA is used as reference. The copper MPA has a resonance frequency at 6.04GHz at a temperature of 20°C. For any change in temperature, a change in the dielectric loss of the substrate and the antenna's dimension i.e. L, W and t occurs. However, and as the thickness of the patch is very small about few micrometers and the change of temperature is also relatively small, the change in the thickness is negligible. Also, the MPA resonance frequency is as function of antenna length, as its dominant mode is the TM_{010} transmission mode and therefore, the change is the width due to temperature is also neglected. Thus, the change in the dielectric constant of the substrate and the patch's length can be calculated as follow:

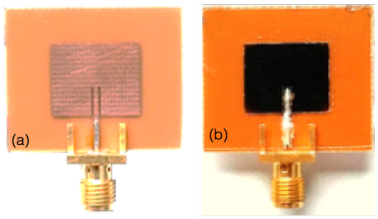

Figure 8.20: MPA based temperature sensor (a) Copper MPA and (b) rGO:MWCNT nanocomposite MPA

$$\Delta T = \frac{\Delta \epsilon_{re}}{\epsilon_{re}} \times \frac{1}{\alpha_{re}} \tag{8.20}$$

$$\Delta T = \frac{\Delta L}{L} \times \frac{1}{\alpha_L} \tag{8.21}$$

where α_{re} and α_L are the thermal coefficient of the substrate dielectric loss and the patch's length, respectively.

The normalized frequency (f_{norm}) as a change in temperature can be calculated by substituting equation 8.20 and equation 8.21 in equation 8.17,

$$f_{norm} = \frac{\Delta f_{ref}}{f_{ref_{(T_{20})}}} = (-\frac{1}{2} \times \alpha_{re} - \alpha_L) \times \Delta T \tag{8.22}$$

Previously, Maurya et al. in [38] and Chen et al. in [39] showed that, the effect of temperature from 10°C to 160°C on the dielectric constant of the FR4 substrate is very small and therefore it is negligible. However, this is not the case for the substrate used here. Therefore, a copper MPA is examined under temperature from 20°C to 80°C, and Figure 8.21 shows change in its resonance frequency as function of temperature.

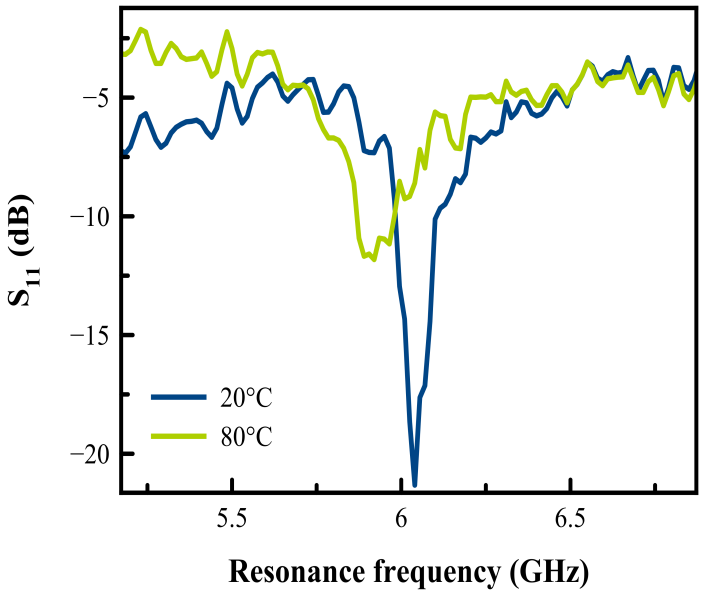

Figure 8.21: Shift in the resonance frequency under temperature of copper based MPA

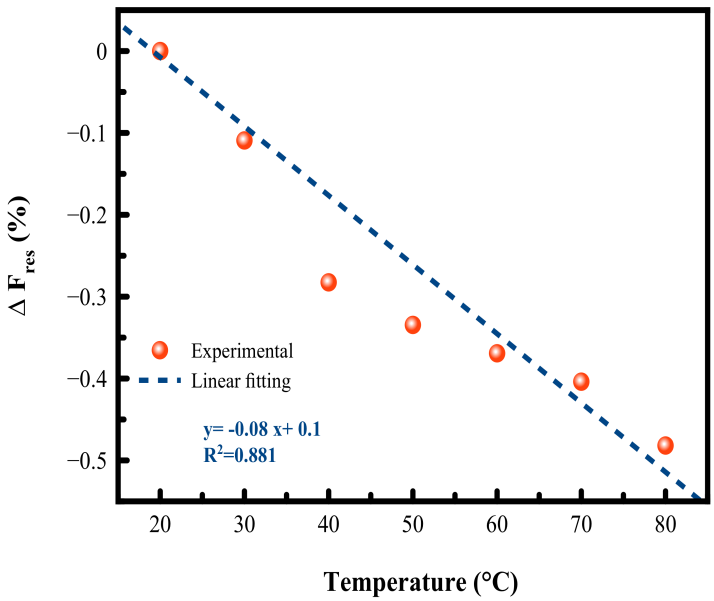

Figure 8.22: Linear fitting of copper MPA based temperature sensor

As it is shown in Figure 8.21, the increase in the temperature leads to a decrease in the resonance frequency, as it is anticipated from Eq. 8.22. Figure 8.22 determines the temperature sensitivity ($S_{temp}\%$) which can be calculated as follow,

$$S_{temp}\% = \frac{\Delta f_{ref}}{f_{ref_{(T_{20})}}} \times \frac{1}{\Delta T} \times 100\% \tag{8.23}$$

where Δf_{ref} is the change in the resonance frequency, $f_{ref_{(T_{20})}}$ is the resonance frequency at 20°C and ΔT is the change in the temperature.

By replacing the copper patch by rGO:MWCNT nanocomposite, the same trend change is noticed (Figure 8.23) but with higher sensitivity (Figure 8.24). From Figure 8.22 and Figure 8.24, the temperature sensitivity is calculated to be 0.78MHz/°C and 46.1MHz/°C for copper and rGO:MWCNT, respectively. This indicates the high potential of using this nanocomposite for wireless temperature sensing. This temperature sensitivity is 59 times higher than the copper temperature MPA. Table 8.5 shows a comparison between the results of using rGO:MWCNT nanocomposites as patch layer and metal patch. The hysteresis of the rGO:MWCNT was higher than its copper counterparts with about 2.36%, as shown in Table 8.6. To determine the stability of the fabricated sensor, longterm measurements were carried out for rGO:MWCNT MPA for duration of one week at two different temperatures i.e. 20°C and 80°C. Relatively low change is noticed with about 0.1% at 80°C and 3.05% at 20°C as shown in Figure 8.26.

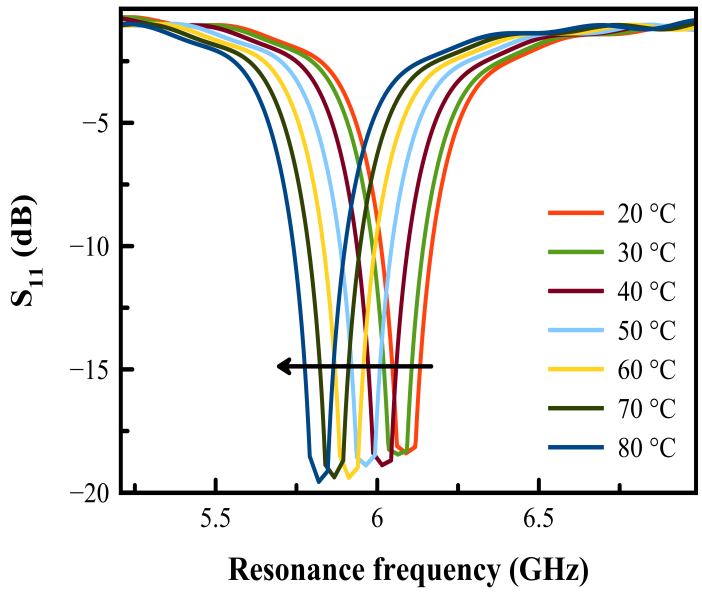

Figure 8.23: Shift in the resonance frequency under temperature of MPA with rGO:MWCNT as patch layer

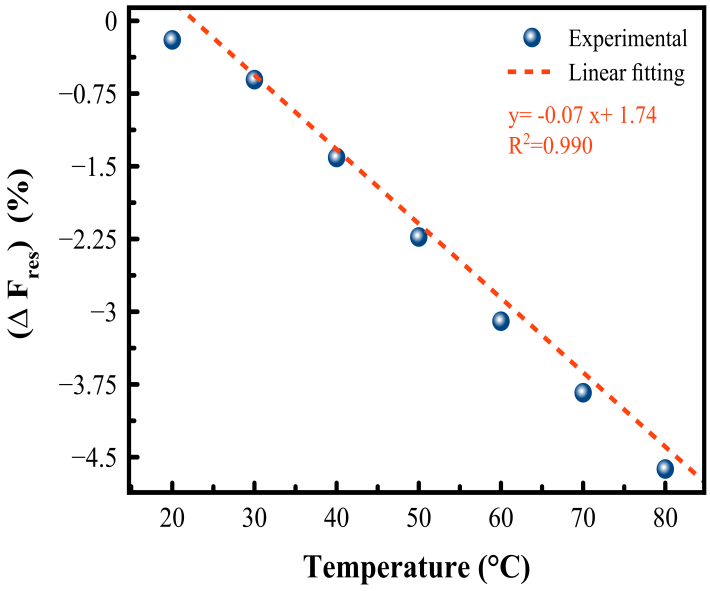

Figure 8.24: Linear fitting of rGO:MWCNT MPA based temperature sensor

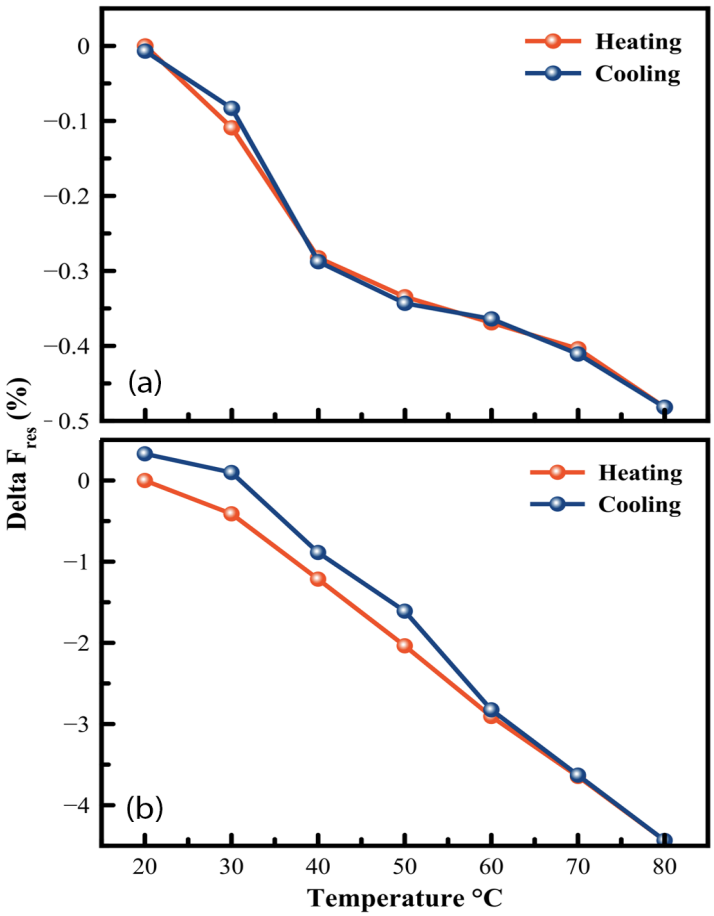

Figure 8.25: Temperature hysteresis of the (a) Copper MPA and (b) rGO:MWCNT MPA

Table 8.5: Comparison of different MPA used for temperature sensing

Ref.	Temperature range (°C)	Substrate	Patch material	Freqeuncy at T_0	Sensitivity (MHz/°C)
Maurya et al. [38]	27 -117	FR4	Copper	2.94	-8.51×10^{-3}
Maurya et al. [38]	27 -117	Quartz	Copper	3.13	-9.41×10^{-3}
Maurya et al. [38]	27 -117	Polyamide	Copper	3.25	-9.37×10^{-3}
Maurya et al. [38]	27 -117	Teflon	Copper	4.08	-16.35×10^{-3}
Cheng et al. [39]	50- 1050	Alumina	Platinium	5.07	-0.58
Sanders et al. [40]	40- 110	PTFE	Copper	5- 6	-0.764
Sanders et al. [40]	40- 110	PTFE	Aluminium	5- 6	-0.665
Sanders et al. [40]	40- 110	PTFE	Steel	5- 6	-0.593
Yoo et al. [41]	20- 280	RO3210		2.45	-0.47
Tan et al. [42]	25- 400	LTCC		2.29	-0.24
This work	20- 80	FR4	rGO:MWCNT	6.2	-46.1

Table 8.6: Comparison between copper and rGO:MWCNT temperature MPA sensor

	Copper based MPA	rGO:MWCNT based MPA
Hysteresis (%)	0.15	2.36
Sensitivity (MHz/°C)	-0.78	-46.1

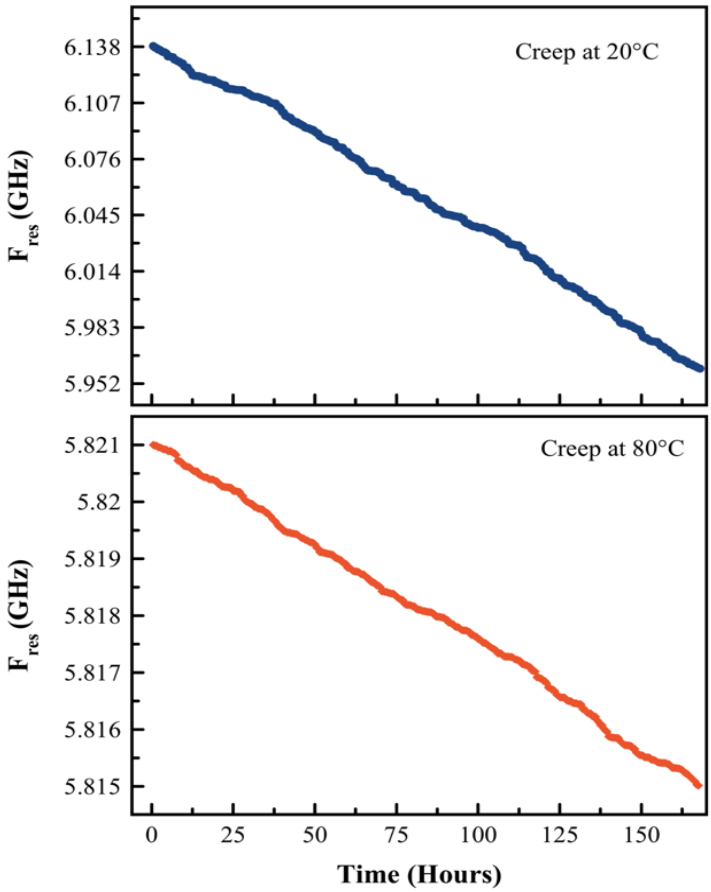

Figure 8.26: Long term temperature stability of MPA with rGO:MWCNT as patch layer

Conclusion and Future Work

9

In this thesis, the synthesis, characterization of nanocomposites based on CNTs and GO and PEDOT:PSS is successfully investigated and their application as sensing layer for passive strain and temperature wireless sensors is proved. A solution processing approach is proposed to prepare a nanocomposite with high conductivity and appropriate temperature and strain characteristics. The high film conductivity is required to be suitable as sensing layer on microstrip patch antenna for passive wireless sensing.

9.1 Conclusion

In this work, the percolation threshold of the MWCNT:SDBS/PEDOT:PSS nanocomposite is reached at very low CNTs content about 0.025wt.% MWCNT through non-covalently functionalization of the CNTs with an anionic surfactant (SDBS). In its aqueous state, it is found that the interfacial tension between the MWCNT:SDBS and PEDOT:PSS is lowered compared to the pure PEDOT:PSS due to the use of SDBS surfactant. The morphological structure of the MWCNT:SDBS/PEDOT:PSS nanocomposite forms a highly dense and excellent homogeneous films when MWCNT is dissolved in it. The optical investigations reveal the tunability of the optical bandgap of the nanocomposite using CNTs. The presence of sharp absorption peaks in the NIR region, is an indication of an occurrence of new local states in the Fermi level. Due to the good wrapping between the MWCNTs and the PEDOT:PSS, the prepared nanocomposites showed a good conduction although low CNT contents are used. This is referred to the strong π-π interaction interfacial coupling between the MWCNT and the thiophene rings of PEDOT, which let the charge carrier mobility to be more delocalized in the PEDOT chain. For pure PEDOT:PSS specimen, a decrease in the films resistance is observed when a tension force is applied due to the reduce in the distance between the PEDOT segments in PSS chains, adding MWCNT, the strain sensitivity is altered. For high MWCNT content, the behavior changed to be positive piezoresistive instead of negative in the pristine PEDOT:PSS and at low CNT content. This is referred to domination of the transport through the CNT instead of the PEDOT segments. Under temperature influence, MWCNT:SDBS/PEDOT:PSS nanocomposite shows a semiconducting behavior where increasing the temperature tends to reduce the resistance. The PEDOT:PSS is a highly hygroscopic material, therefore it showed an excellent sensitivity to humidity and it can be used for humidity sensing. However, films with high CNT content show less sensitivity to temperature and humidity effects and high electrical conductivity, thus it can be used in application such bulk hetero-junction in an organic thin-film solar cells. Instead of dispersing the CNT using a surfactant, the GO colloids are used as dispersant medium, and different MWCNT content are dispersed in GO aqueous solution. No big influence of the MWCNT content on the interfacial tension of the nanocomposite is remarked, but the GO:MWCNT hybrid nanocomposite shows a good wetting properties as the contact angle is always less than $\leq$90. The optical bandgap is tuned using different MWCNT content due to the partial recovery of the π-conjugation system. The surface morphological in terms of SEM revealed that the MWCNTs are good coated by the GO sheets, therefore high homogeneity are observed and a dense 3D network is formed.

Due to the insolation properties of the GO, a chemical reduction is involved. Raman and XPS measurement are used to quantitively determine the effect of the chemical reduction of the GO and GO:MWCNTs. Adding MWCNTs to rGO improve the electrical conduction, the improvement in the transport mechanism of the rGO:MWCNT films originates from the strong $\pi - \pi$-interfacial coupling between benzene rings of the MWCNT and the rGO, that promotes more mobile charge carrier delocalization between their electronic densities. Both GO and MWCNT have individually good piezoresistive properties, making hybrids based on GO and MWCNTs also a hybrid nanocomposite with a good piezoresistive characteristics, especially at 0.01wt.% MWCNTs, the mechanism controlling this behavior is due to the change of the tunneling distance either between the GO sheets or between the MWCNT. In addition, the change in the number of contact points between the GO and MWCNT, an increase in the resistance is noticed for an applied force and higher k-factor is obtained than the films based on rGO:MWCNT. Under temperature effect, the hybrid nanocomposite shows excellent sensitivity to temperature. Beside that, the rGO:MWCNT nanocomposite with 0.05wt.% MWCNTs shows a high electrical conductivity about 10^4S/m, which can have a good potential to be used as wireless temperature sensor. Due to the presence of the functional groups at the basal plane and the edges of the GO, the GO sheet shows an adequate sensitivity to humidity, whereas, the films based rGO:MWCNT shows less sensitivity to humidity. The electrical transport occurs mainly due the altering of the hole concentration within the GO sheet and the penetration of the water molecules between the GO sheet, these two effects are reduced in the presence of the MWCNT. The reduced rGO:MWCNT with 0.05wt.% MWCNT shows a high conductivity, low strain sensitivity as well as good temperature sensitivity. To further improve its electrical properties, mixing it with different volume of high conductive PEDOT:PSS polymer is introduced. The GO:MWCNT/PEDOT:PSS shows a good wettability properties with a contact angle less than 64°. For non-reduced films, a negative and low piezoresistivity is remarked, referred mainly to the PEDOT:PSS which dominates the conduction mechanism. After treating the films with strong acid, the electrical properties improved in the range of 10^5S/m which makes them very suitable for wireless sensing. Beside that, the piezoresistivity is dramatically improved and reached k-factor of about 97. On the other side, the effect of temperature is reduced, which makes the rGO:MWCNT/PEDOT:PSS nanocomposites having a great potential for strain sensing.
In this work, we show that the nanocomposite as patch layer of microstrip antenna introduces a new generation of wireless sensors, with high sensitivity and low cost as well as easy to implement. By choosing the appropriate nanocomposite for a specific application broad range of wireless sensors can be fabricated. Two wireless sensors are proposed and discussed. Strain wireless sensor based on GO:MWCNT/PEDOT:PSS that gives a sensitivity up to -4MHz/$\mu\varepsilon$ which up to date the highest strain sensitivity recorded for any wireless sensors, previously the strain sensitivity was in the range of few kHz/$\mu\varepsilon$ only. For the temperature wireless sensing, using GO:MWCNT as patch layer gave also a high temperature sensitivity (-46.1MHz/°C) which is almost 60 times higher than its metallic counterpart. Beside the high sensitivity of the patch antenna based nanocomposites, a low hysteresis is observed with less than 3% and adequate repeatability. The results show a highly potential of microstrip patch antenna based on nanocomposites as high robust, low cost and high sensitive passive wireless strain and temperature sensors.

9.2 Future Work

The results obtained in this thesis are already good achievement, but further investigation and development are of great benefits to be explored.

- Use of the dielectric relaxation spectroscopy to characterize the dielectric properties of the nanocomposites, to understand their behavior in different frequencies.
- Use of other characterization techniques such as Fourier transform infrared spectroscopy (FTIR) to analyze the bonding between the polymer matrix and carbon nanoparticles.
- The adhesion forces between the nanocomposites and the substrate can be investigated using AFM and scratch test, to improve the strain transfer between the substrate and the nanocomposite.
- Investigate the temperature dependency of the nanocomposites on broader temperature range, so the conduction mechanism can be better understood. Also, it is very helpful to investigate the α-transition in polymers and their nanocomposites, which is related to the Brownian motion of the main chains, such as glass transition, melting point, crystallization and curing using Differential Scanning Calorimetry (DSC). Also for the strain sensing, it is for interests to investigated more mechanical characteristics such as using Nanoindentation and three-point bending test.
- Optimization of the fabrication parameters of the nanocomposites and the deposition technique to obtain high yield of the nanocomposites wireless sensor. This included also the investigation of the rheological properties of the nanocomposites.
- Use of advanced deposition techniques such as inkjet, screen printing to deposit the nanocomposites on the substrate with high precision. As well as, to improve the scalability and reproducibility of the wireless sensor characteristics as well as reducing the production costs.
- Investigation of a suitable coating materials for the strain wireless antennas to prevent the effect of the environmental effects such as gases (water molecules) and temperature.
- Coupling the wireless sensor with an IC-chip, so antenna characteristic such as Q-factor, and the interrogation distance between the antenna and the reader can be further investigated.
- To measure the strain and temperature over broad area, and MPA array can be fabricated. Also, a strain in multidirection can be measured by fabricating a nanocomposite MPA with double resonance frequency.
- Use of different substrates, for instance for strain sensors, use of the low loss and high dielectric constant thin substrate and very flexible substrate such as PDMS substrate to fabricate a stretchable strain sensor. For temperature sensors, substrate with bi-linear temperature dependency can improve the temperature sensitivity significantly.
- Investigation of multi-resonance frequency antenna for multi-directional strain measurement and use of ceramic substrate for high temperature application.
- To avoid the hazardous effect of the chemical treatment, UV-light and thermal treatment, or combination between them can be used for reduction of the graphene oxide and carbon nanotubes hybrid nanocomposite and the tertiary nanocomposites.
- High sensitive wireless sensor based on patch antenna made of nanocomposite can be implemented in structural health monitoring, aerospace and automotive application. Also flexible substrates can be used for flexible electronics application. The high

electrical conductivity obtained from the tertiary nanocomposites indicates the attractive applications as electrical connectors in flexible electronics and organic solar cells.

Bibliography

1. Kaur, G., Adhikari, R., Cass, P., Bown, M., & Gunatillake, P. (2015). ***Electrically conductive polymers and composites for biomedical applications.*** RSC Advances, 5(47), 37553-37567.
2. *NASA Book Reveals Fascination with Wing Twist* [Online]. Available: `https://www.nasa.gov/sites/default/files/ec02-0203-46_full.jpg` [Accessed: 10-Sep-2017].
3. Lynch, J. P., & Loh, K. J. (2006). ***A summary review of wireless sensors and sensor networks for structural health monitoring.*** Shock and Vibration Digest, 38(2), 91-130.
4. Hanley, P., Fergus, P., & Bouhafs, F. (2013). ***A wireless body sensor platform to detect progressive deterioration in musculoskeletal systems***. Advances in Internet of Things, 3(02), 53.
5. *About High Frequency (HF) RFID Wireless Sensors* [Online]. Available: http://www.phaseivengr.com/wireless-technologies/wireless-technologies-overview /about-wireless-rfid-sensors/about-hf-rfid-wireless-sensors/ [Accessed: 10-Sep-2017].
6. Ahbe, D., Beer, S., Zwick, T., Wang, Y., & Tentzeris, M. M. (2012). ***Dual-band antennas for frequency-doubler-based wireless strain sensing.*** IEEE Antennas and wireless propagation letters, 11, 216-219.
7. Song, L., Myers, A. C., Adams, J. J., & Zhu, Y. (2014). ***Stretchable and reversibly deformable radio frequency antennas based on silver nanowires.*** ACS applied materials & interfaces, 6(6), 4248-4253.
8. Dobkin, D. M. (2012). ***The rf in RFID: uhf RFID in practice.*** Newnes.
9. Turcu, C. (Ed.). (2011). ***Designing and deploying RFID applications.*** InTech.
10. Huang, Q. A., Dong, L., & Wang, L. F. (2016). ***LC Passive Wireless Sensors Toward a Wireless Sensing Platform: Status, Prospects, and Challenges.*** Journal of Microelectromechanical Systems, 25(5), 822-841.
11. Martín, F. (2012). ***Metamaterials for wireless communications, radiofrequency identification, and sensors.*** ISRN Electronics, 2012.
12. Chen, T., Li, S., & Sun, H. (2012). ***Metamaterials application in sensing.*** Sensors, 12(3), 2742-2765.
13. Melik, R., Unal, E., Perkgoz, N. K., Puttlitz, C., & Demir, H. V. (2009). ***Metamaterial-based wireless strain sensors.*** Applied Physics Letters, 95(1), 011106.
14. Fatemi, H., Modarres-Zadeh, M. J., & Abdolvand, R. (2015, January). ***Passive wireless temperature sensing with piezoelectric MEMS resonators.*** In Micro Electro Mechanical Systems (MEMS), 2015 28th IEEE International Conference on (pp. 909-912). IEEE.

15. Duan, Y., Chang, Y., Liang, J., Zhang, H., Duan, X., Zhang, H., & Zhang, M. (2016). ***Wireless gas sensing based on a passive piezoelectric resonant sensor array through near-field induction.*** Applied Physics Letters, 109(26), 263503.
16. Shi, X., Yang, F., Xu, S., & Li, M. (2017). ***A Passive Temperature-Sensing Antenna Based on a Bimetal Strip Coil.*** Sensors, 17(4), 665.
17. Kimionis, J., Tentzeris, M. M., & Nikolaou, S. (2014, July). ***Inkjet-printed UHF RFID folded dipole antennas for remote sensing applications.*** In Antennas and Propagation Society International Symposium (APSURSI), 2014 IEEE (pp. 332-333). IEEE.
18. Occhiuzzi, C., Rida, A., Marrocco, G., & Tentzeris, M. (2011). ***RFID passive gas sensor integrating carbon nanotubes.*** IEEE Transactions on Microwave Theory and Techniques, 59(10), 2674-2684.
19. Yang, L., Zhang, R., Staiculescu, D., Wong, C. P., & Tentzeris, M. M. (2009). ***A novel conformal RFID-enabled module utilizing inkjet-printed antennas and carbon nanotubes for gas-detection applications.*** IEEE Antennas and Wireless Propagation Letters, 8, 653-656.
20. Lee, J. N., Park, J. D., Lee, K. C., & Park, J. K. (2014). ***Design of a meander dipole antenna with dielectric loading for a sensor node of a wireless sensor network.*** Microwave and Optical Technology Letters, 56(7), 1526-1531.
21. Das, N. K., Khorrami, F., & Nourbakhsh, S. (1998, July). ***New integrated piezoelectric-dielectric microstrip antenna for dual wireless actuation and sensing functions.*** In 5th Annual International Symposium on Smart Structures and Materials (pp. 133-146). International Society for Optics and Photonics.
22. Tata, U., Huang, H., Deb, S., Wang, J., & Chiao, J. C. (2008, December). ***A patch antenna-based strain sensor for structural health monitoring.*** In Smart Structures, Devices, and Systems IV (Vol. 7268).
23. Tata, U., Huang, H., Carter, R. L., & Chiao, J. C. (2008). ***Exploiting a patch antenna for strain measurements.*** Measurement Science and Technology, 20(1), 015201.
24. Mohammad, I., & Huang, H. (2010). ***Monitoring fatigue crack growth and opening using antenna sensors.*** Smart Materials and Structures, 19(5), 055023.
25. Deshmukh, S., & Huang, H. (2010). ***Wireless interrogation of passive antenna sensors.*** Measurement Science and Technology, 21(3), 035201.
26. Mohammad, I., Gowda, V., Zhai, H., & Huang, H. (2011). ***Detecting crack orientation using patch antenna sensors.*** Measurement Science and Technology, 23(1), 015102.
27. Daliri, A., Galehdar, A., John, S., Rowe, W., & Ghorbani, K. (2010). ***Circular microstrip patch antenna strain sensor for wireless structural health monitoring.*** In Proceedings of the World Congress on Engineering (Vol. 2, p. 1173).
28. Daliri, A., Galehdar, A., John, S., Rowe, W. S., & Ghorbani, K. (2011). ***Slotted circular microstrip patch antenna application in strain based structural health monitoring.*** In AIAC14 Fourteenth Australian International Aerospace Congress.
29. Daliri, A., Galehdar, A., Rowe, W. S., Ghorbani, K., & John, S. (2012). ***Utilising microstrip patch antenna strain sensors for structural health monitoring.*** Journal of Intelligent Material Systems and Structures, 23(2), 169-182.
30. Yi, X., Wu, T., Wang, Y., Leon, R. T., Tentzeris, M. M., & Lantz, G. (2011). ***Passive wireless smart-skin sensor using RFID-based folded patch antennas.*** International Journal of Smart and Nano Materials, 2(1), 22-38.

31. Yi, X., Cho, C., Cooper, J., Wang, Y., Tentzeris, M. M., & Leon, R. T. (2013). ***Passive wireless antenna sensor for strain and crack sensing—Electromagnetic modeling, simulation, and testing.*** Smart Materials and Structures, 22(8), 085009.
32. Salmani, Z., Xie, Y., Zheng, G., Zhang, H., & Zhang, H. (2011, March). ***Application of antenna in strain measurement.*** In Antenna Technology (iWAT), 2011 International Workshop on (pp. 336-339). IEEE.
33. Thai, T. T., Aubert, H., Pons, P., DeJean, G., Tentzeris, M. M., & Plana, R. (2013). ***Novel design of a highly sensitive RF strain transducer for passive and remote sensing in two dimensions.*** IEEE Transactions on Microwave Theory and Techniques, 61(3), 1385-1396.
34. Xu, X., & Huang, H. (2011). ***Multiplexing passive wireless antenna sensors for multi-site crack detection andmonitoring.*** Smart Materials and Structures, 21(1), 015004.
35. Huang, H. (2013). ***Flexible wireless antenna sensor: A review.*** IEEE sensors journal, 13(10), 3865-3872.
36. Wang, W., Liu, T., Ge, H., & Liu, M. (2015, January). ***Strain measurement based on microstrip patch antennas.*** In Reliability and Maintainability Symposium (RAMS), 2015 Annual (pp. 1-6). IEEE.
37. Sharma, I., & Thakare, V. (2015). ***Analysis of a Microstrip Rectangular Patch Antenna as a Strain Sensor.*** Analysis, 2(2).
38. Maurya, S., Yadava, R. L., & Yadav, R. K. (2013). ***Effect of temperature variation on microstrip patch antenna and temperature compensation technique.*** Int. J. Wireless Commun. Mobile Comput., 1(1), 35-40.
39. Cheng, H., Ebadi, S., Ren, X., & Gong, X. (2015). ***Wireless passive high-temperature sensor based on multifunctional reflective patch antenna up to 1050 degrees centigrade.*** Sensors and Actuators A: Physical, 222, 204-211.
40. Sanders, J. W., Yao, J., & Huang, H. (2015). ***Microstrip patch antenna temperature sensor.*** IEEE Sensors Journal, 15(9), 5312-5319.
41. Yao, J., Tchafa, F. M., Jain, A., Tjuatja, S., & Huang, H. (2016). ***Far-Field Interrogation of Microstrip Patch Antenna for Temperature Sensing Without Electronics.*** IEEE Sensors Journal, 16(19), 7053-7060.
42. Tan, Q., Wei, T., Chen, X., Luo, T., Wu, G., Li, C., & Xiong, J. (2015). ***Antenna-resonator integrated wireless passive temperature sensor based on low-temperature co-fired ceramic for harsh environment.*** Sensors and Actuators A: Physical, 236, 299-308.
43. Verma, A., Fumeaux, C., Truong, V. T., & Bates, B. D. (2010, December). ***Effect of film thickness on the radiation efficiency of a 4.5 GHz polypyrrole conducting polymer patch antenna.*** In Microwave Conference Proceedings (APMC), 2010 Asia-Pacific (pp. 95-98). IEEE.
44. Kirsch, N. J., Vacirca, N. A., Plowman, E. E., Kurzweg, T. P., Fontecchio, A. K., & Dandekar, K. R. (2009, April). ***Optically transparent conductive polymer RFID meandering dipole antenna.*** In RFID, 2009 IEEE International Conference on (pp. 278-282). IEEE.
45. Kirsch, N. J., Vacirca, N. A., Kurzweg, T. P., Fontecchio, A. K., & Dandekar, K. R. (2010, October). ***Performance of transparent conductive polymer antennas in a MIMO ad-hoc network.*** In Wireless and Mobile Computing, Networking and Communications (WiMob), 2010 IEEE 6th International Conference on (pp. 9-14). IEEE.

46. Kaufmann, T., Verma, A., Truong, V. T., Weng, B., Shepherd, R., & Fumeaux, C. (2012). ***Efficiency of a compact elliptical planar ultra-wideband antenna based on conductive polymers.*** International Journal of Antennas and Propagation, 2012.
47. Chen, S. J., Kaufmann, T., Shepherd, R., Chivers, B., Weng, B., Vassallo, A., & Fumeaux, C. (2015). ***A compact, highly efficient and flexible polymer ultra-wideband antenna.*** IEEE Antennas and Wireless Propagation Letters, 14, 1207-1210.
48. Manzari, S., Occhiuzzi, C., Nawale, S., Catini, A., Di Natale, C., & Marrocco, G. (2012). ***Humidity sensing by polymer-loaded UHF RFID antennas.*** IEEE Sensors Journal, 12(9), 2851-2858.
49. Abbasi, M. A. B., Vryonides, P., & Nikolaou, S. (2015, July). ***Humidity sensor devices using PEDOT: PSS.*** In Antennas and Propagation & USNC/URSI National Radio Science Meeting, 2015 IEEE International Symposium on (pp. 1366-1367). IEEE.
50. Nieuwoudt, A., & Massoud, Y. (2006). ***Evaluating the impact of resistance in carbon nanotube bundles for VLSI interconnect using diameter-dependent modeling techniques.*** IEEE Transactions on Electron Devices, 53(10), 2460-2466.
51. Karthikeyan, A., & Mallick, P. S. (2017). ***Optimization Techniques for CNT Based VLSI Interconnects—A Review.*** Journal of Circuits, Systems and Computers, 26(03), 1730002.
52. Naeemi, A., & Meindl, J. D. (2009). ***Carbon nanotube interconnects.*** Annual Review of Materials Research, 39, 255-275.
53. Awano, Y., Sato, S., Nihei, M., Sakai, T., Ohno, Y., & Mizutani, T. (2010). ***Carbon nanotubes for VLSI: interconnect and transistor applications.*** Proceedings of the IEEE, 98(12), 2015-2031.
54. Marulanda, J. M., & Srivastava, A. (2010). ***Numerical modeling of the IV characteristics of carbon nanotube field effect transistors.*** In Carbon Nanotubes. InTech.
55. Demoustier, S., Minoux, E., Le Baillif, M., Charles, M., & Ziaei, A. (2008). ***Review of two microwave applications of carbon nanotubes: nano-antennas and nano-switches.*** Comptes Rendus Physique, 9(1), 53-66.
56. Berres, J. A., & Hanson, G. W. (2011). ***Multiwall carbon nanotubes at RF-THz frequencies: scattering, shielding, effective conductivity, and power dissipation.*** IEEE Transactions on Antennas and Propagation, 59(8), 3098-3103.
57. Hanson, G. W. (2005). ***Fundamental transmitting properties of carbon nanotube antennas.*** IEEE Transactions on antennas and propagation, 53(11), 3426-3435.
58. Kumar, S. (2016). ***Nanoantenna–A Review on Present and Future Perspective.*** Science, Engineering and Technology, 8.
59. Mehdipour, A., Rosca, I. D., Sebak, A. R., Trueman, C. W., & Hoa, S. V. (2011). ***Carbon nanotube composites for wideband millimeter-wave antenna applications.*** IEEE Transactions on Antennas and Propagation, 59(10), 3572-3578.
60. Zhou, Y., Bayram, Y., Du, F., Dai, L., & Volakis, J. L. (2010). ***Polymer-carbon nanotube sheets for conformal load bearing antennas.*** IEEE Transactions on Antennas and Propagation, 58(7), 2169-2175.
61. Qian, Z., Emrick, R. M., Li, Z., & Scheer, R. L. (2011). U.S. Patent No. 7,898,481. Washington, DC: U.S. Patent and Trademark Office.
62. Elwi, T. A., Al-Rizzo, H. M., Rucker, D. G., Dervishi, E., Li, Z., & Biris, A. S. (2009). ***Multi-walled carbon nanotube-based RF antennas.*** Nanotechnology, 21(4), 045301.

63. Mehdipour, A., Aliakbarian, H., & Kamarei, M. (2007, April). ***A Novel Ultra Wideband Antenna for UWB Applications.*** In Antennas and Propagation Conference, 2007. LAPC 2007. Loughborough (pp. 213-216). IEEE.
64. Occhiuzzi, C., Rida, A., Marrocco, G., & Tentzeris, M. M. (2011, July). ***Passive ammonia sensor: RFID tag integrating carbon nanotubes.*** In Antennas and Propagation (APSURSI), 2011 IEEE International Symposium on (pp. 1413-1416). IEEE.
65. Keller, S. D., & Zaghloul, A. I. (2011, October). ***Multifunctional meshed carbon nanotube thread patch antenna.*** In Sensors, 2011 IEEE (pp. 631-634). IEEE.
66. Bayram, Y., Zhou, Y., Shim, B. S., Xu, S., Zhu, J., Kotov, N. A., & Volakis, J. L. (2010). ***E-textile conductors and polymer composites for conformal lightweight antennas.*** IEEE Transactions on Antennas and Propagation, 58(8), 2732-2736.
67. Mohammadi, A., Ismail, A., Mahdi, M. A., Abdullah, R. S. A. R., Isa, M. M., & Sadrolhosseini, A. R. (2012). ***Carbon-nanotube-based fr-4 patch antenna as a bio-material sensor.*** Procedia Engineering, 41, 724-728.
68. Tang, Q. Y., Pan, Y. M., Chan, Y. C., & Leung, K. W. (2012). ***Frequency-tunable soft composite antennas for wireless sensing.*** Sensors and Actuators A: Physical, 179, 137-145.
69. Feng, Y., Cabezas, A. L., Chen, Q., Zheng, L. R., & Zhang, Z. B. (2012). ***Flexible UHF resistive humidity sensors based on carbon nanotubes.*** IEEE Sensors Journal, 12(9), 2844-2850.
70. Puchades, I., Rossi, J. E., Cress, C. D., Naglich, E., & Landi, B. J. (2016). ***Carbon nanotube thin-film antennas.*** ACS applied materials & interfaces, 8(32), 20986-20992.
71. Perruisseau-Carrier, J. (2012, November). ***Graphene for antenna applications: Opportunities and challenges from microwaves to THz.*** In Antennas and Propagation Conference (LAPC), 2012 Loughborough (pp. 1-4). IEEE.
72. Gomez-Diaz, J. S., & Perruisseau-Carrier, J. (2012, October). ***Microwave to THz properties of graphene and potential antenna applications.*** In Antennas and Propagation (ISAP), 2012 International Symposium on (pp. 239-242). IEEE.
73. Zhang, C., Huang, J. Q., & Huang, Q. A. (2013, June). ***A passive wireless graphene oxide based humidity sensor and associated portable telemetry unit.*** In Solid-State Sensors, Actuators and Microsystems (TRANSDUCERS & EUROSENSORS XXVII), 2013 Transducers & Eurosensors XXVII: The 17th International Conference on (pp. 278-281). IEEE.
74. Chiang, C. K., Fincher Jr, C. R., Park, Y. W., Heeger, A. J., Shirakawa, H., Louis, E. J., & MacDiarmid, A. G. (1977). ***Electrical conductivity in doped polyacetylene.*** Physical review letters, 39(17), 1098.
75. Shirakawa, H., Louis, E. J., MacDiarmid, A. G., Chiang, C. K., & Heeger, A. J. (1977). ***Synthesis of electrically conducting organic polymers: halogen derivatives of polyacetylene,(CH) x.*** Journal of the Chemical Society, Chemical Communications, (16), 578-580.
76. Cao, Y., & Smith, P. (1993). ***Liquid-crystalline solutions of electrically conducting polyaniline.*** Polymer, 34(15), 3139-3143.
77. King, Z. A., Shaw, C. M., Spanninga, S. A., & Martin, D. C. (2011). ***Structural, chemical and electrochemical characterization of poly (3, 4-ethylenedioxy thiophene)(PEDOT) prepared with various counter-ions and heat treatments.*** Polymer, 52(5), 1302-1308.

78. Cui, X., & Martin, D. C. (2003). ***Electrochemical deposition and characterization of poly (3, 4-ethylenedioxythiophene) on neural microelectrode arrays.*** Sensors and Actuators B: Chemical, 89(1), 92-102.
79. Wang, Y. (2009). ***Research progress on a novel conductive polymer–poly (3, 4-ethylenedioxy thiophene)(PEDOT).*** In Journal of Physics: Conference Series (Vol. 152, No. 1, p. 012023). IOP Publishing.
80. Lewis, J. (2006). ***Material challenge for flexible organic devices.*** Materials today, 9(4), 38-45.
81. Elschner, A. (2011). ***The spectral sensitivity of PEDOT: PSS films.*** Solar Energy Materials and Solar Cells, 95(5), 1333-1338.
82. Potyrailo, R. A., Surman, C., Go, S., Lee, Y., Sivavec, T., & Morris, W. G. (2009). ***Development of radio-frequency identification sensors based on organic electronic sensing materials for selective detection of toxic vapors.*** Journal of Applied Physics, 106(12), 124902.
83. Crispin, X., Jakobsson, F. L. E., Crispin, A., Grim, P. C. M., Andersson, P., Volodin, A., & Berggren, M. (2006). ***The origin of the high conductivity of poly (3, 4-ethylenedioxythiophene) poly (styrenesulfonate)(PEDOT-PSS) plastic electrodes.*** Chemistry of Materials, 18(18), 4354-4360.
84. Wei, W., Wang, H., & Hu, Y. H. (2014). ***A review on PEDOT-based counter electrodes for dye-sensitized solar cells.*** International Journal of Energy Research, 38(9), 1099-1111.
85. Vosgueritchian, M., Lipomi, D. J., & Bao, Z. (2012). ***Highly conductive and transparent PEDOT: PSS films with a fluorosurfactant for stretchable and flexible transparent electrodes.*** Advanced functional materials, 22(2), 421-428.
86. Kim, Y. H., Sachse, C., Machala, M. L., May, C., Müller-Meskamp, L., & Leo, K. (2011). ***Highly conductive PEDOT: PSS electrode with optimized solvent and thermal post-treatment for ITO-free organic solar cells.*** Advanced Functional Materials, 21(6), 1076-1081.
87. Zhou, H., Zhang, Y., Mai, C. K., Collins, S. D., Nguyen, T. Q., Bazan, G. C., & Heeger, A. J. (2014). ***Conductive Conjugated Polyelectrolyte as Hole-Transport -ing Layer for Organic Bulk Heterojunction Solar Cells.*** Advanced Materials, 26(5), 780-785.
88. Krebs, F. C., & Norrman, K. (2010). ***Using light-induced thermocleavage in a roll-to-roll process for polymer solar cells.*** ACS applied materials & interfaces, 2(3), 877-887.
89. Nambiar, S., & Yeow, J. T. (2011). ***Conductive polymer-based sensors for biomedical applications.*** Biosensors and Bioelectronics, 26(5), 1825-1832.
90. Yin, Z., & Zheng, Q. (2012). ***Controlled Synthesis and Energy Applications of One-Dimensional Conducting Polymer Nanostructures: An Overview.*** Advanced Energy Materials, 2(2), 179-218.
91. Nardes, A. M. (2007). ***On the conductivity of PEDOT: PSS thin films.*** Technische Universiteit Eindhoven. Eindhoven, 132.
92. Groenendaal, L., Zotti, G., Aubert, P. H., Waybright, S. M., & Reynolds, J. R. (2003). ***Electrochemistry of Poly (3, 4-alkylenedioxythiophene) Derivatives.*** Advanced Materials, 15(11), 855-879.
93. Schweizer, T. M. (2005). ***Electrical characterization and investigation of the piezoresistive effect of PEDOT: PSS thin films*** (Doctoral dissertation, Georgia Institute of Technology).

94. Skotheim, T. A., & Reynolds, J. (Eds.). (2007). ***Handbook of Conducting Polymers,*** 2 Volume Set. CRC press.
95. Kirchmeyer, S., & Reuter, K. (2005). ***Scientific importance, properties and growing applications of poly (3, 4-ethylenedioxythiophene).*** Journal of Materials Chemistry, 15(21), 2077-2088.
96. Gelinck, G. H., Marsman, A. W., Touwslager, F. J., Setayesh, S., De Leeuw, D. M., Naber, R. C. G., & Blom, P. W. M. (2005). ***All-polymer ferroelectric transistors.*** Applied Physics Letters, 87(9), 092903.
97. Le, T. H., Kim, Y., & Yoon, H. (2017). ***Electrical and electrochemical properties of conducting polymers.*** Polymers, 9(4), 150.
98. Kronemeijer, A. J., Huisman, E. H., Katsouras, I., Van Hal, P. A., Geuns, T. C. T., Blom, P. W. M., & De Leeuw, D. M. (2010). ***Universal scaling in highly doped conducting polymer films.*** Physical review letters, 105(15), 156604.
99. Aleshin, A., Kiebooms, R., Menon, R., & Heeger, A. J. (1997). ***Electronic transport in doped poly (3, 4-ethylenedioxythiophene) near the metal-insulator transition.*** Synthetic metals, 90(1), 61-68.
100. Aleshin, A. N., Kiebooms, R., & Heeger, A. J. (1999). ***Metallic conductivity of highly doped poly (3, 4-ethylenedioxythiophene).*** Synthetic metals, 101(1-3), 369-370.
101. Kroto, H. W., Heath, J. R., O'Brien, S. C., Curl, R. F., & Smalley, R. E. (1985). ***C60: Buckminsterfullerene.*** Nature, 318(6042), 162-163.
102. Iijima, S. (1991). ***Helical microtubules of graphitic carbon.*** nature, 354 (6348), 56.
103. Novoselov, K. S., Geim, A. K., Morozov, S. V., Jiang, D., Zhang, Y., Dubonos, S. V., & Firsov, A. A. (2004). ***Electric field effect in atomically thin carbon films.*** science, 306(5696), 666-669.
104. Nemec, N. (2007). ***Quantum transport in carbon-based nanostructures*** (Doctoral dissertation).
105. Liu, M., Artyukhov, V. I., Lee, H., Xu, F., & Yakobson, B. I. (2013). ***Carbyne from first principles: chain of C atoms, a nanorod or a nanorope.*** ACS nano, 7(11), 10075-10082.
106. *Graphene: 2D carbon* [Online]. Available: http://graphita.bo.imm.cnr.it/graphita 2011/graphene.html [Accessed: 13-Sep-2017].
107. *Allotropes of carbon* [Online]. Available: https://en.wikipedia.org/wiki/ Allotropes_of_ carbon [Accessed: 13-Sep-2017].
108. Radushkevich, L. V., & Lukyanovich, V. M. (1952). ***O strukture ugleroda, obrazujucegosja pri termiceskom razlozenii okisi ugleroda na zeleznom kontakte. (About the structure of carbon formed by thermal decomposition of carbon monoxide on iron substrate)*** Zurn Fisic Chim, 26(1), 88-95.
109. Monthioux, M., & Kuznetsov, V. L. (2006). ***Who should be given the credit for the discovery of carbon nanotubes?.*** Carbon, 44(9), 1621-1623.
110. Iijima, S., & Ichihashi, T. (1993). ***Single-shell carbon nanotubes of 1-nm diameter.*** nature, 363(6430), 603-605.
111. Bethune, D. S., Kiang, C. H., De Vries, M. S., Gorman, G., Savoy, R., Vazquez, J., & Beyers, R. (1993). ***Cobalt-catalysed growth of carbon nanotubes with single-atomic-layer walls.*** Nature, 363(6430), 605-607.
112. Gogotsi, Y. (Ed.). (2006). ***Nanomaterials handbook.*** CRC press.

113. Murray, A. R., Kisin, E., Leonard, S. S., Young, S. H., Kommineni, C., Kagan, V. E., & Shvedova, A. A. (2009). ***Oxidative stress and inflammatory response in dermal toxicity of single-walled carbon nanotubes.*** Toxicology, 257(3), 161-171.
114. Velasco-Santos, C., Martinez-Hernandez, A. L., & Castano, V. M. (2005). ***Carbon nanotube-polymer nanocomposites: The role of interfaces.*** Composite Interfaces, 11(8-9), 567-586.
115. Wong, H. S. P., & Akinwande, D. (2011). ***Carbon nanotube and graphene device physics.*** Cambridge University Press.
116. Kuzum, D., Yu, S., & Wong, H. P. (2013). ***Synaptic electronics: materials, devices and applications.*** Nanotechnology, 24(38), 382001.
117. Ando, Y., Zhao, X., Shimoyama, H., Sakai, G., & Kaneto, K. (1999). ***Physical properties of multiwalled carbon nanotubes.*** International journal of inorganic materials, 1(1), 77-82.
118. Bandaru, P. R. (2007). ***Electrical properties and applications of carbon nanotube structures.*** Journal of nanoscience and nanotechnology, 7(4-1), 1239-1267.
119. Qian, D., Wagner, G. J., Liu, W. K., Yu, M. F., & Ruoff, R. S. (2002). ***Mechanics of carbon nanotubes.*** Applied mechanics reviews, 55(6), 495-533.
120. Lukes, J. R., & Zhong, H. (2007). ***Thermal conductivity of individual single-wall carbon nanotubes.*** Journal of Heat Transfer, 129(6), 705-716.
121. Sukhadolau, A. V., Ivakin, E. V., Ralchenko, V. G., Khomich, A. V., Vlasov, A. V., & Popovich, A. F. (2005). ***Thermal conductivity of CVD diamond at elevated temperatures.*** Diamond and related materials, 14(3), 589-593.
122. Walters, D. A., Casavant, M. J., Qin, X. C., Huffman, C. B., Boul, P. J., Ericson, L. M., & Smalley, R. E. (2001). ***In-plane-aligned membranes of carbon nanotubes.*** Chemical Physics Letters, 338(1), 14-20.
123. Guldi, D. M., & Martín, N. (Eds.). (2010). ***Carbon nanotubes and related structures: synthesis, characterization, functionalization, and applications.*** John Wiley & Sons.
124. Ebbesen, T. W., & P M, A. (1992). ***Large-scale synthesis of carbon.*** Nature, 358, 16.
125. O'Connell, M. J., Boul, P., Ericson, L. M., Huffman, C., Wang, Y., Haroz, E., & Smalley, R. E. (2001). ***Reversible water-solubilization of single-walled carbon nanotubes by polymer wrapping.*** Chemical physics letters, 342(3), 265-271.
126. Harris, P. J. F. (2009). ***Carbon nanotube science: synthesis, properties and applications.*** Cambridge University Press.
127. Krueger, A. (2010). ***Carbon materials and nanotechnology.*** John Wiley & Sons.
128. Prasek, J., Drbohlavova, J., Chomoucka, J., Hubalek, J., Jasek, O., Adam, V., & Kizek, R. (2011). ***Methods for carbon nanotubes synthesis.*** Journal of Materials Chemistry, 21(40), 15872-15884.
129. Farhat, S., Lamy de La Chapelle, M., Loiseau, A., Scott, C. D., Lefrant, S., Journet, C., & Bernier, P. (2001). ***Diameter control of single-walled carbon nanotubes using argon–helium mixture gases.*** The Journal of Chemical Physics, 115(14), 6752-6759.
130. Haubner, K., Murawski, J., Olk, P., Eng, L. M., Ziegler, C., Adolphi, B., & Jaehne, E. (2010). ***The route to functional graphene oxide.*** ChemPhysChem, 11(10), 2131-2139.
131. Lerf, A., He, H., Forster, M., & Klinowski, J. (1998). ***Structure of graphite oxide revisited‖.*** The Journal of Physical Chemistry B, 102(23), 4477-4482.
132. Li, D., Müller, M. B., Gilje, S., Kaner, R. B., & Wallace, G. G. (2008). ***Processable aqueous dispersions of graphene nanosheets.*** Nature nanotechnology, 3(2), 101-105.

133. Park, S., An, J., Piner, R. D., Jung, I., Yang, D., Velamakanni, A., & Ruoff, R. S. (2008). ***Aqueous suspension and characterization of chemically modified graphene sheets.*** Chemistry of materials, 20(21), 6592-6594.
134. Kim, F., Cote, L. J., & Huang, J. (2010). ***Graphene Oxide: Surface Activity and Two-Dimensional Assembly.*** Advanced Materials, 22(17), 1954-1958.
135. Hofmann, U., & Holst, R. (1939). ***The acidic nature and the methylation of graphitoxide.*** Berichte der deutschen chemischen Gesellschaft, 72, 754-771.
136. Ruess, G. (1947). ***Über das graphitoxyhydroxyd (graphitoxyd).*** Monatshefte für Chemie/Chemical Monthly, 76(3), 381-417.
137. Boehm, H. P., Clauss, A., Fischer, G. O., & Hofmann, U. (1962). ***Das adsorptionsverhalten sehr d/"unner kohlenstoff-folien.*** Zeitschrift f/"ur anorganische und allgemeine Chemie, 316(3-4), 119-127.
138. Chen, Y., Fu, K., Zhu, S., Luo, W., Wang, Y., Li, Y., & Danner, V. A. (2016). ***Reduced Graphene Oxide Films with Ultrahigh Conductivity as Li-Ion Battery Current Collectors.*** Nano letters, 16(6), 3616-3623.
139. Brodie, B. C. (1860). ***Sur le poids atomique du graphite.*** Ann. Chim. Phys, 59(466), e472.
140. Staudenmaier, L. (1898). ***Verfahren zur darstellung der graphitsäure.*** European Journal of Inorganic Chemistry, 31(2), 1481-1487.
141. Hummers Jr, W. S., & Offeman, R. E. (1958). ***Preparation of graphitic oxide.*** Journal of the American Chemical Society, 80(6), 1339-1339.
142. Khan, Z. U., Kausar, A., Ullah, H., Badshah, A., & Khan, W. U. (2016). ***A review of graphene oxide, graphene buckypaper, and polymer/graphene composites: Properties and fabrication techniques.*** Journal of Plastic Film & Sheeting, 32(4), 336-379.
143. Dreyer, D. R., Park, S., Bielawski, C. W., & Ruoff, R. S. (2010). ***The chemistry of graphene oxide.*** Chemical Society Reviews, 39(1), 228-240.
144. Goh, M. S., & Pumera, M. (2011). ***Graphene-based electrochemical sensor for detection of 2, 4, 6-trinitrotoluene (TNT) in seawater: the comparison of single-, few-, and multilayer graphene nanoribbons and graphite microparticles.*** Analytical and bioanalytical chemistry, 399(1), 127-131.
145. Zhang, C., Ren, L., Wang, X., & Liu, T. (2010). ***Graphene oxide-assisted dispersion of pristine multiwalled carbon nanotubes in aqueous media.*** The Journal of Physical Chemistry C, 114(26), 11435-11440.
146. Chua, C. K., & Pumera, M. (2014). ***Chemical reduction of graphene oxide: a synthetic chemistry viewpoint.*** Chemical Society Reviews, 43(1), 291-312.
147. Konios, D., Stylianakis, M. M., Stratakis, E., & Kymakis, E. (2014). ***Dispersion behaviour of graphene oxide and reduced graphene oxide.*** Journal of colloid and interface science, 430, 108-112.
148. Amieva, E. J. C., López-Barroso, J., Martínez-Hernández, A. L., & Velasco-Santos, C. (2016). ***Graphene-Based Materials Functionalization with Natural Polymeric Biomolecules***. In Recent Advances in Graphene Research. InTech.
149. Mathkar, A., Tozier, D., Cox, P., Ong, P., Galande, C., Balakrishnan, K., & Ajayan, P. M. (2012). ***Controlled, stepwise reduction and band gap manipulation of graphene oxide.*** The journal of physical chemistry letters, 3(8), 986-991.
150. Acik, M., & Chabal, Y. J. (2013). ***A review on thermal exfoliation of graphene oxide.*** Journal of Materials Science Research, 2(1), 101.

151. Design, G. (2013). ***Prospects of Graphene-Based Nanocomposites for Solar Energy Conversion, Storage, and Sensing Light.*** cap, Ian V.; Kamat, Prashant V. Accounts of Chemical Research, 46(10), 2235-2243.
152. Velasco-Soto, M. A., Pérez-García, S. A., Alvarez-Quintana, J., Cao, Y., Nyborg, L., & Licea-Jiménez, L. (2015). ***Selective band gap manipulation of graphene oxide by its reduction with mild reagents.*** Carbon, 93, 967-973.
153. Fernández-Merino, M. J., Paredes, J. I., Villar-Rodil, S., Guardia, L., Solís-Fernández, P., Salinas-Torres, D., & Tascón, J. M. D. (2012). ***Investigating the influence of surfactants on the stabilization of aqueous reduced graphene oxide dispersions and the characteristics of their composite films.*** Carbon, 50(9), 3184-3194.
154. Pei, S., Zhao, J., Du, J., Ren, W., & Cheng, H. M. (2010). ***Direct reduction of graphene oxide films into highly conductive and flexible graphene films by hydrohalic acids.*** Carbon, 48(15), 4466-4474.
155. Moon, I. K., Lee, J., Ruoff, R. S., & Lee, H. (2010). ***Reduced graphene oxide by chemical graphitization.*** Nature communications, 1(6), 73.
156. Eda, G., & Chhowalla, M. (2009). ***Graphene-based composite thin films for electronics.*** Nano Letters, 9(2), 814-818.
157. Yang, W., Zhao, Y., He, X., Chen, Y., Xu, J., Li, S., & Jiang, Y. (2015). ***Flexible conducting polymer/reduced graphene oxide films: synthesis, characterization, and electrochemical performance.*** Nanoscale research letters, 10(1), 222.
158. King, A. A., Davies, B. R., Noorbehesht, N., Newman, P., Church, T. L., Harris, A. T., & Minett, A. I. (2016). ***A New Raman Metric for the Characterisation of Graphene oxide and its Derivatives.*** Scientific reports, 6.
159. Mkhoyan, K. A., Contryman, A. W., Silcox, J., Stewart, D. A., Eda, G., Mattevi, C., & Chhowalla, M. (2009). ***Atomic and electronic structure of graphene-oxide.*** Nano letters, 9(3), 1058-1063.
160. Gomez-Navarro, C., Meyer, J. C., Sundaram, R. S., Chuvilin, A., Kurasch, S., Burghard, M., & Kaiser, U. (2010). ***Atomic structure of reduced graphene oxide.*** Nano letters, 10(4), 1144-1148.
161. Konios, D., Petridis, C., Kakavelakis, G., Sygletou, M., Savva, K., Stratakis, E., & Kymakis, E. (2015). ***Reduced graphene oxide micromesh electrodes for large area, flexible, organic photovoltaic devices.*** Advanced Functional Materials, 25(15), 2213-2221.
162. Kumar, A., & Zhou, C. (2010). ***The race to replace tin-doped indium oxide: which material will win?.*** ACS nano, 4(1), 11-14.
163. Jia, S., Sun, H. D., Du, J. H., Zhang, Z. K., Zhang, D. D., Ma, L. P., & Ren, W. C. (2016). ***Graphene oxide/graphene vertical heterostructure electrodes for highly efficient and flexible organic light emitting diodes.*** Nanoscale, 8(20), 10714-10723.
164. Bonaccorso, F., Sun, Z., Hasan, T., & Ferrari, A. C. (2010). ***Graphene photonics and optoelectronics.*** Nature photonics, 4(9), 611-622.
165. Suk, J. W., Piner, R. D., An, J., & Ruoff, R. S. (2010). ***Mechanical properties of monolayer graphene oxide.*** ACS nano, 4(11), 6557-6564.
166. Gómez-Navarro, C., Burghard, M., & Kern, K. (2008). ***Elastic properties of chemically derived single graphene sheets.*** Nano letters, 8(7), 2045-2049.
167. Pillai, S. K., & Ray, S. S. (2011). ***Epoxy-based carbon nanotubes reinforced composites.*** In Advances in Nanocomposites-Synthesis, Characterization and Industrial Applications. InTech.

168. Chiolerio, A., Castellino, M., Jagdale, P., Giorcelli, M., Bianco, S., & Tagliaferro, A. (2011). ***Electrical properties of CNT-based polymeric matrix nanocomposites.*** In Carbon Nanotubes-Polymer Nanocomposites. InTech.
169. Min, B. G., Chae, H. G., Minus, M. L., & Kumar, S. (2009). ***Polymer/carbon nanotube composite fibers—an overview.*** Functional Composites of Carbon Nanotubes and Applications, 2, 43-73.
170. Jin, L., Bower, C., & Zhou, O. (1998). ***Alignment of carbon nanotubes in a polymer matrix by mechanical stretching.*** Applied physics letters, 73(9), 1197-1199.
171. Diez-Pascual, A. M., Naffakh, M., Gomez, M. A., Marco, C., Ellis, G., Martinez, M. T., & Simard, B. (2009). ***Development and characterization of PEEK/carbon nanotube composites.*** Carbon, 47(13), 3079-3090.
172. Ogasawara, T., Tsuda, T., & Takeda, N. (2011). ***Stress–strain behavior of multi-walled carbon nanotube/PEEK composites.*** Composites science and technology, 71(2), 73-78.
173. Mahmood, N., Islam, M., Hameed, A., & Saeed, S. (2013). ***Polyamide /multiwalled carbon nanotubes nanocomposites with modified morphology and thermal properties.*** Polymers, 5(4), 1380-1391.
174. Kuila, B. K., Malik, S., Batabyal, S. K., & Nandi, A. K. (2007). ***In-situ synthesis of soluble poly (3-hexylthiophene)/multiwalled carbon nanotube composite: Morphology, structure, and conductivity.*** Macromolecules, 40(2), 278-287.
175. Gajendran, P., & Saraswathi, R. (2008). ***Polyaniline-carbon nanotube composites.*** Pure and Applied Chemistry, 80(11), 2377-2395.
176. Abd Razak, S. I., Wahab, I. F., Fadil, F., Dahli, F. N., Md Khudzari, A. Z., & Adeli, H. (2015). ***A review of electrospun conductive polyaniline based nanofiber composites and blends: processing features, applications, and future directions.*** Advances in Materials Science and Engineering, 2015.
177. Gerwig, R., Fuchsberger, K., Schroeppel, B., Link, G. S., Heusel, G., Kraushaar, U., & Stelzle, M. (2012). ***PEDOT–CNT composite microelectrodes for recording and electrostimulation applications: fabrication, morphology, and electrical properties.*** Frontiers in neuroengineering, 5.
178. Loh, K. P., Bao, Q., Ang, P. K., & Yang, J. (2010). ***The chemistry of graphene.*** Journal of Materials Chemistry, 20(12), 2277-2289.
179. Loh, K. P., Bao, Q., Eda, G., & Chhowalla, M. (2010). ***Graphene oxide as a chemically tunable platform for optical applications.*** Nature chemistry, 2(12), 1015-1024.
180. Georgakilas, V., Tiwari, J. N., Kemp, K. C., Perman, J. A., Bourlinos, A. B., Kim, K. S., & Zboril, R. (2016). ***Noncovalent functionalization of graphene and graphene oxide for energy materials, biosensing, catalytic, and biomedical applications.*** Chem. Rev, 116(9), 5464-5519.
181. Chen, D., Feng, H., & Li, J. (2012). ***Graphene oxide: preparation, functionalization, and electrochemical applications.*** Chemical reviews, 112(11), 6027-6053.
182. Huang, Y., Qin, Y., Zhou, Y., Niu, H., Yu, Z., & Dong, J. Y. (2010). ***Polypropylene/graphene oxide nanocomposites prepared by in situ Ziegler- Natta polymerization.*** Chemistry of Materials, 22(13), 4096-4102.
183. Yuan, B., Bao, C., Song, L., Hong, N., Liew, K. M., & Hu, Y. (2014). ***Preparation of functionalized graphene oxide/polypropylene nanocomposite with significantly improved thermal stability and studies on the crystallization behavior and mechanical properties.*** Chemical Engineering Journal, 237, 411-420.

184. Kashyap, S., Pratihar, S. K., & Behera, S. K. (2016). ***Strong and ductile graphene oxide reinforced PVA nanocomposites.*** Journal of Alloys and Compounds, 684, 254-260.
185. Abdullah, S. I., & Ansari, M. N. M. (2015). ***Mechanical properties of graphene oxide (GO)/epoxy composites.*** HBRC Journal, 11(2), 151-156.
186. Pham, V. H., Dang, T. T., Hur, S. H., Kim, E. J., & Chung, J. S. (2012). ***Highly conductive poly (methyl methacrylate)(PMMA)-reduced graphene oxide composite prepared by self-assembly of PMMA latex and graphene oxide through electrostatic interaction.*** ACS applied materials & interfaces, 4(5), 2630-2636.
187. Konwer, S., Guha, A. K., & Dolui, S. K. (2013). ***Graphene oxide-filled conducting polyaniline composites as methanol-sensing materials.*** Journal of Materials Science, 48(4), 1729-1739.
188. Mitra, M., Kulsi, C., Chatterjee, K., Kargupta, K., Ganguly, S., Banerjee, D., & Goswami, S. (2015). ***Reduced graphene oxide-polyaniline composites—synthesis, characterization and optimization for thermoelectric applications.*** RSC Advances, 5(39), 31039-31048.
189. Lee, D. C., Yang, H. N., Park, S. H., & Kim, W. J. (2014). ***Nafion/graphene oxide composite membranes for low humidifying polymer electrolyte membrane fuel cell.*** Journal of Membrane Science, 452, 20-28.
190. Lue, S. J., Pai, Y. L., Shih, C. M., Wu, M. C., & Lai, S. M. (2015). ***Novel bilayer well-aligned Nafion/graphene oxide composite membranes prepared using spin coating method for direct liquid fuel cells.*** Journal of Membrane Science, 493, 212-223.
191. Upadhyay, R., Naskar, S., Bhaskar, N., Bose, S., & Basu, B. (2016). ***Modulation of protein adsorption and cell proliferation on polyethylene immobilized graphene oxide reinforced HDPE bionanocomposites.*** ACS applied materials & interfaces, 8(19), 11954-11968.
192. Gan, L., Shang, S., & Jiang, S. X. (2016). ***Impact of vinyl concentration of a silicone rubber on the properties of the graphene oxide filled silicone rubber composites.*** Composites Part B: Engineering, 84, 294-300.
193. Zhao, X. W., Zang, C. G., Wen, Y. Q., & Jiao, Q. J. (2015). ***Thermal and mechanical properties of liquid silicone rubber composites filled with functionalized graphene oxide.*** Journal of Applied Polymer Science, 132(38).
194. Fujigaya, T., & Nakashima, N. (2015). ***Non-covalent polymer wrapping of carbon nanotubes and the role of wrapped polymers as functional dispersants.*** Science and technology of advanced materials, 16(2), 024802.
195. Islam, M. F., Rojas, E., Bergey, D. M., Johnson, A. T., & Yodh, A. G. (2003). ***High weight fraction surfactant solubilization of single-wall carbon nanotubes in water.*** Nano letters, 3(2), 269-273.
196. Yu, J., Grossiord, N., Koning, C. E., & Loos, J. (2007). ***Controlling the dispersion of multi-wall carbon nanotubes in aqueous surfactant solution.*** Carbon, 45(3), 618-623.
197. Rastogi, R., Kaushal, R., Tripathi, S. K., Sharma, A. L., Kaur, I., & Bharadwaj, L. M. (2008). ***Comparative study of carbon nanotube dispersion using surfactants.*** Journal of colloid and interface science, 328(2), 421-428.
198. Ausman, K. D., Piner, R., Lourie, O., Ruoff, R. S., & Korobov, M. (2000). ***Organic solvent dispersions of single-walled carbon nanotubes: toward solutions of pristine nanotubes.*** The Journal of Physical Chemistry B, 104(38), 8911-8915.

199. Bahr, J. L., Yang, J., Kosynkin, D. V., Bronikowski, M. J., Smalley, R. E., & Tour, J. M. (2001). ***Functionalization of carbon nanotubes by electrochemical reduction of aryl diazonium salts: a bucky paper electrode.*** Journal of the American Chemical Society, 123(27), 6536-6542.
200. Amirani, M. C., & Tang, T. (2015). ***A QM: MM model for the interaction of DNA nucleotides with carbon nanotubes.*** Physical Chemistry Chemical Physics, 17(11), 7564-7575.
201. Wallace, E. J., & Sansom, M. S. (2008). ***Carbon nanotube self-assembly with lipids and detergent: a molecular dynamics study.*** Nanotechnology, 20(4), 045101.
202. Kuilla, T., Bhadra, S., Yao, D., Kim, N. H., Bose, S., & Lee, J. H. (2010). ***Recent advances in graphene based polymer composites.*** Progress in polymer science, 35(11), 1350-1375.
203. Potts, J. R., Dreyer, D. R., Bielawski, C. W., & Ruoff, R. S. (2011). ***Graphene-based polymer nanocomposites.*** Polymer, 52(1), 5-25.
204. *Die Vorteile der Heißschmelzextrusion* [Online]. Available: https://www.thermo fisher.com /de/de/home/industrial/pharma-biopharma/drug- formulation-manufacturing/hot-melt-extrusion.html [Accessed: 15-Sep-2017].
205. Krause, B., Pötschke, P., & Häußler, L. (2009). ***Influence of small scale melt mixing conditions on electrical resistivity of carbon nanotube-polyamide composites.*** Composites Science and Technology, 69(10), 1505-1515.
206. Pan, Y., Li, L., Chan, S. H., & Zhao, J. (2010). ***Correlation between dispersion state and electrical conductivity of MWCNTs/PP composites prepared by melt blending.*** Composites Part A: Applied Science and Manufacturing, 41(3), 419-426.
207. Mittal, G., Dhand, V., Rhee, K. Y., Park, S. J., & Lee, W. R. (2015). ***A review on carbon nanotubes and graphene as fillers in reinforced polymer nanocomposites.*** Journal of Industrial and Engineering Chemistry, 21, 11-25.
208. Wu, Z., Wang, H., Tian, X., Ding, X., Zhou, H., & Ye, X. (2014). ***Fabrication and properties of carbon nanotube/ styrene–ethylene–butylene–styrene composites via a sequential process of (electrostatic adsorption aided dispersion) -plus-(melt mixing).*** Journal of Applied Polymer Science, 131(9).
209. Gopakumar, T. G., & Page, D. J. Y. S. (2004). ***Polypropylene/graphite nanocomposites by thermo-kinetic mixing.*** Polymer Engineering & Science, 44(6), 1162-1169.
210. El Achaby, M., Arrakhiz, F. E., Vaudreuil, S., Essassi, E. M., Qaiss, A., & Bousmina, M. (2013). ***Nanocomposite films of poly (vinylidene fluoride) filled with polyvinylpyrrolidone -coated multiwalled carbon nanotubes: Enhancement of ß-polymorph formation and tensile properties.*** Polymer Engineering & Science, 53(1), 34-43.
211. Tong, J., Huang, H. X., & Wu, M. (2016). ***Facile green fabrication of well dispersed poly (vinylidene fluoride)/graphene oxide nanocomposites with improved properties.*** Composites Science and Technology, 129, 183-190.
212. Huh, S. H. (2011). ***Thermal reduction of graphene oxide. In Physics and Applications of Graphene-Experiments.*** InTech.
213. Pei, S., & Cheng, H. M. (2012). ***The reduction of graphene oxide.*** Carbon, 50(9), 3210-3228.
214. Lahelin, M., Annala, M., Nykänen, A., Ruokolainen, J., & Seppälä, J. (2011). ***In situ polymerized nanocomposites: Polystyrene/CNT and Poly (methyl methacrylate)/CNT composites.*** Composites Science and Technology, 71(6), 900-907.

215. Schnoor, T. I., Smith, G., Eder, D., Koziol, K. K., Burstein, G. T., Windle, A. H., & Schulte, K. (2013). ***The production of aligned MWCNT/polypyrrole composite films.*** Carbon, 60, 229-235.
216. Choi, C. S., Park, B. J., & Choi, H. J. (2007). ***Electrical and rheological characteristics of poly (vinyl acetate)/multi-walled carbon nanotube nanocomposites.*** Diamond and related materials, 16(4), 1170-1173.
217. Reddy, K. R., Sin, B. C., Ryu, K. S., Kim, J. C., Chung, H., & Lee, Y. (2009). ***Conducting polymer functionalized multi-walled carbon nanotubes with noble metal nanoparticles: synthesis, morphological characteristics and electrical properties.*** Synthetic Metals, 159(7), 595-603.
218. Zhao, Y., Tang, G. S., Yu, Z. Z., & Qi, J. S. (2012). ***The effect of graphite oxide on the thermoelectric properties of polyaniline.*** Carbon, 50(8), 3064-3073.
219. Wei, Q., Wang, X., & Zhou, F. (2012). ***A versatile macro-initiator with dual functional anchoring groups for surface-initiated atom transfer radical polymerization on various substrates.*** Polymer Chemistry, 3(8), 2129-2137.
220. Ferreira, F. V., Cividanes, L. D. S., Brito, F. S., de Menezes, B. R. C., Franceschi, W., Simonetti, E. A. N., & Thim, G. P. (2016). ***Functionalization of Carbon Nanotube and Applications.*** In Functionalizing Graphene and Carbon Nanotubes (pp. 31-61). Springer International Publishing.
221. Liu, J., Ye, Y., Xue, Y., Xie, X., & Mai, Y. W. (2017). ***Recent advances in covalent functionalization of carbon nanomaterials with polymers: Strategies and perspectives.*** Journal of Polymer Science Part A: Polymer Chemistry, 55(4), 622-631.
222. Banerjee, S., Hemraj-Benny, T., & Wong, S. S. (2005). ***Covalent surface chemistry of single-walled carbon nanotubes.*** Advanced Materials, 17(1), 17-29.
223. Ram, R., Rahaman, M., Aldalbahi, A., & Khastgir, D. (2017). ***Determination of percolation threshold and electrical conductivity of polyvinylidene fluoride (PVDF)/short carbon fiber (SCF) composites: effect of SCF aspect ratio.*** Polymer International, 66(4), 573-582.
224. Bello, A., Laredo, E., Marval, J. R., Grimau, M., Arnal, M. L., Müller, A. J., & Dubois, P. (2011). ***Universality and percolation in biodegradable poly (ε-caprolactone)/ multiwalled carbon nanotube nanocomposites from broad band alternating and direct current conductivity at various temperatures.*** Macromolecules, 44(8), 2819-2828.
225. Kilbride, B. E., Coleman, J. N., Fraysse, J., Fournet, P., Cadek, M., Drury, A., & Blau, W. J. (2002). ***Experimental observation of scaling laws for alternating current and direct current conductivity in polymer-carbon nanotube composite thin films.*** Journal of Applied Physics, 92(7), 4024-4030.
226. Bergman, D. J., & Imry, Y. (1977). ***Critical behavior of the complex dielectric constant near the percolation threshold of a heterogeneous material.*** Physical Review Letters, 39(19), 1222.
227. Ji, X. L., Jing, J. K., Jiang, W., & Jiang, B. Z. (2002). ***Tensile modulus of polymer nanocomposites.*** Polymer Engineering & Science, 42(5), 983-993.
228. Lu, W., Lin, H., Wu, D., & Chen, G. (2006). ***Unsaturated polyester resin/ graphite nanosheet conducting composites with a low percolation threshold.*** Polymer, 47(12), 4440-4444.

229. Shrivastava, N. K., & Khatua, B. B. (2011). ***Development of electrical conductivity with minimum possible percolation threshold in multi-wall carbon nanotube/ polystyrene composites.*** Carbon, 49(13), 4571-4579.
230. Bauhofer, W., & Kovacs, J. Z. (2009). ***A review and analysis of electrical percolation in carbon nanotube polymer composites.*** Composites Science and Technology, 69(10), 1486-1498.
231. Essam, J. W. (1980). ***Percolation theory.*** Reports on Progress in Physics, 43(7), 833.
232. Berger, C., Yi, Y., Wang, Z. L., & De Heer, W. A. (2002). ***Multiwalled carbon nanotubes are ballistic conductors at room temperature.*** Applied Physics A, 74(3), 363-365.
233. Yu, Y., Song, G., & Sun, L. (2010). ***Determinant role of tunneling resistance in electrical conductivity of polymer composites reinforced by well dispersed carbon nanotubes.*** Journal of Applied Physics, 108(8), 084319.
234. Hu, N., Karube, Y., Yan, C., Masuda, Z., & Fukunaga, H. (2008). ***Tunneling effect in a polymer/carbon nanotube nanocomposite strain sensor.*** Acta Materialia, 56(13), 2929-2936.
235. Simmons, J. G. (1963). ***Generalized formula for the electric tunnel effect between similar electrodes separated by a thin insulating film.*** Journal of applied physics, 34(6), 1793-1803.
236. Frogley, M. D., Ravich, D., & Wagner, H. D. (2003). ***Mechanical properties of carbon nanoparticle-reinforced elastomers.*** Composites Science and technology, 63(11), 1647-1654.
237. Vad, T., Wulfhorst, J., Pan, T. T., Steinmann, W., Dabringhaus, S., Beckers, M., & Weirich, T. E. (2013). ***Orientation of Well-Dispersed Multiwalled Carbon Nanotubes in Melt-Spun Polymer Fibers and Its Impact on the Formation of the Semicrystalline Polymer Structure: A Combined Wide-Angle X-ray Scattering and Electron Tomography Study.*** Macromolecules, 46(14), 5604-5613.
238. Gupta, P., Rajput, M., Singla, N., Kumar, V., & Lahiri, D. (2016). ***Electric field and current assisted alignment of CNT inside polymer matrix and its effects on electrical and mechanical properties.*** Polymer, 89, 119-127.
239. Kim, Y. J., Shin, T. S., Do Choi, H., Kwon, J. H., Chung, Y. C., & Yoon, H. G. (2005). ***Electrical conductivity of chemically modified multiwalled carbon nanotube/epoxy composites.*** Carbon, 43(1), 23-30.
240. Rahmandoust, M., & Ayatollahi, M. R. (2016). ***CNT-Based Nanocomposites.*** In Characterization of Carbon Nanotube Based Composites under Consideration of Defects (pp. 117-175). Springer International Publishing.
241. Zhao, H., Zhou, Z., Dong, H., Zhang, L., Chen, H., & Hou, L. (2013). ***A facile method to align carbon nanotubes on polymeric membrane substrate.*** Scientific reports, 3.
242. Sun, L., Banhart, F., Krasheninnikov, A. V., Rodriguez-Manzo, J. A., Terrones, M., & Ajayan, P. M. (2006). ***Carbon nanotubes as high-pressure cylinders and nanoextruders.*** Science, 312(5777), 1199-1202.
243. Oliva-Avilés, A. I., Avilés, F., Sosa, V., & Seidel, G. D. (2014). ***Dielectrophoretic modeling of the dynamic carbon nanotube network formation in viscous media under alternating current electric fields.*** Carbon, 69, 342-354.
244. Prolongo, S. G., Meliton, B. G., Del Rosario, G., & Urena, A. (2013). ***New alignment procedure of magnetite–CNT hybrid nanofillers on epoxy bulk resin with permanent magnets.*** Composites Part B: Engineering, 46, 166-172.

245. Jia, X., Li, W., Xu, X., Li, W., Cai, Q., & Yang, X. (2015). ***Numerical characterization of magnetically aligned multiwalled carbon nanotube–Fe3O4 nanoparticle complex.*** ACS applied materials & interfaces, 7(5), 3170-3179.
246. Moaseri, E., Karimi, M., Bazubandi, B., Baniadam, M., & Maghrebi, M. (2017). ***Alignment of carbon nanotubes in bulk epoxy matrix using a magnetic-assisted method: Solenoid magnetic field.*** Polymer Science, Series A, 1-8.
247. Goh, P. S., Ismail, A. F., & Ng, B. C. (2014). ***Directional alignment of carbon nanotubes in polymer matrices: contemporary approaches and future advances.*** Composites Part A: Applied Science and Manufacturing, 56, 103-126.
248. Downes, R., Wang, S., Haldane, D., Moench, A., & Liang, R. (2015). ***Strain-Induced Alignment Mechanisms of Carbon Nanotube Networks.*** Advanced Engineering Materials, 17(3), 349-358.
249. Alian, A. R., El-Borgi, S., & Meguid, S. A. (2016). ***Multiscale modeling of the effect of waviness and agglomeration of CNTs on the elastic properties of nanocomposites.*** Computational materials Science, 117, 195-204.
250. Zhang, R., Ning, Z., Zhang, Y., Zheng, Q., Chen, Q., Xie, H., & Wei, F. (2013). ***Superlubricity in centimetres-long double-walled carbon nanotubes under ambient conditions.*** Nature nanotechnology, 8(12), 912-916.
251. Guo, J., Liu, Y., Prada-Silvy, R., Tan, Y., Azad, S., Krause, B., & Grady, B. P. (2014). ***Aspect ratio effects of multi-walled carbon nanotubes on electrical, mechanical, and thermal properties of polycarbonate/MWCNT composites.*** Journal of Polymer Science Part B: Polymer Physics, 52(1), 73-83.
252. Maiti, S., Shrivastava, N. K., Suin, S., & Khatua, B. B. (2013). ***A strategy for achieving low percolation and high electrical conductivity in melt-blended polycarbonate (PC)/multiwall carbon nanotube (MWCNT) nanocomposites: Electrical and thermo-mechanical properties.*** Express Polymer Letters, 7(6).
253. Risi, C. L., Hattenhauer, I., Ramos, A., Coelho, L. A., & Pezzin, S. H. (2015). ***A contribution from dielectric analysis to the study of the formation of multi-wall carbon nanotubes percolated networks in epoxy resin under an electric field.*** Materials Chemistry and Physics, 160, 289-295.
254. Maurer, F. H., & Arza, C. R. (2015). ***Dispersion and interaction of graphene oxide in amorphous and semi-crystalline nano-composites: a PALS study.*** In Journal of Physics: Conference Series (Vol. 618, No. 1, p. 012020). IOP Publishing.
255. Hu, N., Fukunaga, H., Atobe, S., Liu, Y., & Li, J. (2011). ***Piezoresistive strain sensors made from carbon nanotubes based polymer nanocomposites.*** Sensors, 11(11), 10691-10723.
256. *SWeNT SMW Technical Data Sheet* [Online]. Available: `http://thenanoholdings.com/data/goodsImages/GOODS1_1273454997.pdf` [Accessed: 15-Sep-2017].
257. *Nano Graphene Oxide Solution, 125 ml* [Online]. Available: https://graphene-supermarket.com/Nano-Graphene-Oxide-Solution-125-ml.html [Accessed: 15-Sep-2017].
258. Yang, K., Yi, Z., Jing, Q., Yue, R., Jiang, W., & Lin, D. (2013). ***Sonication-assisted dispersion of carbon nanotubes in aqueous solutions of the anionic surfactant SDBS: The role of sonication energy.*** Chinese Science Bulletin, 58(17), 2082-2090.
259. Jain, D., Rouhi, N., Rutherglen, C., Densmore, C. G., Doorn, S. K., & Burke, P. J. (2011). ***Effect of source, surfactant, and deposition process on electronic properties of nanotube arrays.*** Journal of Nanomaterials, 2011, 10.

260. Bystrzejewski, M., Huczko, A., Lange, H., Gemming, T., Büchner, B., & Rümmeli, M. H. (2010). ***Dispersion and diameter separation of multi-wall carbon nanotubes in aqueous solutions.*** Journal of Colloid and Interface Science, 345(2), 138-142.
261. *Owens, Wendt, Rabel and Kaelble (OWRK) method* [Online]. Available: https://www.kruss.de/services/ education-theory/glossary/owens-wendt-rabel-and-kaelble-owrk-method/ [Accessed: 15-Sep-2017].
262. Osswald, T. A., & Menges, G. (2012). ***Materials science of polymers for engineers.*** Carl Hanser Verlag GmbH Co KG.
263. Birdi, K. A. S. (Ed.). (2015). ***Handbook of surface and colloid chemistry.*** CRC Press.
264. Lang, U., Müller, E., Naujoks, N., & Dual, J. (2009). ***Microscopical investigations of PEDOT: PSS thin films.*** Advanced Functional Materials, 19(8), 1215-1220. ISO 690
265. Nardes, A. M., Kemerink, M., Janssen, R. A., Bastiaansen, J. A., Kiggen, N. M., Langeveld, B. M., & De Kok, M. M. (2007). ***Microscopic understanding of the anisotropic conductivity of PEDOT: PSS thin films.*** Advanced Materials, 19(9), 1196-1200.
266. Timpanaro, S., Kemerink, M., Touwslager, F. J., De Kok, M. M., & Schrader, S. (2004). ***Morphology and conductivity of PEDOT/PSS films studied by scanning–tunneling microscopy.*** Chemical Physics Letters, 394(4), 339-343.
267. Lauret, J. S., Voisin, C., Cassabois, G., Delalande, C., Roussignol, P., Jost, O., & Capes, L. (2003). ***Ultrafast carrier dynamics in single-wall carbon nanotubes.*** Physical review letters, 90(5), 057404.
268. Torrens, F. (2006). ***Calculations of organic-solvent dispersions of single-wall carbon nanotubes.*** International journal of quantum chemistry, 106(3), 712-718.
269. Hamada, N., Sawada, S. I., & Oshiyama, A. (1992). ***New one-dimensional conductors: Graphitic microtubules.*** Physical review letters, 68(10), 1579.
270. Saito, R., Fujita, M., Dresselhaus, G., & Dresselhaus, U. M. (1992). ***Electronic structure of chiral graphene tubules.*** Applied physics letters, 60(18), 2204-2206.
271. Kataura, H., Kumazawa, Y., Maniwa, Y., Umezu, I., Suzuki, S., Ohtsuka, Y., & Achiba, Y. (1999). ***Optical properties of single-wall carbon nanotubes.*** Synthetic metals, 103(1-3), 2555-2558.
272. Garreau, S. (2000). ***Etude des potentialités du poly (3, 4- éthylènedioxythiophè -ne)(PEDT) et de ses dérivés à travers les spectroscopies optiques et vibrationnelles.*** (Doctoral dissertation, Université de Nantes).
273. Stafström, S., Bredas, J. L., Epstein, A. J., Woo, H. S., Tanner, D. B., Huang, W. S., & MacDiarmid, A. G. (1987). ***Polaron lattice in highly conducting polyaniline: theoretical and optical studies.*** Physical Review Letters, 59(13), 1464.
274. Qiu, L., Yang, X., Gou, X., Yang, W., Ma, Z. F., Wallace, G. G., & Li, D. (2010). ***Dispersing carbon nanotubes with graphene oxide in water and synergistic effects between graphene derivatives.*** Chemistry-A European Journal, 16(35), 10653-10658.
275. Zhang, C., Ren, L., Wang, X., & Liu, T. (2010). ***Graphene oxide-assisted dispersion of pristine multiwalled carbon nanotubes in aqueous media.*** The Journal of Physical Chemistry C, 114(26), 11435-11440.
276. Stöcker, T., Köhler, A., & Moos, R. (2012). ***Why does the electrical conductivity in PEDOT: PSS decrease with PSS content? A study combining thermoelectric measurements with impedance spectroscopy.*** Journal of polymer science part B: polymer physics, 50(14), 976-983.

277. Kronemeijer, A. J., Katsouras, I., Huisman, E. H., van Hal, P. A., Geuns, T. C., Blom, P. W., & de Leeuw, D. M. (2011). ***Universal Scaling of the Charge Transport in Large-Area Molecular Junctions.*** small, 7(11), 1593-1598.
278. Kim, Y., Ballantyne, A. M., Nelson, J., & Bradley, D. D. (2009). ***Effects of thickness and thermal annealing of the PEDOT: PSS layer on the performance of polymer solar cells.*** Organic Electronics, 10(1), 205-209.
279. Lang, U., Rust, P., Schoberle, B., & Dual, J. (2009). ***Piezoresistive properties of PEDOT: PSS.*** Microelectronic Engineering, 86(3), 330-334.
280. Wang, J. C., Karmakar, R. S., Lu, Y. J., Huang, C. Y., & Wei, K. C. (2015). ***Characterization of piezoresistive PEDOT: PSS pressure sensors with inter-digitated and cross-point electrode structures.*** Sensors, 15(1), 818-831.
281. Barberio, M., Camarca, M., Barone, P., Bonanno, A., Oliva, A., & Xu, F. (2007). ***Electric resistivity of multi-walled carbon nanotubes at high temperatures.*** Surface science, 601(13), 2814-2818.
282. Zhang, H. L., Li, J. F., Zhang, B. P., Yao, K. F., Liu, W. S., & Wang, H. (2007). ***Electrical and thermal properties of carbon nanotube bulk materials: experimental studies for the 328–958 K temperature range.*** Physical Review B, 75(20), 205407.
283. Arya, V. P., Prasad, V., & Kumar, P. A. (2012). ***Effect of magnetic field on Mott's variable-range hopping parameters in multiwall carbon nanotube mat.*** Journal of Physics: Condensed Matter, 24(24), 245602.
284. Loutherback, K. (2006). ***High temperature resistance of metallic single-walled carbon nanotubes.*** Project report, University of California, Irvine.
285. Kuş, M., & Okur, S. (2009). ***Electrical characterization of PEDOT: PSS beyond humidity saturation.*** Sensors and Actuators B: Chemical, 143(1), 177-181.
286. Zhou, J., Anjum, D. H., Chen, L., Xu, X., Ventura, I. A., Jiang, L., & Lubineau, G. (2014). ***The temperature-dependent microstructure of PEDOT/PSS films: insights from morphological, mechanical and electrical analyses.*** Journal of Materials Chemistry C, 2(46), 9903-9910.
287. Huang, J. Y., Chen, S., Jo, S. H., Wang, Z., Han, D. X., Chen, G., & Ren, Z. F. (2005). ***Atomic-scale imaging of wall-by-wall breakdown and concurrent transport measurements in multiwall carbon nanotubes.*** Physical review letters, 94(23), 236802.
288. Varghese, O. K., Kichambre, P. D., Gong, D., Ong, K. G., Dickey, E. C., & Grimes, C. A. (2001). ***Gas sensing characteristics of multi-wall carbon nanotubes.*** Sensors and Actuators B: Chemical, 81(1), 32-41.
289. Crispin, X., Marciniak, S., Osikowicz, W., Zotti, G., van der Gon, A. W., Louwet, F., & Salaneck, W. R. (2003). ***Conductivity, morphology, interfacial chemistry, and stability of poly (3, 4-ethylene dioxythiophene)–poly (styrene sulfonate): A photoelectron spectroscopy study.*** Journal of polymer science Part B: Polymer physics, 41(21), 2561-2583.
290. Stankovich, S., Piner, R. D., Nguyen, S. T., & Ruoff, R. S. (2006). ***Synthesis and exfoliation of isocyanate-treated graphene oxide nanoplatelets.*** Carbon, 44(15), 3342-3347.
291. Wang, S., Zhang, Y., Abidi, N., & Cabrales, L. (2009). ***Wettability and surface free energy of graphene films.*** Langmuir, 25(18), 11078-11081.
292. Perrozzi, F., Prezioso, S., & Ottaviano, L. (2014). ***Graphene oxide: from fundamentals to applications.*** Journal of Physics: Condensed Matter, 27(1), 013002.

293. Ren, P. G., Yan, D. X., Ji, X., Chen, T., & Li, Z. M. (2010). ***Temperature dependence of graphene oxide reduced by hydrazine hydrate.*** Nanotechnology, 22(5), 055705.
294. Wei, T., Luo, G., Fan, Z., Zheng, C., Yan, J., Yao, C., & Zhang, C. (2009). ***Preparation of graphene nanosheet/polymer composites using in situ reduction–extractive dispersion.*** Carbon, 47(9), 2296-2299.
295. Stankovich, S., Dikin, D. A., Piner, R. D., Kohlhaas, K. A., Kleinhammes, A., Jia, Y., & Ruoff, R. S. (2007). ***Synthesis of graphene-based nanosheets via chemical reduction of exfoliated graphite oxide.*** carbon, 45(7), 1558-1565.
296. Estrade-Szwarckopf, H. (2004). ***XPS photoemission in carbonaceous materials: A "defect" peak beside the graphitic asymmetric peak.*** Carbon, 42(8), 1713-1721.
297. Im, H., & Kim, J. (2012). ***Thermal conductivity of a graphene oxide–carbon nanotube hybrid/epoxy composite.*** Carbon, 50(15), 5429-5440.
298. Zhang, Q., Yang, S., Zhang, J., Zhang, L., Kang, P., Li, J., & Song, X. M. (2011). ***Fabrication of an electrochemical platform based on the self-assembly of grapheneoxide–multiwall carbon nanotube nanocomposite and horseradish peroxidase: directelectrochemistry and electrocatalysis.*** Nanotechnology, 22 (49), 494010.
299. Hintze, P. E., Kjaergaard, H. G., Vaida, V., & Burkholder, J. B. (2003). ***Vibrational and electronic spectroscopy of sulfuric acid vapor.*** The Journal of Physical Chemistry A, 107(8), 1112-1118.
300. Qiu, L., Yang, X., Gou, X., Yang, W., Ma, Z. F., Wallace, G. G., & Li, D. (2010). ***Dispersing carbon nanotubes with graphene oxide in water and synergistic effects between graphene derivatives.*** Chemistry-A European Journal, 16(35), 10653-10658.
301. Cai, D., Song, M., & Xu, C. (2008). ***Highly Conductive Carbon-Nanotube/ Graphite-Oxide Hybrid Films.*** Advanced Materials, 20(9), 1706-1709.
302. Liu, L., Zhang, J., Zhao, J., & Liu, F. (2012). ***Mechanical properties of graphene oxides.*** Nanoscale, 4(19), 5910-5916.
303. Mohiuddin, M., & Van Hoa, S. (2011). ***Electrical resistance of CNT-PEEK composites under compression at different temperatures.*** Nanoscale research letters, 6(1), 419.
304. Di Bartolomeo, A., Sarno, M., Giubileo, F., Altavilla, C., Iemmo, L., Piano, S., & Cucolo, A. M. (2009). ***Multiwalled carbon nanotube films as small-sized temperature sensors.*** Journal of Applied Physics, 105(6), 064518.
305. Kuo, J. T., Yu, L., & Meng, E. (2012). ***Micromachined thermal flow sensors—A review.*** Micromachines, 3(3), 550-573.
306. Russ, B., Glaudell, A., Urban, J. J., Chabinyc, M. L., & Segalman, R. A. (2016). ***Organic thermoelectric materials for energy harvesting and temperature control.*** Nature Reviews Materials, 1, 16050.
307. Zhang, D., Tong, J., & Xia, B. (2014). ***Humidity-sensing properties of chemically reduced graphene oxide/polymer nanocomposite film sensor based on layer-by-layer nano self-assembly.*** Sensors and Actuators B: Chemical, 197, 66-72.
308. Su, P. G., & Chiou, C. F. (2014). ***Electrical and humidity-sensing properties of reduced graphene oxide thin film fabricated by layer-by-layer with covalent anchoring on flexible substrate.*** Sensors and Actuators B: Chemical, 200, 9-18.
309. Lu, G., Ocola, L. E., & Chen, J. (2009). ***Reduced graphene oxide for room-temperature gas sensors.*** Nanotechnology, 20(44), 445502.
310. Jung, I., Vaupel, M., Pelton, M., Piner, R., Dikin, D. A., Stankovich, S., & Ruoff, R. S. (2008). ***Characterization of thermally reduced graphene oxide by imaging ellipsometry.*** The Journal of Physical Chemistry C, 112(23), 8499-8506.

311. Kumar, P., Singh, A. K., Hussain, S., Hui, K. N., San Hui, K., Eom, J., & Singh, J. (2013). ***Graphene: synthesis, properties and application in transparent electronic devices.*** Reviews in Advanced Sciences and Engineering, 2(4), 238-258.
312. Borini, S., White, R., Wei, D., Astley, M., Haque, S., Spigone, E., & Ryhanen, T. (2013). ***Ultrafast graphene oxide humidity sensors.*** ACS nano, 7(12), 11166-11173.
313. Cerveny, S., Barroso-Bujans, F., Alegria, A., & Colmenero, J. (2010). ***Dynamics of water intercalated in graphite oxide.*** The Journal of Physical Chemistry C, 114(6), 2604-2612.
314. Agmon, N. (1995). ***The grotthuss mechanism.*** Chemical Physics Letters, 244(5), 456-462.
315. Sarker, A. K., Kim, J., Wee, B. H., Song, H. J., Lee, Y., Hong, J. D., & Lee, C. (2015). ***Hydroiodic acid treated PEDOT: PSS thin film as transparent electrode: an approach towards ITO free organic photovoltaics.*** RSC Advances, 5(64), 52019-52025.
316. Ouyang, J., Xu, Q., Chu, C. W., Yang, Y., Li, G., & Shinar, J. (2004). ***On the mechanism of conductivity enhancement in poly (3, 4- ethylenedioxythiophene): poly (styrene sulfonate) film through solvent treatment.*** Polymer, 45(25), 8443-8450.
317. Bae, E. J., Kang, Y. H., Jang, K. S., & Cho, S. Y. (2016). ***Enhancement of thermoelectric properties of PEDOT: PSS and tellurium-PEDOT: PSS hybrid composites by simple chemical treatment.*** Scientific reports, 6, 18805.
318. Zuppiroli, L., Bussac, M. N., Paschen, S., Chauvet, O., & Forro, L. (1994). ***Hopping in disordered conducting polymers.*** Physical Review B, 50(8), 5196.
319. Abraham, A., Okram, G. S., Jacob, R., Sreenivasan, P. V., & Philip, R. R. (2016). ***Low temperature electrical conductivity and seebeck coefficient of nanostructured CuSe thin films with Ga addition.*** Vacuum, 129, 74-78.
320. Sharma, P., Gupta, A., Rao, K. V., Owens, F. J., Sharma, R., Ahuja, R., & Gehring, G. A. (2003). ***Ferromagnetism above room temperature in bulk and transparent thin films of Mn-doped ZnO.*** Nature materials, 2(10), 673.
321. Massarani, B., Bourgoin, J. C., & Chrenko, R. M. (1978). ***Hopping conduction in semiconducting diamond.*** Physical Review B, 17(4), 1758.
322. Zürcher, J. F., & Gardiol, F. E. (1995). ***Broadband patch antennas*** (No. LEMA-BOOK-1995-001). Artech House.
323. Deschamps, G. A., & Sichak, W. (1953, October). ***Microstrip microwave antennas.*** In 3rd USAF Symposium on Antennas (pp. 103-105).
324. Munson, R. (1974). ***Conformal microstrip antennas and microstrip phased arrays.*** IEEE Transactions on Antennas and propagation, 22(1), 74-78.
325. Balanis, C. A. (Ed.). (2011). ***Modern antenna handbook.*** John Wiley & Sons.
326. Daliri, A., Galehdar, A., Rowe, W. S., John, S., Wang, C. H., & Ghorbani, K. (2014). ***Quality factor effect on the wireless range of microstrip patch antenna strain sensors.*** Sensors, 14(1), 595-605.
327. Jackson, D. R., Williams, J. T., Bhattacharyya, A. K., Smith, R. L., Buchheit, S. J., & Long, S. A. (1993). ***Microstrip patch designs that do not excite surface waves.*** IEEE Transactions on antennas and propagation, 41(8), 1026-1037.
328. Elmezughi, A. S., Rowe, W. S. T., & Waterhouse, R. B. (2008, July). ***Cavity backed hi-lo stacked patch antennas.*** In Antennas and Propagation Society International Symposium, 2008. AP-S 2008. IEEE (pp. 1-4). IEEE.

329. Gonzalo, R., De Maagt, P., & Sorolla, M. (1999). ***Enhanced patch-antenna performance by suppressing surface waves using photonic-bandgap substrates.*** IEEE Transactions on Microwave Theory and Techniques, 47(11), 2131-2138.
330. Jaglan, N., & Gupta, S. D. (2015). ***Design and analysis of performance enhanced microstrip patch antenna with EBG substrate.*** International Journal of Microwave and Optical Technology, 10(2), 79-88.
331. Weng, L. H., Guo, Y. C., Shi, X. W., & Chen, X. Q. (2008). ***An overview on defected ground structure.*** Progress In Electromagnetics Research B, 7, 173-189.
332. Lo, Y. T., Solomon, D., & Richards, W. (1979). ***Theory and experiment on microstrip antennas.*** IEEE Transactions on Antennas and Propagation, 27(2), 137-145.
333. Carver, K., & Mink, J. (1981). ***Microstrip antenna technology.*** IEEE transactions on antennas and propagation, 29(1), 2-24.
334. Rana, I., & Alexopoulos, N. (1981). ***Current distribution and input impedance of printed dipoles.*** IEEE Transactions on Antennas and Propagation, 29(1), 99-105.
335. Kumar, G., & Ray, K. P. (2003). ***Broadband microstrip antennas.*** Artech House.
336. Matin, M. A., & Sayeed, A. I. (2010). ***A design rule for inset-fed rectangular microstrip patch antenna.*** WSEAS Transactions on Communications, 9(1), 63-72.

List of Figures

List of Tables

Curriculum Vitae

Education

- **2013–2017** PhD. Student, Technische Universität Chemnitz, Faculty of Electrical Engineering and Information Technology, Professorship of Measurement and Sensor Technology, Chemnitz, Germany
- **2008–2012** M.Sc. in Micro and Nanosystem, Technische Universität Chemnitz, Faculty of Electrical Engineering and Information Technology, Chemnitz, Germany
- **2000–2006** B.Sc. University of Al-Jabal Al-Garby, Faculty of Engineering, Department of Electrical and Electronic Engineering, Gharien, Libya

Work Experience

- **02.2012–10.2017** University Researcher Assistant: Professorship of Measurement and Sensor Technology, Faculty of Electrical Engineering and Information Technology, Technische Universität Chemnitz, Chemnitz, Germany
- **07.2010–07.2010** Hiwi-Job: Professorship of Measurement and Sensor Technology, Faculty of Electrical Engineering and Information Technology, Technische Universität Chemnitz, Chemnitz, Germany
- **10.2010–11.2010** Hiwi-Job: Printed Functionality Department, ENAS Fraunhofer, Chemnitz, Germany
- **07.2010–07.2010** Hiwi-Job: Professorship of Measurement and Sensor Technology, Faculty of Electrical Engineering and Information Technology, Technische Universität Chemnitz, Chemnitz, Germany
- **05.2010–07.2010** Hiwi-Job: Professorship of Electronic Components, Faculty of Electrical Engineering and Information Technology, Technische Universität Chemnitz, Chemnitz, Germany
- **02.2009–04.2009** Hiwi-Job: Center for Micro Technology, Faculty of Electrical Engineering and Information Technology, Technische Universität Chemnitz, Chemnitz, Germany

Trainings and Courses

- **09.2017** Advanced School in Impedance Spectroscopy: Technische Universität Chemnitz, Chemnitz, Germany
- **10.2016** Nano- Tech Summer School: Jordan University, Amman, Jordan
- **09.2016** Nano- Tech Summer School: Technische Universität Chemnitz, Chemnitz, Germany
- **05.2016** Training: Introduction to teaching software using CES EduPack, Technische Universität Dresden, Dresden, Germany
- **05.2016** Training: Material selection for research using CES Selector, Technische Universität Dresden, Dresden, Germany
- **06.2009** Training: Introduction to PIC18 Architecture MCU2101, Technische Universität Chemnitz, Chemnitz, Germany
- **06.2009** Training: Introduction to integrated development of MPLAB-IDE TLS101, Technische Universität Chemnitz, Chemnitz, Germany

Awards

- **09.2016** Best Paper Winner: 9^{th} International Workshop on Impedance Spectroscopy, Chemnitz, Germany

Publications

Patent

2017

- **A. Benchirouf**, O. Kanoun, "Ultra High Sensitive Microwave Antenna Integrated with Tertiary Nanocomposite Material", USt-IdNr. DE140857609.

Peer-Reviewed Journals

2017

- **A. Benchirouf**, V. Dzhagan, D. Zahn, O. Kanoun, "Conduction Dependency on Temperature and Humidity of rGO:MWCNT Films", submitted to Carbon.
- **A. Benchirouf**, O. Kanoun, "Inductive Coupling of Passive Strain Sensor based on Inkjet Printed MWCNTs", submitted to Composites Science and Technology.
- R. Torres, A. Jalasutram, **A. Benchirouf**, C. Müller and O. Kanoun, "Study of Elongation and Temperature Effects on Nanocomposite Based on Elastic Fiber", Proceedings, vol. 1 (389).
- A. Sanli, **A. Benchirouf**, C. Müller, O. Kanoun, "Piezoresistive Performance Characterization of Strain Sensitive Multi-Walled Carbon Canotube-Epoxy Nanocomposites", Sensor & Actuators :A. Physical, vol. 254, pp. 61-68.

2016

- A. Sanli, **A. Benchirouf**, C. Müller, O. Kanoun, "Progress Reports on Impedance Spectroscopy Measurements, Modeling, and Application", Proc. of AC Impedance Investigation of the Multiwalled Carbon Nanotubes /PEDOT:PSS Nanocomposites Fabricated at Different Sonication Time, Oldenburg, Germany. Berlin: Walter De Gruyter GmbH & KG.
- **A. Benchirouf**, C. Müller, O. Kanoun, "Electromechanical Behavior of Chemically Reduced Graphene Oxide and Multi-walled Carbon Nanotube Hybrid Material", Nanoscale Research Letters, vol. 4, pp-1-70.

2015

- **A. Benchirouf**, S. Panaliyappan, R. Ramalingame, P. Raghunandan, T. Jagemann, C. Müller, M. Hietschold, O. Kanoun, "Electrical Properties of Multi-Walled Carbon Nanotubes/PEDOT:PSS Nanocomposites Thin Films under Temperature and Humidity Effects", Sensors and Actuators B: Chemical, vol. 224 (1), pp. 344-350.
- **A. Benchirouf**, R. Zichner, C. Müller, O. Kanoun, "Electromagnetic Simulation of Flexible Strain Sensor based Microstrip Patch Antenna'", International Journal of Microwave and Optical Technology, vol. 10 (6), pp. 397-401.

2014

- O. Kanoun, C. Müller, **A. Benchirouf**, A. Sanli, T. Dinh, A. Al-Hamry, L. Bu, C. Gerlach, A. Bouhamed, "Flexible Carbon Nanotube Films for High Performance Strain Sensors", Sensors, vol. 14(6), pp. 10042-71.
- O. Kanoun, C. Müller, **A. Benchirouf**, A. Sanli, A. Bouhamed, A. Al-Hamry, "Potential of Flexible Carbon Nanotube Films for High Performance Strain and Pressure Sensors", Nanotechnology for optics and sensors, Chapter: 6, Publisher: One Central Press (OCP), Editors: Mahmood Aliofkhazraei, pp. 148-183.

Oral Presentations

2017

- **A. Benchirouf**, O. Kanoun, "Ultrahigh Sensitive Temperature Sensor based Microstrip Patch Antenna using Nanocomposites". 16^{th} International Symposium on Microwave and Optical Technology (ISMOT 2017), 26-28 June, Seoul, South Korea

2016

- A. Sanli, V. Jayaraman, **A. Benchirouf**, C. Müller, O. Kanoun, "Study of the Humidity Effect on the Electrical Impedance of MWCNTs/Epoxy Nanocomposites". 9^{th} International Workshop on Impedance Spectroscopy (IWIS), Chemnitz, Germany

2015

- **A. Benchirouf**, R. Zichner, C. Müller, O. Kanoun, "Flexible Strain Sensor based Microstrip Patch Antenna", 11^{th} International Symposium on Microwave and Optical Technology, Dresden, Germany
- **A. Benchirouf**, A. Sanli, S. Palanisamy, A. Bouhamed, C. Müller, O. Kanoun, "The Piezoresistive Performance Investigation of Multifunctional Genuine Nanocomposites Thin Films", 12^{th} International Multi-Conference on Systems, Signals and Devices, Mahdia, Tunisia
- O. Kanoun, C. Müller, **A. Benchirouf**, A. Sanli, C. Gerlach, A. Bouhamed: "Carbon Nanotube Polymer Composites for High Performance Strain Sensors, 1^{st} Workshop on Nanotechnology in Instrumentation and Measurement- NANOfIM. ISSN: 9788896496381. Lecce, Italy, July 2015.
- A. Sanli, **A. Benchirouf**, J. Kurian, S. Choudhary, S. Paul, A. Bouhamed, C. Müller, O. Kanoun, "Physical Aging Investigation of Carbon Nanotube/ PEDOT:PSS Nanocomposites by Electrochemical Impedance Spectroscopy", 12^{th} International Multi-Conference on Systems, Signals and Devices, Mahdia, Tunisia
- A. Bouhamed, **A. Benchirouf**, A. Sanli, C. Müller, O. Kanoun, "Piezoresistive Behavior of Epoxy/MWCNTs Nanocomposites Thin Films for Strain Sensing Application", 12^{th} International Multi-Conference on Systems, Signals and Devices, Mahdia, Tunisia
- A. Sanli, **A. Benchirouf**, A. D. Thakur, C. Müller, O. Kanoun, "Impedance Characterization of Multiwalled Carbon Nanotubes/Polymer based Flexible Thin Film Piezoresistive Strain Sensors", 16^{th} Topical Meeting of the International Society of Electrochemistry, Angra DOS Reis, Brazil

2014

- A. Abdelkafi, A. Fendri, F. Wendler, P. Büschel, T. Günther, **A. Benchirouf**, R. Gruden, O. Kanoun, "Investigation of Electrode Surfaces of a Water Quality Sensor by Local Impedance Spectroscopy", 2014 IEEE International Instrumentation and Measurement Technology Conference, Montevideo, Uruguay
- A. Sanli, **A. Benchirouf**, S. Panaliyappan, R. Ramalingame, R. Sharma, C. Müller, O. Kanoun, "DC-Bias effect on the dielectric properties of multiwalled carbon nan-

otubes/PEDOT:PSS nanocomposites", 2014 IEEE International Instrumentation and Measurement Technology Conference (I^2MTC), Montevideo, Uruguay

- A. Sanli, **A. Benchirouf**, P. Soumya, S. Choudhary, D. T. Abhimanyu, I. El-Houdaigui, C. Müller, O. Kanoun, "AC Impedance Investigation of the Multi-walled Carbon Nanotubes/PEDOT: PSS Nanocomposites Fabricated at Different Sonication Times" 9^{th} International Workshop on Impedance Spectroscopy, Chemnitz, Germany
- R. Sharma, A. Al-Hamry, S. Vijayragavan, **A. Benchirouf**, A. Sanli, C. Müller, O. Kanoun, "Single-Wall Carbon Nanotubes Based Near-Infrared Sensors on Flexible Substrate", International Multi-Conference on Systems, Signals and Devices, Barcelona, Spain
- **A. Benchirouf**, A. Sanli, I. El-Houdaigui, M. Bashorun, J. Ciers, C. Müller, O. Kanoun, "Evaluation of the Piezoresistive Behavior of Multifunctional Nanocomposites Thin Films", International Multi-Conference on Systems, Signals and Devices, Barcelona, Spain

2013

- A. Sanli, **A. Benchirouf**, R. Ramalingame, S. Palaniyappan, R. Sharma, C. Müller, O. Kanoun, "Characterization of the dielectric properties of multiwalled carbon nanotubes (MWCNTs) /PEDOT:PSS nanocomposites", International Multi-Conference on Systems, Signals and Devices, Barcelona, Spain, 2014.
- **A. Benchirouf**, I. El-Houdaigui, A. Sanli, C. Müller, O. Kanoun, "Influence of Processing Parameters on the Electrochemical Performance and Aging of Aqueous Multi-Walled Carbon Nanotube/PEDOT:PSS Suspensions", 6^{th} International Conference on Carbon NanoParticle Based Composites, Dresden, Germany, 22-25 September 2013.
- **A. Benchirouf**, A. Jalil, O. Kanoun, "Effect of Humidity on Thin Films based dispersed Multi-Walled Carbon Nanotubes", International Multi-Conference on Systems, Signals and Devices, March 2013, Hammammet, Tunis.

Poster Presentations

2013

- **A. Benchirouf**, A. Sanli, M. Bashorun, R. Ramalingame, S. Palaniyappan, C. Müller, O. Kanoun, "AC-Study of Electrochemical Properties of Multi-Walled Carbon Nanotubes / PEDOT:PSS Composites", 6^{th} International Workshop on Impedance Spectroscopy (IWIS'13), Chemnitz, Germany, 2013.
- **A. Benchirouf**, A. Al-Hamry, T. Jagemann, C. Müller, S. Schulze, M. Hietschold, O. Kanoun, "Sensitive Strain Sensor Based Chemically Reduced Graphene Oxide and Multi Walled Carbon Nanotubes Hybrid Materials", 14^{th} Trends in Nanotechnology International Conference, Seville, Spain, 9-13 September 2013.
- A. Al-Hamry, **A. Benchirouf**, S. Vijayaragavan, D. Lehmann, C. Müller, D. R. Zahn and O. Kanoun, "Infrared Sensors Based Graphene Oxide and Graphene Oxide/Carbon Nanotube Nanocomposites", 14^{th} Trends in Nanotechnology International Conference, Seville, Spain, 9-13 September 2013.
- **A. Benchirouf**, A. Al-Hamry, A. Jalil, O.D. Gordan, C. Müller, O. Kanoun, D.R.T. Zahn, "Humidity Sensitivity of Thin Films Based on Dispersed Multi-Walled Carbon Nanotubes", 14^{th} International Conference on the Science and Application of Nanotubes, Aalto University, Espoo, Finland, 24-28 June 2013.
- A. Al-Hamry, **A. Benchirouf**, S. Vijayaragavan, D. Lehmann, C. Müller, D.R.T. Zahn, O. Kanoun, "Infrared Sensors Based Graphene Oxide and Graphene Oxide/Carbon Nanotube Nanocomposites", Graphene Week 2013, Chemnitz, Germany, 2-7 June 2013.

List of Supervised Students with Topics

Master Thesis

2017

- Swati Poduval: Development of control and data processing routines for a redox flow battery test bench
- Ramesh Rinya: Design and Development of a Compact Dynamic Test Bench for a Power Pack in Steering Systems

2016

- Laveen Prabhu Selvaraj: Multiphysics Simulation of CNT Nanocomposites based Tactile Array Pressure Sensor

2015

- Prabhu Nama Krishna Murthy: Multiphysics Simulation of CNT Nanocomposites
- Poornima Raghunandan: Flexible Piezoresistive Pressure Sensor using MWCNT and PDMS
- Saurabh Kumar Choudhary: Alignment of Silver Nanowires for Printed Electronics Applications
- Rajarajan Ramalingame: Simulation and Fabrication of SHF RFID Strain Sensor based on Nanocomposites
- Saravanan Palaniyappan: Simulation and Fabrication of SHF RFID Strain Sensor based on Nanocomposites

2013

- Nabile Kristou: Design and simulation of flexible patch antenna-based strain sensor

Diplomarbeit

2014

- Issam El Houdaigui: Piezoresistive Empfindlischkeit von Elektromeschanischen Sensoren basieren auf mehrwandigen Kohlenstoffnanoröhrchen MWCNT/ PEDOT:PSS-Filmschichten

Research Projects

2017

- Bhushan Subhash Todkar: Humidity Study of Carbon Nanotubes Polymer Composites Thin Films
- Rinya Ramesh: Control and Acquisition System of an Universal Force Test Machine
- Swati Poduval: Control and Acquisition System of an Universal Force Test Machine

2015

- Shanmuganathan Palanisamy: Piezoresistive Investigation of MWCNT:GO/ PEDOT:PSS Nanocomposite on Flexible Substrate
- Poornima Raghunandan: Temperature Dependency of Carbon Nanotube Resistivity based Polymer Thin Films
- Varun Sharma: Strain Sensitivity Improvement of PEDOT:PSS Thin Films based Gold Nanoparticles doped Carbon Nanomaterials

2014

- Rajarajan Ramalingame: Morphological, Electrical and Enviromental Study of CNT/ Conductive Polymer Composite Film
- Saravanan Palaniyappan: Morphological, Electrical and Enviromental Study of CNT/ Conductive Polymer Composite Film

2013

- Senaz Mehdipour: Literature Survey of the Temperature Dependency of Carbon Nanotube Conductivity

2012

- Abdu-ur-Rehman Jalil: Humidity Sensing using Physically treated Multi-Walled Carbon Nanotubes Thin Films

Scientific Reports on Measurement and Sensor Technology

1. Bouchaala, Dhouha (2016):
   Investigation of Current Excitation for Personal Health and Biological Tissues Monitoring
   ISBN 978-3-941003-96-9
   Volltext: http://nbn-resolving.de/urn:nbn:de:bsz:ch1-qucosa-204801

2. Heidary Dastjerdi, Maral (2016):
   Ein Beitrag zur Verbesserung der Eigenschaften magnetisch-induktiver Tastspulen
   ISBN 978-3-944640-98-3
   Volltext: http://nbn-resolving.de/urn:nbn:de:bsz:ch1-qucosa-207628

3. Guermazi, Mahdi (2016):
   In-Vitro Biological Tissue State Monitoring based on Impedance Spectroscopy
   ISBN 978-3-96100-003-6
   Volltext: http://nbn-resolving.de/urn:nbn:de:bsz:ch1-qucosa-206710

4. Viehweger, Christian (2017):
   Modellbasiertes Energiemanagement fur die intelligente Steuerung solarversorgter- drahtloser Sensorsysteme
   ISBN 978-3-96100-022-7
   Volltext: http://nbn-resolving.de/urn:nbn:de:bsz:ch1-qucosa-224040

5. Gerlach, Carina (2017):
   Dispersionsoptimierung von Kohlenstoffnanorohren fur die Herstellung von Polymer-Komposit-Drucksensoren
   ISBN 978-3-96100-025-8
   Volltext: http://nbn-resolving.de/urn:nbn:de:bsz:ch1-qucosa-226222

6. Sanli, Abdulkadir (2018):
   Synthesis and Characterization of Strain Sensitive Multi-walled Carbon Nanotubes/Epoxy based Nanocomposites
   ISBN 978-3-96100-047-0
   Volltext: http://nbn-resolving.de/urn:nbn:de:bsz:ch1-qucosa-233763

7. Weber, Christian (2018):
   Entwicklung eines Verfahrens zur Anhaftungserkennung und Trennung von Einflussgroßen bei kapazitiven Naherungsschal- tern mit Hilfe der Impedanzspektroskopie
   ISBN 978-3-96100-056-2
   Volltext: http://nbn-resolving.de/urn:nbn:de:bsz: ch1-qucosa2-234856

8. Benchirouf, Abderrahmane (2018):
   Carbonaceous Nanofillers and Poly (3,4- ethylenedioxythiophene) Poly(styrenesulfonate) Nanocomposites for Wireless Sensing Applications
   ISBN 978-3-96100-068-5
   Volltext: http://nbn-resolving.de/urn:nbn:de:bsz:ch1-qucosa2-319037